New directions in cosmology and astrophysics

Imperial College London

Selim Can Hotinli

Department of Physics
Imperial College London

A thesis submitted for the degree of
Doctor of Philosophy

October 2020

Abstract

To a good approximation, our Universe is flat and homogeneous, strongly suggesting a period like inflation, a rapid accelerated expansion, in the early Universe. We believe inflation also transformed quantum mechanical perturbations to classical, seeding the large-scale structure today. Overwhelming empirical evidence suggests, moreover, that these perturbations were nearly Gaussian and are well described by adiabatic initial conditions that are predicted by the simplest inflationary models. Following inflation, we find the Universe can be characterised by the ΛCDM model which has become the bedrock of modern cosmology, and survived many challenges from the influx of cosmological data in the past decade. In the upcoming years, however, the field of cosmology will see a wealth of new and high quality data from the current Stage-3 (and the forthcoming Stage-4) surveys of the cosmic microwave background (CMB) and large-scale structure (LSS). Simultaneously, low-frequency gravitational wave background (GWB) observations with pulsar-timing arrays (PTAs) and surveys of the 21cm hydrogen-line will achieve sufficient accuracy for cosmological inference. These create unique and exciting opportunities to study the fundamental components of the Universe. These experiments will provide the strongest challenges to our modern cosmological picture yet, and have the potential of revolutionising our understanding of the most fundamental properties of our Universe. In this work I discuss various new opportunities provided by upcoming precision measurements of CMB and galaxy surveys, as well as the upcoming measurements of 21cm hydrogen brightness temperature. This thesis utilises some of these upcoming cosmological probes for the detection of physics different than what is predicted by ΛCDM with the simplest inflationary models.

Declaration

This dissertation is the result of my own work and does not include work of others and is not the outcome of work done in collaboration *except* as declared below and in the text, where specific reference is made to the work of others. Note modern research in cosmology is predominantly done in collaboration and the results in this dissertation and most of the material is a result of such collaborative research. In particular Chapters 3, 5, 6, 7, 8 and 9 are based on work done in collaboration with collaborators. Work in Chapter 3 is done in collaboration with Jonathan Frazer, Andrew Jaffe, Joel Meyers, Layne Price and Ewan Terrant. Work in Chapter 5 is done in collaboration with Joel Meyers, Neal Dalal, Andrew Jaffe, Matthew Johnson, Kendrick Smith, Moritz Munchmeyer, Alex van Engelen, James Mertens. Work in Chapter 6 is done in collaboration with Matthew Johnson, James Mertens, Marc Kamionkowski as well as Neal Dalal and Mat Madhavacheril. Work in Chapter 7 is done in collaboration with Daniel Green, Joel Meyers and Alex van Engelen. Work in Chapter 8 is done in collaboration with Tom Binnie, Bikash Dinda, Marc Kamionkowski and Julian Munoz. Work in Chapter 9 is done in collaboration with Marc Kamionkowski and Andrew Jaffe. I have made major contributions to the research in all of these Chapters both in terms of results and writing. All figures presented in this dissertation are either produced or adapted by or received contribution from myself. My contributions as well as contributions of my collaborators to the presented works are described clearly in the Introduction as well as at the beginning of every Chapter.

I hereby declare that this dissertation is not substantially the same as any other dissertations I have submitted or being currently submitted for a degree, diploma or other qualifications at the Imperial College London, or any other University of similar institution.

Selim Can Hotinli
October 2020

Acknowledgements

First, I thank my supervisor Andrew Jaffe who has been a limitless source of inspiration and intellectual drive throughout my degree. I have no doubt that the high standard of academic brilliance set by his example will continue to guide me in my academic career.

I also thank Joel Meyers, whose supervision, guidance and example has made me a much better young academic than I could ever hoped for. Alongside his brilliance, Joel's kindness and humbleness has provided me with an example of decency that I hope I will look up to throughout my life.

I thank Matthew Johnson who has also been the most thoughtful, kind and generous supervisor I could have ever wished for. His ongoing support and guidance has been absolutely invaluable.

I thank Marc Kamionkowski, whose endless kind support and whose belief in me, I only hope I can live up to. His influence on how I think about research is unmatched and I am excited beyond measure to get to continue working together in the future where I will continue to be inspired by his brilliance, his creativity and his limitless enthusiasm.

I also thank my other inspiring co-workers, supervisors and collaborators, including Kendrick Smith, whose positivity and kindness is only matched by his genius; as well as Jonathan Braden, Neal Dalal, Stephen Feeney, Jonathan Frazer, Dan Green, Mathew Madhavacheril, James Mertens, Moritz Munchmeyer, Emanuel Schaan, Alex van Engelen. I wish to thank my fantastic friends and colleagues from Imperial, Tom, Sanjay, Connor, Sebastian, Janina and Marija who made past few years much more wonderful. I continue to be inspired by their dedication and brilliance and have learned so much from each one of them.

I also like to thank the President's Scholarship, which made my studies possible and comfortable. I thank the Imperial astrophysics group for their support in various ways.

Finally, I wish to thank my parents. I love you both and I can't thank you enough for your kind and thoughtful support throughout the years, and for giving me the sense of thrust and belief in myself to pursue and overcome this challenge.

To my loving parents . . .

Contents

List of figures

List of tables

Chapter 1

Introduction

In this thesis I explore the prospects of utilising some of the upcoming observables for the purpose of understanding fundamental properties of the Universe. I take the ΛCDM model as the basis of modern cosmological prediction and discuss various ways in which physics different than that dictated by ΛCDM can affect observables. I develop various novel methods to evaluate the sensitivity of the upcoming cosmology experiments to these deviations.

In Chapter 2, I begin with a pedagogical introduction to the modern cosmological picture. I follow textbooks on modern cosmology by Weinberg [1], Dodelson [2], Mukhanov [3] and Peebles [4], as well as various review articles and lecture notes including [5–10]. In Sections 2.2.2, 2.3.2 and 2.7, I follow on the lines of the pedagogical review I have written for my upcoming paper in collaboration with Janina Renk, Patrick Stöcker, Sanjay Bloor and others [11].

In Chapter 3, I discuss my work on multi-field inflation and reheating in collaboration with Jonathan Frazer, Andrew Jaffe, Joel Meyers, Layne Price and Ewan Tarrant [12]. The work in the chapter is motivated by the fact that the single-field inflationary models discussed in Chapter 2 are not always natural from a theoretical point of view, for example, string compactifications often result in hundreds of scalar fields.

In Chapter 4, I introduce second-order perturbations in the CMB, so-called 'CMB Secondaries'. Secondary effects on the cosmological radiation observed by our telescopes will become observationally much more significant in the near future as CMB and LSS surveys will achieve the necessary precision. The statistics of these secondaries and their cross-correlations with the LSS carry information about cosmological fluctuations on large scales and at late times. The relevant scientific program is focused on various inter-connected tasks, including the mitigation of these effects on the primary CMB and reconstruction of large-scale

cosmological density and velocity fields. Similar to Chapter 2, I follow seminal textbooks on modern cosmology, as well as various review articles and lecture notes [1–10, 13, 14].

In Chapter 5, I introduce the moving lens effect and describe my works in [15], in collaboration with Joel Meyers, Neal Dalal, Andrew Jaffe, Matthew Johnson, Moritz Munchmeyer, James Mertens and Alex van Engelen, and in [16], in collaboration with Matthew Johnson and Joel Meyers.

In Chapter 6, I discuss my published work with James Mertens, Matthew Johnson and Marc Kamionkowski [17] on utilising the kSZ reconstructed radial velocity measurements to constrain a specific form of isocurvature, and my upcoming work with Mathew Madhavacheril and Neal Dalal on developing a novel method to evaluate the detection prospects of the dark-energy clustering.

In Chapter 7, I discuss ongoing work with Daniel Green, Joel Meyers and Alex van Engelen on mitigating the effects of lensing from the CMB spectra. I introduce an all-orders delensing method which iteratively applies the quadratic lensing reconstruction estimator. This project will be published in the near future with a publicly available code and an accompanying science paper.

In Chapter 8, I discuss my upcoming work with Marc Kamionkowski, Bikash Dinda, Tom Binnie and Julian Munoz on utilising 21cm hydrogen signal from the epoch of cosmic dawn to constrain compensated isocurvature perturbations.

In Chapter 9, I digress and discuss prospects of detecting deviations from statistical isotropy in the gravitational wave background from super-massive black holes. This chapter discusses the work I have done with Marc Kamionkowski and Andrew Jaffe.

Chapter 2

Modern Cosmological Picture

Cosmology is the branch of physics that studies the origin, structure and evolution of the Universe quantitatively. Thanks to many significant experimental efforts, he scientific study of cosmology has drastically evolved in the past decades, emerging as a data-driven field of precision science. The analysis and observation of the temperature anisotropies in the cosmic microwave background (CMB) by COBE [18], WMAP [19] and *Planck* [20] as well as the distance measurements to type Ia Supernovae [21, 22] and the large-scale structure from galaxy surveys such as 2DFGRS [23], SDSS [24] and BOSS [25] have greatly improved our understanding of the contents and the physics of our Universe. In this chapter I discuss the standard modern cosmological picture afforded by these advances in observations and analysis in the past decade. I begin by describing the Universe in the homogeneous limit in Section 2.1 where I introduce the Friedman-Lemaître-Robertson-Walker (FLRW) metric and the dynamical equations of motion of the background in Section 2.1.1. I then discuss the standard cosmological paradigm: ΛCDM in Section 2.1.2. I introduce the cosmological perturbations around the background in 2.2. I continue with the discussion of inflation and reheating in Section 2.3. I discuss the thermal and isotropic Universe in Section 2.4 and deviations from isotropy with the Boltzmann equation in Sections 2.5 and 2.6. I introduce various cosmological observables in Section 2.7.

The pedagogical discussions in this chapter introduce the canonical cosmological understanding and use common notation. Overall, I follow seminal textbooks on modern cosmology by Weinberg [1], Dodelson [2], Mukhanov [3] and Peebles [4], as well as various review articles and lecture notes including [5–10].

2.1 Homogeneous cosmology

2.1.1 Geometry and dynamics

Observations of the distribution of light and matter on large scales strongly indicates that the Universe is homogeneous and statistically isotropic over long distances, meaning our position is not special (i.e. observers in other places in the Universe would agree with the large-scale characteristics of the Universe) and that observations appear the same from all directions in the sky. This is called the *cosmological principle* and is the basis of modern cosmology. Under the assumptions of homogeneity and isotropy, the geometry of the universe can be described by the FLRW metric [26–29]

$$\mathrm{d}s^2 = \bar{g}_{\mu\nu}\mathrm{d}x^\mu \mathrm{d}x^\nu = -\mathrm{d}t^2 + a^2(t)\gamma_{ij}\mathrm{d}x^i\mathrm{d}x^j, \tag{2.1}$$

where overbar denotes unperturbed quantities, γ_{ij} denotes the metric of a maximally symmetric 3-space and $a(t)$ is the scale factor, or equivalently, by the metric that is conformally invariant in Minkowski space, by introducing conformal time $\mathrm{d}\eta := \mathrm{d}t/a$, as

$$\mathrm{d}s^2 = a^2(\eta)\left(-\mathrm{d}\eta^2 + \mathrm{d}\vec{x}^2\right), \tag{2.2}$$

where $\mathrm{d}\vec{x}^2 := \gamma_{ij}\mathrm{d}x^i\mathrm{d}x^j$. Note observations constrain the three-curvature to very close to zero suggesting $\gamma_{ij} \simeq \delta_{ij}$ in Cartesian coordinates.[1]

Assuming General Relativity, the dynamics of the Universe is governed by Einstein's field equations [30]

$$G_{\mu\nu} = 8\pi G T_{\mu\nu}, \tag{2.3}$$

where G is Newton's constant, $G_{\mu\nu}$ is the Einstein tensor, which is defined by the metric $g_{\mu\nu}$ and its first two derivatives, and $T_{\mu\nu}$, which captures the contents of the Universe. The evolution of the scale factor a is determined by the Einstein equations in terms of the stress-energy content of the Universe via the Friedman equations

$$3\mathscr{H}^2 = 8\pi G a^2 \bar{\rho}, \tag{2.4}$$

$$2\dot{\mathscr{H}} + \mathscr{H}^2 = -8\pi G a^2 \bar{P}, \tag{2.5}$$

[1] I make this approximation generally in this thesis, unless stated otherwise.

where $\bar{\rho}$ and $\bar{P}$ are the background density and pressure, respectively, and $\mathscr{H} := aH := \dot{a}/a$ is the conformal Hubble parameter where $H := (\mathrm{d}a/\mathrm{d}t)/a$ is the Hubble parameter and I use overdot to indicate derive with respect to conformal time. Equations (2.4) and (2.5) can be combined to give the evolution equation for the density

$$\dot{\bar{\rho}} = -3\mathscr{H}(\bar{\rho} + \bar{P}), \tag{2.6}$$

giving $\bar{\rho}_m \propto a^{-3}$ for pressureless matter ($\bar{P}_m \simeq 0$), $r\bar{h}o_r \propto a^{-4}$ for radiation ($\bar{P}_r = \bar{\rho}_r/3$), and $\bar{\rho}_\Lambda =$ constant for vacuum energy which has negative pressure ($\bar{P}_\Lambda = -\bar{\rho}_\Lambda$) and does not dilute with the expansion of space.

2.1.2 The standard cosmological paradigm: ΛCDM

All cosmological data is well-fitted by the simple ΛCDM model which forms the backbone of the standard cosmological paradigm. At late times, ΛCDM predicts the Universe to be dominated by a cosmological constant Λ, and the total matter distribution to be dominated at all times by the cold dark matter (CDM). Other components that contribute to the energy content of the Universe include photons (γ) and neutrinos (ν), which constitute to radiation (r); and matter (m), which (along with CDM) consist of baryons (b): a term used in cosmology to refer to visible matter comprised of the Standard Model particles [such as electrons (e) and protons (p)]. The standard ΛCDM universe is typically defined in terms of six independent physical parameters: the density of baryons (ω_b) and cold dark matter (ω_c) today, the present day Hubble expansion rate (H_0), the optical depth at reionisation ($\tau_{\rm reio}$) and the amplitude (A_s) and the spectral index (n_s) of the primordial scalar perturbations. In the remainder of this section I briefly describe these components.

Cosmological constant Λ: Observations that the expansion of the Universe is accelerating suggest the energy content of the Universe at late times sees a dominant contribution from an unknown so-called 'dark energy' component. One of the simplest explanations used in the ΛCDM model is the presence of a cosmological constant, Λ, which can interpreted by the vacuum energy component contributing to $T^{\mu\nu} \in T^{\mu\nu}_\Lambda := -\rho_\Lambda g^{\mu\nu}$ where the conservation law for this component, $T^{\mu\nu}_{;\mu} = 0$, require $\rho_\Lambda =$ constant, independent of spacetime position. One can also write the Einstein equations with the $T^{\mu\nu}_\Lambda$ interpreted as a *cosmological constant*,

$$R_{\mu\nu} - \frac{1}{2}g_{\mu\nu}R - \Lambda g_{\mu\nu} = -8\pi G T^M_{\mu\nu}, \tag{2.7}$$

where

$$\Lambda = 8\pi G\rho_\Lambda\,, \tag{2.8}$$

and $T^M_{\mu\nu}$ is the energy-stress tensor *excluding* the vacuum energy component. For zero curvature this dark energy component has the solution $a(t) \propto \exp(Ht)$ where $H = \sqrt{8\pi G\rho_\Lambda/3}$. In most of the standard cosmological models (including the ΛCDM) the dark energy component remains subdominant until late times, when it becomes dominant, leading to a number of observational signatures including the recession velocities of the observed Supernovea, a late-time ISW effect on the CMB (see Section 2.7.1) and affecting the redshift-space galaxy clustering and lensing (see Section 2.7.3).

Cold dark matter: The combined observations of the CMB, galaxy rotation curves and clustering statistics as well as the considerations of the cosmological nucleosynthesis leads to the conclusion that moss of the mass in the Universe is in a different from than the baryonic matter. In particular, we know that this matter must not interact with radiation significantly, hence *dark*, both since we do not see it and also because, from measurements of rotation curves of galaxies, it has not lost its kinetic energy to electromagnetic interactions. Furthermore from the distributions of galaxies and galaxy clusters we anticipate this dark matter to be *cold*, i.e. non-relativistic. One of the most widely accepted models for cold dark matter is a weakly interacting massive particle (WIMP) where a stable, massive and neutral particle falls out of equilibrium (i.e. stops annihilating) when the temperature of the Universe falls sufficiently below its mass. The abundance of CDM in the Universe is then determined by the CDM annihilation cross-section where larger cross-section corresponds to more efficient annihilation and lower abundance today. I discuss the consequences of having a CDM component in the Universe throughout this thesis.

Photons: All cosmological surveys measure light sourced either in the early Universe or by stars or hot gas in dense regions. In particular, the temperature from the CMB photons has been measured to very high precision by the COBE satellite mission, $T_{\rm CMB} = 2.725 \pm 0.002$K [31]. The photon energy density at zeroth order Bose-Einstein distribution function is

$$\rho_\gamma = 2\int \frac{\mathrm{d}^3 p}{(2\pi)^3}\frac{p}{e^{p/T}-1} \tag{2.9}$$

where the factor 2 is due to the two helicity states of the photon. This integral can be solved to give $\rho_\gamma = (\pi^2/15)T^4$ suggesting $T \propto a^{-1}$ since $\rho_\gamma \propto a^{-4}$ as found earlier. Using this scaling relation and the critical energy density, $\rho_{\rm cr} = 3H^2/(8\pi G)$, we find $\rho_\gamma/\rho_{\rm cr} \simeq 2.5\times10^{-5}/(h^2a^4)$, suggesting the radiation density is small today, but was large in the early Universe. The parameter h is defined with the relation $H_0 = h\times 100{\rm km}/({\rm s\,Mpc})$. Going beyond the mean photon energy density, I discuss the small perturbations around the zeroth order Bose-Einstein distribution function in the upcoming sections.

Baryons: In cosmology, baryons refer to all standard model (SM) nuclei and electrons in the Universe. Baryons can be observed mainly in the form of starts in galaxies and from the gas in the intergalactic medium (IGM) in groups of galaxies. The absorption spectrum of distant quasars (mainly by intervening hydrogen) also provide a measurement of the baryon content in the Universe, as well as the baryon density also impacts the statistical characteristic of the anisotropies in the Universe. These measurements are in general in agreement. Measurements of the CMB fluctuations predict a baryon density $\omega_b := \Omega_b h^2 \simeq 0.0224 \pm 0.0001$, for example, where Ω_b is defined with the equality $\rho_b/\rho_{\rm cr} = \Omega_b a^{-3}$, with $\rho_{\rm cr}$ set equal to its current-day value.

Neutrinos: Lastly, the radiation component of the Universe also receives contribution from the cosmic neutrinos. As will be discussed in the following sections, neutrinos are well-understood to be once in thermal equilibrium with the rest of the components of the Universe. Neutrinos are fermions and are a part of the SM of particle physics. They contribute to the energy density significantly at early times, influencing the evolution of cosmological perturbations. Understanding the properties of neutrinos remain an active field of research in cosmology.

2.2 Inhomogenous Cosmology

Although homogeneity and isotropy are good approximations when describing our Universe on large scales, even the very early Universe was not perfectly homogeneous and isotropic. The small primordial perturbations that are imprinted on the FLRW metric and the stress-energy tensor grew under gravity and make up the structure we see around us today. In the remained of this chapter, I will describe the spacetime by perturbation theory as this is a good approximation given the departure from spatial homogeneity and isotropy is measured

to be small on cosmological scales. [2] Perturbation theory breaks down on small scales and high-density regions such as galaxies that form through gravitational collapse of material. As the observations are approaching high-enough fidelities to measure these scales, higher order effects will be important for cosmological inference in the near future. I will discuss these effects in the following chapters.

One can write the perturbation of the FLRW metric and of the energy-momentum tensor of a perfect fluid as

$$g_{\mu\nu}(\eta,\vec{x}) = \bar{g}_{\mu\nu}(\eta) + \delta g_{\mu\nu}(\eta,\vec{x}), \tag{2.10}$$
$$T_{\mu\nu}(\eta,\vec{x}) = \overline{T}_{\mu\nu}(\eta) + \delta T_{\mu\nu}(\eta,\vec{x}). \tag{2.11}$$

Note, however, that the set of equations describe these perturbations do not define them uniquely: they depend on the choice of coordinates (or the 'gauge' choice). Different choices of coordinates can change the values and the interpretation of the perturbation variables and can even introduce unphysical additional fluctuations. Throughout this work I make effort to justify my gauge choices, as well as describing their limitations where suitable. Perturbations can be decomposed into scalars, divergenceless vectors and divergenceless traceless symmetric tensors, which, at linear order, evolve separately under Einstein equations. This can be seen by writing the metric perturbation in the form [1]

$$\delta g_{00} = -E \tag{2.12}$$
$$\delta g_{i0} = a\left[\partial_i F + G_i\right] \tag{2.13}$$
$$\delta g_{ij} = a^2\left[A\delta_{ij} + \partial_i\partial_j B + \partial_j C_i + \partial_i C_j + D_{ij}\right] \tag{2.14}$$

where perturbations $\{A, B, C_i, D_{ij}, E, F, G_i\}$ are functions of time and space and satisfy

$$\partial_i C_i = \partial_i G_i = 0, \qquad \partial_i D_{ij} = 0, \qquad D_{ii} = 0. \tag{2.15}$$

The energy-momentum tensor has four scalar degrees of freedom and is described by the density and pressure (defined above) as well as the bulk velocity v_i and the anisotropic stress Σ_{ij}. For a perfect fluid, perturbed energy-momentum tensor (separately) satisfies equalities,

$$T^0_0 = \bar{\rho} + \delta\rho, \tag{2.16}$$
$$T^i_0 = [\bar{\rho} + \bar{P}]v^i, \tag{2.17}$$
$$T^i_j = -[\bar{P} + \delta P]\delta^i_j - (\bar{\rho} + \bar{P})\Sigma^i_j, \tag{2.18}$$

[2] The spatial variations on the CMB, for example, are of order $\sim \mathcal{O}(10^{-5})$.

where $\delta\rho$ and δP are perturbations to the density and pressure, respectively, and I omitted showing the time dependence of all the parameters above. The momentum density can be defined as $q^i := (\bar{\rho}+\bar{P})v^i$. Similar to the metric perturbations, the velocity vector and the anisotropic stress tensor can be decomposed as[3]

$$v_i = \partial_i \delta u + \delta u_i^V \tag{2.19}$$

$$\Sigma_{ij} = \partial_i\partial_j\pi^S + \partial_i\pi_j^V + \partial_j\pi^V + \pi_{ij}^T \tag{2.20}$$

where π_i^V, π_{ij}^T, $\delta\pi_i^V$ satisfy the same conditions as Eq. (2.15),

$$\partial_i\pi_i^V = \partial_i\delta u_i^V = 0\,, \qquad \partial_i\pi_{ij}^T = 0\,, \qquad \pi_{ii}^T = 0\,. \tag{2.21}$$

In this thesis I will be interested in the scalar perturbations (involving the eight scalars defined: $\{E,F,A,B,\delta\rho,\delta P,\pi^S,\delta u\}$, and omit more detailed discussion of tensor and vector perturbations.

2.2.1 Perturbation equations

The two most common gauge choices in the cosmology literature are the *Newtonian gauge* and the *synchronous gauge*.

In *Newtonian gauge*, we choose $B = F = 0$, and the convention $E := 2\Psi$ and $A := -2\Psi$. In this gauge, the perturbed metric can be written as

$$\mathrm{d}s^2 = a^2(\eta)\{(1+2\Psi)\mathrm{d}\eta^2 - (1-2\Phi)\delta_{ij}\mathrm{d}x^i\mathrm{d}x^j\}\,, \tag{2.22}$$

where Ψ and Φ are scalar perturbations related to the gravitational potential: Ψ is the gravitational potential and satisfies the Poisson equation, and Φ is a local perturbation of the average scale factor, related to the intrinsic Ricci scalar curvature of the constant time hyper-surfaces $R^{(3)} = \nabla^2\Phi/a^2$.

In the *synchronous gauge* one sets $E = 0$ and $F = 0$. The synchronous gauge choice does not completely fix the gauge dependence, however, and a further (well-motivated, see discussion in [1], for example) assumption is made in the presence a component (like cold dark matter) whose particles are much slower than the speed of light. In this case, momentum conservation of this fluid requires the velocity perturbations to be time independent. The time independent velocity perturbations can be removed by the (residual) gauge transformation,

[3] Note $\pi^S = 0$ for a perfect fluid by definition.

leaving no ambiguity on the choice of gauge. The synchronous gauge is then argued to be a physically well-motivated choice that can be approximated to be related to the observed matter fluctuations, possibly up to a bias. (Although note that CDM is at rest with this choice.)

I begin by analysing scalar fluctuations in the Newtonian gauge. Approximating the Universe as composed of separate perfect fluids, the perturbations in the density, pressure, momentum and anisotropic stress add as

$$\delta\rho = \sum_a \delta\rho_a \,, \tag{2.23}$$

$$\delta P = \sum_a \delta P_a \,, \tag{2.24}$$

$$q^i = \sum_a q^i_a \,, \tag{2.25}$$

$$\Pi^{ij} = \sum_a \Pi^{ij}_a \,, \tag{2.26}$$

where I defined $\Pi^i_j := (\bar{\rho} + \bar{P})\Sigma^i_j$ and the subscript a run over the species. Note it is often more convenient to write the density perturbations in terms of the dimensionless *overdensity* $\delta := 1 + \delta\rho/\bar{\rho}$. Other useful quantities describing the fluid include the equation-of-state $w := \bar{P}/\bar{\rho}$ and the speed of sound $c_s^2 := \delta P/\delta\rho$.

For a perfect fluid that is not interacting with other components (except through the metric), the density δ and velocity $\vec{v}$ perturbation equations can be solved by using the conservation of the stress-energy tensor, $\nabla^\mu T_{\mu\nu} = 0$, which satisfy at linear level,

$$\dot{\delta} = -(1+w)\left(\theta - 3\dot{\Phi}\right) - 3\mathscr{H}\left(\frac{\delta P}{\delta\rho} - w\right)\delta \tag{2.27}$$

$$\dot{\theta} = -\mathscr{H}(1-3w)\theta - \frac{\dot{w}}{1+w}\theta + \frac{\delta P/\delta\rho}{1+w}k^2\delta - k^2\sigma + k^2\Psi \,, \tag{2.28}$$

where $k = |\vec{k}|$ is the Fourier space wavenumber, the pressure P and energy density ρ are defined at rest with the fluid, $\theta = ik^j v_j$ is the divergence, σ is the anisotropic stress defined with the equality $\Sigma_{ij} = 3[\nabla_i\nabla_j - (1/3)\delta_{ij}\nabla^2]\sigma/2$. From the above equations it is easy to see for a constant equation of state satisfying $\delta P/\delta\rho - w = 0$, density perturbations decouple from the metric when $w = -1$, since terms including the Hubble parameter vanish.

For a non-relativistic fluid-like matter, the pressure and the anisotropic stress vanish, $P_m = 0$ and $\Pi_m^{ij} = 0$, and one obtains the continuity and Euler equations of motion,

$$\dot{\delta}_m = -\vec{\nabla}\cdot\vec{v}_m + 3\dot{\Phi}\,, \tag{2.29}$$

$$\dot{\vec{v}}_m = -\mathscr{H}\vec{v}_m - \vec{\nabla}\Psi\,, \tag{2.30}$$

respectively. Similarly for a relativistic fluid-like radiation that satisfy $P_r = \rho_r/3$ and $\Pi_r^{ij} = 0$, these equations become

$$\dot{\delta}_r = -\frac{4}{3}\vec{\nabla}\cdot\vec{v}_m + 4\dot{\Phi}\,, \tag{2.31}$$

$$\dot{\vec{v}}_r = -\frac{1}{4}\vec{\nabla}\delta_r - \vec{\nabla}\Psi\,. \tag{2.32}$$

The dynamics of the perturbed spacetime can also be calculated from Einstein equations using the perturbation of the total stress energy tensor. Going through the equality in Eq. (2.3), the 00−Einstein equation give the relativistic *Poisson equation*,

$$\nabla^2\Phi - 3\mathscr{H}(\dot{\Phi} + \mathscr{H}\Psi) = 4\pi G a^2\delta\rho\,, \tag{2.33}$$

which simplify to $\nabla^2\Phi \simeq 4\pi G a^2\delta\rho$ on small (sub-horizon) scales where Fourier modes satisfy $k \gg \mathscr{H}$ and $|\nabla^2\Phi| \gg 3\mathscr{H}|\dot{\Phi} + \mathscr{H}\Psi|$. Following on similar lines, the trace-free spatial part of the Einstein equations give

$$\nabla^2(\Phi - \Psi) = -8\pi G a^2(\bar{\rho} + \bar{P})\sigma\,, \tag{2.34}$$

which vanish for a perfect matter fluid with $\sigma = 0$, indicating that the absence of anisotropic stress and in the Newtonian gauge $\Psi = \Phi$. Free-streaming relativistic species such as photons and neutrinos, on the other hand, source anisotropic stress although their effect is small. Finally, the trace of the spatial part of the Einstein equation satisfy

$$\ddot{\Phi} + 3\mathscr{H}\dot{\Phi} + (2\dot{\mathscr{H}} + \mathscr{H}^2)\Phi = 4\pi G a^2\delta P\,. \tag{2.35}$$

2.2.2 Initial conditions

Primordial perturbations manifest themselves in all cosmological observables visible today. Seminal reviews of the cosmological perturbation theory can be found in e.g. [32–36]. Due to the stochastic nature of the quantum fluctuations in the early universe, our cosmological

theories predict only the statistics of initial conditions (rather than individual values of fluctuations in different specific directions).

Assuming Gaussian initial conditions, the power spectrum of these primordial perturbations is often considered an initial condition that corresponds to a part of the ΛCDM model. In particular, for scalar fluctuations, a simple spectrum with two free phenomenological parameters, A_s and n_s, has been observed to fit data very well. The primordial power-spectrum is given by

$$\mathscr{P}_\zeta(k) := \frac{k^3}{2\pi^2}\langle|\zeta_k|^2\rangle \simeq A_s\left(\frac{k}{k_\star}\right)^{n_s-1}, \tag{2.36}$$

where I dropped a delta-function on the left hand side. By default, I choose a comoving pivot scale of $k_\star = 0.05\,\mathrm{Mpc}^{-1}$. The best-fit value in ΛCDM is $n_s = 0.965 \pm 0.004$ [37]. Here, I expressed scalar perturbations in terms of the (gauge-invariant) curvature perturbation on uniform-density hyper-surfaces [38],

$$-\zeta := \Psi + \mathscr{H}\,\delta\rho/\dot{\bar{\rho}}\,. \tag{2.37}$$

On super-horizon scales, $k \ll \mathscr{H}$, ζ has a single constant non-vanishing adiabatic solution[4] [39] which satisfies Eq. ((2.36)). Note that another gauge-invariant measure of scalar perturbations (often adopted in the study of inflation, for example) is the comoving curvature perturbation

$$\mathscr{R} = \Psi - \mathscr{H}/(\bar{\rho}+\bar{p})\delta q\,, \tag{2.38}$$

where δq is a perturbation to the 3-momentum field. $\mathscr{R}$ is equal to ζ up to a term scaling with $[k/(\mathscr{H})]^2$ which vanishes on super-horizon scales (for a review, see e.g. Ref. [7]). Finally, if present, multiple dynamical degrees of freedom, such as additional scalar fields that are not in thermal and kinetic equilibrium with the inflaton or the adiabatic fluctuations, can contribute to non-vanishing isocurvature fluctuations that can evolve on super horizon scales. I discuss some implications of multiple dynamical degrees of freedom on Chapter 3.

The most widely-accepted cosmological scenario for generating such primordial perturbations is inflation: an early epoch of accelerated expansion of space where quantum fluctuations are amplified to classical scales. During inflation, perturbations that are in causal

[4] I mean by 'adiabatic fluctuations' those for which the perturbation to any four-scalar in the system is proportional to the rate of change of the scalar, with the same proportionality for all scalars.

contact with each other are driven beyond the horizon before re-entering the horizon as the Universe continues to expand after the end of inflation.

Well inside the horizon, where gauge-dependence is negligible for standard gauge choices, scalar perturbations are commonly expressed in terms of the density contrast, $\delta := \delta\rho/\bar{\rho}$. The difference between density contrast and curvature perturbations is parametrised by the transfer function $\mathscr{T}$, which factors out the time-dependence of perturbations. The transfer function for δ_i is defined through

$$\left\langle |\delta_i(t,k)|^2 \right\rangle := \mathscr{T}_i^2(t,k)\, \mathscr{P}_\zeta(k)\,. \tag{2.39}$$

At linear scales, the transfer function can be obtained by solving the equations of motion resulting from the linearised field equations discussed above. Different transfer functions describe the evolution of the different components of the Universe i as they enter the horizon. In what follows, I briefly discuss how fluctuations in the main components of ΛCDM evolve during different epochs.

During radiation domination, the relative normalisation between adiabatic radiation and matter fluctuations that enter the horizon satisfy $\delta_r/\delta_m = 4/3$. Inside the horizon, any density contrast in the radiation fluid sees rapid oscillations and decays quickly. During this time, baryons are tightly coupled to the photons, satisfying $(4/3)\delta_b \simeq \delta_\gamma$. Fluctuations in the non-interacting DM component, however, grow at a rate close to logarithmic [40].

Radiation and baryon fluctuations continue to oscillate and quickly decay inside the horizon during matter domination. During this time, the linear DM fluctuations start to grow at the rate $\delta_c(t) \propto a(t)$. At the epoch of recombination, baryons become decoupled from photons and start to fall into the gravitational potentials following DM perturbations. As time passes baryons follow the DM distribution more closely. Until the dark energy domination in the late Universe, the DM and baryonic density contrasts continue to grow at the same pace in the linear regime. The dark energy domination in the late Universe stalls this growth.

The perturbation theory at the leading order fails to describe fluctuations at a given scale, k, accurately, if the scale approaches the non-linear regime. Perturbations under non-linear evolution eventually collapse under gravity and result in virialisation of DM halos. This procedure of structure formation occurs hierarchically in the standard ΛCMB: smallest halos form first before merging to form larger halos.

Studies comparing the theoretical predictions I cite in Section 2.7.3 to data suggest perturbation theory remains a good approximation even at the scale of galaxy clusters today, where the matter power spectrum is only mildly non-linear. On smaller scales, the non-linear

matter power spectrum still carries valuable information for cosmology via its sensitivity to the mass and number of neutrinos, for example, as well as to the effects of gravity on galactic scales. Nevertheless, uncertainties related to non-linear structure formation and baryonic effects make modelling of the matter power spectrum difficult on these small scales. I expand this discussion in Section 2.7.3.

2.3 Inflation and Reheating

The inflationary paradigm [41–45] solves many of the classical problems associated with the hot Big Bang scenario, while providing a natural mechanism for generating primordial cosmological fluctuations [46–49, 38]. Observations are currently consistent with the simplest single-field, slow-roll models of inflation, *e.g.*, the *Planck* observations of the cosmic microwave background (CMB) [50] indicate a featureless power-law shape for the primordial power spectrum of scalar fluctuations and no detectable primordial non-Gaussianity or tensor fluctuations.

2.3.1 Problems of the hot big bang

Flatness problem: As I mentioned earlier, current observations suggest the value of the curvature is consistent with zero. Note curvature[5] is defined as $\Omega_K := -K/a^2H^2$ and increases as $t^{2/3}$ and as t in the eras of matter- and radiation-domination, respectively. This means since the beginning of radiation-dominated expansion, curvature must have been monotonically increasing. Our measurement of small curvature today then suggests a much more smaller curvature in the past, raising the question of the naturalness of such a finely tuned parameter. Accelerated expansion solves this problem since the near-constant Hubble rate allows curvature to decrease as a^2 during inflation. Given a period of inflation, the curvature today can be written as $|\Omega_K| = \exp\{-2N_e\}(a_I H_I/a_0 H_0)^2$ where N_e is the number of e-foldings of inflation and a_I and H_I are the scale factor and Hubble rate at the end of inflation. It follows that the flatness problem is then solved if the inflation exceeds a certain amount that compares to the amount of expansion since inflation, suggesting $N \gtrsim 70$.

[5]The curvature parameter, K, is defined with the γ_{ij} metric in Eq. (2.1) via the relation $\gamma_{ij} := \delta_{ij} + Kx^i x^j/1 - K|\vec{x}|^2$ where $K = \{+1, -1, 0\}$ corresponds to spherical, hyperspherical and Euclidean hyperspace geometries respectively.

Horizon problem: The CMB is observed to have almost the same temperature in all directions in the sky. Nevertheless the standard hot big bang evolution from the onset of radiation-domination predicts the early Universe was made of many causally disconnected patches in the sky. The fact that these seemingly disconnected patches have nearly the same temperature is called the *horizon problem*. The maximum distance that an observer at time t could have received a signal from the past at time $t = 0$ is called the *particle horizon*. In physical coordinates this distance is given by $D_p(t) = a(t)\int_0^t \mathrm{d}t/a(t)$. For a Universe with decelerated expansion (as in the matter or radiation domination eras), this integral converges to $D(t) = \{3t, 2t\}$ for $\{\text{matter, radiation}\}$ which predicts the angle subtended by the particle horizon at the surface of last scattering is around a degree, demanding the universe to be consisting of many causally-disconnected patches. A period of accelerated expansion where $\mathrm{d}a^2/\mathrm{d}t^2 > 0$ (i.e. inflation), however, reverts this problem since now the particle horizon diverges in the past. The expansion needed to solve the horizon problem turns out to be the same needed to solve the flatness problem, where inequality $\exp\{N_e\} > a_I H_I/a_0 H_0$ needs to be satisfied. The condition $\mathrm{d}a^2/\mathrm{d}t^2 > 0$ can in turn be satisfied with a universe composed of a fluid whose equation of state satisfies $w := \bar{P}/\bar{\rho} < -1/3$.

2.3.2 Inflationary cosmology

The equation-of-state parameter must satisfty $w < -1/3$ to realise a period of accelerated expansion. Typically, models that successfully sustain for a sufficiently long (but a finite-) amount of time satisfy $w \approx -1$. The simplest way to achieve this is by introducing a scalar field, inflaton ϕ, that is minimally coupled to gravity, and whose contribution to the scalar field action is

$$S_\phi = \int \mathrm{d}^4x\sqrt{-g}\left[\frac{1}{2}g^{\mu\nu}\partial_\mu\phi\,\partial_\nu\phi - V(\phi)\right], \tag{2.40}$$

where$g := \det(g_{\mu\nu})$ and the inflationary condition having the potential $V(\phi)$ dominate over the kinetic energy. In an expanding FLRW space-time this is equivalent to demanding that the evolution of ϕ remains very slow compared to the expansion of the Universe.

The *background* evolution of this field is described by the Klein-Gordon and Friedmann equations,

$$\ddot{\phi} + 3H\dot{\phi} + V'(\phi) = 0 \tag{2.41}$$

$$H^2 = \frac{1}{3\bar{m}_{\mathrm{pl}}^2}\left[\frac{1}{2}\dot{\phi}^2 + V(\phi)\right], \tag{2.42}$$

where $\bar{m}_{\rm pl} := 1/\sqrt{8\pi G}$ is the reduced Planck mass and dots denote differentiation with respect to time, and primes denote partial differentiation with respect to inflaton background field value ϕ. The requirement satisfying inflation I discussed above is generally parameterised with the so-called slow-roll parameters ε_i. These are defined as

$$\varepsilon_1 := -\frac{\dot{H}}{H^2} = \frac{1}{2\bar{m}_{\rm pl}^2}\left(\frac{{\rm d}\phi}{{\rm d}N}\right)^2 \tag{2.43}$$

$$\varepsilon_{i+1} := \dot{\varepsilon}_i/(H\varepsilon_i)\,, \tag{2.44}$$

and satisfy $\varepsilon_i \ll 1$ during inflation. This energy scale can be as large as the GUT scale, 10^{16} GeV, depending on the inflationary model, and can be probed directly with the tensor-to-scalar ratio, which satisfies the relation $r \propto A_t \propto V\bar{m}_{\rm pl}^{-4}$. Inflation occurring at the GUT scale corresponds to $r \geq 0.01$. Note I also defined ${\rm d}N := H{\rm d}t = {\rm d}\ln a$, with N the number of e-foldings of expansion. Successful inflation requires $\varepsilon_1,\ \varepsilon_2 \ll 1$. Another useful notation is to introduce first and second slow-roll parameters in terms of the inflationary potential as[6]

$$\varepsilon_{\rm v} := \frac{\bar{m}_{\rm pl}^2}{2}\left(\frac{V'}{V}\right)^2 \quad \text{and} \quad \eta_{\rm v} := \bar{m}_{\rm pl}^2\frac{V''}{V}\,. \tag{2.45}$$

The scalar perturbations of the inflation field source the primordial power spectrum I introduced in Eq. (2.36). Under slow-roll one can express the parameters describing the primordial power spectrum directly in terms of the slow-roll parameters,

$$n_s - 1 = 2\eta_{\rm v} - 6\varepsilon_{\rm v} \tag{2.46}$$

$$A_s = \frac{1}{24\pi^2\varepsilon_{\rm v}^\star}\frac{V_\star}{\bar{m}_{\rm pl}^4}\,, \tag{2.47}$$

where with star ($\star$) I imply that the corresponding quantity is evaluated at the time the pivot scale satisfies $k_\star = aH$. More generally, however, the slow-roll parameters are functions of k and different in the case of ΛCDM, the parameters that describe the power spectrum can receive higher order corrections in slow-roll parameters. The scalar spectral index, for example, can exhibit a running in the form,

$$n_s = n_s^\star + \frac{{\rm d}n_s}{{\rm d}\ln k}\ln(k/k_\star) + \ldots\,, \tag{2.48}$$

which in principle can be used to distinguish inflationary models [see e.g. 51]. Another fundamentally significant characteristic of inflation is it naturally generates not only scalar

[6]Note the parameters ε_v and η_v are related to slow-roll parameters ε_i as $\varepsilon_v \simeq \varepsilon_1$ and $\eta_v \simeq \varepsilon_1 + \varepsilon_2$.

but also tensor perturbations. The tensor perturbation power spectrum have the form

$$\mathscr{P}_t(k) = \frac{k^3}{2\pi^2}|h_k|^2 = A_t \left(\frac{k}{k_\star}\right)^{n_t}, \tag{2.49}$$

with a tensor-to-scalar ratio given by

$$r := \mathscr{P}_t(k_\star)/\mathscr{P}_\zeta(k_\star) = 16\varepsilon_{\rm v}^\star . \tag{2.50}$$

Going beyond the ΛCDM, the power spectra generated during inflation may exhibit a richer structure in general which can not be always be conveniently described with a power-series expansion of the spectral index. Models of inflation such as axion monodromy [52–54], for example, cannot be described by simple slow-roll dynamics and predict oscillatory features on the primordial spectrum. Going beyond the slow-roll approximation, moreover, necessities accounting for the effect of general first-order perturbations to the FLRW metric. A useful parametrisation to the perturbations used widely in the context of inflation is

$$\mathrm{d}s^2 = -(1+2\Psi)\mathrm{d}t^2 - 2a^2\partial_i B \mathrm{d}t\mathrm{d}x^i + a^2\left[(1-2\Psi)\delta_{ij} - 2\partial_i\partial_j E\right]\mathrm{d}x^i\mathrm{d}x^j . \tag{2.51}$$

For the purposes of this section, I will only keep general scalar metric perturbations (Ψ, B, E), thus will neglect vector perturbations and tensor perturbations (describing gravitational waves). Note that vector perturbations have decaying solutions during standard models of inflation and are anticipated to be small or vanishing. In spatially flat gauge ($\Psi = E = 0$) the Klein-Gordon equation at first order then becomes

$$\begin{aligned} 0 = \frac{\mathrm{d}^2\delta\phi(N,k)}{\mathrm{d}N^2} + (3-\varepsilon)\frac{\mathrm{d}\delta\phi(N,k)}{\mathrm{d}N} \\ + \frac{k^2}{a^2H^2}\delta\phi(N,k) + \left[\frac{V''}{H^2} + \frac{2}{H^2}\frac{\mathrm{d}\phi(N)}{\mathrm{d}N}V' + (3-\varepsilon)\frac{\mathrm{d}\phi(N)}{\mathrm{d}N}\right], \end{aligned} \tag{2.52}$$

where I defined

$$\varepsilon := \frac{1}{2\bar{m}_{\rm pl}^2}\left(\frac{\mathrm{d}\phi(N)}{\mathrm{d}N}\right)^2 \tag{2.53}$$

in the same way as the slow-roll parameter ε_1. Note that ε does not necessarily have to be small. Solving this mode equation, the (gauge-invariant) power spectrum of the curvature perturbations is obtained as $\mathscr{P}_{\mathscr{R}}(k) = |\delta\phi(N,k)|^2/2\varepsilon$.

2.3.3 Reheating after inflation

Regardless of the inflationary model, or how many scalar fields were present during inflation, the Universe must eventually evolve to the radiation-dominated era of the standard Big Bang model. This can be achieved by coupling the fields ϕ_i to relativistic particle species. As the fields approach, overshoot, and begin to oscillate about the minimum of their potentials, interactions with lighter particles lead to dissipation which drains energy from the ϕ_i zero-mode and excites relativistic particles. I refer to these collective processes as reheating [see e.g. 55–57, for reviews].

Exactly how reheating following inflation occurs is a significant source of uncertainty when testing inflationary models. In particular for simple single-field inflation scenarios fluctuations remain outside of horizon during reheating and are unaffected by the potentially complicated reheating dynamics. Nevertheless, the uncertainty to details of reheating does raise an important problem for observables by obscuring the relation between the length scales in the early Universe and those observed today. Defining the end of reheating to be the point at which the Universe has fully thermalised and standard hot big bang begins, the problem can be characterised as connecting length scales at the end of inflation to those at the end of reheating. This matching can be expressed in terms of the equation [58, 59]

$$\frac{k_\star}{a_0 H_0} = \frac{a_\star}{a_{\rm end}} \frac{a_{\rm end}}{a_{\rm reh}} \frac{a_{\rm reh}}{a_{\rm eq}} \frac{H_\star}{H_{\rm eq}} \frac{a_{\rm eq} H_{\rm eq}}{a_0 H_0}\,, \tag{2.54}$$

where the pivot scale $k_\star := a_\star H_\star$ is defined as usual at horizon crossing, and the various values of the scale factor a (and Hubble rate H) refer, respectively, to the end of inflation and reheating, matter-radiation equality and today. In this equation, the quantities evaluated today and at the time of matter-radiation equality are observationally well constrained, while the parameters $H_\star$ and $N_\star := \ln(a_{\rm end}/a_\star)$ are derived quantities that are predicted by the particular inflationary model. The remaining ratio, $a_{\rm end}/a_{\rm reh}$, can *in principle* be predicted by the reheating model.

2.4 Thermal history

I now briefly discuss the evolution of different species in the Universe after reheating where the SM particles (as well as possible extensions) are produced, which I take as the beginning of the hot thermal big bang. A key concept in describing the thermal history following reheating is the competition between the expansion rate of the Universe H and the interaction

rate of particles Γ: when $H \ll \Gamma$, particles maintain equilibrium, when $H \leq \Gamma$ they freeze out. At early times, all SM particles are in local thermal equilibrium where the interactions between them efficiently keep them in local thermal contact.

The phase space distribution of all thermal particle species can then be described by the number of particles per unit phase space volume. Due to homogeneity and isotropy, this distribution can depend neither on the position $\vec{x}$ of the particle nor the direction of the momentum vector $\vec{p}$. Distributions satisfying these conditions relevant to the contents of our Universe are the thermal Fermi-Dirac and Bose-Einstein distributions that are given by

$$f_a(p) = \left[e^{E_a(p)/T} \pm 1\right]^{-1}, \tag{2.55}$$

where $(+)$ is for fermions and $(-)$ for bosons, respectively, $p = |\vec{p}|$, E_a is the relativistic energy (which includes the mass m_a), and I assumed vanishing chemical potential for all SM particles. The temperature T is the same for all particles in the thermal equilibrium.

It follows from Eq. (2.55) that the average energy density and pressure can be calculated by integrating over the phase space as

$$\bar{\rho} = g_a \int \frac{\mathrm{d}^3\vec{p}}{(2\pi)^3} E_a(p) f_a(p) \quad \text{and} \quad P_a = g_a \int \frac{\mathrm{d}^3\vec{p}}{(2\pi)^3} \frac{p^2}{3E_a(p)} f_a(p)\,, \tag{2.56}$$

where g_a is the degeneracy of the species (e.g., is equal to two for photons). Equation (2.56) satisfy $\bar{P}_a \ll \bar{\rho}_a$ and $\bar{P}_a = \bar{\rho}_a/3$ in the non-relativistic and the relativistic limit respectively. For the latter, the total radiation density can be written as

$$\bar{\rho}_r = \sum_a \bar{\rho}_a = \frac{\pi^2}{30} g_*(T) T^4\,, \tag{2.57}$$

where the sum is over all relativistic species and $g_*(T)$ is the effective number of relativistic degrees of freedom.

At the onset of the thermal history, the energy scale at this time could be around 10^{16}GeV where all SM particles were massless. The temperature of the Universe eventually drops to $\simeq 100$GeV and the electroweak symmetry of SM gets spontaneously broken, having SM particles acquire mass through Higgs mechanism. This period is followed by the QCD phase transition, or the confinement of quarks and gluons in composite hadronic states around, 150MeV. During these times the effective number of relativistic degrees of freedom drops from around ~ 100 to around ~ 10.

The thermal history follows QCD phase transition with neutrino decoupling from the rest of the plasma around 0.8MeV, releasing the cosmic neutrino background due to the inefficiency of weak interactions to maintain the local thermal equilibrium. Shortly after, electrons and positrons get annihilated and the energy from the annihilation gets transferred to photons, increasing photon temperature compared to the neutrinos. This period is followed by neutron-proton interactions becoming inefficient, leading to relic abundance of neutrons.

By around three minutes after the big bang, neutrons and protons synthesise deutrium and helium (as well as lithium and beryllium) via the big bang nucleosynthesis (BBN) around 100keV. This coupled system of nuclear reaction chains that drive the formation of light elements start with the formation of deuterium through the combination of a proton and a neutron, i.e.

$$n + p \to D + \gamma. \tag{2.58}$$

In what follows, the formation of elements ^{3}He and ^{4}He follow through the reactions

$$D + D \to n + {}^3\mathrm{He} \quad \text{and} \quad D + {}^3\mathrm{He} \to {}^4\mathrm{He} + p\,. \tag{2.59}$$

Note that at the BBN temperatures ($0.1-1$MeV), the formation of light elements are very sensitive to physics: any modification to the energy content of the Universe will change its expansion rate and the final abundance of light elements. These include scenarios of early dark energy, extra relativistic species and alterations in some of the initial conditions including the baryon density $\Omega_b h^2$ or the baryon-to-photon ratio $\eta_b := n_b/n_\gamma$. A particularly important primordial elemental abundance that gets impacted by the initial conditions and in turn affect cosmology is the primordial helium fraction $Y_P := n_{^4He}/n_p$. Y_p is predicted from theory to be approximately ~ 0.25 in the ΛCDM universe.

Following the formation of light elements, the primordial plasma collapses towards over-dense regions through gravitational attraction. Photons and baryons in the primordial plasma are coupled via Thomson scattering. The radiation pressure of photons and the expansion of the Universe counteract the inwards gravitational pull, causing the photon-baryon plasma to undergo so-called baryon acoustic oscillations (BAOs), which propagate through the plasma at the sound speed. I discuss BAOs in more detail in the next sections. Around $380,000$ years after the Big Bang, the plasma cools down sufficiently to allow electrons and protons to combine to form neutral hydrogen. This epoch is called recombination, where photons decouple from baryons and stream almost entirely freely through the Universe. These relic photons are observable today from the cosmic microwave background (CMB) radiation,

which has an almost perfect black body spectrum with a temperature of $T_{\rm CMB} = 2.7255$ K [60] with small anisotropies of order $\mathcal{O}(10^{-5})$.

2.5 Anisotropic Boltzmann equations

So far I described the metric and primordial perturbations and gave a brief qualitative review of the thermal history of the Universe. Metric perturbations couple to all of these inhomogeneities in matter and radiation gravitationally, while photons are affected also by Thomson scattering with free electrons and electrons are tightly coupled to protons via Coulomb scattering, for example. Determining the evolution of radiation and matter distributions hence requires a systematic way of accounting for all these couplings. The quintessential tool for doing this is the *Boltzmann equation*, which describe the evolution of the distribution function f, schematically as

$$\frac{\mathrm{d}f}{\mathrm{d}t} = C[\{f\}] \tag{2.60}$$

where all possible collision terms are contained on the right-hand side of the Boltzmann equation. The distribution f depends on time t, position $\vec{x}$, the (comoving) energy $\varepsilon := pa$, and the momentum $\vec{p}$. In the absence of collisions, the Boltzmann equation simplifies to

$$\frac{\mathrm{d}f}{\mathrm{d}t} = 0\,, \tag{2.61}$$

which still captures the non-trivial spatial dependence of the metric. I write the collisionless Boltzmann equation in the form

$$\frac{\mathrm{d}}{\mathrm{d}t} f(t,\vec{x},\varepsilon,\hat{p}) = \frac{\partial f}{\partial t} + \frac{\partial f}{\partial \vec{x}} \cdot \frac{\mathrm{d}\vec{x}}{\mathrm{d}t} + \frac{\partial f}{\partial \ln \varepsilon} \frac{\mathrm{d}\ln\varepsilon}{\mathrm{d}t} + \frac{\partial f}{\partial \hat{p}} \cdot \frac{\mathrm{d}\hat{p}}{\mathrm{d}t} = 0\,, \tag{2.62}$$

where $\hat{p} = \vec{p}/|\vec{p}|$.

2.5.1 Boltzmann equation for photons

I now turn our attention to massless photons. First I calculate the collisionless Boltzmann equation. In the Newtonian gauge (Eq. (2.22)), the FRLW metric can be written as

$$\begin{aligned} g_{00}(\vec{x},t) &= 1+2\Psi(\vec{x},t)\,, \\ g_{0i}(\vec{x},t) &= 0\,, \\ g_{ij}(\vec{t},t) &= a^2\delta_{ij}(1-2\Phi(\vec{x},t))\,. \end{aligned} \tag{2.63}$$

In order to calculate the partial derivatives in Eq. (2.62) I begin by defining the 4-momentum vector,

$$P^\mu := \frac{\mathrm{d}x^\mu}{\mathrm{d}\lambda}\,, \tag{2.64}$$

where $x^\mu = (t,\vec{x})$ is the space-time 4-vector and λ parameterises the particle's path. Note that the masslessness of photon implies $P^2 := g_{\mu\nu}P^\mu P^\nu = 0$. Using the metric of Eq. (2.63), We find

$$P^2 = (1+2\Psi)(P^0)^2 + p^2 = 0 \tag{2.65}$$

where up to first order in perturbation theory, i.e. assuming Φ and Ψ are small quantities, the time component satisfies

$$P^0 = \frac{p}{\sqrt{1+2\Psi}} = p(1-\Psi)\,, \tag{2.66}$$

and I defined $p^2 := -g_{ij}P^iP^j$. With these definitions one can redefine

$$\frac{\mathrm{d}x^i}{\mathrm{d}t} = \frac{\mathrm{d}x^i}{\mathrm{d}\lambda}\frac{\mathrm{d}\lambda}{\mathrm{d}t} = \frac{P^i}{P^0}\,. \tag{2.67}$$

By setting the comoving momentum P^i proportional to $\hat{p}^i$ up to a constant, one can see

$$P^i = p\hat{p}^i\frac{1+\Phi}{a}\,, \tag{2.68}$$

such that

$$\frac{\mathrm{d}x^i}{\mathrm{d}t} = \frac{\hat{p}^i}{a}(1+\Psi+\Phi)\,. \tag{2.69}$$

From this equation and noting that an overdense (underdense) region satisfies $\Psi < 0$ and $\Phi > 0$ ($\Psi > 0$ and $\Phi < 0$), its indicative that a photon looses (gains) energy when travelling and overdense (underdense) region. It is also straightforward to show the momentum component satisfies

$$\frac{\mathrm{d}\ln\varepsilon}{\mathrm{d}t} = \frac{\partial\Phi}{\partial t} - \frac{\hat{p}^i}{a}\frac{\partial\Psi}{\partial x^i}\,. \tag{2.70}$$

The first term in Eq. (2.70) accounts for the loss of momentum due to Hubble expansion. The second expression suggests that the photon losses energy in a deepening gravitational potential well (see sign conventions described above). Finally, the third term indicates that a photon travelling into (away from) a gravitational potential well, $\hat{p}^i\partial\Psi/\partial x^i < 0$ ($\hat{p}^i\partial\Psi/\partial x^i > 0$), gains (looses) energy. The collisionless Boltzmann equation for a photon can then be written with these terms as

$$\frac{\mathrm{d}f}{\mathrm{d}t} = \frac{\partial f}{\partial t} + \frac{\hat{p}^i}{a}\frac{\partial f}{\partial x^i} - p\frac{\partial f}{\partial p}\left[\mathscr{H} - \frac{\partial\Phi}{\partial t} + \frac{\hat{p}^i}{a}\frac{\partial\Psi}{\partial x^i}\right]. \tag{2.71}$$

Next, I expand the photon distribution function f about its zero-order Bose-Einstein value given in Eq. (2.9), for example, which can be written incorporating the anisotropy as

$$f(\vec{x},\varepsilon,\hat{p},t) = \left[\exp\left\{\frac{\varepsilon/a}{\overline{T}[1+\Theta(\vec{x},\hat{p},t)]}\right\} - 1\right]^{-1}, \tag{2.72}$$

where $\overline{T}$ is the redshift dependent mean photon temperature which scale as a^{-1} and $\Theta := \delta T/\overline{T}$ is the perturbation to the distribution function where $\delta T = \overline{T} - T$. For small perturbations one can write approximate the distribution function as

$$f(\vec{x},\varepsilon,\hat{p},t) = \bar{f}(\varepsilon)\left[1 - \Theta(\vec{x},\hat{p},t)\frac{\mathrm{d}\ln\bar{f}(\varepsilon)}{\mathrm{d}\ln\varepsilon}\right]. \tag{2.73}$$

where

$$\bar{f}(\varepsilon) := \left[\exp\left\{\frac{p}{\bar{T}}\right\} - 1\right]^{-1} \tag{2.74}$$

At zeroth-order, the photon Boltzmann equation gives $\bar{T} \propto a^{-1}$. At first order, this collisionless Boltzmann equation can be found to satisfy

$$\left.\frac{\mathrm{d}f}{\mathrm{d}t}\right|_{(1)} = -p\frac{\partial\bar{f}}{\partial p}\left[\frac{\partial\Theta}{\partial t} + \frac{\hat{p}^i}{a}\frac{\partial\Theta}{\partial x^i} + \frac{\partial\Phi}{\partial t} - \frac{\hat{p}^i}{a}\frac{\partial\Psi}{\partial x^i}\right]. \tag{2.75}$$

The first two terms inside the brackets on the left-hand side in Eq. (2.75) account for the 'free-streaming' of photon anisotropies, while the last two terms account for the interaction between gravity and photons.

Next in this section, I quantify how the photon distribution is influenced by the Thomson scattering[7] of photons off free electrons in the plasma and non-relativistic gas. This interaction has the form

$$e + \gamma \leftrightarrow e + \gamma, \tag{2.76}$$

and in the rest frame of electron (indicated with 'e_r' subscript), the collision term in the Boltzmann equation can be written in the form

$$C_{e_r}[f_{e_r}(\varepsilon_{e_r}, \hat{p}_{\mathrm{out},e_r})] = n_e \int \mathrm{d}\hat{p}_{\mathrm{in},e_r} \frac{\mathrm{d}\sigma}{\mathrm{d}\Omega} \left[f(\varepsilon_{\mathrm{e_r}}, \hat{p}_{\mathrm{in},e_r}) - f(\varepsilon_{e_r}, \hat{p}_{\mathrm{out},e_r}) \right], \tag{2.77}$$

where n_e is the proper number density of electrons and $\mathrm{d}\sigma(\Omega)/\mathrm{d}\Omega = \sigma_T/4\pi$ is the differential scattering cross-section for Thomson scattering.[8] The parameter σ_T is the Thomson scattering cross section $\sigma_T = 6.65 \times 10^{-29}\mathrm{m}^2$. First and second terms in Eq. (2.77) captures the in- and out- scattering terms respectively. One can take the latter outside the integral to get

$$C_{e_r}[f_{e_r}(\varepsilon_{e_r}, \hat{p})_{e_r}] = -n_e \sigma_T f(\varepsilon_{e_r}, \hat{p}_{e_r}) + n_e \sigma_T \int \frac{\mathrm{d}\hat{p}_{\mathrm{in},e_r}}{4\pi} f(\varepsilon_{e_r}, \hat{p}_{\mathrm{in},e_r}). \tag{2.78}$$

Enforcing Lorentz invariance as well as the energy momentum conservation and taking the relativistic (non-relativistic) limit for photons (electrons), the collision term in in some general frame can be found as

$$C[f(\varepsilon, \hat{p})] = a\bar{n}_e \sigma_T \frac{\mathrm{d}\bar{f}}{\mathrm{d}\ln\varepsilon} \left[\Theta(\hat{p}) - \hat{p}\cdot\vec{v}_e - \frac{3}{16\pi} \int \mathrm{d}\hat{p}_{\mathrm{in}} \Theta(\hat{p}_{\mathrm{in}}) \left[1 + (\hat{p}_{\mathrm{in}}\cdot\hat{p})^2 \right] \right]. \tag{2.79}$$

where $\vec{v}_e$ is the electron peculiar velocity relative to the CMB recombination surface. Adding the collision term to Eq. (2.75) and using the expansion of the total derivative as

$$\frac{\Theta(t,\vec{x},\hat{p})}{\mathrm{d}t} = \frac{\partial\Theta}{\partial t} + \frac{\partial\Theta}{\partial\vec{x}}\cdot\frac{\mathrm{d}\vec{x}}{\mathrm{d}t} + \frac{\Theta}{\hat{p}}\cdot\frac{\mathrm{d}\hat{p}}{\mathrm{d}t} = \frac{\partial\Theta}{\partial t} + \hat{p}\cdot\vec{\nabla}\Theta, \tag{2.80}$$

[7] Thomson scattering is the low energy limit of Compton scattering where the mass-energy of electrons is significantly larger than the photon momentum.

[8] Note I ignored the anisotropic component of the Thomson scattering here. The general expression is $\mathrm{d}\sigma(\Omega)\mathrm{d}\Omega = 3\sigma_T/(16\pi)[1 + (\hat{p}'_{\mathrm{in}}\cdot\hat{p}')^2]$ where $\hat{p}_{\mathrm{in}}$ is the direction of the in-scattering photon and $\hat{p}$ is the line-of-sight.

we now find

$$\frac{\mathrm{d}\Theta}{\mathrm{d}t} = \frac{\mathrm{d}\ln\varepsilon}{\mathrm{d}t} - a\bar{n}_e\sigma_T\left[\Theta - \Theta_0 - \hat{p}\cdot\vec{v}_e\right], \tag{2.81}$$

where I defined the integral of perturbation over all directions

$$\Theta_0(\vec{x},t) := \int \frac{\mathrm{d}^2\hat{p}_{\rm in}}{4\pi}\,\Theta(\hat{p}_{\rm in},\vec{x},t)\,, \tag{2.82}$$

which is the *monopole* part of the perturbation. Having calculated the $\mathrm{d}\ln\varepsilon/\mathrm{d}\ln t$ term above, the photon Boltzmann equation becomes (in Fourier space),

$$\boxed{\dot{\Theta} + ik\mu\Theta = \dot{\Phi} - ik\mu\Psi - a\bar{n}_e\sigma_T\left[\Theta - \Theta_0 - i\mu v_e\right],} \tag{2.83}$$

where $\vec{v}_e := iv_e\hat{k}$ and $\mu := \hat{k}\cdot\hat{p}$.

2.5.2 Boltzmann equation for CDM

I now continue on our programme of calculating the standard cosmological Boltzmann equations with the non-relativistic CDM, whose constraint equation satisfies

$$g_{\mu\nu}P^\mu P^\nu = -m^2\,, \tag{2.84}$$

where m is the mass of the CDM particle and the energy can be defined as $E := \sqrt{p^2+m^2}$ where $p^2 = g_{ij}P^iP^j$ as before. Different from the case of photons, the four-momentum of a massive particle can be written as

$$P^\mu = \left[E(1-\Psi), p\hat{p}^i\frac{1-\Phi}{a}\right], \tag{2.85}$$

and the total time derivative of the CDM distribution, f_c, can be written as

$$\begin{aligned}\frac{\mathrm{d}f_c}{\mathrm{d}t} =& \frac{\partial f_c}{\partial t} + \frac{\partial f_c}{\partial x^i}\frac{\mathrm{d}x^i}{\mathrm{d}t} + \frac{\partial f_c}{\partial E}\frac{\mathrm{d}E}{\mathrm{d}t} + \frac{\partial f_c}{\partial \hat{p}^i}\frac{\mathrm{d}\hat{p}^i}{\mathrm{d}t}\\ =& \frac{\partial f_c}{\partial t} + \frac{\hat{p}^i}{a}\frac{p}{E}\frac{\partial f_c}{\partial x^i} - \frac{\partial f_c}{\partial E}\left[\frac{\mathrm{d}a/\mathrm{d}t}{a}\frac{p^2}{E} + \frac{p^2}{E}\frac{\partial\Phi}{\partial t} + \frac{\hat{p}^i p}{a}\frac{\partial\Psi}{\partial x^i}\right] = 0\end{aligned} \tag{2.86}$$

where in the second line of Eq. (2.86) I used results from the earlier part of this section and assumed no collision term for the CDM. Rather then expanding in f_c distribution, it is more common to multiply both sides of Eq. (2.86) with the phase-space volume $\mathrm{d}^3p/(2\pi)^3$ and

integrate as well as making definitions for the dark matter density and velocity as

$$n_c := \int \frac{\mathrm{d}^3 p}{(2\pi)^3} f_c \,, \tag{2.87}$$

and

$$v^i := \frac{1}{n_c} \int \frac{\mathrm{d}^3 p}{(2\pi)^3} f_c \frac{p\hat{p}^i}{E} \,. \tag{2.88}$$

The zeroth moment of the Boltzmann equation then gives the continuity equation for CDM,

$$\frac{\partial n_c}{\partial t} + \frac{1}{a}\frac{\partial (n_c v^i)}{\partial x^i} + 3\left[\frac{\mathrm{d}a/\mathrm{d}t}{a} + \frac{\partial \Phi}{\partial t}\right] n_c = 0 \,. \tag{2.89}$$

Note at zeroth order (where v_i and Φ vanish) one recovers $n_c^{(0)} \propto a^{-3}$. Setting n_c in terms multiplying v_i and Φ to $n_c^{(0)}$ and expanding CDM density to first order perturbations as

$$n_c = n_c^{(0)}[1 + \delta(\vec{x}, t)] \,, \tag{2.90}$$

the first order equations of motion (continuity and Euler equations) become (in Fourier space),

$$\boxed{\dot{\delta} + ikv + 3\dot{\Phi} = 0} \quad \text{and} \quad \boxed{\dot{v} + \mathscr{H} v + ik\Psi = 0 \,,} \tag{2.91}$$

where $v = (k^i/k)v$ and we modelled the CDM as a perfect fluid with vanishing anisotropic stress and pressure.

2.5.3 Boltzmann equation for baryons

Finally I calculate the Boltzmann equations for the electrons and protons, grouped together as baryons in cosmology. At early times, electrons and protons are coupled by Coulomb scattering in the form,

$$e + p \leftrightarrow e + p \,, \tag{2.92}$$

whose rate is larger than the expansion rate, satisfying $(\rho_e - \bar{\rho}_e)/\bar{\rho}_e = (\rho_p - \bar{\rho}_p)/\bar{\rho}_p := \delta_b$ and $\vec{v}_e = \vec{v}_p := \vec{v}_b$. I now derive equations for δ_b and $\vec{v}_b$.

The collision terms for the electrons and protons can be written as

$$\frac{\mathrm{d}f_e(\vec{x},\vec{q},t)}{\mathrm{d}t} = \langle C_{ep}\rangle_{QQ'q} + \langle C_{e\gamma}\rangle_{pp'q'} \tag{2.93}$$

and

$$\frac{\mathrm{d}f_p(\vec{x},\vec{Q},t)}{\mathrm{d}t} = \langle C_{ep}\rangle_{qq'Q}\,, \tag{2.94}$$

where I assigned the 3-momentum wave-vectors $\vec{q}$ and $\vec{q}'$ to the electron and $\vec{Q}$ and $\vec{Q}'$ to the proton. C_{ep} and $C_{e\gamma}$ are unintegrated Coulomb and Compton collision terms, respectively and

$$\langle(\ldots)\rangle_{pp'q'} := \int \frac{\mathrm{d}^3p}{(2\pi)^3}\frac{\mathrm{d}^3p'}{(2\pi)^3}\frac{\mathrm{d}^3q'}{(2\pi)^3}(\ldots)\,, \tag{2.95}$$

for example.

Similar to before, multiplying both sides of Eq. (2.93) with the phase space volume and integrating give

$$\frac{\partial n_e}{\partial t} + \frac{1}{a}\frac{\partial(n_e v_b^i)}{\partial x^i} + 3\left[\frac{\mathrm{d}a/\mathrm{d}t}{a} + \frac{\partial\Phi}{\partial t}\right] n_e = \langle C_{ep}\rangle_{QQ'q'q} + \langle C_{e\gamma}\rangle_{pp'q'q}\,. \tag{2.96}$$

It is important to emphasise that the full integrals on the right-hand side of Eq. (2.96) are symmetric under $Q \leftrightarrow Q'$ and $q \leftrightarrow q'$ and hence vanish once integrated over the phase space volume $\mathrm{d}^3q/(2\pi)^3$. More intuitively, the scattering process conserve electron number and do not contribute to $\mathrm{d}n/\mathrm{d}t$. Hence the first equation for the baryon density is equivalent to the CDM equation of motion and take the form

$$\boxed{\dot{\delta}_b + ikv_b + 3\dot{\Psi} = 0\,.} \tag{2.97}$$

The second equation gives

$$\boxed{\dot{v}_b + \mathscr{H}v_b + ik\Psi = \dot{\tau}\frac{4\rho_\gamma}{3\rho_b}\left[3i\Theta_1 + v_b\right]\,,} \tag{2.98}$$

where $\dot{\tau} = \sigma_T a n_e$ is the time derivative of the optical depth, and

$$\Theta_1 := i\int_{-1}^{1}\frac{\mu\mathrm{d}\mu}{2}\Theta(\mu)\,, \tag{2.99}$$

is the first moment of the perturbation Θ.

2.6 Cosmic sound waves

2.6.1 Photon-baryon fluid

Let's now return to the photon Boltzmann equation Eq. (2.83). I expand the perturbations Θ in terms of Legendre polynamials:

$$\Theta(\eta,\vec{k},\hat{p}) \to \Theta(\eta,\vec{k},\mu) := \sum_{\ell=0}^{\infty}(-i)^{\ell}\Theta_{\ell}(\eta,\vec{k})P_{\ell}(\mu)\,, \tag{2.100}$$

where Θ are the multipole moments of the distribution. The lowest order multipoles can be related to the perturbed stress-energy tensor in a simple way,

$$\Theta_0 = \frac{1}{4}\delta_{\gamma}, \tag{2.101}$$
$$\Theta_1 = -v_{\gamma}, \tag{2.102}$$
$$\Theta_2 = -\frac{5}{3}\sigma_{\gamma}, \tag{2.103}$$

and the equations of motion for the temperature anisotropy moments can be found by multiplying Eq. (2.83) by $P_0(\mu)$ and $P_1(\mu)$ and integrating over μ, which give:

$$\dot{\Theta}_0 = -\frac{1}{3}k\Theta_1 + \dot{\Phi} \tag{2.104}$$
$$\dot{\Theta}_1 = k\Theta_0 - k\Psi - n_e\sigma_T(\Theta_1 + v_b)\,. \tag{2.105}$$

One now needs to input the baryon velocity which I have calculated earlier. I rearrange Eq. (2.98) to get

$$v_b = -\Theta_1 - \frac{R}{\Gamma}\left[\dot{v}_b + \mathscr{H}v_b + k\Psi\right], \tag{2.106}$$

where

$$\Gamma = a\bar{n}_e\sigma_T \qquad \text{and} \qquad R = 3\rho_b/4\gamma_b\,. \tag{2.107}$$

Note Γ^{-1} is comoving mean-free path of CMB photons $\Gamma^{-1} \simeq 4.9\times10^4(\Omega_b h^2)^{-1}(1+z)^{-2}$Mpc. On scales larger than Γ^{-1}, Thomson scattering forces the photon distribution

to be isotropic in the fluid's rest frame. The diffusion scale r_D, a key parameter in describing CMB fluctuations, is defined by integrating Γ^{-1} from $\eta = 0$ and gives the squared diffusion length

$$r_D^2 \sim \int_0^\eta \Gamma^{-1} \mathrm{d}\eta' \,. \tag{2.108}$$

By setting the $v_b \simeq -\Theta_1$ on the right-hand side of Eq. (2.106) I get

$$v_b \simeq -\Theta_1 + \frac{R}{\Gamma}\left[\dot{\Theta}_1 + H\Theta_1 - k\Psi\right] , \tag{2.109}$$

such that the equation for the first multipole moment of Θ becomes

$$\dot{\Theta}_1 = -\frac{\mathscr{H}R}{1+R}\Theta_1 + \frac{k}{1+R}\Theta_0 - k\Psi \,. \tag{2.110}$$

These equations for $\dot{\Theta}_0$ and $\dot{\Theta}_1$ can be combined to give the oscillatory equation of motion for the temperature monopole:

$$\boxed{\ddot{\Theta}_0 + \frac{\mathscr{H}R}{1+R}\dot{\Theta}_0 + c_s^2 k^2 \Theta_0 = -\frac{1}{3}k^2\Psi + \ddot{\Phi} + \frac{\dot{R}}{1+R}\dot{\Phi} \,,} \tag{2.111}$$

where combined effects of pressure (last term on the left-hand side) and gravity (first term on the right-hand side) is evident. The speed of sound of the baryon-photon fluid is defined as

$$c_s^2 := \frac{1}{3(1+R)} \,. \tag{2.112}$$

2.6.2 Oscillatory solutions

Equation (2.111) is essential for understanding the CMB fluctuations discussed in the following sections. Before describing the CMB observable, however, let us comment on the solutions of this equation. Treating R as approximately constant, we can write the evolution equation above in the form a differential equation of a harmonic oscillator with frequency $c_s k$. I consider the solution where I ignore time variations in the metric potentials Φ and Ψ. One can now rewrite Eq. (2.111) as

$$\ddot{\Theta}_0 + c_s^2 k^2 \Theta_0 = -\frac{k^2}{3}\Psi \,, \tag{2.113}$$

which is a simple harmonic oscillator equation with a gravitational forcing term. Reminding ourselves the adiabatic initial conditions, where $\dot{\Theta}_0(\eta = 0) = 0$ [39], the solutions of this equation satisfy

$$\Theta_0(\eta,\vec{k}) = [\Theta_0(\eta = 0,\vec{k}) + (1+R)\Psi(\vec{k})](\vec{k})\cos(kr_s) - (1+R)\Psi(\vec{k}) \quad (2.114)$$

$$\Theta_1(\eta,\vec{k}) = -3[\Theta_0(\eta = 0,\vec{k}) + (1+R)\Psi(\vec{k})](\vec{k})c_s\sin(kr_s)\,, \quad (2.115)$$

where I defined the sound horizon, $r_s := c_s(a\mathscr{H})^{-1} = \int_0^\eta c_s \mathrm{d}\eta' \simeq c_s\eta$. Photon fluctuations remain constant beyond the horizon until they cross the sound horizon, after which they start to oscillate.

First, I focus on Eq. (2.114). At early times when photons dominate the fluid $R \to 0$ and the solution corresponds to a harmonic oscillator whose zero-point (where gravity and pressure are balanced) is displaced by gravity. Since gravitational infall increase the number density and the energy of the photon, displacement satisfying $-\Psi > 0$ results in hotter (redshifted) photons in the potential well. After decoupling, photons loose energy as they have to climb out of the potentials and the correspond redshift cancels the initial $-\Psi$ blueshift. These emerging photons satisfy

$$\Theta_0(\eta,\vec{k}) + \Psi(\vec{k}) = [\Theta_0(\eta = 0,\vec{k}) + \Psi(\vec{k})]\cos(kr_s)\,, \quad (2.116)$$

which correspond to the peaks of the CMB spectrum, approximately corresponding to the set of wavenumbers $k_n = n\pi/r_s(\eta_*)$ where n_* is the time of decoupling. In the presence of baryons the sound speed decreases and the gravitational infall leads to a greater compression of the baryon-photon fluid inside potential wells. This results in a larger displacement of the zero-point, enhancing peaks from compression and suppress those from rarefaction. Finally, during radiation dominated era where potentials Ψ and Φ are time dependent, the decay of potential enhances temperature fluctuations, resulting in the higher peaks to bet additionally enhanced amplitudes. These effects afforded by the first term in Equation (2.114) are called the 'Sachs-Wolfe' [61] contributions to the CMB.

Equation (2.115) corresponds to the Doppler contribution to the CMB which arises from the peculiar (bulk) velocity of the electrons. Photons scatter from moving electrons and receive an energy boosts proportional to the electron velocity projected onto the photon scattering direction. Because $v_\gamma \simeq v_b$ and vanish outside the sound horizon, the Doppler effect is suppressed on large-scales.

2.7 Observational probes

2.7.1 Cosmic microwave background anisotropies

The CMB anisotropies are a remarkable observational probe of the primordial density fluctuations, the acoustic oscillations, the evolution of the gravitational potentials and today's structure of the Universe through lensing effects. In this section I give a brief review of CMB fluctuations which I use extensively throughout this thesis.

The CMB is described by its temperature and polarisation anisotropies. Following the same notation as before, the fractional temperature anisotropy $\Theta(\hat{\mathbf{n}})$ is defined as

$$\Theta(\hat{\mathbf{n}}) := \frac{T(\hat{\mathbf{n}}) - \bar{T}_{\rm CMB}}{\bar{T}_{\rm CMB}} = \sum_{\ell=0}^{\infty} \sum_{m=-\ell}^{\ell} a_{\ell m} Y_{\ell m}(\hat{\mathbf{n}}) \,, \tag{2.117}$$

where $T(\hat{\mathbf{n}})$ is the CMB temperature field at a given position on the sky. In the second equality, $\Theta(\hat{\mathbf{n}})$ is decomposed in terms of the spherical harmonics $Y_{\ell m}(\hat{\mathbf{n}})$ for a given integer multipole $\ell \geq 0$, and $m = -\ell, \ldots, +\ell$. $a_{\ell m}$ are spherical harmonic coefficients. The monopole temperature $\bar{T}_{\rm CMB}$ corresponds to $\ell = 0$, and the dipole, dominated by our motion relative to the CMB via Doppler shift, corresponds to $\ell = 1$.

Given stochastic quantum fluctuations in the early Universe, sourced temperature fluctuations are random and have zero mean. For the case of Gaussian initial conditions, the 2-point correlations of the multipole moments $a_{\ell m}$, i.e. the angular power spectrum of perturbations, C_ℓ, therefore contains the cosmological information. The rotational invariance of the angular power spectrum means it only depends on the multipole moment ℓ, not m. The temperature auto-correlation defines the temperature power spectrum C_ℓ^{TT},

$$C_\ell^{TT} = \frac{1}{2\ell+1} \sum_m \langle |a_{\ell m}|^2 \rangle \,, \tag{2.118}$$

where $\langle\ \rangle$ denotes an ensemble average over many sky realisations. For any given value of ℓ, there are $2\ell+1$ measurements m to constrain a given C_ℓ, indicating observations are fundamentally limited to measuring $2\ell+1$ independent modes. This gives rise to a large variance on large scales (small ℓ), and is known as *cosmic variance*.

The temperature anisotropies in the CMB are complemented by the polarisation of the CMB photons, which provide additional information about the early Universe. The non-instantaneous nature of recombination leads to the surface of last scattering to have some finite thickness. Within the surface of last scattering, CMB photons scatter off on free

electrons via Thomson scattering. Any anisotropy in the spectrum of incoming photons lead to a linear polarisation of the CMB radiation from the scattered photons. The polarisation anisotropy spectrum can be measured in a similar vein to the temperature spectra. The polarisation field $P(\hat{\mathbf{n}})$ can be described by two Stokes parameters Q and U (given a choice of coordinate description on the sky), $P = Q + iU$. P can also be decomposed in terms of (spin-weighted) spherical harmonics using E and B modes which correspond to 'electric' (gradient) and 'magnetic' (curl) components of the polarisation field,

$$P(\hat{\mathbf{n}}) = Q(\hat{\mathbf{n}}) + iU(\hat{\mathbf{n}}) \tag{2.119}$$

$$= \sum_{\ell=2}^{\infty} \sum_{m=-\ell}^{\ell} (E_{\ell m} + iB_{\ell m})\, {}_2Y_{\ell m}(\hat{\mathbf{n}})\,, \tag{2.120}$$

where the additional index 2 indicates that P is a spin-2 field,

$$C_\ell^{EE} = \frac{1}{2\ell+1} \sum_{m=-\ell}^{\ell} |E_{\ell m}|^2 \tag{2.121}$$

$$C_\ell^{BB} = \frac{1}{2\ell+1} \sum_{m=-\ell}^{\ell} |B_{\ell m}|^2\,. \tag{2.122}$$

The primordial E modes are originated from scalar fluctuations in the density field; whereas at linear order, B modes are sourced by tensor fluctuations, i.e. gravitational waves (such as from inflation). This makes the polarisation spectra of the CMB, C_ℓ^{EE} and C_ℓ^{BB}, an important probe for fluctuations in the early Universe. Lastly, cross-correlations of CMB temperature and E-mode polarisation, C_ℓ^{TE}, provide an additional independent observable, and is useful for foregrounds and instrumental effect calibration.

In addition to the polarisation of the CMB, another important consequence of non-instantaneous recombination is the damping of power of anisotropies on small scales. During recombination, CMB photons brownian scatter with free electrons many times. The average distance a photon travels is the mean free path λ_d,

$$\lambda_d \simeq \frac{1}{\sqrt{n_e \sigma_T H}}\,, \tag{2.123}$$

where σ_T is the Thomson scattering cross-section and n_e is the number density of electrons. Through n_e, the damping scale depends both on the baryon density of the Universe and on the primordial helium fraction Y_p. Through the Hubble rate H, the damping scale is sensitive to cosmological parameters related to the expansion history of the Universe prior

to recombination, including the effective number of free-streaming relativistic degrees of freedom, $N_{\rm eff}$, for example.

Next, CMB power spectrum also shows distinct acoustic features due to BAOs. BAOs are sourced by the baryon-photon fluid which oscillates in time and space with a period determined by its sound speed c_s. The comoving distance travelled by a sound wave of the baryon-photon fluid by time η is called the sound horizon. The sound horizon is defined as

$$r_s(\eta) = \int_0^\eta \mathrm{d}\eta' c_s(\eta')\,, \tag{2.124}$$

which is measured to be approximately $r_s \simeq 150$Mpc in comoving length at last scattering. The frequency of the harmonic series of modes seen in CMB is set by the sound horizon, and the peaks in the CMB power spectrum are modes caught at extrema of their oscillations. Peak positions are described by the θ_s parameter, which depends on the angular diameter distance at which we are observing the fluctuations, D_A, and the sound horizon, as $\theta_s = r_s/D_A$, allowing for the BAO signature in the CMB to give an extremely precise measurement of the geometry of the Universe at early times. Furthermore, analogous to mass oscillating on a spring, oscillations of baryon-photon plasma in- and out- of the potentials wells are sensitive to the ratio of baryons and the total matter. (Increasing baryon density increases the rarefraction inside potential wells while correspondingly decreasing the compression away from the potential wells, changing the ratio of the amplitudes of even and odd peaks, respectively.)

In addition to the intrinsic temperature fluctuations, CMB anisotropies can be sourced by gravitational redshift (or blueshift) due to potentials at the last scattering, i.e. the Sachs-Wolfe effect (SW) effect [61], by time-evolving potentials along the line of sight [the integrated SW (ISW) effect], by velocity-dependent Doppler effects at the last scattering surface, and due to the gravitational weak lensing effect. The lensing effect also provides an important observable accessible to the CMB measurements: the gravitational weak lensing potential.

Cosmological models make distinct predictions for the lensing potential power-spectrum $C_\ell^{\phi\phi}$, similar to variances of temperature anisotropies of intensity and polarisation. Lensing of the CMB is local in the observed direction, and takes the form

$$\tilde{\Theta}(\hat{\boldsymbol{n}}) = \Theta(\hat{\boldsymbol{n}} + \vec{\alpha}(\hat{\boldsymbol{n}}))\,, \tag{2.125}$$

(similarly for the polarisation field) where the lensing deflection angle is approximated as a pure gradient, $\vec{\alpha}(\hat{\boldsymbol{n}}) = \boldsymbol{\nabla}\phi$, and ϕ is the lensing potential. Lensing of the CMB (along with the ISW effect) provides sensitivity to the matter distribution and the growth of LSS along

the line of sight, providing constraining power on cosmological parameters including the sum of neutrino masses $\sum m_\nu$. Neutrinos slow the growth of LSS by delaying the cooling of the ultra-relativistic gas due to cosmic expansion.

2.7.2 21cm hydrogen-line signal from reionization and cosmic dawn

The hyperfine splitting of the ground state of neutral hydrogen possesses a triplet and singlet ground state. These two states are spin-flip states and the forward (backward) transition from the triplet state to singlet state is accompanied by an emission (absorption) of a 21cm wavelength photon. Whether cosmological hydrogen emits or absorbs 21cm photons can be understood by calculating its spin temperature. The spin temperature local to the hydrogen, T_s, can be described by the relation

$$\frac{n_1}{n_0} = \frac{g_1}{g_0} e^{-T_*/T_s}\,, \tag{2.126}$$

where n_0 (n_1) is the comoving number density of the hydrogen atoms in the singlet (triplet) state, $g_0 = 1$ ($g_1 = 3$) are the numbers of degrees of freedom of the singlet (triplet) state, and $T_* = 0.068$ is the temperature corresponding to the 21cm hyperfine transition. Observations are made in reference to the CMB. When the local spin temperature is larger (lower) than the CMB temperature, hydrogen emits (absorbs) photons from the CMB. The distribution of these photons at the corresponding wavelength can be studied to understand the astrophysics and cosmology of our Universe in dark ages. The main observable of interest is the brightness temperature of the 21cm hydrogen-line whose perturbations take the form [62],

$$\delta T_{21} = 38\text{mK}\left(1 - \frac{T_\gamma}{T_s}\right)\left(\frac{1+z}{20}\right)^{1/2} x_{\rm HI}(1+\delta n_b)\frac{\partial_r v_r}{H(z)}\,, \tag{2.127}$$

where $x_{\rm HI}$ is the neutral-hydrogen fraction, $\partial_r v_r$ is the line-of-sight gradient of the velocity, δn_b is the fractional number density and T_γ is the local CMB temperature.

The epoch of interest to the study in the thesis is the cosmic dawn era, defined by the formation of the first stars. This is theorised to begin around $z \sim 35$ with the bulk of galactic star formation occurring $z \sim 25$ e.g. [63]. Initially, after recombination, the gas temperature remains coupled to the CMB temperature, $\bar{T}_{CMB}$, at high redshifts $z > 200$ due to rapid Compton scattering of the background photons off electrons left over in the IGM gas. Both $\bar{T}_{CMB}$ and gas temperature drop as $1+z$ until the gas decouples from the CMB and start

adiabatic cooling, after which its temperature drops as $(1+z)^2$ until first collapsed objects form at low redshifts, $z \lesssim 30$. The spin temperature, moreover, remains coupled to the gas temperature until around redshifts $z \simeq 100$, where the efficiency of collisional coupling to gas drops due to cosmic expansion. During this time, the spin temperature is excepted to couple again to the CMB temperature due to absorption of CMB photons [64]. Spin temperature eventually re-couples to the gas, however, as the first astrophysical objects produce a Lyman-α background and start ionizing the IGM, boosting the gas temperature above the $\bar{T}_{CMB}$. Remnants of these first stars are likely to produce a diffuse background of $\sim 0.1-2$ keV X-rays, which causes shock heating throughout the gas before reionization progresses largely after $z \sim 10$. As the tail-end of reionization is approached ($z < 10$), the effects of streaming velocities in the IGM on the 21cm signal are reduced by Lyman-Werner feedback [63]. Please see [65] for more detail on this context.

The power spectrum of the 21cm signal can be written as

$$\langle \delta T_{21}(\vec{k},z)\delta T_{21}^{*}(\vec{k}',z)\rangle = (2\pi)^3\delta(\vec{k}-\vec{k}')P_{21}(\vec{k},z)\,, \tag{2.128}$$

where $\delta T_{21}(\vec{k},z)$ is the Fourier transform of $[T_{21}(\vec{x})-\bar{T}_{21}]/\bar{T}_{21}$, the zero mean fluctuations of the 21cm hydrogen brightness temperature at redshift z. An important feature of the 21cm power spectrum observable from the cosmic dawn is the BAOs. The modulation of the 21cm power-spectrum due to DM-baryon relative velocity can be captured to a good approximation from the statistics of the collapsed baryonic density. The effect of bulk relative velocity is analogous to that of the gas pressure, suppressing the accretion of baryons. As the gas falls into the DM halo, its bulk kinetic energy is converted into thermal energy resulting in a change in the effective sound speed $c_{\rm eff,s} \simeq (c_s^2+v_{\rm cb}^2)^{1/2}$, the critical mass scale and the baryon collapsed fraction. The effect of the relative velocities on the amplitude of the 21cm brightness temperature power-spectrum can then be parametrised as

$$\Delta^2_{21,\rm vel}(k,z) = A_{\rm vel}(z)\Delta^2_{v^2}(k,z)|W(k,z)|^2\,, \tag{2.129}$$

where $A_{\rm vel}$ is some redshift-dependent amplitude of fluctuations, $W(k,z)$ is some window function that can be utilised to isolate the different contributors to the 21cm power-spectrum such as Lyman-α coupling and X-ray heating. I defined $\Delta^2_{v^2}(k)$ as the power-spectrum of the quantity

$$\delta_{v^2} = \sqrt{\frac{3}{2}}\left(\frac{v_{\rm cb}^2}{v_{\rm rms}^2}-1\right)\,, \tag{2.130}$$

which accurately captures the shape of the effect of relative velocities on the observables for the scales of interest where the 'streaming' bulk relative velocity can be approximated with a root-mean-squared value $v_{\rm rms} \simeq 30{\rm km\,s^{-1}}$ at recombination. Note that the coefficient $A_{\rm vel}$ is a model-dependent amplitude that is not directly observable, similar to the BAO amplitude. As the Velocity Acoustic Oscillations (VAOs) are statistically independent from the density fluctuations at first order, the amplitude of the 21cm power-spectrum can be written as

$$\Delta^2_{21}(k,z) = \Delta^2_{21,\rm vel}(k,z) + \Delta^2_{21,\rm nw}(k,z)\,, \tag{2.131}$$

where I defined $\Delta^2_{21} := k^3 P_{21}(k,z)/2\pi^2$, following a similar notation as in [66], and $\Delta_{21,\rm nw}(k,z)$ is the component *excluding* VAOs. I will make use of these definitions in Chapter 8.

2.7.3 Large-scale structure, BAO and SNe Ia

The utility of the primary CMB as a instrument for cosmological inference from the early Universe is complemented by measurements of the late-time expansion and growth history from surveys of galaxies, large samples of SNe Ia, strong gravitational lenses as well as the weak gravitational lensing of the CMB. The different sensitivities of these probes to the late-time evolution and structure growth provide cosmologists with strong tools in developing our cosmological understanding.

Compared to the CMB, a main benefit of LSS surveys is the prospect of measuring many more Fourier modes in three dimensions, with scaling $N_{\rm modes} \propto k^3_{\rm max}$, where $k_{\rm max}$ is the highest wavenumber accessible to measurements that can be modelled robustly. Increased number of modes in turn can potentially reduce errors on cosmological measurements significantly. Observables most relevant to cosmology include 3-dimensional clustering of galaxies and the weak gravitational lensing.

While galaxy clustering is a sensitive probe of the distribution of matter in the Universe, they also suffer from various issues. Most importantly, they are biased tracers of the underlying matter field and they are measured with redshifts, rather than real-space positions. For the former, a galaxy survey analysis must model galaxy bias and the bias parameters must be marginalised, often reducing the quality of cosmological parameter constraints. The former introduces a well-known effect called redshift-space distortions (RSDs) which can provide a good way to phase the redshift dependent growth rate, while potentially playing a limiting role in the sensitivity of the LSS surveys.

Features of the galaxy power spectrum include a characteristic peak determining the transition from radiation to matter domination and sensitive to the matter density ω_m. The BAOs discussed in this review also leave a distinct oscillatory feature in the galaxy power spectrum due to their influence on the galaxy distribution today. The BAO feature in the galaxy power spectrum provides a 'standard ruler' with which to measure the expansion rate of the Universe, providing constraints on ω_m, H_0 and the properties of dark energy [67–69]. Lastly, the evolution of clustering of galaxies is also sensitive to the growth rate which allows for testing of different gravitational models [70–72].

The major challenge of inferring cosmology from clustering measurements is the need of modelling non-linear effects at short distances and high densities. These effects often introduce large and poorly-understood theoretical and systematic uncertainties, which can also affect the larger scales via mode coupling. These problems can either be surmounted by careful modelling of systematics and uncertainties (which boosts the number of parameters that need to be marginalised [73–82]), or partially avoided by utilising templates designed to optimally select cosmological signatures robust against complicated non-linearities, such as BAO scale measurements [83–89].

In addition to galaxy clustering, shape distortions of galaxies in photometric surveys probe weak gravitational lensing due to LSS. Unlike the galaxy measurements, the weak gravitational lensing observable traces the integrated matter density and is not subject to the unknown biases suffered by the former. The weak gravitational lensing observations are hence often accepted to be a purer probe of cosmology. Similar to galaxy measurements, however, the non-linearity of the lensing field is also subject to theoretical uncertainties and the shape of the non-linear matter power spectrum including its modifications due to baryonic effects, for example, needs to be modelled. Baryon displacements are subject to complicated feedback processes that can affect the gravitational potential within and around the dark matter halos and change the power spectrum of the halo observables on small scales. These effects also propagate to lensing observables [90–92].

Issues related to modelling non-linearities and baryonic effects are complemented with other systematics which include those associated with the actual measurements (recovering redshifts and shape of galaxies, for example), obtaining photometric redshifts for the lenses for the purpose of tomography, as well as modelling of the intrinsic correlations of galaxy shapes due to effects other than lensing [e.g. 93, 94]. Recent years have seen a wealth of new techniques for overcoming these systematics [see, e.g. 95–98], and correspondingly tighter cosmological constraints. Modern lensing surveys predominantly constrain $S_8 =$

$\sigma_8\sqrt{\Omega_m/0.3}$, along with dark energy equation of state and curvature of the Universe [99, 97, 100].

Finally, type Ia supernova (SNe Ia) measurements have been proved to be an important instrument for constraining the expansion history of the Universe at lower redshifts than LSS surveys. These measurements are calibrated using nearby distance anchors, and provide local measurements of H_0 with the advantage of not needing to assume a cosmological model [101–103]. At high redshifts, measurements of supernovea can constrain the properties of dark energy [104]. The high-precision modern supernova measurements are subject to systematics including effects of contamination and host galaxy properties on supernova magnitudes [105–107] as well as observational systematics [108, 109]. Careful consideration and modelling of these systematics allow robust cosmological constraints from SNe Ia measurements [110, 111, 104].

Chapter 3

Multi-field inflation and reheating

In this chapter I discuss the effect of reheating on observational predictions following multiple-field inflation. The chapter follows my published work in Ref. [12], where I made leading contributions, in collaboration with Jonathan Frazer, Andrew Jaffe, Joel Meyers, Layne Price and Ewan Tarrant. The chapter includes calculations by Ewan Tarrant and Joel Meyers. These are calculations of the semi-analyic predictions for the change in total curvature perturbations in the presence of multiple curvaton-like fields during reheating, and lead to Eqs. (3.20) and (3.23), for example. They are described in detail in text and depend on the so-called sudden decay approximation, which is also described. The results use publicly available MULTIMODECODE inflation solver [112–115], whose leading developer, Layne Price, is also a co-author in Ref. [12]. Contributions from Layne Price also include the calculation leading to Eq. 3.36. The text and presentation of the results has also seen important contributions from Joel Meyers, Jonathan Frazer and Andrew Jaffe. These three authors also contributed to the presentation of the work as well as the conceptualisation of the project. My essential contributions include recovering and contributing to the calculations overall, coding the needed modifications to MULTIMODECODE in order to solve reheating equations of motion and realise the sudden-decay process, producing all of the results, essentially providing the analysis and the presentation including all of the plots except the pedagogical plot in Fig. 3.1 as well as major contributions to the text throughout.

3.1 Introduction

Despite the phenomenological success of single-field models, they lack the generality of more complex scenarios, representing only a limited class of possible models. Importantly, they

are not always natural from a theoretical point of view, for example, string compactifications often result in hundreds of scalar fields appearing in the low energy effective action [116–119]. Models with multiple fields naturally produce non-adiabatic fluctuations, whose presence allows the curvature perturbation and its correlation functions to evolve outside the Hubble radius. Therefore, in order to make predictions in multi-field models, it is necessary to understand the evolution of the correlation functions until either the curvature fluctuations become adiabatic or they are directly observed. Unless an 'adiabatic limit' [120–126] is established before the onset of reheating, then the observable predictions of multi-field models will be sensitive to post-inflationary dynamics that must be accurately modeled before comparing the results to data.

Predictions of single-field inflation are largely insensitive to the details of reheating. Single-field inflation models produce purely adiabatic curvature perturbations ζ_k, which guarantees that the n-point correlation functions, $\langle\zeta^n\rangle$, do not evolve on scales exceeding the Hubble radius $k \lesssim aH$ during and after inflation [1, 39, 127, 128]. As a consequence, post-inflationary dynamics will not cause the perturbation spectra to evolve on super-Hubble scales, and only the integrated expansion following single-field inflation affects the prediction of cosmological observables [129, 59, 130, 131, 113, 132].

Non-adiabatic fluctuations can become adiabatic if the Universe passes through a phase of effectively single-field inflation [120–126] or through a period of local thermal and chemical equilibrium with no non-zero conserved quantum numbers [133–135]. The latter conditions are often established during the late stages of reheating, though notable exceptions include models in which dark matter is not a thermal relic, or where baryon number was produced before the end of inflation [136]. We will assume throughout this work that the result of reheating is a relativistic thermal plasma described entirely by its temperature. In this chapter we will focus on developing a methodology for calculating the predictions of multi-field inflation for the fully adiabatic power spectrum of curvature perturbations after reheating.

For two-field inflation, numerical studies [123, 137, 138] have demonstrated that observables such as the power spectrum $\mathscr{P}(k)$, and the local-shape bispectrum parameter $f_{\rm NL}$ can be very sensitive to the details of reheating. This sensitivity was quantified in Ref. [139], where it was shown that the adiabatic observables take values within finite ranges that are determined completely by the details of the underlying inflationary model. The effect of reheating is to preferentially enhance or suppress the initial fluctuations of some fields compared to others, depending on the details of the reheating model. This gives predictions that effectively interpolate between those obtained by projecting the non-adiabatic perturbations

along each of the two field direction ϕ_i in isolation. If the projection into each direction is the same, then the sensitivity to reheating for two-field inflation models is minimal.

In this chapter we extend the results of Ref. [139] and provide a general methodology for calculating the adiabatic power spectrum of curvature perturbations after multi-field inflation for any number of scalar fields. The regime of many-field inflation ($\mathcal{N} \gtrsim 10$) typically yields a range of predictions for curvature perturbations at the end of inflation that is surprisingly easy to categorize in comparison to the apparently large dimensionality of parameter space (see e.g. Refs [140–148], though stochastic effects can be important in the presence of many fields [149]). Scenarios with many fields also tend to predict an amount of isocurvature perturbations at the end of inflation which increases with the number of fields [142, 147], thereby elevating the importance of studying the effects of reheating for these models.

As in Ref. [139], we restrict ourselves to perturbative reheating. This ignores interesting dynamics such as preheating, which may non-perturbatively produce radiation quanta through parametric resonance [150] potentially leading to rich phenomena including primordial non-Gaussianity [151–153] and perhaps the production of primordial black holes [154–156]. However, perturbative reheating is a generically good phenomenological description for inflationary models with many degrees of freedom, as periods of exponential particle production become much harder to realize when many fields must conspire together to resonate [157–159], although single-field attractor behavior is common for some multiple-field models with non-minimal couplings to gravity [160]. Therefore, the methodology we develop here is quite generic for inflation with many fields $\mathcal{N} \gg 2$.

3.2 Overview

We begin here with a broad description of the methods that will be described in more detail in subsequent sections. We are interested in calculating the two-point statistics of the curvature perturbation after reheating has completed following multiple-field inflation. We will focus in particular on the scalar spectral index n_s and the tensor-to-scalar ratio r.

The δN formalism is a useful method for calculating the superhorizon evolution of the curvature perturbation in terms of the initial fluctuations of a set of scalar fields [161–165]. In this method one calculates the expansion from some initial time $t_\star$ on a spatially-flat hypersurface $g_{ij}(t_\star, \mathbf{x}) = a^2(t_\star)\delta_{ij}$, to some final time t_c on a uniform density hypersurface $\rho(t_c, \mathbf{x}) = \bar{\rho}(t_c)$. In practice we will take the initial hypersurface to be at horizon exit and the uniform density hypersurface to be after the conclusion of reheating when the Universe is

dominated by a thermal bath of radiation. The number of e-folds of expansion, defined as $N = \ln a_c/a_\star$, is given by

$$N(t_\star, t_c) = \int_{t_\star}^{t_c} H(t)\mathrm{d}t\,. \tag{3.1}$$

The perturbation to the number of e-foldings of expansion is equal to the difference in the curvature perturbation on these two hypersurfaces

$$\zeta = \delta N = \sum_i N_{,i}\delta\phi_i^\star + \frac{1}{2}\sum_{ij} N_{,ij}\delta\phi_i^\star\delta\phi_j^\star + \ldots\,; \tag{3.2}$$

where $N_{,i}$ refers to the derivative of the number of e-folds of expansion with respect to the initial scalar field value $N_{,i} = \partial N/\partial\phi_i^\star$.

Using Eq. (3.2) we can then calculate the observables of interest. Focusing on the two-point statistics, we find the curvature power spectrum,

$$\mathscr{P}_\zeta = \mathscr{P}_\star \sum_i N_{,i}^2\,, \tag{3.3}$$

the scalar spectral index,

$$n_s - 1 = -2\varepsilon_\star - \frac{2}{\sum_i N_{,i}^2}\left[1 - \sum_{ij}\eta_{ij}^\star N_{,i}N_{,j}\right]\,, \tag{3.4}$$

and the tensor-to-scalar ratio

$$r = \frac{8P_\star}{P_\zeta}\,, \tag{3.5}$$

where sums are carried out over all field indices $i = 1\ldots\mathscr{N}$. We have introduced the initial spectrum of scalar field fluctuations $\mathscr{P}_\star = H_\star^2/2k_\star^3$, and the slow-roll parameters $\varepsilon_\star = -(\dot{H}/H^2)_\star$ and $\eta_{ij}^\star = (V_{,ij}/V)_\star$, which are calculated at horizon crossing and V is the inflationary potential.

In order to calculate the expansion history and how it depends on the initial scalar field configuration, one in general needs to solve the perturbed field equations from horizon exit all the way through reheating. This is typically quite challenging due to the wide range of time and energy scales involved in the problem. The methods we will describe allow us to treat the post-inflationary evolution in a simplified manner, thus greatly reducing the computational cost of making predictions in multi-field inflationary models.

We proceed by splitting the problem into two parts. We first treat the evolution from horizon exit through inflation to a phase where the scalar fields are coherently oscillating about the minima of their potentials. This portion of the evolution is treated by numerically solving the perturbed field equations and is described in detail in Sec. 3.4. Next, we treat the process of reheating, when the scalar fields decay into radiation. As described in detail in Sec. 3.3, this part of the evolution can be treated semi-analytically by using a fluid approximation at very low computational cost, thus allowing us to quickly calculate how a wide range of reheating scenarios impacts the observable predictions of a particular multi-field inflationary model. For this part of the evolution, the unperturbed fluid equations are evaluated numerically, and the sudden decay approximation is applied to determine the impact of reheating on the cosmological perturbations.

As will be shown below, the impact of reheating following multiple field inflation is to mix together perturbations present in individual scalar fields present at the end of inflation into the final curvature perturbation with weights determined by the reheating parameters. Additionally, reheating impacts how the length scales we observe today are related to the scales during inflation. Even in single-field inflation, reheating affects how many e-foldings $N_\star$ before the end of inflation the observed fluctuations have crossed the Hubble horizon. Predicting this quantity requires matching the Hubble scale today to the Hubble scale during inflation, hence the modeling of the entire expansion history of the Universe. A simple comparison (approximating transitions between different epochs in the history of the Universe as instantaneous and ignoring the recent phase of dark energy domination) can be made by using the classical matching equation we defined in Eq. (2.54), where the number of e-foldings between the end of inflation and when the pivot scale crosses the Hubble horizon $k_\star = a_\star H_\star$ is defined as $N_\star = \ln a_{\rm end}/a_\star$, and $a_{\rm reh}$ is the scale factor at the the end of reheating, i.e. after all fields have decayed into radiation. The remaining quantities in the above expression are the Hubble horizon H_0 and the scale factor a_0 today and at the time of matter-radiation equality: $H_{\rm eq}$, $a_{\rm eq}$. The latter four quantities are well known from large-scale observations of the Universe. The remaining quantities are predicted by the inflationary model and the details of reheating, which fixes $N_\star$, the number of e-foldings of inflation after the pivot scale exits the horizon.

3.3 Reheating

During perturbative reheating, the relativistic energy densities gain energy at a rate

$$\dot{\rho}_i^{\gamma} + 4H\rho_i^{\gamma} = \Gamma_i \rho_i \tag{3.6}$$

whilst damping of the inflaton zero mode due to this decay process can be approximated by

$$\ddot{\phi}_i + (3H + \Gamma_i)\dot{\phi}_i + m_i^2 \phi_i = 0\,, \tag{3.7}$$

and the energy density stored in the oscillating field is $\rho_i = \frac{1}{2}(\dot{\phi}_i^2 + m_i^2\phi_i^2)$. Perturbative decay of the oscillating fields relies on the assumption that the decay rates can be calculated by standard methods in perturbative quantum field theory.[1] If, however, the amplitude of the field oscillations, and the couplings to gauge fields are sufficiently large, perturbation theory breaks down and reheating proceeds in a different way, through parametric resonance [167–169].

The impact of reheating on cosmological observables is well captured by appealing to the sudden decay approximation [170–172]. This approximation has been used frequently in the past to calculate the statistics of the primordial curvature perturbation for various models of inflation [171–175], the most widely known example with multiple fields being the curvaton scenario [176, 177, 170, 178, 179]. Furthermore, numerical studies have shown that for the curvaton scenario, and general models of two–field inflation, sudden decay reproduces the gradual decay result obtained by solving Eqs. (3.6) and (3.7) (together with the Friedmann constraint) remarkably well [172, 139].

We will focus on fields ϕ_i rolling in potentials with quadratic minima. During the phase of coherent oscillations, we will treat these fields as perfect fluids with vanishing pressure. In this approximation, the density of these matter fluids scale as a^{-3} and do not interact with their decay products until they instantly decay at some time t_i. These dynamics are schematically illustrated in Fig. 3.1 for the specific example of $\mathcal{N} = 5$ fields. We are interested in the statistics of the curvature perturbation $\zeta(t,\vec{x})$ at the final time $t = t_f$, when reheating has completed (all fields have decayed). Field ϕ_i (represented in Fig. 3.1 by its energy density ρ_i) is labelled according to its decay time t_i, where $i = 1,2,\ldots,\mathcal{N}$ and $t_1 < t_2 < \ldots < t_{\mathcal{N}}$. With

[1] Schematically, for example, consider inflaton interactions in the form $S_{\phi,\rm int} \in \int \mathrm{d}^4x\sqrt{-g}(-\sigma\phi\psi^2)$ where ψ is some scalar decay product. To tree-level order, for decay products lighter than the infaton quanta, the decay rate can be defined as $\Gamma_{\phi\to\psi\psi} = \sigma^2/(8\pi m)$ where we assumed the inflaton potential to be $V = m^2\phi^2/2$ for illustrative purposes. The decay rate determines the time evolution of the inflaton quanto at some fixed co-moving volume $\mathrm{d}(a^2 n_{\bar{\phi}})/\mathrm{d}t = -\Gamma a^3 n_{\bar{\phi}}$ where $n_{\bar{\phi}} = \rho_{\bar{\phi}}/m$ and hence, $\mathrm{a}^3(t)n_{\bar{\phi}}(t) \sim \exp(-\Gamma t)$. This additional exponential decay can be taken into account by including the friction term in Eq. (3.7) and the source term in Eq. (3.6) (see e.g. [166] and references therein).

this notation, the final time $t_f = t_{\mathscr{N}}$. Our derivation in this section is a generalization of the methods described in Refs. [172, 180, 139].

The underlying assumption of the sudden decay approximation is that the fields decay instantly into radiation when the Hubble rate becomes equal to the decay rate $H(t_i) = \Gamma_i$, which defines the decay time t_i. Furthermore, the decay hypersurfaces are taken to be surfaces of uniform energy density, upon which

$$\begin{aligned} \bar{\rho}_{\rm tot}(t_1) &= \bar{\rho}_\phi(t_1) = \sum_{i=1}^{\mathscr{N}} \rho_i(t_1,\vec{x})\,, && (3.8)\\ \bar{\rho}_{\rm tot}(t_j) &= \rho_\gamma(t_j,\vec{x}) + \rho_\phi(t_j,\vec{x}) \\ &= \sum_{i=1}^{j-1} \rho_i^\gamma(t_j,\vec{x}) + \sum_{i=j}^{\mathscr{N}} \rho_i(t_j,\vec{x})\,, \quad j \geq 2\,, && (3.9) \end{aligned}$$

where $\rho_i(t_j,\vec{x}) = \bar{\rho}_i(t_j) + \delta\rho_i(t_j,\vec{x})$ and $\rho_i^\gamma(t_j,\vec{x}) = \bar{\rho}_i^\gamma(t_j) + \delta\rho_i^\gamma(t_j,\vec{x})$. Here, ρ_ϕ denotes the total energy density stored in the oscillating scalar fields, and ρ_γ denotes the total energy density stored in the decay products

$$\rho_\phi = \sum_i \rho_i\,, \qquad \rho_\gamma = \sum_i \rho_i^\gamma\,. \tag{3.10}$$

Our first task is to determine how the individual curvature perturbation, ζ_i, associated with field ϕ_i, passes its fluctuation over to its decay product, ζ_i^γ. Within the confines of the sudden decay approximation this conversion is instantaneous. In the absence of interactions, fluids with barotropic equation of state, such as dust–like oscillating scalar fields and their radiation fluid decay products, have an individually conserved curvature perturbation [165, 172]

$$\zeta_i = \delta N + \frac{1}{3}\int_{\bar{\rho}_i(t)}^{\rho_i(t,\vec{x})} \frac{{\rm d}\tilde{\rho}_i}{\tilde{\rho}_i + P_i(\tilde{\rho}_i)}\,. \tag{3.11}$$

Here, δN is the perturbed amount of expansion, which, working within the separate universe assumption [164, 165], is equivalent to the difference in curvature perturbations measured from an initial flat hypersurface, up to one of constant energy density: $\delta N = \zeta$. In this notation, fluctuations are purely adiabatic if $\zeta_i = \zeta$ for all constituents of the Universe.

From this point on, all unbarred quantities will have an implicit dependence on position, while barred quantities have no spatial dependence. With $P_i = 0$ (relevant for the dust–like oscillating scalar fields before they decay), and $P_i^\gamma = \rho_i^\gamma/3$ (for the radiation decay products)

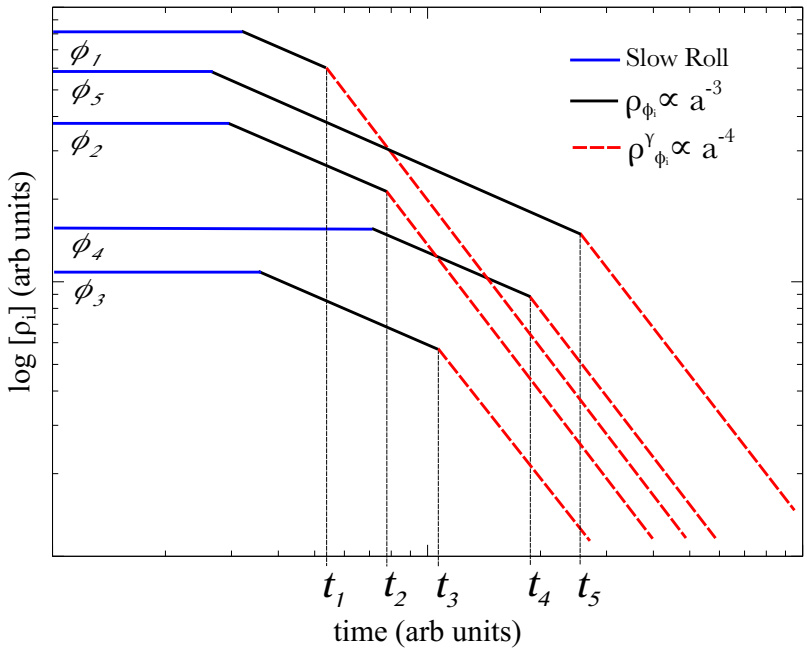

Figure 3.1: A typical "sudden decay" energy diagram illustrating the decay of $\mathcal{N} = 5$ fields. After the fields leave slow roll (blue sold lines) they begin to oscillate about their quadratic minima, their energy density scaling as a^{-3} (back sold lines). When $H(t_i) = \Gamma_i$ field ϕ_i decays instantly into radiation (red dashed lines) which scales as a^{-4} [12].

we can easily perform the integral in Eq. (3.11) to find:

$$\rho_i(t_j) = \bar{\rho}_i(t_j) e^{3(\zeta_1(t_1)-\zeta(t_1))}, \quad i \geq j, \tag{3.12}$$

$$\rho_i^{\gamma}(t_j) = \bar{\rho}_i^{\gamma}(t_j) e^{4(\zeta_1^{\gamma}(t_1)-\zeta(t_1))}, \quad i \leq j. \tag{3.13}$$

The $i \geq j$ and $i \leq j$ conditions reflect the fact that the decay products do not exist until the field has decayed. We have retained the explicit t_j dependence for the individual ζ_i for clarity, but it is to be understood that ζ_i is conserved between $t_i^{\rm osc} \leq t \leq t_i$, where $t_i^{\rm osc}$ is the time then the field ϕ_i begins to oscillate.

Making use of Eqs. (3.8) and (3.12), we have on the first decay hypersurface:

$$1 = \sum_{i=1}^{\mathcal{N}} \Omega_i(t_1) e^{3(\zeta_1(t_1)-\zeta(t_1))}, \quad \Omega_i(t_1) \equiv \left. \frac{\bar{\rho}_i}{\bar{\rho}_\phi} \right|_{t_1}. \tag{3.14}$$

Since decay is instantaneous, $\rho_1^{\gamma}(t_1, \vec{x}) = \rho_1(t_1, \vec{x})$, which, making use of Eq. (3.13), is equivalent to

$$\bar{\rho}_1^{\gamma}(t_1) e^{4(\zeta_1^{\gamma}(t_1)-\zeta(t_1))} = \bar{\rho}_1(t_1) e^{3(\zeta_1(t_1)-\zeta(t_1))}. \tag{3.15}$$

This must hold true even in the absence of fluctuations (where $\bar{\rho}_1^\gamma(t_1) = \bar{\rho}_1(t_1)$) and so

$$\zeta_1^\gamma(t_1) = \frac{3}{4}\zeta_1(t_1) + \frac{1}{4}\zeta(t_1)\,. \tag{3.16}$$

This expression provides the matching condition for the curvature perturbation on surfaces of uniform ρ_1 and uniform ρ_1^γ either side of the decay time t_1, and straightforwardly generalises to all subsequent decay times:

$$\zeta_i^\gamma(t_i) = \frac{3}{4}\zeta_i(t_i) + \frac{1}{4}\zeta(t_i)\,. \tag{3.17}$$

Having determined these matching conditions, we seek an expression for the total curvature perturbation at time $t_{\mathcal{N}}$. This is straightforward to obtain by repeating the above calculation for all subsequent decay times. Using Eqs. (3.13) and (3.9), we find, for $j \geq 2$:

$$1 = \sum_{i=1}^{j-1} \Omega_i^\gamma(t_j) e^{4(\zeta_i^\gamma(t_j) - \zeta(t_j))} + \sum_{i=j}^{\mathcal{N}} \Omega_i(t_j) e^{3(\zeta_i(t_j) - \zeta(t_j))}\,, \tag{3.18}$$

where

$$\Omega_i(t_j) = \left.\frac{\bar{\rho}_i}{\bar{\rho}_\gamma + \bar{\rho}_\phi}\right|_{t_j}, \qquad \Omega_i^\gamma(t_j) = \left.\frac{\bar{\rho}_i^\gamma}{\bar{\rho}_\gamma + \bar{\rho}_\phi}\right|_{t_j}. \tag{3.19}$$

Eq. (3.18) constitutes a non–linear expression for $\zeta(t_{\mathcal{N}}, \vec{x})$ if one takes $j = \mathcal{N}$. In order to solve Eq. (3.18) for $\zeta(t_{\mathcal{N}}, \vec{x})$, we proceed perturbatively. Expanding to first order and rearranging slightly:

$$\zeta(t_j) = \frac{4}{3}\sum_{i=1}^{j-1} r_{ij}\zeta_i^\gamma(t_j) + \sum_{i=j}^{\mathcal{N}} r_{ij}\zeta_i(t_j)\,, \quad j \geq 2\,, \tag{3.20}$$

where we have defined the 'sudden decay parameters'

$$r_{ij} \equiv r_i(t_j) \equiv \begin{cases} \left.\frac{3\bar{\rho}_i}{4\bar{\rho}_\gamma + 3\bar{\rho}_\phi}\right|_{t_j} & \text{for} \quad i \geq j \\ \left.\frac{3\bar{\rho}_i^\gamma}{4\bar{\rho}_\gamma + 3\bar{\rho}_\phi}\right|_{t_j} & \text{for} \quad i < j\,. \end{cases} \tag{3.21}$$

Since the ζ_i^γ are conserved for $t \geq t_i$, we may write $\zeta_i^\gamma(t_j) = \zeta_i^\gamma(t_i)$ for $i \leq j$, and use Eq. (3.17) in Eq. (3.20) to substitute for $\zeta_i^\gamma(t_i)$. Similarly, we may write $\zeta_i(t_j) = \zeta_i(t_i^{\rm osc})$ for

$i \geq j$. Making these two replacements, we find:

$$\zeta(t_j) = \frac{1}{3}\sum_{i=1}^{j-1} r_{ij}\zeta(t_i) + \sum_{i=1}^{\mathscr{N}} r_{ij}\zeta_i(t_i^{\rm osc})\,. \tag{3.22}$$

Evaluating this expression for $j = \mathscr{N}$ gives us a recursive expression for curvature perturbation at the end of reheating. After some straightforward manipulation, the expression for $\zeta(t_{\mathscr{N}})$ can be put into a slightly more convenient form:

$$\zeta(t_{\mathscr{N}},\vec{x}) = \sum_{i=1}^{\mathscr{N}} W_i\,\zeta_i(t_i^{\rm osc},\vec{x})\,, \tag{3.23}$$

where

$$W_i = \sum_{j=0}^{\mathscr{N}-1} A_j\, r_{i(\mathscr{N}-j)}\,, \tag{3.24}$$

and we have defined

$$A_j = \frac{1}{3}\sum_{k=0}^{j-1} A_k\, r_{(\mathscr{N}-j)(\mathscr{N}-k)}\,, \tag{3.25}$$

and $A_0 = 1$. Eq. (3.23) is our final expression for the primordial curvature perturbation at the completion of reheating. It is the statistics $\langle\zeta^n(t_{\mathscr{N}},\vec{x})\rangle$ of this fluctuation that are relevant for observation. It is clear from Eq. (3.23) that the effect of reheating (captured by the weights W_i) is to re–scale the $\zeta_i(t_i^{\rm osc},\vec{x})$. The W_i are functions of the sudden decay parameters r_{ij}, which can be directly related to the physical decay rates Γ_i within the confines of the sudden decay approximation. As discussed in [139], this is one area where the sudden decay approximation falls short and for this reason we compute the mapping from Γ_i to r_{ij} numerically.

Using numerical simulations, the individual curvature fluctuations $\zeta_i(t_i^{\rm osc},\vec{x})$ are determined completely by the details of inflation (the form of the potential and the field values at horizon crossing), and do not depend in any way upon reheating. As can be seen from Eqs. (3.23)-(3.25) once the curvature fluctuations are known, the effect of reheating on the cosmological perturbations can be calculated using only unperturbed energy densities evaluated at various times during the reheating phase. In the following section we discuss the calculation of the curvature fluctuations resulting from inflation.

3.4 Inflationary Perturbations

Generically, $\zeta_i(t,\vec{x})$ will evolve during multi-field inflation until an adiabatic limit is reached, at which point they become equal and conserved [120, 121, 123]. Whether conservation is achieved before the end of inflation depends upon the specifics of the inflationary model. Regardless of these specifics however, it is guaranteed that the $\zeta_i(t,\vec{x})$ will (to a very good approximation) be conserved quantities during the period when field ϕ_i is oscillating and before it has decayed appreciably into radiation. It is therefore sufficient to compute these quantities at $t = t_i^{\rm osc}$.

We use the publicly available MULTIMODECODE inflation solver [112–115] to evaluate the first-order mode equations for each scalar field, without using the slow-roll approximation. Following the convention of Ref. [181] we expand each of the first-order field perturbations in terms of a complex valued matrix q_{ij} as

$$\delta\phi^i(t,\vec{k}) = q_{ij}(t,k)\hat{a}^j(\vec{k}) + q^*_{ij}(t,k)\hat{a}^{\dagger,j}(-\vec{k}) \ , \tag{3.26}$$

where $(\dagger)$ and $(*)$ represent Hermitian and complex conjugation, respectively, and the creation and annihilation operators satisfy $[\hat{a}^j(\vec{k})]^\dagger = \hat{a}^j(-\vec{k})$ and the canonical commutation relations. The transformed variable $\psi_{ij} = q_{ij}/a$ satisfies the Mukhanov-Sasaki equation of motion with a "mixed" mass matrix $\mathscr{M}_{ij}$

$$\frac{{\rm d}^2\psi_{ij}}{{\rm d}N^2} + (1-\varepsilon)\frac{{\rm d}\psi_{ij}}{{\rm d}N} + \left(\frac{k^2}{a^2H^2} - 2 - \varepsilon\right)\psi_{ij} + \mathscr{M}_{im}\psi^m_j = 0 \tag{3.27}$$

where

$$\mathscr{M}_{ij} \equiv \frac{\partial_i\partial_j V}{H^2} + \frac{1}{H^2}\left(\frac{{\rm d}\phi_i}{{\rm d}N}\partial_j V + \frac{{\rm d}\phi_j}{{\rm d}N}\partial_i V\right) + (3-\varepsilon)\frac{{\rm d}\phi_i}{{\rm d}N}\frac{{\rm d}\phi_j}{{\rm d}N} \ , \tag{3.28}$$

with $\partial_i \equiv \partial/\partial\phi_i$ and N is the number of e-folds. We use the Bunch-Davies initial condition [182] for the transformed variable $\psi_{ij} \sim \delta_{ij}$ since for modes deep inside horizon $k \gg aH$, the mode matrix ϕ_{ij} obeys the free wave question in conformal time ${\rm d}^2\psi_{ij}/{\rm d}\eta^2 + k^2\psi_{ij} = 0$ [115].

The components of curvature perturbation are defined in the spatially-flat gauge as

$$\zeta_i(t,\vec{k}) \equiv \frac{H}{\dot{\bar{\rho}}_i}\delta\rho_i(t,\vec{k}) \ . \tag{3.29}$$

The density perturbations $\delta\rho_i(t,\vec{k})$ are given by

$$\delta\rho_i(t,\vec{k}) = \dot{\phi}_i(t)\dot{\delta\phi}_i(t,\vec{k}) - \frac{\dot{\phi}_i(t)^2}{2H}\sum_m \dot{\phi}_m(t)\delta\phi_m(t,\vec{k}) + V_{,i}\delta\phi_i(t,\vec{k}) \ . \tag{3.30}$$

Similar to the field perturbations, we expand each of the curvature perturbation components in the same basis by defining a new complex valued matrix ξ_{ij} as

$$\zeta_i(t,\vec{k}) \equiv \xi_{ij}(t,k)\hat{a}^j(\vec{k}) + \xi^*_{ij}(t,k)\hat{a}^{\dagger,j}(-\vec{k}) \ , \tag{3.31}$$

and similarly for $\delta\rho_i(t,\vec{k})$, which is related to $\delta\phi_i(t,\vec{k})$ and its derivatives. Substituting $q_{ij}(t,k)$ and its derivative into Eq. (3.29) gives

$$\xi_{ij}(t,k) = \frac{q'_{ij}(t,k)}{3\phi'_i(t)} - \frac{1}{6}\sum_m \phi'_m(t)q_{mj}(t,k) + \left[\frac{V_{,i}(t)}{3H^2(t)\phi'^2_i(t)}\right] q_{ij}(t,k) \ . \tag{3.32}$$

where $(')$ is a derivative with respect to e-folds N. A similar expression is available for $\xi^*_{ij}(t,k)$, which is linearly independent of ξ_{ij}. We evaluate this quantity by evolving the q_{ij} (or ψ_{ij}) and background quantities numerically as a function of t for a given k.[2]

We expand $\zeta_i(t_i^{\rm osc},\vec{x})$ in terms of field fluctuations at horizon exit,

$$\zeta_i(t_i^{\rm osc},\vec{x}) = \sum_{j=1}^{\mathcal{N}} C_{ij}\delta\phi_j(t_\star,\vec{x}) \ , \tag{3.33}$$

where C_{ij} is a real matrix. Substituting our $\delta\phi_i(t,\vec{k})$ from Eq. (3.26) into Eq. (3.33) gives

$$\xi_{ij}(t,k) = \sum_m C_{im}(t)q_{mj}(t_\star,k) \ . \tag{3.34}$$

While Eq. (3.34) is not invertible for general q_{mj}, we match to the slow-roll approximation above by first discarding the off-diagonal elements of the perturbation matrix q_{ij} at horizon crossing and define a vector $v_j(t_\star,k)$ as

$$q_{ij}(t_\star,k) \equiv {\rm diag}[v_1(t_\star,k),\ldots,v_N(t_\star,k)] \ . \tag{3.35}$$

[2]For more details of the numerical methodology see Ref. [115].

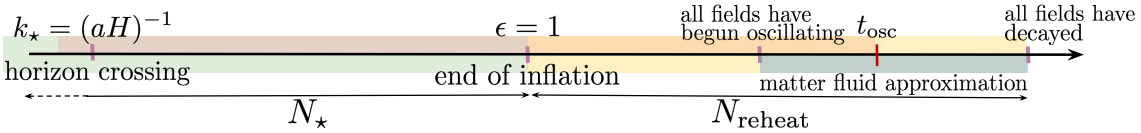

Figure 3.2: Timeline of inflation and reheating. The method we describe numerically evolves the perturbed scalar field equations until all fields have begun oscillating, after which we switch to evolving unperturbed fluid equations [12].

Since q_{ij} is complex and C_{ij} is real, we take

$$C_{ij} \approx -\mathrm{sgn}\left(\mathrm{Re}[q_{ij}]\right)\frac{|\xi_{ij}(t,k)|}{|v_j|}\,, \tag{3.36}$$

where the overall sign is chosen to match the two-field results of Ref. [139].

With this, we have all the ingredients to relate the curvature fluctuations at the end of reheating to the quantum fluctuations during inflation as in Eq. (3.2) where using Eqs. (3.23) and (3.33), the derivative of the number of e-folds of expansion can now be written as

$$N_{,i} = \sum_j W_j C_{ji}\,. \tag{3.37}$$

3.5 Numerical implementation

While the recursive definition of the reheating parameters introduced in Sec. 3.3 require solving numerically the homogeneous background equations until the end of reheating, it is sufficient to evolve the field fluctuations only until a few e-folds into the phase of coherent oscillations, after which the curvature perturbations of the fields $\zeta_i(t_i^{\rm osc},\mathbf{x})$ are individually conserved. The prescription for solving such a system of equations will typically involve evolving first the background equations in order to determine the number of e-foldings $N_\star$ at which the pivot scale (which we take to be $k_{\rm piv} = 0.05$ Mpc^{-1}) leaves the horizon during inflation, and then the first order fluctuations for each field from deep inside the horizon until the time where the curvature perturbations are conserved. Note that since we mainly want to explore the impact of reheating on inflationary observables, we will sample from many different Γ_i distributions while keeping the parameters describing the inflationary model unchanged. Hence this approach is quite inefficient for our purposes, as it requires solving for the inflationary dynamics as well as reheating for each assignment of decay parameters Γ_i. Instead in this work we have chosen to solve the inflationary fluctuations on a grid of $N_\star$

values in the range $N_\star \in (40-60)$ and perform a local linear fit to determine[3] the individual elements of the C_{ij} matrix in Eq. (3.36) for a given $N_\star$.

Following the methods outlined in MULTIMODECODE [112–115], we first solve the Klein-Gordon equations for the homogeneous background fields with initial conditions $\phi_{i,0}$ which determines the field-space positions at the end of the inflation defined by $\varepsilon = 1$. We then continue evolving the background fields after the end of inflation, well into the oscillatory phase. For the simulations in this chapter, we have evolved the field equations until each field ϕ_i has crossed its minimum 5 times, although the exact number does not effect the results significantly after each field has oscillated a few times. Knowing the times for the end of inflation and the onset of coherent oscillations, the C_{ij} matrix can be calculated by evolving the mode equations as described in Sec. 3.4 for a given value of $N_\star$. We calculate the C_{ij} matrix during the oscillatory period and evaluate the average of the maximum and minimum values for each C_{ij} matrix entry. We use this averaged C_{ij} matrix in calculating the observables. For the reasons explained above, we repeat this step multiple times while varying the quantity $N_\star$.

Since the exact value of $N_\star$ and the normalization of the potential $V_\star$ will depend on the details of reheating, we first solve the post-inflationary dynamics for some fiducial values $V_\star^{\rm fid}$ and $N_\star^{\rm fid}$. We calculate the W_i array by solving the scalar field equations for the background solution, using the end-of-inflation values $\phi_{i,\rm end}$ as the new initial conditions. Once a field ϕ_i has crossed the minimum of its potential, we turn on the decay term in its equation of motion, which sources the corresponding radiation fluid ρ_i^γ for that field. After all the fields have passed through their potential minima and started decaying into radiation, we stop evolving the Klein-Gordon equations and switch to a fluid description with equations of motion

$$\begin{aligned} \dot\rho_i + 3H\rho_i &= -\Gamma_i\rho_i \\ \dot\rho_i^\gamma + 4H\rho_i^\gamma &= \Gamma_i\rho_i\,, \end{aligned} \tag{3.38}$$

with the Hubble rate given by the Friedmann equation

$$3H^2 = \sum_i (\rho_i + \rho_i^\gamma)\ . \tag{3.39}$$

Note that the fluid densities have a mild dependence on when this transition is implemented, but the change to observables is negligible compared to the full range of predictions. We

[3] In order to smooth the small round-off error in our simulations, and to capture the underlying scaling with $N_\star$, we linearly fit the C_{ij} matrix elements from the elements of the calculated grid within ± 1 e-fold of the desired $N_\star$.

allow this fluid simulation run until all matter fluids have decayed into radiation. From the results of this numerical evolution, we are able to read off the quantities we need to apply the sudden decay approximation and determine the final curvature perturbation in the adiabatic limit at the end of reheating. Each time a decay rate becomes equal to the Hubble rate $\Gamma_i = H$, we evaluate the sudden decay parameters r_{ij} described in Sec. 3.3. After all the fields have decayed into radiation, we assume that all decay products quickly come to thermal and chemical equilibrium. The solutions will then rapidly approach the adiabatic limit, and we can calculate the curvature perturbation and its power spectrum as described in Eq. (3.2) and Eq. (3.3). This calculation results in a scalar amplitude given by $\mathscr{P}_\zeta^{\rm fid}$ which then needs to be rescaled to match observations.

The amplitude of the scalar fluctuations is fixed by the observations of the CMB anisotropies to be $\mathscr{P}_\zeta^{\rm CMB} \approx 2.142 \times 10^{-9}$ [183]. We rescale the inflationary potential in order to set the power spectrum calculated in Eq. (3.3) equal to this value. The relative quantities transform under the rescaling of the potential as $V \to \alpha V$ follows:

$$\rho \to \alpha\rho \ , \ H \to \alpha^{\frac{1}{2}} H \ , \ \mathscr{P}_\zeta \to \alpha \mathscr{P}_\zeta \ , \ \zeta \to \alpha^{\frac{1}{2}} \zeta \ , \tag{3.40}$$

where the scaling for our purposes is $\alpha = \mathscr{P}_\zeta^{\rm CMB} / \mathscr{P}_\zeta^{\rm fid}$. Having solved the dynamics of reheating, we also know from Eq. (2.54) the quantity

$$\ln \frac{a_{\rm reh}}{a_{\rm end}} = N_{\rm reheat} \ . \tag{3.41}$$

Rescaling the potential in order to match the CMB observations in turn fixes the remaining quantities in Eq. (2.54) where $N_\star$ (for a given $k_\star$) now takes an exact value (see Fig. 3.2 for a sketch of the timeline). We then fit the C_{ij} matrix elements corresponding to the calculated $N_\star$ from the grid of C_{ij} matrices we already calculated. This rescaling step after solving the dynamics of reheating is repeated for all simulations. Having determined the value $N_\star$, the corresponding C_{ij} matrix and the W_i array, we calculate the power spectrum and the cosmological observables as described in Sec. 3.2.

3.6 A Case Study

We consider inflation with canonical kinetic terms, a minimal coupling to Einstein gravity and $\mathscr{N}$-quadratic potential,

$$S = \int \mathrm{d}^4x\sqrt{-g}\left(\frac{R}{2} - \sum_i \frac{1}{2}g^{\mu\nu}\partial_\mu\phi_i\partial_\nu\phi_i - \sum_i m_i^2\phi_i^2\right), \tag{3.42}$$

a model which has been studied extensively elsewhere, e.g. [184–192]. We study the regime where one (or a few) field(s) dominates the energy density during inflation while the rest remain sub-dominant. We achieve this by setting the field masses m_i and initial field positions $\phi_{i,0}$ to be distributed linearly in log-space with equal spacing and the same ordering. In this regime the impact of reheating on the inflationary predictions is maximized when the sub-dominant fields get assigned smaller decay parameters, hence scaling like matter for a longer period, dominating the contributions to the curvature perturbation at the end of reheating. In our simulations we kept the ratio between the maximum and minimum masses constant and equal to $m_{\rm max}/m_{\rm min} = 10^3$ and fixed the initial field positions to be in the range $[10^{-3}, 20]$ $\mathrm{M_{pl}}$.

We are interested in determining how reheating impacts two-point statistics for a wide range of decay rates, and so we sample the very large parameter space as follows. First, we take the decay rates to be determined by the mass hierarchy as

$$\Gamma_i := 10^{-4}H_{\rm end}\left(\frac{m_i}{m_{\rm max}}\right)^{\alpha}, \tag{3.43}$$

where $H_{\rm end}$ is the Hubble parameter at the end of inflation, for some choice of the parameter α. Next, we perform a permutation σ_i on this first set of decay rates randomly chosen from the $\mathscr{N}!$ possible permutations in order to generate another set $\Gamma_i = \sigma_i(\Gamma)$. We perform this same procedure for several choices of the parameter α which allows us to adjust the hierarchy between the decay parameters. In all cases, the minimum decay rate is bounded from below by Big Bang nucleosynthesis which constrains the energy scale at the end of reheating to be larger than about 4 MeV, and perhaps higher if fields decay into hadrons [193, 194], and the maximum decay rate is constrained by the validity of sudden decay approximation to be less than the Hubble parameter at the end of inflation $\Gamma_{\rm max} < H_{\rm end}$. Note that increasing (decreasing) the value of the maximum decay constant $\Gamma_{\rm max}$ will in turn increase (decrease) the value of $N_\star$ that satisfies Eq. (2.54). The results shown in this chapter have values of $N_\star$ lower than the instant reheating case, in the range $N_\star \in (45-55)$.

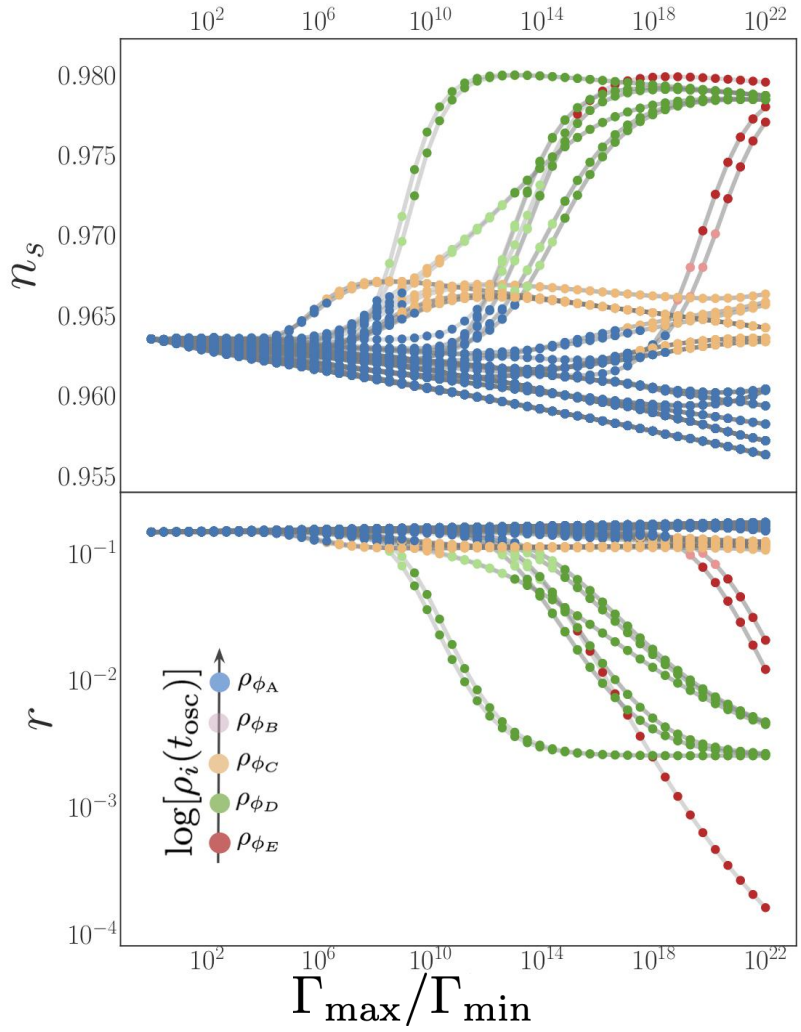

Figure 3.3: The effect of reheating on the scalar spectral index n_s and tensor-to-scalar ratio r for the case study in Sec. 3.6 with $\mathcal{N} = 5$ fields with $k_{\rm piv} = 0.05$ Mpc^{-1}. Colored circles show the results from simulations for a particular choice of decay rates Γ_i, chosen as described in text following Eq. (3.43). Each line (in gray) connects the results from simulations with an identical ordering of Γ_i values while the parameter α which determines their spacing is varied in the range $\alpha \in [0, \frac{22}{3}]$ in 50 steps. We plot the results from all possible 120 permutations of Γ_i. The colors mark the field that has the largest $N_{,i}$ at the end of reheating, for a particular simulation (except for the circles with lighter color, which highlight the simulations with the most energetic ϕ_A field still having the largest $N_{,i}$, although a second field is within 50% of $N_{,\phi_A}$). The labeling of the fields is ordered with respect to their energy densities at the end of inflation $\rho_i(t_{\rm osc})$ where ϕ_A has the largest energy density and ϕ_E has the smallest [12].

Fig. 3.3 demonstrates the effect of reheating on the two-point observables, the spectral index n_s and the tensor-to-scalar ratio r. The results from numerical simulations described in Sec. 3.5 are plotted with colored circles. Each line (in gray) connects the results from simulations with the decay rates assigned with the same permutation while the parameter α

is varied in the range $\alpha \in [0, \frac{22}{3}]$. The colors of the circles indicate the field with the largest measured $N_{,i}$ for that simulation. As shown in Eq (3.23), this parameter depends on two quantities, the C_{ij} matrix and the W_i array which operates on this matrix.

For the $\mathscr{N}$-quadratic case study, C_{ij} matrix has a simple structure where its diagonal elements are significantly larger than its off-diagonal elements. Since fluctuations grow larger in the less massive field directions, the values of the diagonal elements associated with these fields are also larger. Hence, for this study, the subset of simulations where reheating has a significant impact on observables are ones with particular Γ_i assignments resulting in the corresponding W_i arrays to preferentially dampen contributions from the heavier fields, while enhancing those from the lighter fields. These simulations are shown with varying colors in Fig. 3.3 where a large impact on observables is obtained when contributions from the lighter fields $\phi_{C,D,E}$ are enhanced.

For most choices of decay rates, the predictions for n_s and r lie very close to the predictions of a model with a single scalar field in a quadratic potential. The predictions that deviate from this result essentially interpolate between a single field regime and a curvaton-like scenario where a given sub-dominant field dominates the effect on observables, resulting in predictions to asymptotically converge on narrow lines of n_s and r predictions, as can be seen in Fig. 3.3. The values of the observables corresponding to these lines depend on the masses and values of the fields at horizon crossing, or in other words, on the details of the inflationary model. The total range of predictions in these scenarios therefore depends on the choice of the inflationary model parameters.

Fig. 3.4 summarizes our results for the $\mathscr{N}$-quadratic inflation case study with perturbative reheating and sudden decay approximation. Obtained values for the spectral index n_s and tensor-to-scalar ratio r for simulations with $\mathscr{N} = 5,\ 15,\ 35,\ 65$ fields are plotted with the *Planck* 2015 contours [50] with the pivot choice $k_{\rm piv} = 0.05$ Mpc^{-1} and the theory predictions for the single-field quadratic inflationary potential. In populating the $n_s - r$ plane, we show results for the Γ_i chosen from all 120 permutations for the models with 5 fields, and for $\mathscr{N} \geq 15$ we show only the results where the Γ_i are ordered similarly to the field masses.[4] The density of points in this figure does not represent a simple measure on the input m_i and Γ_i parameter space, but are chosen to highlight the wide range of observable parameter values accessible in these scenarios. Most of the possible permutations, which are *outside* this set, fall near the quadratic inflation predictions (solid black line).

[4]This is an exceedingly small subset of all possible permutations for a model with many fields, $\mathscr{N} \gg 2$.

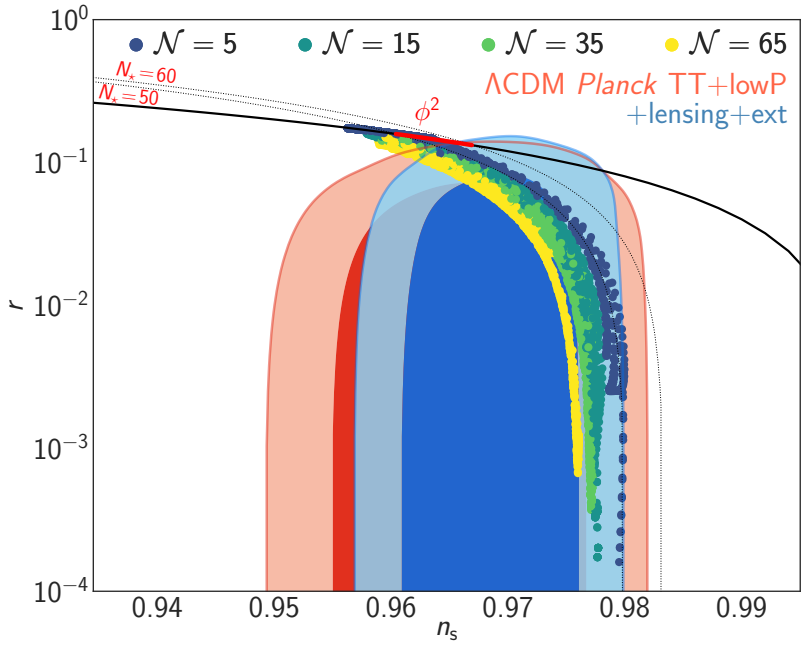

Figure 3.4: The predictions of the $\mathcal{N}$-quadratic inflation case study described in Sec. 3.6 for the scalar spectral index n_s and tensor-to-scalar ratio r from the sudden decay approximation, plotted with the *Planck* 2015 constraints using $k_{\rm piv} = 0.05$ Mpl^{-1} and assuming zero running. Dashed lines show the predictions from single-field inflation models with monomial potentials where the pivot scale exits the horizon 50 or 60 e-folds before the end of inflation (denoted by $N_\star$). The thick black line is the prediction of single-field quadratic inflation. The colored points are the results from our simulations with $\mathcal{N} = 5,\ 15,\ 35$ and 65 fields. See Sec. 3.6 for the details of how the decay rates are chosen. Note that only a small subset of possible choices of the decay rates leads to predictions which differ significantly from the single-field case. In particular, for simulations with a large number of fields $\mathcal{N} \geq 15$, only scenarios in which the decay rates share nearly the same hierarchy as the masses lead to predictions with very low r [12].

3.7 Discussion

We have developed a method to treat the impact of reheating on observables following multiple-field inflation. We have shown how to treat the effects of reheating semi-analytically, greatly reducing the computational cost to make definite predictions with multiple-field models.

Our results focused on one specific form for the inflationary potential, although our method applies much more broadly. Multiple-field models of inflation have a very rich parameter space which remains largely unexplored. The techniques described in this work allow for a thorough exploration of this space, including the potentially very important impact of reheating following multiple-field inflation, as has recently been done for a set of two-field models [195–197]. We restricted numerical results to $\mathcal{N}$-quadratic inflation with

specific choices for both the hierarchy of masses and the initial conditions. We showed that reheating can have an effect on the predictions of multiple-field inflation. For the scenarios we studied, reheating has a significant impact on observables only when the lightest fields are assigned very low decay rates (this is the case that realizes curvaton-like behavior). For choices of parameters where this relation is not present we found almost no sensitivity of the primordial curvature perturbation to the physics of reheating (apart from the dependence on $N_\star$ which is present even in single-field models). At large $\mathscr{N}$ we therefore found only a very small fraction of the tested scenarios exhibited sensitivity to reheating. Different choices of parameters would lead to a different set of perturbations predicted at the end of inflation, and also a different range of predictions for observables following reheating. Our focus has been on exploring a restricted set of initial conditions and model parameters but it would be interesting to perform a statistical analysis of the model as described in [145].

Looking beyond $\mathscr{N}$-quadratic inflation, our method requires only that scalar fields oscillate about quadratic minima, but there is nothing about our technique that restricts the form of the potential away from the minimum, and in fact a straightforward extension of the methods presented here would allow treatment of non-quadratic minima as well. The effects of reheating are expected to be greater than those shown here for more general choices of potential [139, 196].

While the need to include a detailed model of reheating makes multiple-field models of inflation inherently more complicated, the dependence of observables on the reheating phase also presents an opportunity. Very little is known about how reheating took place, though the sensitivity of observables to reheating following multiple-field inflation may allow more information to be gleaned about this weakly constrained phase of the cosmic history than is possible for single-field models [198, 132, 199, 200, 197].

We focused here on the two-point statistics of curvature perturbations, though it would be very interesting to extend our results to include the study of primordial non-Gaussianity [201]. Unlike single-field inflation models, multiple-field inflation models are capable of producing detectable levels of local-type non-Gaussianity [202, 203], therefore making calculation of higher-order statistics a natural next step for the tools we have developed here. Treatment of non-Gaussianity would require carrying out calculations to the next order of perturbation theory, but the general techniques spelled out here should apply without much modification.

Reheating is a necessary component of any successful inflationary model. For single-field inflation the predictions of observables are sensitive only to the integrated expansion history during reheating. However, the details of reheating following multiple-field inflation have an important and direct impact on the evolution of cosmological perturbations, and therefore

must be treated carefully when predicting the observable outcomes of these models. We presented here a method to make this treatment tractable.

Chapter 4

Review of CMB Secondary Anisotropies

Upcoming surveys of the cosmic microwave background (CMB) including those by Simons Observatory [204] and CMB-S4 [205] and galaxy surveys such as the Dark Energy Survey (DES) [206] and the survey by the Large Synoptic Survey Telescope (LSST, a.k.a. Vera C. Rubin Observatory) [207], will provide new opportunities for novel cosmological measurements.

In particular, by using the CMB as a cosmological backlight, secondary anisotropies induced by the interaction of CMB photons with structure along the line of sight, such as the weak gravitational lensing by large-scale structure (see [13] for a review); the integrated Sachs-Wolfe (ISW) [208] and Rees-Sciama effects [209], describing the process by which time-dependent gravitational potentials alter the energy of CMB photons; and the Sunyaev-Zel'dovich (SZ) effect [210–214], whereby CMB photons undergo Compton scattering with free electrons in galaxy clusters and the intergalactic medium, allow for new methods to study the history and evolution of the Universe and there is evidence that the measurement of these small-scale secondary anisotropies will provide strong constraints on a multitude of cosmological signatures (see e.g. [215–220, 17]). The statistics of these secondaries and their cross-correlations with large-scale structure (LSS) surveys carry information about cosmological fluctuations on large scales. Utilising this information will be instrumental in future tests of the standard ΛCDM paradigm.

In this chapter I aim to give a brief pedagogical introduction to CMB secondaries I will discuss in what follows. Similar to Chapter 2, I follow seminal textbooks on modern cosmology [1–4], as well as various review articles and lecture notes including [5–10] as well as [e.g. 221, 13, 14]

4.1 Integrated Sachs-Wolfe effect

The integrated Sachs-Wolfe (ISW) effect is an additional source of anisotropy due to the first term on the right-hand side of Equation (2.83). If the gravitational potentials vary along the line of sight, photons traversing these potentials get redshifted or blueshifted. In a Universe where the gravitational potentials are static, the net ISW effect on the CMB photon then just depends on the difference of the gravitational potential between end points.

On large scales, well-described by linear theory, a significant 'linear' ISW contribution to the CMB may be soured, however, during the times when gravitational potentials in the Universe evolve as a result of cosmic-expansion on large-scales, for example. In the late Universe, as non-linear structures form, the ISW effect also associated with the Rees-Sciama and the moving-lens effects.

4.1.1 Linear ISW

The linear ISW effect is often separated into early- and late-time ISW effects. The former is due to the evolution of the potentials around recombination as the gravitational potentials evolve during radiation domination until the radiation-matter equality. The effect of the early ISW is to enhance the first peak in the CMB. Later during the matter-dominated era the gravitational potentials do not evolve and no ISW is sourced.

When dark-energy starts dominating in the late Universe, the gravitational potentials once again evolve giving rise to the late-time ISW effect. The late time ISW effect can be generated by a cosmological constant, dark energy [222], spatial curvature [223] or modified gravity [224]. The ISW effect preserves the same black-body spectrum of the CMB photons. The late-time ISW effect provides a unique window into measuring the matter distribution and the growth of structure from the large-scale CMB fluctuations.

Due to limitations of cosmic-variance, the ISW is measured by cross-correlation with a tracer of the large-scale structure such as a galaxy catalogue or weak-lensing measurements. These measurements of the ISW signal alone constrain the dark energy density parameter Ω_Λ, to be near $\simeq 0.7$, for example, as well as give upper limits of a few percent for the spatial curvature Ω_K.

4.1.2 Non-linear ISW

The non-linear ISW effect can be sourced on small scales at second order in perturbation theory by the non-linear growth of structure. The collapse of structure leads to a changing gravitational potential on the trajectory of the passing CMB photons. If the evolution of the gravitational potential is non-negligible compared to the photon crossing time, a net effect of a blue or redshift can be left on the CMB.

The prediction of the non-linear ISW effect due to non-linear clustering of structure, named the Rees-Sciama (RS) effect, was first pointed out in [225]. The RS effect has been studied in the literature for its potential contamination of the primary anisotropies and has been understood to be a sub-dominant effect on all scales (see e.g. [226]).

For an isolated gravitational potential of a collapsed structure like a DM halo, a similar non-linear ISW effect is sourced by the time-evolution of the gravitational potential due to the peculiar velocity of the object. This was shown first by [227] and been named the Birkinshaw-Gull or 'moving-lens' effect. While the effect on the CMB anisotropies is small, measurement of this effect can nevertheless potentially give a unique probe of the bulk transverse velocity of the cosmological structure. Prospects of reconstructing the transverse velocity field from measurement of the moving lens effect has been studied in detail recently in [15], whose results I present in Chapter 5.

4.2 Sunyaev-Zel'dovich effect

One of the most well-studied CMB secondaries is the Sunyaev-Zel'dovich (SZ) effect [213], which is a modulation in the apparent brightness of the CMB photons traversing clusters of galaxies in the hot intergalactic medium. The SZ effect is caused by the Thomson interaction between the photons and the free electrons in the hot ionised gas. Early works on Thomson scattering in cosmology include [228]. The most studied types of SZ effect are the thermal SZ (tSZ) effect, where photons are scattered by random motions of the thermal electrons; the kinetic SZ (kSZ) effect, which is sourced by the remote dipole due to the bulk motion of the electrons; and the polarised SZ (pSZ) effect, due to the remote quadrupole moment seen by the electron.

4.2.1 The thermal SZ effect

In late Universe, the temperature of the traversing CMB photon reduces due cosmic to expansion below much less than the gas temperature, which gets heated up to around a few keV in galaxy clusters. In average, hence, CMB photons gain energy from scattering off free electrons in hot plasma. The net fractional change in the effective temperature of the photon satisfies [221],

$$\Theta(\hat{n};\nu) = y(\hat{n}) \left[\left(\frac{h\nu}{k_B T_{\rm CMB}} \right) \right] \coth \left(\frac{h\nu}{2k_B T_{\rm CMB}} - 4 \right) , \tag{4.1}$$

where $y(\hat{n}) := (\sigma_T / m_e c^2) \int p_e \mathrm{d}\chi$, m_e is the electron mass, ν is the frequency, and $p_e = n_e k_B T_e$ is the electron pressure profile on the line of sight. It is clear from Eq. (4.1) that the tSZ effect has a characteristic frequency dependence different than the black-body CMB, which makes the prospects of detecting (and mapping) the Compton-y signal significantly higher. The thermal SZ effect has been measurement by a multitude of CMB experiments. The Equation (4.1) is calculated by solving the Kompaneets equation [229] in the non-relativistic limit for electrons, i.e. $x_e := k_b T_e / m_e c^2 \ll 1$. Eq. (4.1) determines how the observed photon occupation number changes due to scattering of the CMB.

The distinct frequency-dependence of the non-blackbody spectral distortion generated by the tSZ effect can be used to extract information from multi-frequency datasets both at the spectra level and also by reconstructing Compton-y maps, which contain a lot of new information due to the non-Gaussianity of the tSZ [230–238, 229].

The tSZ signal is very sensitive to a multitude of cosmological parameters that affect by the growth of galaxy clusters (see e.g. [239, 240]). These parameters include the density of the total matter fluctuations Ω_m and σ_8, which can both be constrained via modelling and the measurement of the tSZ power-spectrum amplitude or the statistics of the Compton-y field as well as the tSZ cluster number-counts. Furthermore, external measurements of gas temperature of the intercluster medium from X-ray surveys, for example, the redshift-independent physical sizes of cluster can be used to measure H_0. Related, by similarly constraining the halo or cluster mass-function, measurements of tSZ can be used as tool to constrain dark energy models (see e.g. [241]).

The use of tSZ as a probe for cosmology, however, is made difficult by the strong dependency of the tSZ signal on the astrophysical modelling of the cluster medium and feedback processes. Since the tSZ amplitude is determined by the pressure integrated along the line-of-sight, its sensitive to the depth of the dark matter wells, the temperature of the gas in the

well and the surrounding environment, which are sensitive to radiative cooling and galaxy formation processes, for example. These astrophysical effects can significantly affect the measured amplitude and the shape of the tSZ signal (see e.g. [242–246]).

Finally, the tSZ effect is also an important confusion factor for the measurement of the primary CMB temperature anisotropy on small scales. The CMB experiments largely remove the tSZ contamination from the maps by multi-frequency observations mentioned above. Improving the accuracy of tSZ removal from the CMB observations remains a quintessential part of all ongoing and upcoming CMB experiments.

4.2.2 The kinetic SZ effect

Complementary to the tSZ effect discussed above, the doppler boost on the CMB photons due to the velocity of the scattering electron in the hot gas generates the kSZ effect. At leading order the kSZ effect preserves the black-body spectral shape of the CMB. At the non-relativistic limit, the scattering of CMB photons leads to a Doppler shift in intensity and temperature. The kSZ effect provides the dominant source of temperature anisotropies on small angular scales ($\ell > 4000$). The anisotropy induced by the kSZ effect in the $\hat{\mathbf{n}}$ direction on the sky is

$$\Theta(\hat{\mathbf{n}})_{\rm kSZ} = -\sigma_T \int \mathrm{d}\chi a(\chi) n_e(\chi\hat{\mathbf{n}}) v_{\rm eff}(\chi\hat{\mathbf{n}})\,, \tag{4.2}$$

where the remote CMB dipole projected along the line of sight is defined as

$$v_{\rm eff}(\chi\hat{\mathbf{n}}) = 3\int \frac{\mathrm{d}^2\hat{\mathbf{n}}_e}{4\pi}\Theta_1(\chi\hat{\mathbf{n}},\hat{\mathbf{n}}_e)\hat{\mathbf{n}}\cdot\hat{\mathbf{n}}_e\,. \tag{4.3}$$

On small scales, the dominant contribution to the remote dipole field can be approximated by the Doppler term induced by the Newtonian peculiar velocities $v_{\rm eff} \simeq \vec{v}_{\rm pec}\cdot\hat{\mathbf{n}}$, while on larger-scales contributions from the Sachs-Wolfe, integrated Sachs-Wolfe and primordial Doppler effects can be important. In order to probe the large scales accurately, it is therefore important to include these effects. A complete description of the contributions to the remote dipole field can be found in Refs. [247, 248]. Most of the cosmological information is contained in $v_{\rm eff}$, while n_e depends primarily on astrophysics and non-linear large scale structure; see Ref. [249] for a detailed discussion of this point.

First detected in [250] using the pairwise-velocity method, the kSZ effect has been detected to high significance from a multitude of cosmological experiments [251–256, 246]. The upcoming CMB experiments Simons Observatory (SO) and CMB-S4, combined with large-

scale structure surveys, are anticipated to increase the detection significance of the kSZ effect by up to a factor of 100 and 1000, respectively. Motivated with these upcoming advancements, I discuss various potential directions towards doing fundamental science with the kSZ measurements in Chapter 6.

4.2.3 The polarised SZ effect

The polarised Sunyaev-Zel'dovic effect is induced by the primordial quadrupole, which provides the dominant contribution, as well as by the quadrupole induce by the peculiar motion of the cluster (i.e. kinematic quadrupole). The polarised Sunyaev Zel'dovich effect was introduced in [213] and more analysis and higher order corrections to the signal was first done in [257–259]. The value in measuring the pSZ effect was also discussed in [260].

The Stokes parameters Q, U and V that are measured in CMB observations in a coordinate frame centred on the observer can be projected onto a 2-sphere with unit vectors $\{\hat{\theta}, -\hat{\phi}\}$ in the plane perpendicular to line of sight direction $\hat{\mathbf{n}}$, using polarisation vectors $\mathbf{e}_{\pm}(\hat{\mathbf{n}}) = (\hat{\theta} \mp i\hat{\phi})/\sqrt{2}$. The resulting complex CMB polarisation along the line of sight takes the form of an integral in conformal time η,

$$(Q \pm iU)(\hat{\mathbf{n}}) = \int_{\eta_0}^{\eta_\star} \mathrm{d}\eta\, \dot{\tau}(\eta) e^{-\tau(\eta)} p^{\pm}(\hat{\mathbf{n}}, \eta)\,, \tag{4.4}$$

where η_0 is today, η_* is the conformal time at the last scattering, τ is the mean optical depth along the line of sight. I write the cluster optical depth at redshift $z(\eta)$ along $\hat{\mathbf{n}}$ as $\delta\tau(\hat{\mathbf{n}}, \eta) = \sigma_T a \delta n_e(\hat{\mathbf{n}}, \eta)$. The polarisation induced by scattering in a cluster can then be written as

$$(Q \pm iU)(\hat{\mathbf{n}}) = \delta\tau(\hat{\mathbf{n}}) p^{\pm}(\hat{\mathbf{n}})\,, \tag{4.5}$$

where I omit the η dependence. Isolating the polarisation source function, one gets

$$p^{\pm}(\hat{\mathbf{n}}) = \delta\tau^{-1}(\hat{\mathbf{n}})(Q \pm iU)(\hat{\mathbf{n}})\,, \tag{4.6}$$

which can be expanded into spin-2 spherical harmonics as

$$p^{\pm}(\hat{\mathbf{n}}) = \sum_{\ell m} {}_{\mp}a^{p}_{\ell m}\, {}_{\mp 2}Y_{\ell m}(\hat{\mathbf{n}})\,, \tag{4.7}$$

where I note that $(Q \pm iU)(\hat{\mathbf{n}})$ in this formalism is spin ∓ 2 due to the choice of coordinate frame centred at the observer with scattered photon travelling in the $-\hat{\mathbf{n}}$ direction. The detailed studies of the relevant signals, including both the primordial and the kinematic quadrupoles include [e.g. 261–263]. In Refs. [e..g 264, 265] authors also use simulations to analyse the pSZ effect. Further studies include [266, 267]. More attention was given to detection prospects in [268, 230, 269] and the method of pSZ tomography. pSZ tomography aims to reconstruct Eq. (4.7) from measurements of CMB was further developed in [e.g. 270, 248, 271]. pSZ reconstruction is proposed as a probe of large-scale [218] CMB anomalies, of the power asymmetry in the cross-correlation between E or B mode polarization [270] and the reionization history in [271], for example.

4.3 Weak gravitational lensing

4.3.1 Lensing potential

The weak gravitational lensing of the CMB is the deflection of the CMB photons by the large scale structure in the form given in Equation (2.125) (see [13] for a review). The deflection angle $\vec{\alpha} := \nabla\phi$, parameterised by the lensing potential ϕ under the approximation that the lensing field is a pure gradient, can be found by evaluating the equations of motions governing photon momentum 4-vector in spherical harmonic coordinates, and integrating the deflection angles along the photon's geodesic. It satisfies

$$\phi = -2\int_0^{\chi_*} \mathrm{d}\chi \frac{f_K(\chi_* - \chi)}{f_K(\chi_*) f_K(\chi)} \Psi_W(\chi\hat{\mathbf{n}}; \eta_0 - \chi)\,, \tag{4.8}$$

where $\Psi_W = (\Psi + \Phi)/2$ is the Weyl potential. In the remainder of this section I omit the subscript 'W' and use Ψ for the Weyl potential for brevity. The parameter $f_K(\chi)$ is the angular-diameter distance which depends on the curvature of the Universe, and is given by

$$f_K(\chi) = \begin{cases} K^{-1/2}\sin(K^{1/2}\chi) & \text{for } K > 0 \text{ (closed)}\,, \\ \chi & \text{for } K = 0 \text{ (flat)}\,, \\ |K|^{-1/2}\sinh(|K|^{1/2}\chi) & \text{for } K < 0 \text{ (open)}\,. \end{cases} \tag{4.9}$$

I will in general approximate the Universe as flat, setting $f_K(\chi) = \chi$ in what follows.

The lensing potential power-spectrum can also be written as

$$C_\ell^{\phi\phi} = 16\pi \int \frac{\mathrm{d}k}{k} \int_0^{\chi_*} \mathrm{d}\chi \int_0^{\chi_*} \mathrm{d}\chi' \times \mathscr{P}_\Psi(k; \eta_0 - \chi, \eta_0 - \chi') j_\ell(k\chi) j_\ell(k\chi') \left(\frac{\chi_* - \chi}{\chi_* \chi}\right) \left(\frac{\chi_* - \chi'}{\chi_* \chi'}\right), \tag{4.10}$$

which directly trace the gravitational potential, which can be related to the power-spectrum of the density perturbations using the Poisson equation defined in Eq. (2.33). Assuming either dark matter or dark energy domination, using the Poisson equation $\nabla^2\Phi \simeq 4\pi G\delta\rho$ with the Newtonian gauge and assuming vanishing anisotropic stress this relation can be shown to satisfy,

$$\mathscr{P}_\Psi(k,\eta) = \frac{9\Omega_m^2(\eta)H^4(\eta)}{8\pi^2} \frac{P(k,\eta)}{k}, \tag{4.11}$$

where $P(k,\eta)$ is the matter power spectrum. If measured, the lensing potential can provide an invaluable tool for inferring the matter distribution in the Universe (see e.g. [13]).

4.3.2 Lensed CMB temperature

To a good approximation on large scales, the deflection due to lensing can be expanded in a Taylor series

$$\begin{aligned} \tilde{\Theta}(\vec{x}) &= \Theta(\vec{x}') = \Theta(\vec{x} + \vec{\nabla}\phi) \\ &\simeq \Theta(\vec{x}) + \nabla^a\phi(\vec{x})\nabla_a\Theta(\vec{x}) + \frac{1}{2}\nabla^a\phi(\vec{x})\nabla^b\phi(\vec{x})\nabla_a\nabla_b\Theta(\vec{x}) + \ldots; \end{aligned} \tag{4.12}$$

and making the flat sky approximation and up to first order in ϕ, the lensed temperature in 2D Fourier space can be given as

$$\begin{aligned} \tilde{\Theta}(\vec{\ell}) \simeq \Theta(\vec{\ell}) &- \int \frac{\mathrm{d}^2\vec{\ell}'}{2\pi} \vec{\ell}' \cdot (\vec{\ell} - \vec{\ell}')\phi(\vec{\ell} - \vec{\ell}')\Theta(\vec{\ell}') \\ &- \int \frac{\mathrm{d}^2\vec{\ell}'}{(2\pi)^2} \frac{\mathrm{d}^2\vec{\ell}''}{(2\pi)^2} \vec{\ell}' \cdot (\vec{\ell}' + \vec{\ell}'' - \vec{\ell})\vec{\ell}' \cdot \vec{\ell}''\Theta(\vec{\ell}')\phi(\vec{\ell}'')\phi(\vec{\ell}' + \vec{\ell}'' - \vec{\ell}), \end{aligned} \tag{4.13}$$

The power-spectrum of the lensed CMB then takes the form

$$\tilde{C}_\ell^\Theta \simeq (1 - \ell^2\sigma_\phi^2)C_\ell^\Theta + \int \frac{\mathrm{d}^2\vec{\ell}'}{(2\pi)^2} \left[\vec{\ell}' \cdot (\vec{\ell} - \vec{\ell}')\right]^2 C^{\phi\phi}_{|\vec{\ell} - \vec{\ell}'|} C_{\ell'}^{\Theta\Theta}, \tag{4.14}$$

where I defined

$$\sigma_\phi^2 := \frac{1}{2}\langle|\nabla\phi|^2\rangle = \int \frac{\mathrm{d}\ell\ell^3}{4\pi} C_\ell^{\phi\phi}\,, \tag{4.15}$$

$$\tilde{C}_\ell^{\Theta\Theta}(2\pi)^2\delta^2(\vec{\ell}+\vec{\ell}') := \langle\tilde{\Theta}(\vec{\ell})\tilde{\Theta}(\vec{\ell}')\rangle\,, \tag{4.16}$$

$$C_\ell^{\phi\phi}(2\pi)^2\delta^2(\vec{\ell}+\vec{\ell}') := \langle\phi(\vec{\ell})\tilde{\phi}(\vec{\ell}')\rangle\,. \tag{4.17}$$

Equation (4.14) is informative: the integral term on the right-hand side is of a form of convolution, serving to smooth out the features of the CMB such as the BAO peaks in the unlensed spectrum and resulting in a few percent fractional change on the CMB at multipoles ~ 1000, rising to $\sim 10\%$ at $\ell \sim 2000$. Note that even though the typical size of a deflection is around few arc-minutes, because the underlying gravitational potential is correlated on large scales up to around 100 Mpc ($\simeq 1^\circ$), the acoustic peaks on large scales also get smoothed by lensing.

On large scales, $\ell \ll 100$, the unlensed CMB spectrum plateaus, satisfying $\ell^2 C_\ell^{\Theta\Theta} \simeq$ constant. At this limit the second term in Eq. (4.14) cancels the second term inside the brackets suggesting $\tilde{C}_\ell^\Theta \simeq C_\ell^\Theta$, or in other words, lensing does not have an effect on the CMB spectra to a good approximation. For smaller scales, $\ell \gtrsim 100$, the BAO effect leads to scale-dependence on the CMB leading to lensing having an important effect on the observed spectra. On small scales $\ell \gg 100$, the CMB spectra vanishes due to Silk damping. Setting $C_\ell^{\Theta\Theta} = 0$ in Eq. (4.14) on small scales, the effect of lensing can be seen as the temperature (power) being modulated by the power in the lensing deflection: $\tilde{C}_\ell^\Theta \simeq \ell^2 C_\ell^\phi \sigma_\Theta^2$.

4.3.3 Lensed CMB polarisation

Similar to the temperature, the polarisation field also gets deflected by the potentials wells. The resulting effect on the power-spectra of the E- and B-mode polarisation fields introduced earlier give at the lowest order in $C_\ell^{\phi\phi}$,

$$\tilde{C}_\ell^{EE} = (1-\ell^2\sigma_\phi^2)C_\ell^{EE} + \int \frac{\mathrm{d}^2\vec{\ell}'}{(2\pi)^2}[\vec{\ell}'\cdot(\vec{\ell}-\vec{\ell}')]^2 C^{\phi\phi}_{|\vec{\ell}-\vec{\ell}'|} C_{\ell'}^{EE}\cos^2\{2(\varphi_{\vec{\ell}'}-\varphi_{\vec{\ell}})\}\,, \tag{4.18}$$

$$\tilde{C}_\ell^{BB} = \int \frac{\mathrm{d}^2\vec{\ell}'}{(2\pi)^2}[\vec{\ell}'\cdot(\vec{\ell}-\vec{\ell}')]^2 C^{\phi\phi}_{|\vec{\ell}-\vec{\ell}'|} C_{\ell'}^{EE}\sin^2\{2(\varphi_{\vec{\ell}'}-\varphi_{\vec{\ell}})\}\,, \tag{4.19}$$

$$\tilde{C}_\ell^{TE} = (1-\ell^2\sigma_\phi^2)C_\ell^{TE} + \int \frac{\mathrm{d}^2\vec{\ell}'}{(2\pi)^2}[\vec{\ell}'\cdot(\vec{\ell}-\vec{\ell}')]^2 C^{\phi\phi}_{|\vec{\ell}-\vec{\ell}'|} C_{\ell'}^{TE}\cos\{2(\varphi_{\vec{\ell}'}-\varphi_{\vec{\ell}})\}\,. \tag{4.20}$$

These equations show that similar to temperature, the features in the unlensed polarisation spectra also get smoothed out by similar convolutions. Importantly, one can also see that B-mode polarisation is generated from the E field due to lensing. This results in a significant confusion on the primordial B-mode polarisation searches that target finding signs of inflation, which naturally sources gravitational waves as I discussed in Section 2.3. I will return to the discussion of CMB lensing in Chapter 7 in greater detail.

Chapter 5

Detecting the moving lens effect

Here I focus on the moving lens effect [227] as a source of secondary CMB anisotropies and estimate the prospects for detecting the effect with upcoming observations. The temperature fluctuations imprinted by the transverse motion of individual objects are expected to be weak and can be easily confused with other effects, which makes detection challenging [272–274]. I consider new statistical approaches to detecting the moving lens effect, which effectively combine the signal from many objects with a common bulk motion. Using these approaches, we demonstrate that data expected from upcoming CMB experiments and galaxy surveys should have the statistical power to make a first detection of the moving lens effect at high significance.

The moving lens effect provides a measurement of the transverse velocity fields of matter, and has been recently suggested as a tool for cosmological inference in my published paper Ref. [15], where, with my collaborators, we introduced a quadratic estimator for the detection of the moving lens effect and reconstruction of transverse velocity fields. An unambiguous detection of the moving lens effect, however, will further benefit from utilising different methods, including using a real-space matched filter, as I discussed in my recent paper [16], or using pairwise velocities [275].

This chapter is based on my works on evaluating the detection prospects of the moving lens effect. These resulted in a published article on reconstructing the transverse velocity field in Ref. [15], and a recently submitted article in Ref. [16] where I developed a velocity reconstruction method using a matched filter. In both papers I have led the development and conceptualisation of the work. For both papers, I made the analytical and numerical calculations, provided the forecasts and results and have written the text. My paper from 2018 [15] has seen contributions from Joel Meyers, Matthew Johnson, Kendrick Smith, An-

drew Jaffe, Neal Dalal, Moritz Munchmueller, James Mertens and Alex van Engelen, in terms of conceptualisation and improvements to the presentation of the results and calculations. My more recent paper [16] seen contributions to the presentation of the results and to the conceptualisation from Matthew Johnson and Joel Meyers.

The following sections are organised as follows: In Sections 5.1 and 5.2, I briefly introduce the moving lens effect and the shape of the temperature modulation due to bulk velocities of halos. I calculate the optimal real-space matched filter in Section 5.3. I model the halo and galaxy distribution in Section 5.4 and follow up with a reconstruction technique for the components of the transverse velocity field in Section 5.5. I discuss the detection prospects for the moving lens effect using these matched filters and halo model in Section 5.6. I then introduce a quadratic estimator using a spherical harmonic expansion in Section 5.7 and forecast the detection significance of the effect using this alternative formalism in Section 5.8. We discuss various biases induced by other secondaries on the moving lens effect measurement in Section 5.9 before concluding with discussion in Section 5.10.

5.1 Introduction

Gravitational potentials that evolve in time induce a temperature modulation on the CMB known as the integrated Sachs-Wolfe (ISW) effect which has the form

$$\Theta(\hat{\mathbf{n}}) = -\frac{2}{c^2}\int \frac{\mathrm{d}\chi}{c}\,\dot{\Phi}(\chi\hat{\mathbf{n}})\,, \tag{5.1}$$

where $\Phi(\chi\hat{\mathbf{n}})$ is the gravitational potential along the line of sight $\hat{\mathbf{n}}$, χ is the comoving distance, $\Theta = \Delta T(\hat{\mathbf{n}})/\overline{T}$ is the fractional CMB temperature fluctuation and I define the integral from the emission of the photon to the observer, unless shown otherwise. One contribution to the ISW effect in the non-linear regime is the temperature anisotropy due to the peculiar velocity of collapsed structures. This is known as the moving lens effect. We can understand the origin of this effect in a few physically equivalent ways.

The motion of an observer with respect to the CMB induces a kinematic dipole temperature anisotropy due to the Doppler boosting of the CMB monopole, and also results in angular aberration of CMB fluctuations [276, 277]. I define the CMB rest frame as the reference frame in which the aberration of the CMB fluctuations vanishes, which is not identical to a frame in which the temperature dipole vanishes. The observed temperature dipole in the rest frame of the Solar System has a fractional amplitude of about 10^{-3} [278], while the anticipated intrinsic component (the fractional amplitude in the CMB rest frame) is on the

order 10^{-5}, and so the CMB rest frame is often approximated by boosting to a frame in which the observed dipole vanishes [279].

In the rest frame of the CMB, a massive object moving transverse to the line of sight of a stationary observer generates a gravitational potential which evolves in time. As CMB photons traverse this time-dependent potential, they receive a redshift or blueshift in close analogy with the ISW effect

$$\Theta(\hat{\mathbf{n}}) = -2\int_0^{\chi_\star} \mathrm{d}\chi\, \vec{v}_\perp \cdot \boldsymbol{\nabla}_\perp \Phi(\chi\hat{\mathbf{n}}) = \vec{v}_\perp \cdot \vec{\beta}(\chi\hat{\mathbf{n}})\,, \tag{5.2}$$

where $\chi_\star$ is the conformal distance to the surface of last scattering and Φ is the gravitational potential and we set c=1 for brevity. This induces a characteristic dipole pattern of CMB temperature fluctuations oriented along the object's transverse velocity.

Next, viewed from the rest frame of the lens, this effect can be recast as lensing of the (kinematic) CMB dipole seen by the lens. The photons deflected toward the observer have a temperature $T(1+\vec{v}_\perp\cdot(\hat{\mathbf{n}}+\vec{\beta}))$, giving at lowest order $\Theta(\hat{\mathbf{n}}) = \vec{v}_\perp\cdot\vec{\beta}$ after transforming to the observer frame.

Finally, the calculation for an observer moving with the same peculiar velocity as the lens with respect to the CMB is slightly more subtle. Photons deflected into the line of sight of the observer by gravitational lensing originate from the surface of last scattering separated from the observation direction $\hat{\mathbf{n}}$ by an angle $\vec{\alpha}$. In this moving frame, the CMB temperature has a kinematic dipole of the form $T_0[1+\vec{v}\cdot\hat{\mathbf{n}}]$. In the standard treatment, lensing remaps the observed temperature according to $T(\hat{\mathbf{n}}) = \tilde{T}(\hat{\mathbf{n}}+\vec{\alpha}) = \tilde{T}(\hat{\mathbf{n}}) + \boldsymbol{\nabla}\tilde{T}(\hat{\mathbf{n}})\cdot\vec{\alpha}(\hat{\mathbf{n}}) + \cdots$ where $\tilde{T}$ is the unlensed temperature, and in this case gives $\Theta = \vec{v}_\perp\cdot\vec{\alpha}$ at lowest order. It is clear that this differs from what was calculated above since $\vec{\alpha}\neq\vec{\beta}$. However, one must be careful to take into account the fact that the photons which are deflected into the line of sight of the observer were not emitted perpendicular to the surface of last scattering (an effect which is formally of the same order as the lensing deflection). This change to the emission angle is usually negligible for CMB temperature fluctuations [280], but it cannot be ignored in this case since the dominant temperature source at the surface of last scattering is due to the Doppler effect and therefore has an intrinsic dipole anisotropy. The emission angle relative to the line of the sight to the lens is $\vec{\beta}$, and so the observed temperature fluctuation evaluated in the frame comoving with the lens is $\Theta(\hat{\mathbf{n}}) = \vec{v}_\perp\cdot\vec{\beta}(\chi\hat{\mathbf{n}})$. One can also arrive at this expression by treating the kinematic component of the dipole as a source at infinite distance [281]. This analysis also demonstrates that the CMB dipole measured in the rest frame of the CMB (the intrinsic dipole) is physically distinct from the dipole induced by

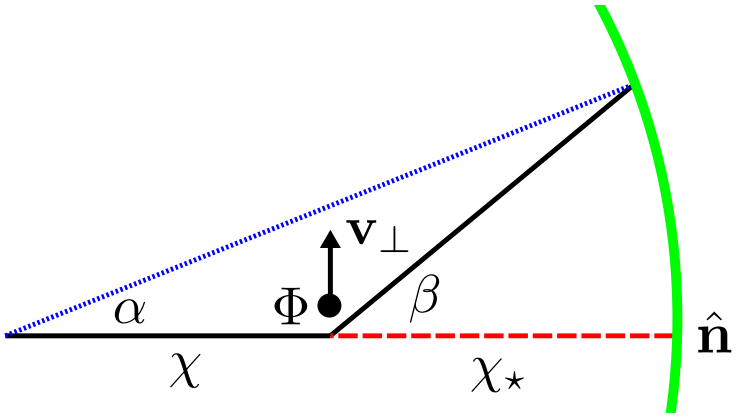

Figure 5.1: Sketch of the geometry in the CMB rest frame, for a lens of potential Φ moving with transverse velocity $\vec{v}_\perp$, as seen by an observer at comoving distance χ from the lens, and distance $\chi_\star$ from the CMB last scattering surface. [15]

boosts away from that frame (the kinematic dipole) [13], and the former can therefore be reconstructed by measuring how it is lensed [282], or by measuring spectral distortion of the low multipoles [283, 284].

5.2 The moving lens dipole

We approximate the gravitational potential near a halo to be spherically symmetric around the halo center and write, $\boldsymbol{\nabla}\Phi(r) = \hat{\mathbf{r}}\,\Phi'(r)$, and $\Phi'(r) = \partial\Phi(r)/\partial r$, where using Figure 5.2, I define the unit vector $\hat{\mathbf{r}} = (\vec{\chi}_h - \vec{\chi})/|\vec{\chi}_h - \vec{\chi}|$ and $r = |\vec{\chi}_h - \vec{\chi}|$. The temperature modulation can then be written as,

$$\Theta(\hat{\mathbf{n}}) \simeq -\frac{2}{c^2}\int \frac{\mathrm{d}\chi}{c}\,\Phi'(r)\,\left[\hat{\mathbf{r}}\cdot\vec{v}_{\mathrm{b},\perp}(\chi\hat{\mathbf{n}})\right]\,, \tag{5.3}$$

where the comoving distance χ depends on r and the distance to the halo.

We write $\mathrm{d}\chi = \mathrm{d}r\,r\,(r^2 - r_\perp^2)^{-1/2}$, where $r_\perp = |\vec{r}_\perp|$ and $\vec{r}_\perp$ is the component of $\vec{r}$ orthogonal to the line of sight. The temperature modulation due to moving lens effect takes the form,

$$\Theta(\hat{\mathbf{n}}) \simeq -\frac{4}{c^3}\left(\vec{v}_{\mathrm{b},\perp}\cdot\vec{r}_\perp\right)\int_{r_\perp}^{\infty}\mathrm{d}r\frac{\Phi'(r)}{\sqrt{r^2 - r_\perp^2}} \tag{5.4}$$

where $\chi_h \gg r_\perp$ and we approximate the velocity field to be constant within the range of the radial integral, defining a long-wavelength (center of mass) bulk-velocity fluctuation as $\vec{v}_\mathrm{b}$ which is the observable we are interested in. There are nevertheless other non-linear ISW

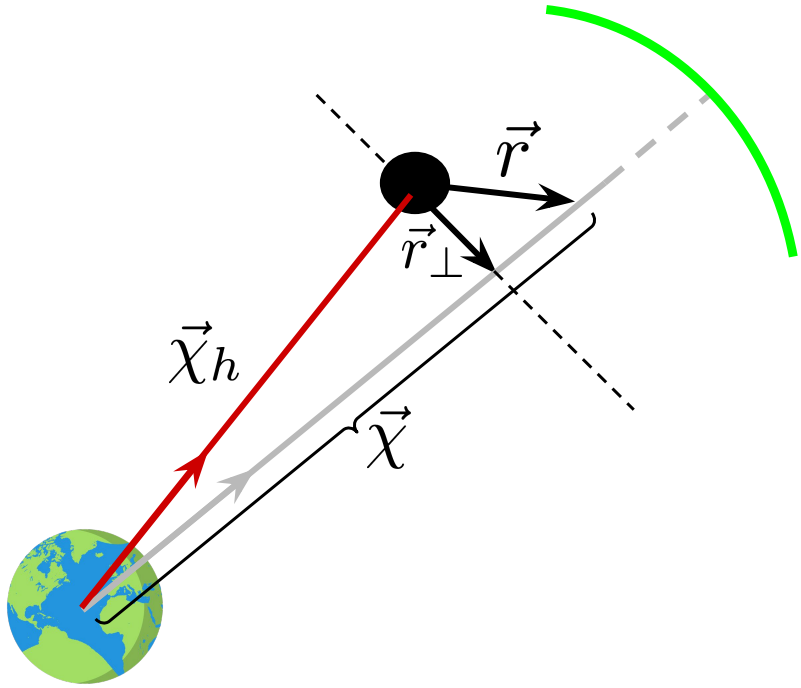

Figure 5.2: A description of the coordinate system and definitions. I define the comoving distance from the observer on Earth to the DM halo (black circle in the figure) as $\chi_h = |\vec{\chi}_h|$. The comoving distance to the CMB photon is $\chi = |\vec{\chi}|$. Vector $\vec{r}$ connects the halo center to the CMB photon and $r_\perp$ is the transverse distance from the halo center to the trajectory of the observed CMB photon. [16]

temperature modulations such as the Rees-Sciama effect, for example, due to the component of the velocity sourced by non-linear growth inside virialized structures (such as clusters), that is uncorrelated with the large-scale bulk flow. While these non-linear contributions add to the noise of the velocity measurement on small-scales, we assume they are subdominant on large-scales. Note also that the contribution to the moving lens effect from the radial component of the bulk 3-velocity sees v/c relativistic correction when boosted into the CMB frame and is hence sub-dominant, leaving moving lens effect sensitive to the transverse velocities instead.

We approximate the functional form of the gravitational potential by using the NFW profile for a spherically symmetric halo with a single parameter, the mass of the halo M in Solar mass units, i.e. $M_\odot \simeq 1.989 \times 10^{30}$ kg. We fix the virial radius as

$$r_{\rm vir}(M,z) := \left(\frac{GM_\odot M}{100H^2}\right)^{1/3}, \tag{5.5}$$

and assume halos have truncated mass at their virial radius satisfying,

$$M = \int_0^{r_{\rm vir}} \mathrm{d}R\, 4\pi R^2 \rho(R|M,z)\,, \tag{5.6}$$

where $\rho(R|M,z)$ is the halo profile. The concentration parameter,

$$c = A\left(\frac{M}{2\times 10^{12}h^{-1}}\right)^{\alpha}(1+z)^{\beta}\,, \tag{5.7}$$

relates the scale radius, $r_s(M,z)$, to the virial radius of a halo via $c = r_{\rm vir}/r_s$, and we omit showing redshift and mass dependence in what follows. Note that both scale radius and virial radius are physical distances. For the model parameters $\{A,\alpha,\beta\}$, we use appropriate values from literature, $\{7.85,-0.081,-0.71\}$. We assume NFW profile for the density of the halo [285],

$$\rho(x|M,z) = \frac{\rho_s}{x(1+x)^2}\,, \tag{5.8}$$

and

$$\Phi(r) = -4\pi G\rho_s r_s^2 \frac{\ln(1+x)}{x}\,. \tag{5.9}$$

where $x = ar/r_s$ and note that r is the radial comoving distance from the halo center and a is the scale factor. We can use the equations above to get

$$\rho_s = \frac{M_\odot M}{4\pi r_s^3}\left[-\frac{r_{\rm vir}}{r_s+r_{\rm vir}} - \ln\left(\frac{r_s+r_{\rm vir}}{r_s}\right)\right]. \tag{5.10}$$

The partial derivative of the gravitational potential with respect to r can then be written as

$$\Phi'(r) = 4\pi G\rho_s r_s^2\left[\frac{\ln(1+x)}{x^2} - \frac{1}{x(1+x)}\right]. \tag{5.11}$$

The moving lens signal from a single halo takes the form

$$\Theta_{\rm ml}(\vec{x}_\perp) = -v_{{\rm b},\perp} a_0 \mathscr{M}(\vec{x}_\perp)\,, \tag{5.12}$$

with

$$a_0 := \frac{16\pi G\rho_s r_s^2}{c^3}\,, \tag{5.13}$$

where $v_{\mathrm{b},\perp}$ is the norm of the bulk comoving transverse velocity vector, which we calculate using WEBSKY[1] halo catalog [286] as the averaged velocity of halos inside a volume. The bulk transverse velocity depends on the volume, which we parametrise with the redshift dept and the sky coverage on the two-sphere. We describe our choices of volume throughout this work. $\vec{x}_\perp = a\vec{r}_\perp/r_s$ and the radial dependence is found by solving Eqn. (5.4) with Eqn. (5.11) as

$$\mathscr{M}(x_\perp,\varphi) := \frac{1}{2x_\perp}\left[\left|\frac{2\mathrm{arcsec}(x_\perp)}{\sqrt{x_\perp^2-1}}\right| + \ln\left(\frac{x_\perp^2}{4}\right)\right]\cos\varphi\,, \tag{5.14}$$

where $x_\perp := ar_\perp/r_s$ and φ is the azimuthal angle between the comoving transverse velocity vector and $\vec{r}$, describing the rotation around the halo center orthogonal to $\vec{r}_\perp$. The template (shown in Fig. 5.3) depends on the mass and redshift of the halo, the direction of the transverse velocity on two-sphere direction as well as the cosmology through the scale factor.

5.3 The optimal matched filter

We begin by writing the observed real-space intensity map around a dark matter (DM) halo in 2-dimensions as composed of the moving lens signal $\mathscr{M}(\vec{r})$ and all other effects

$$\Theta^{\mathrm{obs}}(\vec{r}) = -v_{\mathrm{b},\perp}a_0\,\mathscr{M}(\vec{r}) + \tilde{\Theta}(\vec{r})\,. \tag{5.15}$$

We filter our data, $\Theta^{\mathrm{obs}}(\vec{r})$, to get the *unbiased and minimum variance estimate for the norm of our bulk transverse velocity signal* $\hat{v}_{b,\perp}$, which we define as

$$\hat{v}_{\mathrm{b},\perp} := a_0^{-1}\int \mathrm{d}^2\vec{r}\,\Psi(\vec{r})\Theta^{\mathrm{obs}}(\vec{r})\,, \tag{5.16}$$

Here, we have assumed that the filter is oriented along the transverse velocity vector. We relax this assumption below. The transverse velocity amplitude is degenerate with the density and the scale radius of the halo, which are determined by halo mass and redshift. We comment on these degeneracies in the following sections.

[1] Stein et.al. [286] Websky halo catalog covers the full sky up-to redshift $z \sim 4.5$, using a mass resolution of $\sim 1.3\times10^{12}M_\odot$.

The observed fractional intensity maps satisfy

$$\langle\tilde{\Theta}(\vec{\ell})\rangle = 0 \text{ and } \langle\tilde{\Theta}(\vec{\ell})\tilde{\Theta}(\vec{\ell}')\rangle = (2\pi)^2\delta(\vec{\ell}+\vec{\ell}')\tilde{C}_\ell^{TT}\,, \tag{5.17}$$

where $\tilde{C}_\ell^{TT}$ is the CMB spectra including noise and foregrounds, excluding the moving lens effect. We define the matched filter such that the estimator recovers the true velocity, and define the parameter $b := \langle\hat{v}_{\mathrm{b},\perp} - v_{\mathrm{b},\perp}\rangle$ and $N^{\mathrm{rec}} := \langle(\hat{v}_{\mathrm{b},\perp} - v_{\mathrm{b},\perp})^2\rangle$, where

$$b := \int \mathrm{d}^2\vec{r}\,\Psi(\vec{r})\mathscr{M}(\vec{r}) - 1\,, \tag{5.18}$$

and

$$N^{\mathrm{rec}} = a_0^{-2}\int\frac{\mathrm{d}^2\vec{\ell}}{(2\pi)^2}|\tilde{\Psi}(\vec{\ell})|^2\tilde{C}_\ell^{TT}\,. \tag{5.19}$$

We now wish to minimize the variance of our filter under the condition that the bias vanishes. We do this by defining $\mathscr{L} := N^{\mathrm{rec}} + \lambda b$ where λ is now a Lagrange multiplier and

$$\mathscr{L} = \int\frac{\mathrm{d}^2\vec{\ell}}{(2\pi)^2}\tilde{\Psi}^\star(\vec{\ell})\left[a_0^{-2}\tilde{\Psi}(\vec{\ell})\tilde{C}_\ell^{TT} + \lambda\tilde{\mathscr{M}}(\vec{\ell})\right] - \lambda\,. \tag{5.20}$$

The optimal filter that minimizes $\mathscr{L}$ can be written as

$$\tilde{\Psi}(\vec{\ell}) = \left[\int\frac{\mathrm{d}^2\vec{\ell}'}{(2\pi)^2}\frac{|\tilde{\mathscr{M}}(\vec{\ell}')|^2}{\tilde{C}_{\ell'}^{TT}}\right]^{-1}\frac{\tilde{\mathscr{M}}(\vec{\ell})}{\tilde{C}_\ell^{TT}}\,, \tag{5.21}$$

or equivalently,

$$\tilde{\Psi}(\vec{\ell}) = N^{\mathrm{rec}}\frac{\tilde{\mathscr{M}}(\vec{\ell})}{\tilde{C}_\ell^{TT}}\,. \tag{5.22}$$

Note that the optimal estimator is most sensitive to the signal on small scales, where the inverse of the estimator variance is large and the primary CMB signal (which is much larger and acts as a confusion) is small. Lastly, we convolve the moving lens signal with a beam that matches the experimental specifications described below. When applying the matched filter we assume a Gaussian beam satisfying $B(\vec{\ell}) = \exp[-(\theta_{\mathrm{fwhm}}/2\sqrt{\ln 2})^2\ell(\ell+1)]$, where θ_{fwhm} is the full beam-width at half-maximum. In what follows we discuss results with this

beam applied to the moving lens template, i.e. $\tilde{\mathscr{M}}(\vec{\ell}) \to B(\vec{\ell})\tilde{\mathscr{M}}(\vec{\ell})$.

5.4 Halos, galaxies and the $\hat{v}_{\mathrm{b},\perp}$ SNR

The estimated signal-to-noise ratio (SNR) for the velocity amplitude per object with mass M at redshift z is $v_{\mathrm{b},\perp}/\sqrt{N^{\mathrm{rec}}(M,z)}$; the number of such objects needed for total SNR to equal to 1 is $N^{\mathrm{rec}}(M,z)/v_{\mathrm{b},\perp}^2$. (Note that we defined $v_{\mathrm{b},\perp} = |\vec{v}_{\mathrm{b},\perp}|$.) While upcoming surveys will not be able to reconstruct the transverse velocity for each halo, the average transverse velocity can be measured over a sufficiently large patch of the sky.

Surveys of large-scale structure observe galaxies that occupy DM halos. The relation between galaxies and the host DM halos depend on a multitude of effects and mechanisms, including rates of star formation and galaxy mergers, and needs to be modelled and tested against data. The number and spatial distribution of the DM halos can be described by the halo model (see for review e.g. [287]). The distribution of galaxies inside DM halos can be described with a halo occupation distribution (HOD) model (see e.g. [288]) where every DM halo is assumed to have at most 1 central galaxy, as well as additional satellite galaxies whose number can be large for massive halos. The average observable central (satellite) galaxy number count of a DM halo with mass M and at redshift z is parametrised with $\bar{N}_c(m_*,z)$ [with $\bar{N}_s(m_*,z)$] where m_* is the threshold stellar mass determined by the galaxy survey and details of the model can be found in e.g. [288–290]. For calculating the mass and redshift dependence of halo density we assume a Sheth-Tormen collapse fraction [291].

We use the matched filter introduced above and the halo mass function with a normalisation appropriate for a given LSS survey and approximate the expected total SNR for the velocity magnitude from inside a redshift bin and a given patch of size $f_{\mathrm{patch}}^{\mathrm{sky}}$ on the sky as a sum over all halos in a catalog that fall within a redshift range and whose mass distribution matches the halo-model,

$$\mathrm{SNR}^2 = 4\pi f_{\mathrm{sky}} \int_{z-\mathrm{bin}} \mathrm{d}z \int_{\mathrm{catalog}} \mathrm{d}M \bar{N}_c(m_*,z) \frac{v_{\mathrm{b},\perp}(z)^2}{N^{\mathrm{rec}}(M,z)} \chi^2 \frac{\mathrm{d}\chi}{\mathrm{d}z} n(M,z). \tag{5.23}$$

where we approximated the discrete sum over halos with an integral over the mass function and used the SNR for the velocity amplitude per object with mass M at redshift z, $v_{\mathrm{b},\perp}/\sqrt{N^{\mathrm{rec}}(M,z)}$, we defined above. Note that we use only the count of central galaxies, since the bulk transverse velocity is sourced by the center of mass of the halo. We find $\mathrm{SNR}^2 \simeq$

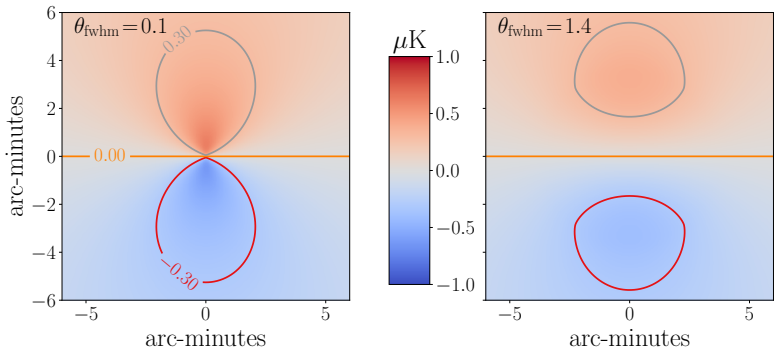

Figure 5.3: The CMB temperature modulation due to the moving lens effect shown as a function of angular distance from halo center (in arc-minutes) for a halo of mass $M = 10^{14} M_{\odot}$ at redshift $z = 1$. The left (right) plots show the templates filtered with a Gaussian beam of radius 0.1 (1.4) arc-minutes. [16]

$10^3 f_{\rm sky}$ for a redshift bin centred at $z = 1$ and of size $\Delta z = 1$, with perfect knowledge of halo mass, location and redshift as well as the transverse velocity direction, using the Vera. C. Rubin Observatory (LSST) and CMB-S4 experimental specifications, and the analytic approximation for the galaxy number density satisfying $dn/dz \propto (z/z_0)^{\alpha} \exp[(-z/z_0)^{\beta}] \text{arcmin}^{-2}$ with $\{z_0, \alpha, \beta, n_{\rm tot}[\text{arcmin}^{-2}]\}$ set equal to $\{0.3, 2, 1, 40\}$, and the CMB temperature noise $N_\ell^{TT} = (\Delta_T/T)^2 \exp[\ell(\ell+1)\theta^2_{\rm fwhm}/(8\log(2))]$ where we set $\{\Delta_T, \theta_{\rm fwhm}\}$ to $\{1.0, 1.4\}$. We use lensed $C_\ell^{\Theta\Theta}$, approximate the kSZ contribution as a constant 3 μK^2 in $\ell(\ell+1)/(2\pi)^2 C_\ell^{\Theta\Theta}$ and assume perfect removal of foregrounds such as the cosmic infrared background and tSZ from the CMB. Note that individual halo masses are expected to be measured imperfectly, with around 40 percent error in $\ln M$, from combinations of lensing and SZ measurements and redshift measurements are subject to photo-z errors [292, 293, 220]. We discuss these in Section 5.6, before forecasting the transverse velocity amplitude reconstruction fidelity of the upcoming surveys in cross correlations of CMB and galaxy measurements.

5.5 Transverse velocity reconstruction

We define the filter response introduced in Eq. (5.16) for a halo 'i' of mass M_i and redshift z_i, as

$$\hat{A}(M_i, z_i) := \int d^2\vec{r}\, \Psi_i(\vec{r}) \Theta^{\rm obs}(\vec{R}_i + \vec{r}) \tag{5.24}$$

where $\Theta^{\rm obs}(\vec{R}_i+\vec{r})$ is the observed CMB around the halo at $\vec{R}_i$ (in polar coordinates) from the patch center $\vec{R}_0 = (0,0)$. The matched filter centered on the halo, $\Psi_i(\vec{r})$, depends on the halo mass and redshift as well as the orientation of the transverse velocity field, which we assumed known in the previous section. In this section we evaluate the prospects for reconstructing the components of the transverse velocity vector from the CMB and halo locations from a galaxy survey.

We are interested in finding the angle $\hat{\varphi}_0$ that best approximates the true average angle of the transverse velocity vector field with respect to a reference vector in a patch of size $4\pi f_{\rm sky}^{\rm patch}$, where we set $\hat{\varphi}_{0,i} = \hat{\varphi}_{0,j} = \hat{\varphi}_0$ equal for all filters $\{i,j\}$ inside the patch. This is the $\hat{\varphi}_0$ that satisfies[2],

$$\int {\rm d}^2\vec{r} \frac{\partial}{\partial \varphi_0} \sum_{i,{\rm halos}} \Psi_i(\vec{r})\Theta^{\rm obs}(\vec{R}_i+\vec{r}) = 0\,, \tag{5.25}$$

where for each filter in the sum, the coordinates are chosen so that the halo is at the center of the template.The CMB acts as noise on the stacked patch, and that φ_0 which maximizes the residual response approximates the true direction of the transverse velocity vector direction on 2-sphere, given sufficient SNR.

Due to the simple angular dependence of the signal profile, we find the equality in Eqn. (5.25) satisfies

$$\tan(\hat{\varphi}_0, z) = \frac{\int {\rm d}^2\vec{r} \sin\varphi \sum_i \Psi_{i,u}(r)\Theta^{\rm obs}(\vec{R}_i+\vec{r})}{\int {\rm d}^2\vec{r} \cos\varphi \sum_i \Psi_{i,u}(r)\Theta^{\rm obs}(\vec{R}_i+\vec{r})}, \tag{5.26}$$

where we define $\Psi_i(r) = \cos(\varphi-\hat{\varphi}_0)\Psi_{i,u}(r)$, $\hat{\mu} := \hat{\alpha}/\hat{\beta} = \tan\hat{\varphi}_0$ (omitting showing the redshift dependence for now); where α and β are the numerator and denominator on the right-hand-side of Eq. (5.26), respectively. The error on the measurement can be written in the form

$$\sigma_\mu/|\mu| = \sqrt{\sigma_\alpha^2/\alpha^2 + \sigma_\beta^2/\beta^2}\,, \tag{5.27}$$

where the errors are independent for a given template due to implicit angular integral and the trigonometric functions in our definition.

We assume the contribution to the *signal* from everything else except the moving lens effect vanish for a large enough patch with sufficiently many halos. With this assumption,

[2] We assume the maxima can be distinguished from the minima from the filter response and accounted for with a sign change, with no additional error to the estimator.

we write[3]

$$\alpha = \int_{\text{template}} \mathrm{d}^2\vec{r} \sin\varphi \sum_{i,\text{halos}} \Psi_{u,i}(r)\Theta^{\text{ml}}(\vec{r})\,, \tag{5.28}$$

where we defined $\Theta^{\text{ml}}(\vec{r}) := A(M,z)\,\mathscr{M}_u(r)\cos(\varphi-\varphi_0)$, $\mathscr{M}_u(r)$ is the radial shape of the moving lens effect on the CMB around a halo where r is the radial distance to the halo center, and we defined the (polar) integral over the patch as equal to the surface area of the patch on 2-sphere, as $\int_{\text{patch}} \mathrm{d}^2\vec{\Omega} \simeq \int_{\text{patch}} \mathrm{d}^2\vec{R} := 4\pi f_{\text{sky}}^{\text{patch}}$ for small patches. A more detailed derivation can be found in Appendix A.1. Errors are calculated using a relation similar to Eq. (5.28), with the CMB component without the moving lens effect instead, and performing the average over the realisations of the CMB as e.g.[3],

$$\sigma_\alpha^2 = \int_{\text{template}} \mathrm{d}^2\vec{r} \sin\varphi\, \mathrm{d}^2\vec{r}' \sin\varphi' \times \sum_{i,j,\text{halos}} \Psi_{i,u}(r)\Psi^*_{j,u}(r')\langle\tilde{\Theta}(\vec{R}_i+\vec{r})\tilde{\Theta}^*(\vec{R}_j+\vec{r}')\rangle\,. \tag{5.29}$$

For compactness of our expressions we define a signal parameter $I_{\text{patch}} := \alpha/(\pi\sin\varphi_0) = \beta/(\pi\cos\varphi_0)$ which satisfy,

$$I_{\text{patch}} = 4\pi f_{\text{patch}}^{\text{sky}} \int_{z-\text{bin}} \mathrm{d}z \int_{\text{catalog}} \mathrm{d}M \bar{N}_c(m_*,z)\,\chi^2 \frac{\mathrm{d}\chi}{\mathrm{d}z} n(M,z)A(M,z)\,, \tag{5.30}$$

where we set the integral over the patch in Eq. (5.28) as $\int_{\text{patch}} \mathrm{d}^2\vec{R} := 4\pi f_{\text{patch}}^{\text{sky}}$ and like before, we promote the sum over halos to an integral over halo masses and the halo locations over the patch. The error on I_{patch} takes the form,

$$\sigma^2_{I_{\text{patch}},\bar{z}} = \int_{r_{\text{min}}}^{r_{\text{max}}} r\mathrm{d}r\, r'\mathrm{d}r'\Lambda(r,r')\mathscr{F}_{\bar{z}}(r)\mathscr{F}^*_{\bar{z}}(r')\,, \tag{5.31}$$

which can be understood as a measure of our estimator variance given a patch of surface area $4\pi f_{\text{patch}}^{\text{sky}}$ and we defined

$$\mathscr{F}_{\bar{z}}(r) := \int_{z-\text{bin}} \mathrm{d}z \int_{\text{catalog}} \mathrm{d}M \bar{N}_c(m_*,z)\,\chi^2(z) \frac{\mathrm{d}\chi}{\mathrm{d}z} n(M,z)\Psi_u(r)\,, \tag{5.32}$$

[3]Similarly equality holds for β, with azimuthal angular integral over $\cos\varphi$ in-place of $\sin\varphi$.

which can be understood as the orientally-stacked image of the moving lens effect given a catalog of halos inside some redshift bin $\bar{z}$, as a function of the radial distance from the image center. The other term in the integral is defined as

$$\Lambda(r,r') := 16\pi^4 \int \frac{L^{-1}\mathrm{d}L}{(2\pi)^2} C_L^{\tilde{\Theta}\tilde{\Theta}} j_1(Lr) j_1(Lr') \left[R_{\rm max} j_1(R_{\rm max}) - R_{\rm min} j_1(R_{\rm min})\right]^2, \quad (5.33)$$

where $r_{\rm max}$ satisfies the inequality $r_{\rm max} \ll R_{\rm max}$ and $j_1(x)$ is the spherical bessel function $j_\ell(x)$ for $\ell = 1$. We set $\{r_{\rm max}, r_{\rm min}, R_{\rm min}\}$ equal to $\{5\,\mathrm{arcmin},\ 1.4\,\mathrm{arcmin}, r_{\rm max}\}$ and find $\Lambda(r,' r') \simeq \mathscr{A} rr'$, where $\mathscr{A} \simeq 2.3\times10^{-11}$ for $R_{\rm max} = 2\times10^{-2}$radians and $\mathscr{A}$ depends on $R_{\rm max}$ non-trivially due to the scale dependence of the CMB. This term can be understood as the r.m.s. contribution of the CMB on the noise estimate for a given patch. Generally the integral limits $\{r_{\rm min}, r_{\rm max}\}$ can be chosen as halo mass dependent to maximize the SNR. Using these relations we get

$$\sigma^2_{I_{\rm patch}} \simeq \mathscr{A} \left| \int \frac{\mathrm{d}\ell}{2\pi} \int_{\rm catalog} \mathrm{d}M \zeta_\ell(M,z) \tilde{\mathscr{F}}'_{(\bar{z})}(\ell) \right|^2, \quad (5.34)$$

where

$$\zeta_\ell(M,z) := \int_{r_{\rm min}}^{r_{\rm max}} r^2 \mathrm{d}r \exp(-i\ell r), \quad (5.35)$$

and $\tilde{\mathscr{F}}'(\ell) := \mathrm{d}\tilde{\mathscr{F}}(\ell)/\mathrm{d}M$ where $\tilde{\mathscr{F}}(\ell)$ is the (1D) Fourier transform of $\mathscr{F}(r)$. Note it is straight forward to show from equations above that $I_{\rm patch}$ satisfies the equality,

$$\sigma_\mu/|\mu| = \sqrt{2}\sigma_{I_{\rm patch}}/|I_{\rm patch}|, \quad (5.36)$$

in the perfect knowledge of the moving-lens amplitude A.[4]

We evaluate the detection significance of the direction component μ (ignoring the uncertainty on the amplitude) using our parameter choices, for a Rubin-like halo catalog and a CMB-S4-like survey, and 6 (uncorrelated) boxes equally spaced in redshift in the range $z \in [0.1, 3]$ with same surface area on the sky. We find SNR $\gtrsim 1$ for a patch with surface area of $\lesssim 10$ square degrees. Next, we follow with a more involved SNR forecast and discussion.

[4]Note that the error on the amplitude A can be added to give

$$\sigma^2_\mu/\mu^2 = 2(\sigma^2_{I_{\rm patch}}/I^2_{\rm patch} + \sigma^2_A/A^2). \quad (5.37)$$

5.6 Reconstruction and Forecasts

We evaluate the detection SNR on the moving lens effect for a given patch and a redshift range as the sum of the SNR on the two transverse velocity components we reconstruct from the velocity amplitude and the *angle* as

$$\vec{v}_{\mathrm{b},\perp} := \{v_1, v_2\} = \{v_{\mathrm{b},\perp}\cos\varphi_0, v_{\mathrm{b},\perp}\sin\varphi_0\} \tag{5.38}$$

and the total SNR *per patch* as sum SNR of the components, $\mathrm{SNR}^2 := \mathrm{SNR}_1^2 + \mathrm{SNR}_2^2$, where

$$\mathrm{SNR}_1^{-2} = \mathrm{SNR}_2^{-2} = \sigma_\mu^2/\mu^2 + \sigma_{v_{\mathrm{b},\perp}}/v_{\mathrm{b},\perp}^2\,, \tag{5.39}$$

and $\sigma_\mu^2/\mu^2 = 2(\sigma_{I_{\mathrm{patch}}}^2/I_{\mathrm{patch}}^2 + \sigma_A^2/A^2)$ due to the angular dependence of the signal template. When estimating the total detection SNR from the full sky we assume no correlation between patches and set $\mathrm{SNR}_{\mathrm{total}}^2 \simeq (f_{\mathrm{sky}}/f_{\mathrm{sky}}^{\mathrm{patch}})\mathrm{SNR}^2$ where f_{sky} is the full sky coverage of the cosmological survey. We calculate the SNR in volumes of redshift depth $\Delta z = 0.5$ in the range $z \in [0.1, 3]$ and surface area corresponding to the patch size.

We display the forecasts for total SNR for moving lens effect detection in Figure 5.4. Our calculation suggest the upcoming surveys of LSS and measurements of CMB may detect the moving lens signal to high significance, where combinations of CMB-S4 and Vera C. Rubin Observatory will achieve SNR of over 20 and combinations of SO and Vera C. Rubin Observatory will achieve SNR of above 8. These results are consistent with the results obtained using the quadratic estimator of Ref. [15].

In reality the velocity measurement from the moving lens effect is a biased estimate of the true velocity field, satisfying the relation $\hat{v}_{\mathrm{b},\perp}^{\mathrm{ml}} = b_{\mathrm{ml}}\hat{v}_{\mathrm{b},\perp}$ on large scales. This arises due to an imperfect knowledge of the background cosmology, halo mass and halo redshift, which the individual moving lens templates depend on. This is analogous to the optical depth degeneracy encountered when attempting to reconstruct the radial velocity field using kinetic Sunyaev Zel'dovich (kSZ) tomography (see Ref. [249] for a discussion).

One potential source of bias is the halo mass. Imperfect knowledge of the halo mass affects the fidelity of the velocity measurement due both to a reduced filter response and the intrinsic degeneracy between the halo mass and true velocity amplitude. The velocity estimator is proportional to $(M/M_\odot)^{-0.6}$, as defined in Eq. (5.16). In order to evaluate the unambiguous detection and reconstruction significance of the upcoming experiments on the transverse velocity amplitude, we have to incorporate the error in halo masses in the velocity SNR calculation. The error on halo mass is expected to satisfy (per halo) $\sigma_M/M \simeq 0.4$,

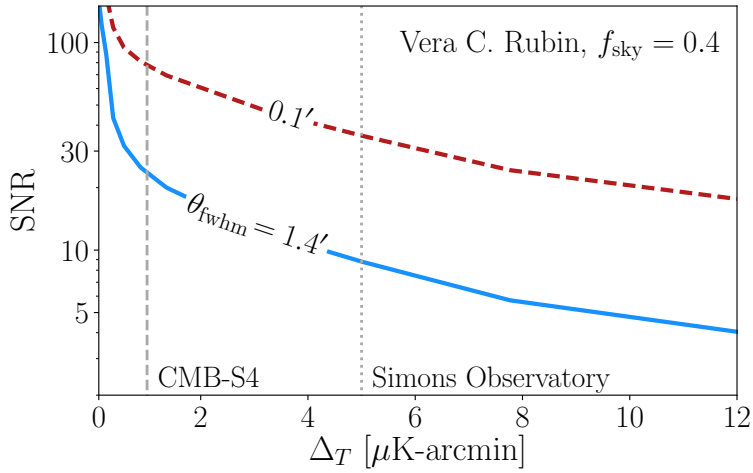

Figure 5.4: The total transverse-velocity detection SNR from the measurement of the moving lens effect, for 1.4- and 0.1-arcminute beams for various CMB rms noise levels. Plotted curves show SNR values for halo counts matching with the expected central galaxies from LSST survey (a.k.a Vera C. Rubin Observatory) and a sky fraction of $f_{\rm sky} = 0.4$ [16].

using mass-richness measurements from weak lensing and SZ surveys [293, 292]. Note that this mass error is already significantly more optimistic than the moving lens SNR per halo; which satisfy (per halo) $\sigma_A/|A| > 1$ for all of the observable redshift and halo mass ranges. Hence we find that the error induced on the velocity SNR due to halo mass degeneracy to be over $\mathscr{O}(10)$ smaller than the error on the moving lens amplitude A. In order to evaluate the reduction in SNR due to mass errors on the template, we calculated moving-lens temperature maps $\Theta_{\rm ml}(\hat{\mathbf{n}})$, as defined above, using the WEBSKY[5] halo catalog [286] with the true and erroneous halo masses, with the latter having random halo masses sampled from a Gaussian distribution with $\sigma_M/M \simeq 0.4$. We find the cross-correlation coefficient of the moving-lens temperature maps remains near 1 for the multipole ranges relevant to this study ($\ell \lesssim 100$) – suggesting the errors induced by the inaccurate template are small on large scales, and furthermore, that the cross-correlations with an external tracer of the density field may be used to potentially boost the SNR.

Another important parameter that can penalize the SNR is the halo redshift, since the velocity reconstruction from galaxy-surveys suffer from known effects of redshift space distortions (RSDs) as well as photometric redshift (photo-z) errors for photometric surveys such as the Vera C. Rubin Observatory, the latter satisfying $\sigma_z = 0.03(1+z)$. Similar to the uncertainty on halo masses, we find the contribution to the error on the velocity measurement

[5] Stein et.al. [286] WEBSKY halo catalog covers the full sky up-to redshift $z \sim 4.5$, using a mass resolution of $\sim 1.3 \times 10^{12} M_\odot$.

due to the redshift degeneracy (induced by dependence of the signal on the scale-radius) to be small, especially since we use large ($\Delta z \sim 0.5$) redshift bins. In order to evaluate the significance of photo-z errors and RSDs on matched filter, we sample from the same halo catalog, a smaller set of halos with halo number count matching the expected central galaxies from the Vera C. Rubin Observatory. We compare the true velocity fields with and without taking into account the photo-z errors and RSDs. We capture the effect of photo-z's by redistributing the halo positions in redshift space randomly with the photo-z error. For RSDs, we add the velocity dependent RSD correction in redshift space, as discussed above. We parametrise the combined effect of RSDs and photo-z with the cross-correlation coefficient $\rho = C_\ell^{xy}/\sqrt{C_\ell^{xx}C_\ell^{yy}}$ as a function or redshift, where $\{x,y\} := \{\text{true}, \text{obs}\}$, which we find remains larger than 90 percent for $\ell \lesssim 100$ – showing (similarly to the mass errors) that the redshift errors do note degrade the SNR from the moving lens measurement and that the velocity field measured from the templates is well correlated with the underlying velocity field.

Note that the transverse velocity fields vary more rapidly along their projected direction and a similar phenomena is also true for the radial velocities, i.e. they vary more rapidly on the radial direction. This suggests that the typical transverse velocity modes vary slower in the radial direction, implying the relative SNR penalty from larger redshift bins (necessitated by the large photo-z errors from photometric surveys) is lower than compared to radial velocity reconstruction for the kSZ effect, for example, motivating the use of photometric surveys for the purpose of moving lens effect detection and velocity reconstruction. Note however that the cross-correlation coefficient suffers due to low number of galaxies in the near Universe ($z < 0.3$) suggesting potential benefits of using different types of observations (such as spectroscopic surveys and other tracers) for the purpose of moving-lens effect detection. We leave a more involved analysis on these lines to future work.

5.7 Quadratic estimator

In addition to the real-space method I introduced in the previous sections, I now wish to construct a complementary quadratic estimator for the transverse velocity field $\vec{v}_\perp(\hat{\mathbf{n}}, z)$ on large angular scales ($\ell \lesssim 100$), given maps of the CMB temperature and of a tracer of the density field at some redshift on small angular scales ($\ell \gtrsim 2000$), analogous to a CMB lensing quadratic estimator [294], for example. Similar to earlier, our focus in what follows is also on the large-scale velocity field, where we anticipate that the velocity is linear and curl-free, such that we can define a transverse velocity potential $\Upsilon(\hat{\mathbf{n}}, z)$, with $\vec{v}_\perp(\hat{\mathbf{n}}, z) = \boldsymbol{\nabla}\Upsilon(\hat{\mathbf{n}}, z)$. We

utilize the typical definition of the gravitational lensing potential ϕ such that $\vec{\alpha} = \boldsymbol{\nabla}\phi$, with

$$\phi(\hat{\mathbf{n}}) = -2\int_0^{\chi_\star} \mathrm{d}\chi\, \frac{\chi_\star - \chi}{\chi_\star \chi}\Phi(\chi\hat{\mathbf{n}})\,, \tag{5.40}$$

where we have assumed spatial flatness. We can construct a similar potential for the deflection as seen by the lens

$$\psi(\hat{\mathbf{n}}) = -2\int_0^{\chi_\star} \mathrm{d}\chi\, \frac{1}{\chi}\Phi(\chi\hat{\mathbf{n}})\,, \tag{5.41}$$

such that $\vec{\beta} = \boldsymbol{\nabla}\psi$, and which differs from the ordinary lensing potential ϕ by a ratio of the lens and source distances.

Given an observed map of the CMB temperature, $\Theta^{\rm obs}$, and a map of $\psi^{\rm obs}$ as derived from, for example, a survey of large-scale structure, we can write the desired quadratic estimator as

$$\hat{\Upsilon}(\mathbf{L}) = N(\mathbf{L})\int \frac{\mathrm{d}^2\boldsymbol{\ell}}{(2\pi)^2} g(\boldsymbol{\ell},\mathbf{L})\Theta^{\rm obs}(\boldsymbol{\ell})\psi^{\rm obs}(\mathbf{L}-\boldsymbol{\ell})\,. \tag{5.42}$$

We have suppressed the redshift dependence of $\hat{\Upsilon}$ and ψ, and the normalization $N(\mathbf{L})$ and filter $g(\boldsymbol{\ell},\mathbf{L})$ are to be determined. We are using the flat-sky approximation so that $\boldsymbol{\ell}$ and $\mathbf{L}$ are two-dimensional Fourier wavevectors, and have found the results agree well with a full-sky estimator, as is also the case with lensing estimators [295]. Following, e.g., Ref. [294], we minimize the estimator variance subject to the constraint that the estimator is unbiased, i.e., that $\Upsilon(\mathbf{L}) = \left\langle\hat{\Upsilon}(\mathbf{L})\right\rangle_{\Theta,\psi}$. At lowest order, the variance is

$$\left\langle\hat{\Upsilon}(\mathbf{L})\hat{\Upsilon}(\mathbf{L}')\right\rangle = (2\pi)^2\delta^{(2)}(\mathbf{L}+\mathbf{L}')\left[C_L^{\Upsilon\Upsilon} + N(\mathbf{L})\right], \tag{5.43}$$

where the transverse velocity potential power spectrum is defined as

$$C_\ell^{\Upsilon\Upsilon} = \frac{4\pi}{\Delta\chi}\int_{\chi_{\rm min}}^{\chi_{\rm max}} \mathrm{d}\chi \int \frac{\mathrm{d}k}{k}\frac{\mathscr{P}_v(k,\chi)}{(k\chi)^2}\left[j_\ell(k\chi)\right]^2, \tag{5.44}$$

and $\mathscr{P}_v$ is the dimensionless power spectrum of the three-dimensional velocity $|\vec{v}|$. We find that we must fix the normalization to

$$N(\boldsymbol{L}) = \left[\int \frac{\mathrm{d}^2\boldsymbol{\ell}}{(2\pi)^2} C^{\psi\psi}_{|\boldsymbol{\ell}-\mathbf{L}|} g(\boldsymbol{\ell},\mathbf{L})\mathbf{L}\cdot(\mathbf{L}-\boldsymbol{\ell})\right]^{-1}, \tag{5.45}$$

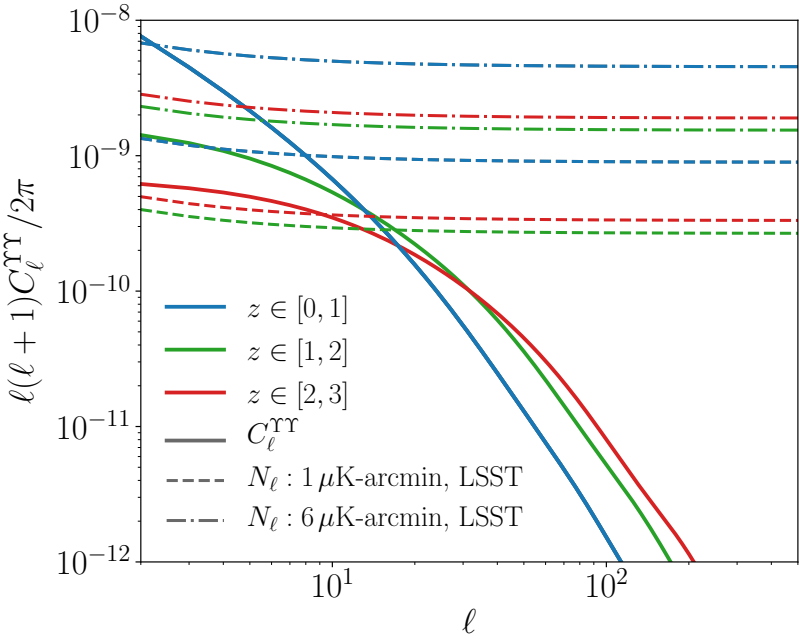

Figure 5.5: Power spectrum of the transverse velocity potential (solid) and reconstruction noise (dashed and dot-dashed) in several redshift bins for two CMB experiments with a 1.4-arcmin beam combined with Vera C. Rubin Observatory. Where the signal curves exceed the reconstruction noise, true mapping of the transverse velocities will be possible. [15]

and that the filter which minimizes the variance is

$$g(\boldsymbol{\ell},\mathbf{L}) = \frac{\mathbf{L}\cdot(\mathbf{L}-\boldsymbol{\ell})}{C_\ell^{\Theta\Theta,\mathrm{obs}}} \frac{C^{\psi\psi}_{|\boldsymbol{\ell}-\mathbf{L}|}}{C^{\psi\psi,\mathrm{obs}}_{|\boldsymbol{\ell}-\mathbf{L}|}}\,, \tag{5.46}$$

thereby giving for the noise on a reconstructed mode

$$N(\boldsymbol{L},z) = \left[\int \frac{\mathrm{d}^2\boldsymbol{\ell}}{(2\pi)^2} \frac{[\mathbf{L}\cdot(\mathbf{L}-\boldsymbol{\ell})]^2}{C_\ell^{\Theta\Theta,\mathrm{obs}}} \frac{\left(C^{\psi\psi(z)}_{|\boldsymbol{\ell}-\mathbf{L}|}\right)^2}{C^{\psi\psi(z),\mathrm{obs}}_{|\boldsymbol{\ell}-\mathbf{L}|}}\right]^{-1} \tag{5.47}$$

where we reintroduced the redshift dependence of our noise estimate.

5.8 Signal-to-noise ratio

We now estimate the signal-to-noise ratio of the reconstructed transverse velocity potential assuming a cosmology consistent with the latest results from *Planck* [37]. We described

the CMB noise and the galaxy number densities we use in our forecast in Section 5.4. We choose the redshift binning taking into account the photometric error expected by the these experiments, $\sigma_z = 0.03(1+z)$, with each redshift bin width fixed to $4\sigma_z$, which amounts to 13 bins in the range $z \in [0, 3.7]$. Finally, we assume constant galaxy bias of unity between galaxy and the matter over-density. The moving lens potential power spectrum $C_\ell^{\psi\psi}$ is calculated with a non-linear matter power spectrum and using the Limber approximation which is valid at small scales [296–299]. All spectra were computed numerically using modified versions of both CAMB [300] and CLASS [301] with non-linear corrections implemented with HALOFIT [302–305], and we checked that the results from the two codes agree with one another and also with the halo model treatment of the matter power described in [306]. We show the transverse velocity signal and the estimator noise in Fig. 5.5.

The most promising route for a first detection of the moving lens effect comes from cross-correlating the large-scale transverse velocity reconstructed from the CMB with that inferred directly from a galaxy survey. We assume that the latter method provides a precise enough measurement of the large-scale density that we can infer the large-scale transverse velocity without noise, which should be a reasonable approximation for the high number densities of galaxies expected in the surveys we are considering. We calculate the total signal-to-noise ratio by approximating the likelihood as Gaussian

$$\left(\frac{S}{N}\right)^2 = \sum_{\ell\ell';XYWZ} C_\ell^{\Upsilon_X\hat{\Upsilon}_Y} \mathbf{cov}^{-1}\left(\tilde{C}_\ell^{\Upsilon_X\hat{\Upsilon}_Y}, \tilde{C}_{\ell'}^{\Upsilon_W\hat{\Upsilon}_Z}\right) C_{\ell'}^{\Upsilon_W\hat{\Upsilon}_Z}, \tag{5.48}$$

where the indices run over redshift bins, the fields with hats refer to transverse velocities reconstructed from the CMB, those without a hat refer to the velocities reconstructed from the galaxy distribution, the tilde refers to spectra including noise, and the covariance is given by

$$\mathbf{cov}\left(\tilde{C}_\ell^{\Upsilon_X\hat{\Upsilon}_Y}, \tilde{C}_{\ell'}^{\Upsilon_W\hat{\Upsilon}_Z}\right) = \frac{\delta_{\ell\ell'}}{2\ell+1} f_{\rm sky}^{-1} \times \left(\tilde{C}_\ell^{\Upsilon_X\Upsilon_W}\tilde{C}_\ell^{\hat{\Upsilon}_Y\hat{\Upsilon}_Z} + \tilde{C}_\ell^{\Upsilon_X\hat{\Upsilon}_Z}\tilde{C}_\ell^{\Upsilon_Y\hat{\Upsilon}_W}\right). \tag{5.49}$$

To assess the detectability of the moving lens effect, we take as a null hypothesis a scenario in which there is no signal in the CMB-reconstructed transverse velocity, which we also take to have noise diagonal in the redshift bins ($\tilde{C}_\ell^{\hat{X}\hat{Y}} = \delta_{\hat{X}\hat{Y}} N_\ell^{\hat{X}}$), and no signal or noise in the cross with the galaxy-derived transverse velocity ($\tilde{C}_\ell^{X\hat{Y}} = 0$) when calculating the covariance matrix.

The results for the signal-to-noise ratio with these assumptions are shown in Fig 5.6. We find that with the method we described, Simons Observatory combined with DES will be

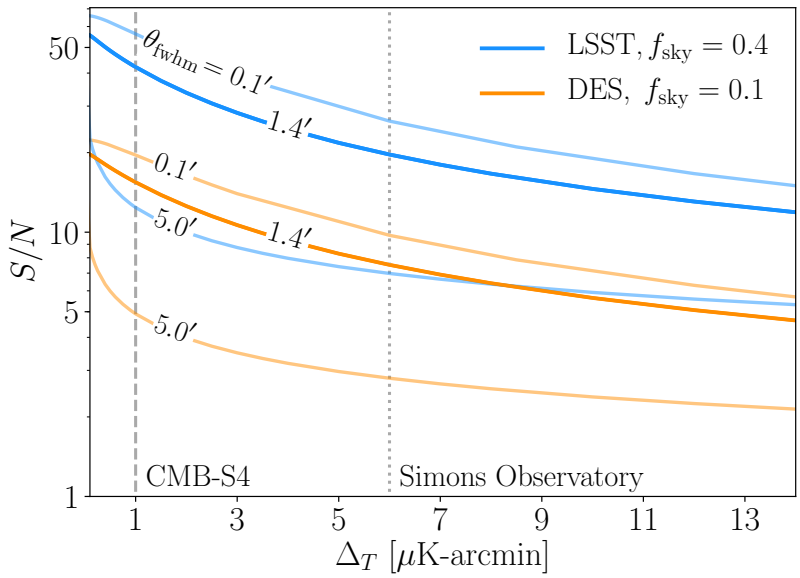

Figure 5.6: Signal-to-noise ratio of the transverse velocity estimator for a range of CMB noise levels and beam sizes, combined with Vera Rubin Observatory (LSST) and DES. The approximate anticipated noise levels of Simons Observatory and CMB-S4 are shown; both have roughly a 1.4-arcminute beam. [15]

able to detect the moving lens effect at about 8σ, and CMB-S4 combined with Vera C. Rubin Observatory at about 40σ, meaning that a first detection and subsequent precision measurement of the moving lens effect should be possible in the next several years. The signal-to-noise ratios in the results we have shown are limited in part by the contributions to the temperature spectrum that come from the kSZ effect and lensing on small scales. Reconstructing and removing the fluctuations from the kSZ effect, which may be possible with the upcoming experiments [248, 249], together with applications of delensing such as in [307] may improve the signal-to-noise ratio.

5.9 Biases

The analysis above ignored other secondary CMB fluctuations which may contribute to the estimator in Eq. (5.42). We now discuss such biases and their mitigation.

Ordinary lensing introduces two biases to the transverse velocity estimator. The first bias is proportional to the long-wavelength temperature gradient and takes the form

$$\Upsilon^{\phi\psi}(\mathbf{L}) \simeq \Theta(\mathbf{L})N(\mathbf{L})\int \frac{\mathrm{d}^2\boldsymbol{\ell}}{(2\pi)^2} C^{\phi\psi}_{|\boldsymbol{\ell}-\mathbf{L}|} g(\boldsymbol{\ell},\mathbf{L})\mathbf{L}\cdot(\mathbf{L}-\boldsymbol{\ell})\,, \tag{5.50}$$

where we have approximated the change to the temperature fluctuations due to lensing to first order in the deflection as $\Delta\Theta(\hat{\mathbf{n}})\big|_{\rm lens} \simeq \nabla\Theta(\hat{\mathbf{n}})\cdot\vec{\alpha}(\hat{\mathbf{n}})$. There exists a second bias from ordinary lensing,

$$\Upsilon^{\Theta\psi}(\mathbf{L}) \simeq \phi(\mathbf{L})N(\mathbf{L})\int\frac{\mathrm{d}^2\boldsymbol{\ell}}{(2\pi)^2}C^{\Theta\psi}_{|\boldsymbol{\ell}-\mathbf{L}|}g(\boldsymbol{\ell},\mathbf{L})\mathbf{L}\cdot(\mathbf{L}-\boldsymbol{\ell})\,, \tag{5.51}$$

which can be understood as the large-scale gravitational potential fluctuations distorting small-scale ISW or Rees-Sciama temperature fluctuations.

The kSZ effect generates CMB temperature fluctuations of the form

$$\Delta\Theta(\hat{\mathbf{n}})\big|_{\rm kSZ} = -\int \mathrm{d}\chi\; v_{\rm d}(\chi\hat{\mathbf{n}})\,d\tau/d\chi(\chi\hat{\mathbf{n}}) \tag{5.52}$$

where $d\tau/d\chi(\chi\hat{\mathbf{n}}) = \sigma_T a n_e(\chi\hat{\mathbf{n}})$, σ_T is the Thomson cross section, a is the scale factor, n_e is the free electron number density, and $v_{\rm d}$ is the remote CMB dipole projected along the line of sight, given by $v_{\rm d} = 3\int \mathrm{d}^2\hat{\mathbf{n}}\,\Theta_1(\hat{\mathbf{n}}_e,\hat{\mathbf{n}})(\hat{\mathbf{n}}_e\cdot\hat{\mathbf{n}})/(4\pi)$. We approximate the dipole seen by distant electrons as dominated by the Doppler effect $\Theta_1 \simeq \vec{v}_e\cdot\hat{\mathbf{n}}$, where $\vec{v}_e$ is the electron velocity. The contribution from the kSZ effect to our transverse velocity estimator is then

$$\Upsilon^{\rm kSZ}(\mathbf{L}) \simeq -v_{\rm d}(\mathbf{L})N(\mathbf{L})\int\frac{\mathrm{d}^2\boldsymbol{\ell}}{(2\pi)^2}C^{\delta\tau\psi}_{|\boldsymbol{\ell}-\mathbf{L}|}g(\boldsymbol{\ell},\mathbf{L})\,, \tag{5.53}$$

where $C_\ell^{\delta\tau\psi}$ is the cross-correlation between ψ and $d\tau/d\chi$.

We now assess how large these biases would be if one were to naively apply the estimator shown in Eq. (5.47) to the data. We define the spectra of the biases as

$$\langle\Upsilon^B(\boldsymbol{\ell})\Upsilon^B(\boldsymbol{\ell}')\rangle = (2\pi)^2\mathscr{B}^B_\ell\,\delta^{(2)}(\boldsymbol{\ell}+\boldsymbol{\ell}') \tag{5.54}$$

where $B\in\{\phi\psi,\Theta\psi,\mathrm{kSZ}\}$ and plot the results in Fig. 5.7 for the redshift bin $z\in[1.00,1.25]$. One can see that the $\phi\psi$-bias introduced in Eq. (5.50) traces the structure of the primary CMB temperature, due to the fact that our transverse velocity estimator is very similar to an estimator designed to reconstruct the large-scale primary temperature fluctuations from observation of small-scale temperature and lenses [308]. This bias is the largest of those we have considered, and it is smaller than the signal on large scales $\ell\lesssim 50$ which make the dominant contribution to the signal-to-noise ratio. Our knowledge of the large-scale CMB temperature allows us to cleanly remove the effects of the $\psi\phi$-bias by subtracting a best-fit multiple of the observed large scale temperature fluctuations from the reconstructed Υ map. This bias could also be reduced by delensing the temperature map [309, 307, 310] before

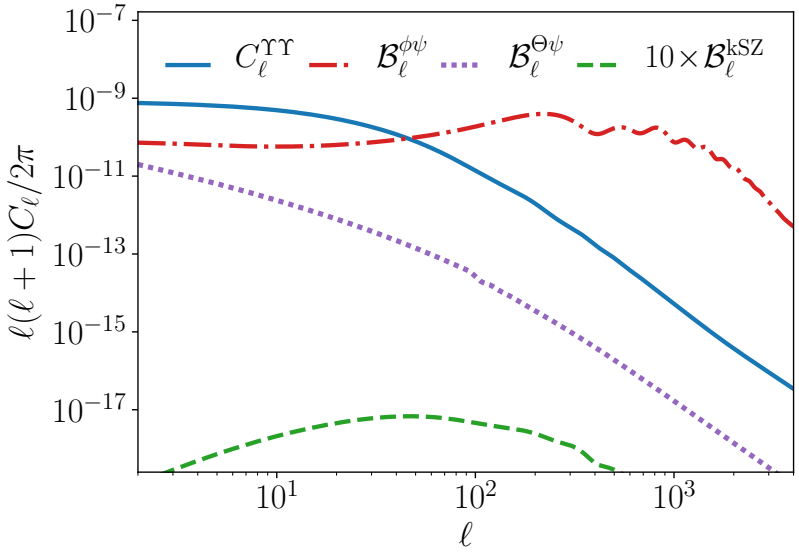

Figure 5.7: Comparison of the transverse velocity power spectrum with ordinary lensing and kSZ biases for the redshift bin $z \in [1.00, 1.25]$ for a CMB experiment with $\Delta_T = 1\,\mu$K-arcmin and a 1.4-arcmin beam combined with RUBIN. The dominant contribution to the signal-to-noise ratio comes from large scales $\ell \lesssim 50$, where the biases are smaller than the transverse velocity signal. Furthermore these biases can be mitigated using the methods described in the main text. [15]

estimating the transverse velocity potential, or by suppressing its contribution to the estimator by bias-hardening [311].

The $\Theta\psi$-bias introduced in Eq. (5.51) is most important on large scales, though it is about two orders of magnitude smaller than the transverse velocity signal on most scales and redshifts. Our estimate of this bias included only the linear contributions to the ISW effect, but the non-linear Rees-Sciama effect may increase $C_\ell^{\Theta\psi}$ on small scales, thereby boosting the bias compared to what we have calculated here. The $\Theta\psi$-bias can also be mitigated by subtracting from the reconstructed Υ map the best-fit multiple of the gravitational lensing field ϕ which will be measured at high significance with the CMB experiments we are considering. The kSZ bias is sub-dominant on all scales of interest, though it too may be possible to reconstruct and remove with the experiments being discussed here [248, 249].

5.10 Discussion

It has long been known that gravitational potentials moving transverse to our line of sight generate temperature fluctuations in the CMB [227]. Individual objects induce small fluctuations in the temperature which are easily confused with other effects making detection

challenging [272–274]. We have shown that the dipolar pattern in the CMB temperature fluctuations around moving DM halos due to the moving lens effect can potentially be detected in the near future by statistically combining the signal from many objects with a common bulk motion, using either a matched filter in real space, or a quadratic estimator in harmonic space. The methods we described in these sections greatly increases the prospects for reconstructing transverse velocities on large scales. We demonstrated that upcoming CMB experiments like Simons Observatory and CMB-S4 combined with galaxy surveys such as DES and Vera C. Rubin Observatory have the statistical power to make a detection of the moving lens effect at high significance. We also computed the leading biases and discussed how they can be mitigated.

We calculated the form of the optimal matched filter, which is imagined to be centered on DM halos inferred from galaxy surveys, and aligned with the cosmological bulk transverse velocities. We discuss the distribution and the detection prospects of halos from galaxy surveys, as well as the effect of photo-z errors and redshift-space distortions on the bulk velocities inferred from a halo catalog. We calculate estimates for the SNR with the upcoming experiments using analytic expressions we derive. We find that a statistically-significant detection will be possible with the Simons Observatory, upon cross-correlation with Rubin galaxy survey, for example. The maximum residual signal resulting from stacking a large number of halos inside volumes of size around the correlation length of the cosmological velocity field can potentially be used to estimate the direction and amplitude of the bulk velocity at a given region. Using the known functional form of the moving lens effect could potentially increase the accuracy of reconstruction by fitting the template calculated Eqn. (5.14). Complementary to quadratic estimator technique introduced in [15], the real-space analysis provides a useful alternative which will allow high SNR detection of the moving lens effect in the near future.

Using the CMB to reconstruct the large-scale transverse velocity field allows for the use of small-scale CMB measurements to probe long-wavelength cosmological fluctuations at lower redshift, much like with CMB lensing [294], the kSZ effect [312, 248, 249], and the polarized SZ effect [260, 267, 270, 271]. Since the observation of large-scale modes is typically challenging, and the number of independent modes on large scales is inherently limited, it is generally useful to expand the list of methods to access large scales observationally. As a specific application, one could imagine using the large-scale velocity modes reconstructed with the moving lens effect to cancel cosmic variance [313] for the purpose of constraining local non-Gaussianity (which induces a scale-dependent bias on large scales [314]), in a way similar to what has been explored for CMB lensing [215] and the kSZ effect [217]. Furthermore, because the moving lens effect is a result of purely gravitational effects, it

can be used to measure quantities which cannot be accessed directly with the kSZ effect alone, such as the absolute growth rate, which is useful for studying dark energy [315], modified gravity [316], and the effects of neutrino mass [317]. Combined with other probes, observations of the moving lens effect can also help reduce degeneracies due to astrophysical uncertainties such as the optical depth degeneracy of the kSZ effect [249]. I explore one potential application of the reconstructed transverse velocities in Appendix B where I evaluate the prospects of constraining optical dept bias from the kSZ tomography that I discuss in the next chapter.

Transverse velocity modes also provide a rare window into measuring the profile of DM halos and can afford constraining power on various halo model parameters upon cross-correlating with other tracers of large-scale structure such as weak gravitational lensing. We leave a more detailed study on the prospects of testing halo models with the moving lens effect to a future work.

Transverse velocity modes also provide a rare window into measuring the profile of DM halos and can afford constraining power on various halo model parameters upon cross-correlating with other tracers of large-scale structure such as weak gravitational lensing. We leave a more detailed study on the prospects of testing halo models with the moving lens effect to a future work.

Note that another velocity-dependent effect on the CMB is the so-called ‘rotational’ kSZ effect due to the rotational motion of the large galaxy clusters [318, 319], sourced by the angular momentum of halos. Various recent studies [e.g. 320, 321] show that ongoing experiments will have the statistical power to detect this dipolar kSZ signature centered around galaxy clusters. On small scales, the dominant contribution to the rotational kSZ is the component of the angular momentum field that is sourced by the non-linear growth and dynamics of the virialized environment, which is not correlated with bulk transverse velocity. This component acts as noise on the moving lens measurement. Nevertheless, the angular momentum field is not expected to be entirely uncorrelated with the long wavelength potential: correlations are induced due to deviations of the proto-halos from perfect spherical symmetry and their alignments, for example. The correlated rotational kSZ effect can bias the moving lens measurement as well as potentially providing information regarding the growth of structure and the initial conditions. We leave a detailed analysis on the implications of large-scale angular momentum correlations on the moving lens and kSZ effect measurements to future work.

Finally, since photons traversing near galaxies trace regions of the Universe with larger density fluctuations, patches we use in our real-space analysis are more noisy in average than

a random location on the sky due to ordinary lensing. The effect of ordinary lensing on the CMB is not random, however, and the induced dipolar pattern is correlated with the large-scale CMB gradient. Since the CMB gradient is very well measured, this correlated boost in variance (which can be understood as a bias induced by ordinary lensing) can potentially be removed. Since the temperature gradient is not correlated with the bulk transverse velocity, we anticipate this procedure will not degrade the detection prospects of the moving lens effect significantly. Note that we also checked for the additive noise effect from (nonphysical) randomly distributed ordinary lensing contribution to the CMB spectra (which is a shot-noise term, $1/N_{\rm source}$, on the templates where $N_{\rm source}$ is the number of sources available from the galaxy catalogue). For the upcoming LSS surveys, together with Simons Observatory and CMB-S4, for example, we find this shot noise remains smaller compared to the noise of the CMB experiment.

The major leaps forward in the precision of near-future CMB and galaxy surveys will open many new cosmological opportunities. We have described a method which will allow for the first detection of the moving lens effect with forthcoming data, and will provide a novel probe of large-scale transverse velocities with a host of cosmological applications.

Chapter 6

Probing fundamental physics with the kSZ effect

This chapter is largely based on my published work in collaboration with James Mertens, Matthew Johnson and Marc Kamionkowski, on constraining Compensated Isocurvature Perturbations (CIPs) with the kSZ measurements [17], and my upcoming work with Mathew Madhavacheril and Neal Dalal, on developing a novel method to isolate and evaluate the detection prospects of the clustering properties of dark energy perturbations [322].

This chapter aims to introduce kSZ tomography for the purpose of studying fundamental physics. The calculations include theoretical predictions for the CIP fluctuations on the *galaxy bias*, b_g, and the effect of DE clustering on the *absolute growth rate*, $f(k)$. Both observables gain scale dependence in the presence of the aforementioned deviations from the ΛCDM paradigm we introduced in Chapter 2. Results in this chapter are forecasts on the detection prospects of these deviations, using the anticipated experimental specifications for the upcoming CMB experiments and LSS surveys. The discussion on the CIPs is also complemented with the upcoming work described in Appendix 8, where we discuss the prospects of utilising the upcoming 21cm hydrogen-line intensity measurements. Note, however, that velocities reconstructed from the kSZ tomography are subject to an unknown bias (so-called kSZ optical depth bias b_v) due to our lack of knowledge of the electron gas density cross-correlation with the galaxy observables on small scales. There has been attempts in literature to measure this bias using fast radio-bursts [323], for example, which will be detected to very high numbers with ongoing radio experiments such as CHIME [324]. Developing alternative methods to overcome the kSZ optical bias is not in the scope of this chapter; however, we discuss one potential method in Appendix B, using the moving lens effect measurement discussed in the previous chapter.

The text, the conceptualisation, calculations and the forecasting work were dominantly contributed by myself with exceptions including contributions to forecasting and plot-making from James Martens for calculations of the CIP constraints using the kSZ effect; and contributions from Mat Madhavacheril, to the development of the concept of the Fisher matrix manipulation in order to isolate the DE perturbations from the background. All collaborators mentioned above has contributed to the conceptualisation of the project and fact-checking, as well as providing feedback for the text.

We start in Section 6.1 by describing the science case and the motivation for using kSZ measurements as a probe of fundamental physics. We give a brief description of the kSZ tomography in Section 6.2. A more robust discussion on reconstruction techniques with the quadratic estimator (or a more in-depth discussion on the kSZ reconstruction) is outside the scope of this thesis. We describe two deviations from the standard ΛCDM in Section 6.3. We give a more detailed discussion on CIPs and their observable consequences in Section 6.4; and on DE perturbations and clustering on Section 6.5. We discuss our forecasts for both effects in Section 6.6 before concluding with a discussion on Section 6.7.

6.1 The search for fundamental physics

A major goal of the scientific program of measuring secondaries is constraining fundamental physics. Large-scale cosmological perturbations leave unique imprints on the small-scale intensity and polarization anisotropies of the CMB. The study of these statistical anisotropies provide new information about the largest scales in the Universe. Large-scale observables are in turn valuable for cosmological inference as they are often protected from local and non-linear late time effects under the equivalence principle. Equivalence principle dictates that local interactions produce density fluctuations that scale with the Fourier wavenumber k like the Laplacian (or the time derivative) of the gravitational potential $\nabla^2\Phi$ (or $\dot{\Phi}$) and have vanishing influence on large scales as $k \to 0$ compared to curvature fluctuations. This makes large-scale observables a powerful probe of the initial conditions that source the large-scale fluctuations in the Universe. Understanding how large-scale fluctuations in the Universe compare to the predictions of ΛCDM provide insight on the details of the primordial Universe.

Measuring velocities on large scales is particularly valuable. For example, in many cases the noise associated with the reconstructed velocity fields is constant, making it possible to infer the matter power spectrum with a noise that scales like k^2. Since the matter power spectrum can be inferred from galaxies only up to a constant shot noise, this advantage of

velocity reconstruction is most important on the largest scales. Of course, inferences on cosmological parameters are still limited by the small number of modes on large scales (cosmic variance). However, as we discuss in section 6.2.3, one can compare a reconstruction with a galaxy survey to measure bias parameters with arbitrary accuracy; this was proposed in Ref. [217] as a means for detecting primordial non-Gaussianity through scale-dependent galaxy bias.

6.2 kSZ tomography

The technique of kSZ tomography [312, 325, 247–249] uses the correlation between a redshift-binned tracer of the electron density, such as the galaxy number counts from a galaxy survey, and the small-angular scale kSZ contribution to the CMB to reconstruct the three dimensional remote dipole field, the CMB dipole as observed at different locations in our Universe. The remote dipole field, which at any location is dominated by the Doppler effect associated with radial peculiar velocities, can be reconstructed with high fidelity on large angular scales using future surveys such as Simons Observatory [204] or CMB-S4 [205] and Vera C. Rubin Observatory (LSST) [207] or DESI [326]. In the present context, it is important to note that the remote dipole field is an unbiased tracer of the total density. Cross-correlation with a galaxy survey can therefore take full advantage of sample variance cancellation in order to extract (scale dependent) galaxy bias to high precision. The reconstruction is in principle of such high quality that it is superior to direct measurements of the density field from the galaxy survey itself, making kSZ tomography a powerful probe of inhomogeneities on the largest scales. These measurements can facilitate strong constraints on primordial non-Gaussianity [217, 327], the physics of cosmic acceleration [219], and inflationary cosmology [218, 325].

6.2.1 Redshift-binned estimator

More specifically, we can write a quadratic estimator for the remote dipole field averaged in a set of top-hat redshift bins, in the form of temperature correlated with galaxy density. We begin with the kSZ contribution to the CMB temperature defined in Eq. (4.2),

$$\Theta_{\rm kSZ}(\hat{\mathbf{n}}) = \int_0^{\chi_*} \mathrm{d}\chi\, \dot{\tau}(\chi\hat{\mathbf{n}}) v_{\rm eff}(\chi\hat{\mathbf{n}})\,, \tag{6.1}$$

where we defined $\dot{\tau} := \sigma_T a n_e$. Decomposing into spherical harmonics

$$\dot{\tau}(\chi\hat{\mathbf{n}}) = \sum_{\ell m} \dot{\tau}_{\ell m}(\chi\hat{\mathbf{n}}) Y_{\ell m}(\hat{\mathbf{n}}) \tag{6.2}$$

$$v_{\rm eff}(\chi\hat{\mathbf{n}}) = \sum_{\ell m} v_{{\rm eff},\ell m}(\chi\hat{\mathbf{n}}) Y_{\ell m}(\hat{\mathbf{n}}) \,, \tag{6.3}$$

the kSZ effect can be written as

$$\Theta_{{\rm kSZ},\ell m} = \sum_{\ell_1 m_1 \ell_2 m_2} \left[(-1)^m \sqrt{\frac{(2\ell+1)(2\ell_1+1)(2\ell_2+1)}{4\pi}} \begin{pmatrix} \ell_1 & \ell_2 & \ell \\ 0 & 0 & 0 \end{pmatrix} \begin{pmatrix} \ell_1 & \ell_2 & \ell \\ m_1 & m_2 & -m \end{pmatrix} \right. \\ \left. \times \left[\int_0^{\chi_*} {\rm d}\chi v_{\ell_1 m_1}(\chi) \dot{\tau}_{\ell_2 m_2}(\chi) \right] \right] \tag{6.4}$$

where we used spherical harmonic relations Some useful spherical harmonics relations are

$$\int {\rm d}^2\hat{\mathbf{n}}\, {}_sY_{\ell m}(\hat{\mathbf{n}})\, {}_sY^{\star}_{\ell' m'}(\hat{\mathbf{n}}) = \delta_{\ell\ell'}\delta_{mm'} \,, \tag{6.5}$$

and

$$\int {\rm d}^2\hat{\mathbf{n}}\, {}_{s_1}Y_{\ell_1 m_1}(\hat{\mathbf{n}})\, {}_{s_2}Y_{\ell_2 m_2}(\hat{\mathbf{n}})\, {}_{s_3}Y_{\ell_3 m_3}(\hat{\mathbf{n}}) \\ = \sqrt{\frac{(2\ell_1+1)(2\ell_2+1)(2\ell_3+1)}{4\pi}} \begin{pmatrix} \ell_1 & \ell_2 & \ell_3 \\ m_1 & m_2 & m_3 \end{pmatrix} \begin{pmatrix} \ell_1 & \ell_2 & \ell_3 \\ -s_1 & -s_2 & -s_3 \end{pmatrix} . \tag{6.6}$$

The correlation with density, $\delta_{\ell m}$, averaged in some redshift bin α, $\delta^{\alpha}_{\ell m} := \int {\rm d}\chi W^{\alpha}(\chi)\delta_{\ell m}(\chi)$, is

$$\langle (\Theta_{\rm kSZ})_{\ell m} \delta^{\alpha}_{\ell' m'} \rangle \\ = \sum_{\ell_1 m_1} \left[(-1)^{m+m'} \sqrt{\frac{(2\ell+1)(2\ell_1+1)(2\ell'+1)}{4\pi}} \begin{pmatrix} \ell & \ell' & \ell_1 \\ 0 & 0 & 0 \end{pmatrix} \begin{pmatrix} \ell & \ell' & \ell_1 \\ m & m' & -m_1 \end{pmatrix} \right] \\ \times \left[\int_0^{\chi_*} {\rm d}\chi v_{{\rm eff},\ell_1 m_1}(\chi) C_{\ell}^{\dot{\tau}\delta}(\chi) \right] . \tag{6.7}$$

We can now define a quadratic estimator for the large-scale remote dipole field, $\widehat{v}^{\alpha}_{{\rm eff},LM}$, from the maps of temperature and galaxy density on small scales. This construction allows measuring the large scale velocity mode from the statistical anisotropy induced by modulations of small-scale cross-correlation power between the temperature and density fields due it

induces, hence, amounting to a non-zero three-point function between temperature, density and velocity at the squeezed limit. The quadratic estimator takes the form,

$$\widehat{v}^{\alpha}_{\mathrm{eff},LM} = N^{vv}_{\alpha L} \sum_{\ell m \ell' m'} (-1)^M \begin{pmatrix} \ell & \ell' & L \\ m & m' & -M \end{pmatrix} g^{\alpha}_{\ell\ell' L} \Theta_{\ell m} \delta^{\alpha}_{\ell' m'}\,, \tag{6.8}$$

where

$$N^{vv}_{\alpha L} := \langle \widehat{v}^{\alpha,*}_{\mathrm{eff},LM} \widehat{v}^{\alpha}_{\mathrm{eff},LM} \rangle = (2L+1) \left(\sum_{\ell\ell'} g^{\alpha}_{\ell\ell'} f^{\alpha\alpha}_{L\ell\ell'} \right)^{-1} \tag{6.9}$$

and

$$f^{\alpha\gamma}_{\ell\ell_1\ell'} := \sqrt{\frac{(2\ell+1)(2\ell_1+1)(2\ell'+1)}{4\pi}} \begin{pmatrix} \ell & \ell' & \ell_1 \\ 0 & 0 & 0 \end{pmatrix} \int_0^{\chi_*} \mathrm{d}\chi' \int_0^{\chi_*} \mathrm{d}\chi C^{\dot{\tau}\delta}_{\ell}(\chi,\chi') W^{\alpha}(\chi')\,. \tag{6.10}$$

The filter $g^{\alpha}_{\ell\ell' L}$ is chosen to minimise the estimator variance and the estimator can be found as

$$\widehat{v}^{\alpha}_{\mathrm{eff},\ell m} = b^{\alpha}_{v} N^{vv}_{\alpha\ell} \times \sum_{\ell_1 m_1 \ell_2 m_2} (-1)^m \Gamma^{\alpha}_{\ell_1\ell_2\ell} \begin{pmatrix} \ell_1 & \ell_2 & \ell \\ m_1 & m_2 & -m \end{pmatrix} \frac{\Theta_{\ell_1 m_1} \delta^{\alpha}_{g,\ell_2 m_2}}{C^{TT}_{\ell_1} C^{gg}_{\alpha\ell_2}}, \tag{6.11}$$

where

$$\Gamma^{\alpha}_{\ell_1\ell_2\ell} = \sqrt{\frac{(2\ell_1+1)(2\ell_2+1)(2\ell+1)}{4\pi}} \begin{pmatrix} \ell_1 & \ell_2 & \ell \\ 0 & 0 & 0 \end{pmatrix} C^{\dot{\tau}g}_{\alpha,\ell_2}\,, \tag{6.12}$$

and the reconstruction noise (e.g. variance of the estimator) is defined by

$$\frac{1}{N^{vv}_{\alpha\ell}} = \frac{1}{(2\ell+1)} \sum_{\ell_1\ell_2} \frac{\Gamma^{\alpha}_{\ell_1\ell_2\ell} \Gamma^{\alpha}_{\ell_1\ell_2\ell}}{C^{\Theta\Theta}_{\ell_1} C^{gg}_{\alpha\ell_2}}. \tag{6.13}$$

The subscript g refers to the density field reconstructed from measurements of galaxy positions. In these expressions, $C^{\Theta\Theta}_{\ell_1}$ is the measured CMB temperature power spectrum, $C^{gg}_{\alpha\ell_2}$ is the measured spectrum of the galaxy number counts in each bin, and $C^{\dot{\tau}g}_{\alpha,\ell_2}$ is the cross-power of the optical depth and galaxy number counts in each bin. In the absence of an external tracer of the electron distribution [323], there is in principle a significant model uncertainty in $C^{\dot{\tau}g}_{\alpha,\ell_2}$. This uncertainty manifests itself as a multiplicative "optical depth bias" b^{α}_{v} on the reconstructed dipole field which must be marginalized over in any cosmological analysis (see e.g. Refs. [328, 329, 249, 323] for further discussion).

The reconstruction noise can in principle become arbitrarily small in the limit where the CMB and number counts can be probed on arbitrarily small angular scales. In reality, the reconstruction noise is limited by the instrumental noise of the CMB experiment and shot noise of the galaxy survey, since this places an effective upper limit in ℓ on the sum in Eq. 6.13. The expected bin-averaged dipole field signal is computed as in Ref. [248].

6.2.2 Co-evaluation box estimator

Note, moreover, as in [216, 249], we can also reconstruct the large-scale velocity modes with wavenumbers k_L from measurement of the kSZ effect and the galaxy-density distribution on small scales *inside a box as at comoving distance* χ_*. This 'box' formalism utilises the 3-dimensional density field, $\delta_g(\vec{k}_S)$, on small scales $\vec{k}_S \gg 1$, taken as a 'snapshot' approximation of the true density field at some redshift z (same for the all box). In this formalism the quadratic estimator takes the form

$$\hat{v}_r(\vec{k}_L) = \int \frac{\mathrm{d}^3\vec{k}_S}{(2\pi)^3}\frac{\mathrm{d}^2\vec{\ell}}{(2\pi)^2} g(\vec{k}_S,\vec{\ell})\delta_g^\star(\vec{k}_S)T^\star(\vec{\ell})(2\pi)^3\delta^3\left(\vec{k}_L+\vec{k}_S+\frac{\vec{\ell}}{\chi_\star}\right) \tag{6.14}$$

where the filter, similar to before, is defined to minimise the variance of the reconstruction subject to the constraint that the reconstructed field is unbiased, that is $\langle\hat{v}_r(\vec{k}_L)\rangle$ is equal to the true velocity field $v_r(\vec{k}_L)$. These conditions are satisfied with a filter defined as

$$g(\vec{k}_S,\vec{\ell}) = N^{vv}_{\rm rec}(k_L)\frac{K_\star}{\chi_\star^2}\frac{P_{ge}(k_S)}{P^{\rm obs}_{gg}(k_S)C_\ell^{TT,\rm obs}}\,, \tag{6.15}$$

where $P_{gg}(k)$ and $P_{ge}(k)$ are the three-dimensional density auto power-spectrum and density-electron cross-power at some redshift $z_\star$. The velocity reconstruction noise is

$$N^{vv}_{\rm rec}(k_L,\mu) = \mu^2\frac{2\pi\chi_*^2}{K_*^2}\left[\int \mathrm{d}k_s k_s \frac{P_{ge}(k_s)^2}{P^{\rm obs}_{gg}(k_s)C^{TT,\rm obs}_{\ell=k_s\chi_*}}\right], \tag{6.16}$$

where $K_* = K(z_*)$ is the kSZ radial weight function at redshift z_*, defined as

$$K(z) = -T_{\rm CMB}\sigma_T n_{e,0}x_e e^{-\tau(z)}(1+z)^2 \tag{6.17}$$

and $T_{\rm CMB}$ is the background CMB temperature, $n_{e,0}$ is the comoving electron number density today, $x_e(z)$ is the ionised fraction and $\tau(z)$ is the optical depth. The parameter μ determines the angle of the mode with respect to the line of sight $\mu := \hat{\mathbf{k}} \cdot \hat{\mathbf{n}}$.

We use both of the formalisms in the following sections when assessing the fidelity of the upcoming experiments upon constraining deviations from the standard ΛCDM.

6.2.3 Sample variance cancellation

As discussed earlier, a major advantage of using a technique like the kSZ tomography is the possibility of overcoming the cosmic sample variance on large scales: the large null-condition, such as the fiducial galaxy power-spectrum, for example, that we need to compare against when measuring a small deviation from the standard LCDM prediction. Schematically, this can be seen from comparing the *ratio* of the kSZ-reconstructed velocities,

$$v \propto \frac{faH}{k}\delta_m\,, \tag{6.18}$$

and the galaxy over-density,

$$\delta_g = b_G\delta_m\,, \tag{6.19}$$

which become independent of the matter density δ_m. In this example, kSZ reconstruction, together with a survey of the galaxy distribution, can measure the galaxy bias b_G or the growth rate f without sample variance and an arbitrary improvement of the measurement quality can potentially be achieved with improving CMB and galaxy survey noise. In practice, the sample variance cancellation is done by measuring all auto- and cross-correlations of the density and velocity fields: $\{P_{gg}, P_{gv}, P_{vv}\}$.

6.3 Fundamental physics beyond the ΛCDM

6.3.1 Compensated isocurvature perturbations

Measurements of the CMB provide the bedrock for the standard cosmological model, ΛCDM. As discussed in Chapter 2, a central feature of ΛCDM is that perturbations are adiabatic, with inhomogeneities in dark matter, baryons, neutrinos, and photons all uniquely determined by the primordial curvature perturbations. Theories of the early Universe which have one degree

of freedom, such as single field inflation discussed in Section 2.3, naturally predict purely adiabatic fluctuations. More generally, theories with multiple degrees of freedom, like those discussed in Chapter 3, can source isocurvature (entropy) perturbations, where the relative mixture of dark matter, baryons, neutrinos, and photons become independent degrees of freedom. While most forms of isocurvature perturbations are tightly constrained by existing measurements of the CMB [330], there is a notable exception: compensated isocurvature perturbations (CIPs).

CIPs are fluctuations of baryons and cold dark matter that leave the total matter perturbations unchanged and adiabatic. CIPs leave an imprint on the CMB only through terms that appear at second order in the matter density contrast, making them challenging to constrain [331–337].

Current measurements from Planck [330] allow for an amplitude of CIPs roughly 580 times larger than the amplitude of the adiabatic modes! [1] This is a surprisingly large gap in our knowledge of the early Universe. A detection of CIPs can provide insight into both the number of primordial fields that contribute to the observed density fluctuations, as well as their decay channels [170, 339, 340], strongly motivating new ways of searching for CIPs.

Variations of the ratio between baryons and cold dark matter changes how structure is distributed in the Universe, altering how galaxies trace the total matter density [341–343]. This leads to a spatially varying galaxy-bias that relates the observed galaxy over-density to the total matter over-density. In particular, CIPs that are correlated with the primordial curvature perturbation (as arises in e.g. curvaton scenarios [170]) will introduce a scale-dependent galaxy-bias [343], similar to the effect of local-type primordial non-Gaussianity [314]. Because correlated CIPs induce a scale dependent galaxy bias, given an unbiased tracer of the total matter density, it is possible to use sample variance cancellation [344, 313] to measure the amplitude of CIPs without cosmic variance, as suggested in Ref. [343]. While it is possible to use different populations within a galaxy survey itself to measure scale-dependent bias, sample variance cancellation is in principle more powerful when using the technique of kSZ tomography [217, 327]. A primary goal of this chapter is to explore the potential for kSZ tomography to probe CIPs using future CMB and galaxy surveys.

Previous work [217, 327] has found that future experiments will be able to detect local-type non-Gaussianity of order $\sigma_{f_{\rm NL}} \sim \mathcal{O}(1)$ by utilising sample variance cancellation between the reconstructed remote dipole field and galaxy number counts. Depending on assumptions,

[1] More recently, constraints on CIPs from their effect on baryon acoustic oscillations [338] (BAO) were analyzed. It was shown that constraints comparable to those from the CMB are possible with future galaxy surveys.

priors on various bias parameters, and whether internal sample variance cancellation is employed, this can represent up to an order of magnitude improvement on what is possible using the galaxy survey alone. Below, we find a similar level of improvement on the amplitude of CIPs when utilising kSZ tomography. In particular, it will be possible to probe CIPs comparable in amplitude to the adiabatic perturbations, which can be thought of as a well-motivated target for future measurements.

In Sec. 6.4 we describe potential sources and observable consequences of CIPs. We examine how well future surveys can measure correlated CIPs in Sec 6.6. We conclude in Sec. 6.7.

6.3.2 Dark energy perturbations

In addition to the study of the characteristic of initial conditions discussed above, another major science program in cosmology is the study and inference of the dark energy component of the Universe. As discussed in Chapter 2, dark energy is parameterised as a cosmological constant in the standard cosmological paradigm, the ΛCDM. While the ΛCDM model provides a robust basis for our understanding of the Universe, observing deviations from its predictions has the potential to provide invaluable insights into the microphysics of its relatively less understood components. Hence, here, we also study the dark energy component of the Universe which we take to be a perfect fluid and evaluate the detection prospects of dark energy perturbations from the effect on the growth of large-scale structure.

There is overwhelming evidence that the Universe today is expanding in an accelerated rate, strongly indicating a dominant dark energy component with a negative equation of state $w_0 < 0$. Numerous ongoing and completed large-scale experiments agree that the equation of state of dark energy is close to -1. While the dark energy sector is decoupled from the metric in the standard ΛCDM, for less constraining models with w_0 different than -1, dark energy can impact the growth of density perturbations (and hence observables accessible to current and future experiments) in a model dependent way. We model the dark energy component as a perfect fluid with a sound speed satisfying $c_s^2 = \delta p_{\rm DE}/\delta\rho_{\rm DE}$ at the rest frame of the fluid, with dark energy density and pressure perturbations. In this model, analogous to other components of the Universe, when w_0 is different from -1, dark energy can cluster under gravity on scales beyond the dark energy sound horizon, and is coupled to other components of the Universe through the metric.

While detection of the dark energy clustering through constraining w_0 would indicate evidence for fundamental physics different than ΛCDM, the effect of dark energy pertur-

bations on the late time observable Universe is subdominant compared to the influence of the dark energy component on the background cosmology. In particular, the parameter w_0 is largely insensitive to the microscopic details of the dark energy component, for example to the degrees of freedom governing the dark energy sector or to the characteristics of the dark energy field. A model parameter that is sensitive to some of these details, on the other hand, is the dark energy sound speed, c_s. In particular, measurement of the dark energy speed of sound would potentially constrain the dark energy perturbations in a non-ambiguous way, as it would amount to measuring the scale beyond which the dark energy perturbations cluster. We discuss the observable consequences of dark energy perturbations in Section 6.5. Unfortunately, however, the observational accuracy of the upcoming experiments suggest measuring c_s with high fidelity in the near future is unlikely, indicating the necessity for an alternative (and robust) way of measuring dark energy perturbations. Furthermore, for the level of deviation of w_0 from the ΛCDM allowed by current galaxy surveys, observable signature of dark energy perturbations on the galaxy auto-spectrum, for example, compares to the experimental uncertainties and anticipated systematics, casting doubt on the use of galaxy statistics alone when inferring such small effects.

For these reasons, in Section 6.6.2 we provide a simple novel method to isolate the signature of dark energy perturbations from their effect on the background cosmology and the systematic uncertainties due to the measurements of the galaxy density. We discuss dark energy fluid equations of motion and analyse the effect of w_0 and sound speed in Section 6.5. We introduce a simple method to isolate the constraining power of the upcoming experiments on dark energy perturbations utilising the measurements of the kSZ effect for forecasting purposes in Section 6.6. The velocity field on large scales contains information on the clustering properties of dark energy through the scale dependence on the growth rate, which is introduced when the dark energy equation satisfies $w \neq -1$. Furthermore, note that the velocity is an unbiased tracer of the total matter density and its cross-correlation with the biased density field, reconstructed from a galaxy survey, allow taking advantage of sample variance cancellation [313] in order to extract the scale dependent variations from the ΛCDM prediction to high precision on large-scales. We discuss the implications of our results in Section 6.7.

6.4 CIPs and their observable consequences

In the early Universe, standard single-field inflation produces purely adiabatic curvature perturbations (see Chapter 2 for a brief review). If the fluctuations seeded in the early Universe

were sourced by multiple fields as discussed in Chapter 3, however, some fraction of these may be entropic (or isocurvature) perturbations where the fractional densities of baryons or dark matter vary with respect to radiation. Isocurvature perturbations can be parameterised by a quantity $S_{i\gamma}$, with γ for photons and $i = \{b, c, \nu\}$ for baryons, cold-dark-matter (CDM) and neutrinos respectively, and

$$S_{i\gamma} = \frac{\delta n_i}{n_i} - \frac{\delta n_\gamma}{n_\gamma}\,, \tag{6.20}$$

where n and δn are the mean number density of a species and its fluctuations, respectively.

We will define the compensated isocurvature mode with Δ as in the literature. The baryon and CDM isocurvature perturbations are then defined as

$$S_{b\gamma} = \Delta, \;\; S_{c\gamma} = -\frac{\rho_b}{\rho_c}\Delta \tag{6.21}$$

where ρ_i is the energy density of species i.

Compensated isocurvature perturbations may be sourced, for example, by a spectator scalar field that is subdominant in the early Universe with respect to the inflaton field driving the inflationary dynamics [345]. In this scenario, after inflation ends, the inflaton decays into relativistic particles and its energy density scales like radiation, while the spectator field (curvaton) oscillates around its potential minimum, its energy density scaling like matter e.g. [176, 170, 340, 346, 170, 339, 347]. We already discussed some other observable impacts of these scenarios in Chapter 3. Depending on the duration of this era, the curvaton may contribute significantly to curvature fluctuations of the Universe upon its decay into relativistic particles.

If the curvaton decays into baryon number and CDM and also dominates the energy density of the Universe at its decay, the CIPs will be fully correlated with the adiabatic curvature fluctuations ζ, satisfying

$$\Delta = A\zeta\,, \tag{6.22}$$

while any residual isocurvature perturbations other than CIPs that are uncorrelated with the adiabatic curvature fluctuations are well constrained by the CMB observations [330]. Similar to earlier works in the literature, e.g. [345, 348, 338], we focus here on these "correlated CIPs" and evaluate the detection significance of the amplitude A below. The two distinct curvaton decay scenarios that produce observationally relevant CIP amplitudes are either $A \simeq 16$, if baryon (CDM) number is produced by (before) curvaton decay; or $A = -3$, if CDM

(baryon) number is produced by (before) curvaton decay [345]. Furthermore, in the former curvaton decay model where $A \simeq 16$, the local non-Gaussianity is found to be relatively large, $f_{\rm NL} \simeq 6$ [172, 345], suggesting future experiments may disfavor the scenarios where CDM preceded the decay of curvaton. Note that an unambiguous statement along these lines will require constraining both the CIP amplitude and $f_{\rm NL}$ simultaneously, as we discuss in Sec. 6.6.

In the absence of primordial isocurvature perturbations after recombination, baryons and CDM can be approximated to move together as a single fluid on large scales where non-gravitational forces can be neglected. However, both before recombination and in the presence of primordial isocurvature perturbations, there can be important differences in the distribution of baryons and CDM. For example, before recombination baryons are tightly coupled to photons while CDM is not. This leads to a modulation in the relative fraction of baryons and CDM on large scales while keeping the total matter density fixed, and therefore is a source of CIPs [341–343]. In addition, we may have the primordially sourced CIPs discussed above. As we will see shortly, primordial correlated CIPs can be distinguished from these more mundane sources of CIPs by their characteristic scale dependent imprint on the distribution of galaxies.

There are a few potential imprints of CIPs on the observed galaxy distribution. First, the sound horizon becomes spacetime dependent, altering the BAO feature in different regions of the Universe [338]. Second, modulating the density of baryons can modulate the strength of various feedback effects in the formation and evolution of galaxies. Finally, because only dark matter can cluster efficiently prior to recombination, modulating the density of dark matter will lead to a modulation in the growth of structure. It is this last effect that provides the dominant contribution on large scales, and which we focus on.

As shown in Ref. [343], the leading effect of CIPs on galaxy density perturbations can be folded into a linear bias $b_{\rm bc}(z)$:

$$\delta_g(\mathbf{k},\tau) \simeq b(z)\,\delta_m(\mathbf{k},\tau) + b_{\rm bc}(z)\,[\delta_{\rm bc}(\mathbf{k},\tau) + f\Delta(\mathbf{k})]\,, \tag{6.23}$$

where we have allowed for both pre-recombination CIPs $\delta_{\rm bc}$, as well as primordially sourced correlated CIPs, $f \equiv 1 + \Omega_b/\Omega_c$ Therefore, we see that primordially sourced correlated CIPs lead to a scale-dependent galaxy bias, becoming increasingly important on the largest scales. This scale dependence can be contrasted with the imprint of $\delta_{\rm bc}$, which is expected to be very small on scales larger than the BAO feature [343]. Indeed, on the scales of interest ($\sim$ Gpc), $\delta_{\rm bc}$ is many orders of magnitude smaller than δ_m and can be safely neglected.

The bias $b_{\rm bc}(z)$ can be estimated in the separate-Universe approximation by simply computing the effect of changing the baryon-CDM fraction on the number density of galaxies. We define

$$b_{\rm bc}(z) = \int dm\, n(m,z) b_{\rm bc}(m,z) \frac{\langle N(m)\rangle}{\bar{n}_g}\,, \tag{6.24}$$

where $n(m,z)$ is the halo mass function, $\langle N(m)\rangle$ is the average number of galaxies per halo of mass m, $\bar{n}_g$ is the comoving number density of galaxies at fixed redshift, and

$$b_{\rm bc}(m,z) = \frac{1}{\Delta_{\rm bc}}\left[\frac{\tilde{n}(m,z)}{n(m,z)} - 1\right]\,, \tag{6.25}$$

with

$$\Delta_{\rm bc} = \left(1 + \frac{\Omega_b}{\Omega_c}\right)\Delta_b\,, \tag{6.26}$$

and the mass function $\tilde{n}$ is evaluated with parameters:

$$\tilde{\Omega}_b = (1+\Delta_b)\,\Omega_b, \quad \tilde{\Omega}_c = \left(1 - \frac{\Omega_b}{\Omega_c}\Delta_b\right)\Omega_c\,. \tag{6.27}$$

To evaluate $b_{\rm bc}(z)$, we use the mass function and Halo Occupation Distribution (HOD) model for $\langle N(m)\rangle$ and $\bar{n}_g$ described in Ref. [249]. For parameters consistent with the LSST gold sample used in the forecast below, we find that a quadratic polynomial provides a good fit over the relevant range of redshifts:

$$b_{\rm bc}(z) \simeq -(0.16 + 0.2z + 0.083z^2)\,. \tag{6.28}$$

The total observed galaxy number counts receive contributions not only from CIPs and intrinsic density perturbations (D), but from all linear-order general relativistic and lightcone projection effects, including redshift space distortions (RSDs), lensing (L), and additional relativistic contributions (GR) that are important on large scales [349, 350]. The spectrum of the total observed galaxy number counts

$$C_\ell^{N,N} = 4\pi \int \frac{dk}{k}\, \mathscr{P}(k) |\Delta_\ell^{\rm N}(k)|^2 \tag{6.29}$$

is defined by the transfer function

$$\Delta_\ell^{\rm N}(k) = \Delta_\ell^{\rm D}(k) + \Delta_\ell^{\rm RSD}(k) + \Delta_\ell^{\rm L}(k) + \Delta_\ell^{\rm GR}(k)\,. \tag{6.30}$$

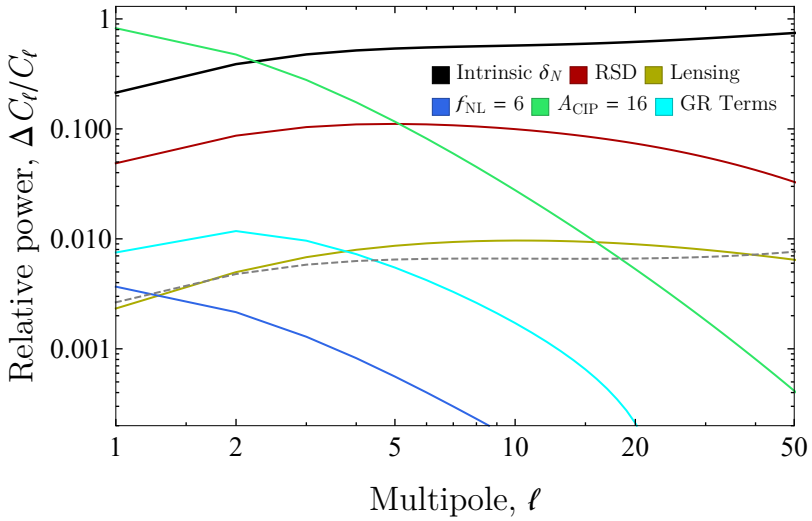

Figure 6.1: Relative contributions to the angular galaxy number counts power spectrum, as labeled in the figure, in a tophat redshift bin from redshift $z = 1.6$ to $z = 1.7$. Shot noise from a LSST-like galaxy survey is shown in dashed grey.

The power spectrum is defined by $\mathscr{P}(k) = A_s(k/k_0)^{n_s-1}$, and the transfer function for the intrinsic galaxy perturbations in a redshift bin is explicitly given by

$$\Delta_\ell^{\rm D}(k) = \int d\chi \tilde{W}(\chi) \left[\frac{5f}{3} A\, b_{\rm cb}(z) S_\psi(k,\chi) + (b_{\rm G}(z) - b_{\rm A}(z)/3 + b_{\rm NG}(z))\, S_{\delta_M,{\rm syn}}(k,\chi) \right] j_\ell(k\chi), \tag{6.31}$$

with $j_\ell(x)$ the spherical Bessel function, $\tilde{W}(\chi)$ a window function selecting the relevant redshift bin, $S_{\delta_M,{\rm syn}}$ the time-evolution function for cold dark matter in comoving-synchronous gauge, and S_ψ the time-evolution function for the Newtonian potential. Galaxy bias ($b_{\rm G}$) and alignment bias [351][2] ($b_{\rm A}$) are marginalised over, and non-Gaussianities are also modeled as an effective scale-dependent bias, $b_{\rm NG} \propto f_{\rm NL}$. These bias functions, as well as the remaining contributions to the number counts transfer function, are modelled identically to [327]. We show the relative contributions from each of these effects to the total power in Fig 6.1.

[2] Alignment bias is an orientation dependent selection effect on galaxy clustering in redshift space due to alignment of galaxies by large-scale tidal fields. This effect is understood to mimick redshift space distortions and potentially bias the measurement of velocity power spectrum [351].

6.5 Dark energy perturbations and scale-dependent growth

The growth of dark energy density perturbations can be solved from perturbed Einstein equations and can influence different components of the Universe via the metric. The standard FRW metric perturbations in the conformal Newtonian gauge take the form in (2.22). For a perfect fluid that is not interacting with other components (except through the metric), the density δ and velocity $\vec{v}$ perturbation equations can be solved by using the conservation of the stress-energy tensor which satisfy the equations given in Eqs. 2.27 and 2.28 at linear level [35]. It is easy to see for a constant equation of state satisfying $\delta P/\delta\rho - w = 0$, density perturbations decouple from the metric when $w = -1$, since terms including the Hubble parameter vanish.

For a negative equation of state satisfying $w \neq -1$, perturbations grow on scales larger than the sound horizon of the fluid, although are suppressed beyond the Hubble scale due to Hubble drag. On scales smaller than the sound horizon of the fluid, the density fluctuations are smooth and the growth is suppressed. The clustering of dark energy on large scales can be seen from comparing the Fourier mode amplitudes of dark matter fluctuations predicted from the ΛCDM with a model where $w \neq -1$ and from measurements of the growth rate of cosmological structure, commonly defined $f = \mathrm{d}\ln D(k,t)/\mathrm{d}\ln a$ where $D(k,t)$ is the matter transfer function (i.e. the time dependent amplitude of the matter fluctuations with the wavenumber k). As shown in Figure 6.2, dark energy fluid enhances the growth of structure on scales beyond the sound horizon $k \sim \mathscr{H}/c_s$, where $\mathscr{H} = aH$ is the comoving Hubble rate.

It is important to note, however, that when describing density fluctuations on large scales relevant to dark energy clustering, the choice of gauge has a significant effect on the predictions that are not directly observable, such as the matter or dark energy overdensities. (Note that there is no ambiguity, of course, if we are instead calculating observables as we did for number counts in the previous section. This raises the question about the gauge choice when relating the observed matter power spectrum to theory, and has been discussed in the literature in detail (see e.g. [350]). For the widely used comoving-Newtonian and synchronous gauges, while the differences between theory predictions are small for large wavenumbers $k \gg \mathscr{H}$; for scales $k \ll 0.01\mathrm{Mpc}^{-1}$, differences become large and the comoving-Newtonian prediction of the matter power spectrum diverges. Due to both this shortcoming of the Newtonian-gauge and the smooth behaviour of matter power spectrum around $\mathscr{H}$, synchronous gauge is more widely used on large-scales in practice. Furthermore, in the limit where the perturbations are dominated by pressure-free matter, density perturbations in synchronous gauge correspond to the perturbations in the comoving gauge, which are gauge-invariant by definition. Finally,

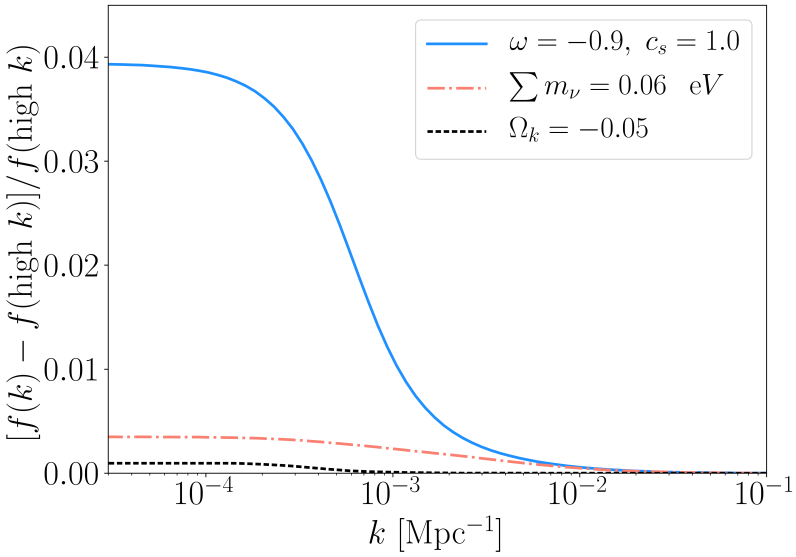

Figure 6.2: Scale dependence of the linear growth rate of matter fluctuations $\delta f(k) := f(k) - f(k \simeq 1)$, defined in the synchronous gauge (see text) at redshift $z = 0.2$, and for DE equation of state $w_0 = -0.9$ and sound speed $c_s = 1.0$, shown in reference to the scale dependence induced by non-zero curvature ($\Omega_k = -0.05$) and massive neutrinos ($\sum m_\nu = 60$meV), for comparison. The clustering of dark energy influences growth on scales larger than the sound horizon of the DE fluid, corresponding to around the Hubble scale for $c_s = 1$ as shown above.

for what follows, we assume that the comoving-Newtonian gauge velocity follows the matter velocity (with no velocity bias) and use CAMB [300] numerical Boltzmann solver to calculate matter and CMB spectra.

6.6 Forecasts

6.6.1 Compensated isocurvature perturbations

We now examine how well future experiments will be able to measure A, assuming an LSST-“gold sample"-like galaxy survey, and kSZ reconstruction from a CMB-S4-like survey. We follow the prescription used in [327] in order to compute galaxy number densities, the kSZ remote dipole field, and the corresponding noise for each tracer.

The galaxy number densities follow from earlier work, e.g. [350, 349, 352, 353], and the kSZ signal from e.g. [248]. We make use of information from each of these tracers individually, as well as the cross-correlations. The Fisher matrix we compute thus has the

Table 6.1: Various parameters, bias functions, and their fiducial values. The biases b_v, b_G, b_A, $f_{\rm evo}$, s, that we refer to throughout are, respectively, the optical depth bias, the galaxy bias, the alignment bias, the evolution bias, and the magnification bias. The fiducial values of bias functions indicated with a † vary with redshift, the modeling of which is described in [327].

Parameter	A	$10^9 A_s$	n_s	Ω_b	Ω_c	h	τ
Fiducial value	0	2.2	0.96	0.0528	0.2647	0.675	0.06
Parameter	$b_v(z)$	$b_{\rm G}(z)$	$b_{\rm A}(z)$	$f_{\rm evo}(z)$	$s(z)$	$b_{\rm bc}(z)$	
Fiducial value	1	†	0	†	†	Eq. 6.28	

form

$$F_{\alpha\beta} = \sum_{\ell=\ell_{\rm min}}^{\ell_{\rm max}} \frac{2\ell+1}{2} {\rm Tr}\left[\left(\partial_\alpha \mathbf{C}_\ell\right) \mathbf{C}_\ell^{-1} \left(\partial_\beta \mathbf{C}_\ell\right) \mathbf{C}_\ell^{-1}\right] + F_{\alpha\beta}^{\rm CMB}\,, \tag{6.32}$$

where we defined $\partial_a := (\partial/\partial a)$ same for a and b which are model parameters we defined. The covariance matrix $\mathbf{C}_\ell$ is given by

$$\mathbf{C}_\ell = \begin{pmatrix} C_\ell^{\rm N,N} & C_\ell^{\rm N,kSZ} \\ C_\ell^{\rm kSZ,N} & C_\ell^{\rm kSZ,kSZ} \end{pmatrix} + N_\ell\,. \tag{6.33}$$

The individual contributions to the covariance matrix are the spectra $C_\ell^{\rm X,Y}$, where $X, Y \in \{{\rm N}, {\rm kSZ}\}$, and are the angular power spectra and cross-spectra of the galaxy number counts and kSZ remote dipole field. The noise computed for each tracer is denoted by N_ℓ. For the galaxy number counts, we assume the dominant source of noise is shot noise from an LSST-like survey. Calibration errors may also exist on large scales that we do not explicitly model [354], although we do explore the dependence of detection prospects on a maximum available ℓ in Fig. 6.4. For the kSZ reconstruction, the noise is the reconstruction noise given by Eq. 6.13, which we assume is uncorrelated with the galaxy shot noise. The CMB contribution to the Fisher matrix, $F_{\alpha\beta}^{\rm CMB}$, is computed using information from the lensed CMB temperature and polarisation power spectra, and is not cross-correlated with the galaxy survey nor remote dipole field. This term acts as an effective prior on standard cosmological parameters only. Lastly, we compute derivatives of the covariance matrices analytically for all cosmological parameters and bias functions, except for the cosmological parameters Ω_b, Ω_c, and h, which we compute numerically. We test for numerical convergence by varying all relevant numerical parameters.

For our fiducial results, we sum over $1 \leq \ell \leq 60$; the vast majority of constraining power on A and $f_{\rm NL}$ comes from $\ell \lesssim 30$. We assume information from a galaxy survey is available in 30 (tophat) redshift bins from $z = 0$ to $z = 3$ (so $\sigma_z \lesssim 0.05$), and a magnitude limit corresponding to the LSST gold sample, $r_{\rm max} = 25.3$. For reconstruction of the remote dipole field, we assume modes up to ℓ of 9000 are available for reconstruction, subject to a 1.0 μK-arcmin noise and 1 arcmin beam for the CMB experiment. We explore the implications of varying this noise, and do not find our constraints change substantially: most of our signal comes from the largest angular scales, where the remote dipole field reconstruction noise is sufficiently low even for a much larger instrument noise.

The main quantity we report is $\sigma_A = \sqrt{F^{-1}_{AA}}$. We marginalise over standard cosmological parameters, as well as different bias functions. The full list of cosmological parameters we marginalise over, as well as the bias functions, are described in Table 6.1 unless stated otherwise[3]. We examine σ_A as a function of different ingredients in the forecast, in order to assess how much additional constraining power is available once new probes are added and theoretical considerations modified. The constraints we find on A for our "fiducial" model described above, as well as for different combinations probes, are shown in Table 6.2. Notably, the remote dipole field improves constraining power over galaxy number densities alone by over an order of magnitude. Fixing standard cosmological parameters and bias functions in addition does not considerably improve constraining power, however we do find a moderate degeneracy of A with the effects of non-Gaussianity, such that additionally marginalising over $f_{\rm NL}$ worsens constraining power by a factor of order 2. There is also a minor degeneracy with general relativistic and lightcone projection effects: although less important, we find a parameter bias of order 1.5σ in A when these effects (excluding lensing) are not modelled, suggesting such effects should be properly accounted for when studying isocurvature perturbations using large-scale survey data.

In order to check how robust the uncertainties we report are to the fiducial values we choose, as well as to draw a connection to a specific model, we re-evaluate our results for a value of $A = 16$ and $f_{\rm NL} = 6$, corresponding to particular curvaton decay models. Because the fiducial value of A is no longer zero, the bias function $b_{\rm bc}(z)$ should be marginalised over. Changes in this bias function are highly degenerate with changes in A, so we must place a prior on the function in order to obtain meaningful results. Enforcing a condition

[3]The evolution bias is due to the fact that new galaxies form, hence the galaxy number density does not simply scale like a^{-3}, see e.g., [355–357]. The magnification bias is due to the change in the number of relative sources detected at a given redshift at a fixed magnitude due to cosmic magnification, the systematic magnification of background sources near foreground matter over-densities. Differently from the standard cosmic distortion effect, cosmic magnification increases the flux received from distant sources and stretches the solid angle, diluting the surface density you source imagines on the sky, see e.g., [356].

Table 6.2: The fiducial uncertainty in A from the model described in the text is bold. Lines above this exclude the cross- and auto-correlation with the kSZ remote dipole field, and additionally exclude the high-ℓ CMB prior on standard cosmological parameters. Lines below fix all cosmological parameters and bias functions, or additionally marginalise over $f_{\rm NL}$ with a fiducial value of zero.

Forecast ingredients	σ_A
N only	3.8
N + CMB	3.2
N + CMB + kSZ	0.25
N + CMB + kSZ + fixed cosmology	0.23
N + CMB + kSZ + variable $f_{\rm NL}$	0.49

on the sign of $b_{\rm bc}$, or adding a "100%" prior $\sigma(b_{\rm bc}) = b_{\rm bc}$ on the function in each redshift bin, results in an uncertainty in A of $\sigma_A = 5.8$. The constraint scales down to $\sigma_A = 0.89$ for a 10% prior, and $\sigma_A = 0.53$ for a 1% prior, nearly recovering the results reported in Table 6.2. As primordial non-Gaussianity may be sourced through other additional mechanisms, we have marginalised over $f_{\rm NL}$ and A separately. The degeneracy between these two parameters can be explicitly seen in Fig 6.3 as a function of the prior on $b_{\rm bc}$. Even with the weakest prior, we see that a definitive detection of this scenario can be made with future datasets.

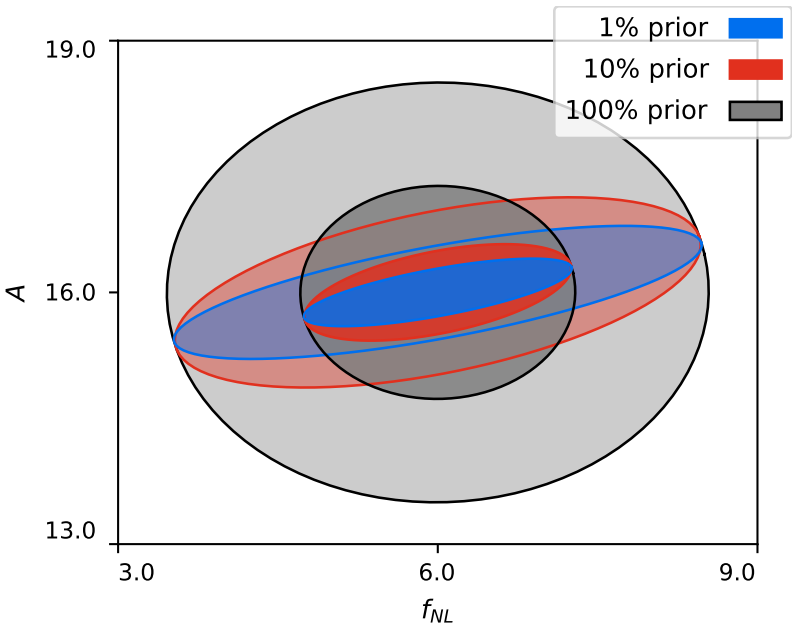

Figure 6.3: Parameter covariance between A and $f_{\rm NL}$, given several choices for a prior on $b_{\rm bc}$.

We lastly show how the uncertainty σ_A varies due to experimental parameters that have not been marginalised over. In particular, we vary: the ℓ summed over in Eq. 8.6, the number and width of the redshift bins we consider (which stand in as an effective redshift uncertainty), the galaxy survey magnitude limit, and CMB experiment noise. These results are summarised in Figure 6.4. The results generally do not change significantly as these are varied, with two exceptions. First, improving the magnitude limit from the LSST gold sample ($r = 25.3$) to a less conservative cut ($r = 27.3$) can improve things by another possible factor of order 2. Second, without a reliable survey or remote dipole field reconstruction on large angular scales, low-ℓ multipoles may not be accessible, degrading our constraint by a similar factor.

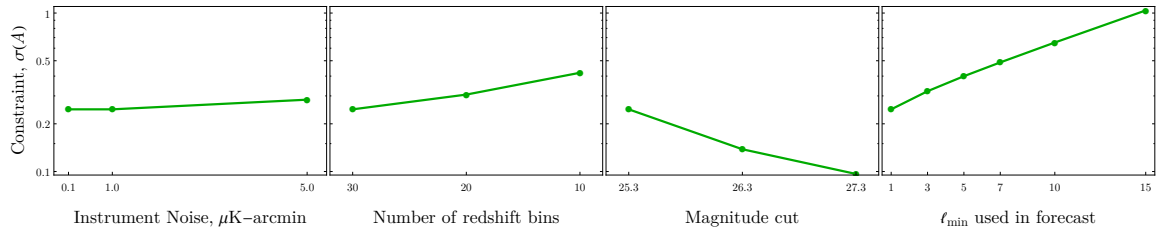

Figure 6.4: The impact of changing various parameters relevant for, or related to, experiments for the "fiducial" forecast we perform.

6.6.2 Dark Energy Perturbations

Similar to above, the accuracy with which future experiments will be able to detect the dark energy perturbations can be assessed with a Fisher matrix analysis. We again assume an LSST-'gold sample"-like galaxy survey and a CMB-S4-like survey for the kSZ reconstruction. The galaxy-survey (shot) noise depends on the number density function $n(z)$ which we define as

$$n(z) = \frac{n_{\rm tot}}{2z_0}\left(\frac{z}{z_{\rm piv}}\right)^{\alpha} \exp\left[\left(\frac{z}{z_{\rm piv}}\right)^{\beta}\right] \tag{6.34}$$

and we take $\{z_{\rm piv}, \alpha, \beta, n_{\rm tot}[\text{arcmin}^{-2}]\}$ to be $\{0.3, 2, 1, 40\}$ to match LSST survey forecasts. The photo-z errors predicted for the LSST experiment is $\sigma_z = 0.03(1+z)$. For the CMB-S4 experiment the forecasted beam size is 1.4-arcmin and the total CMB power-spectrum $C_\ell^{\rm tot}$ where ℓ's are spherical harmonic multipoles, gets contributions most significantly from weak-gravitational lensing, kSZ effect (both from reionization and late times) and the experimental

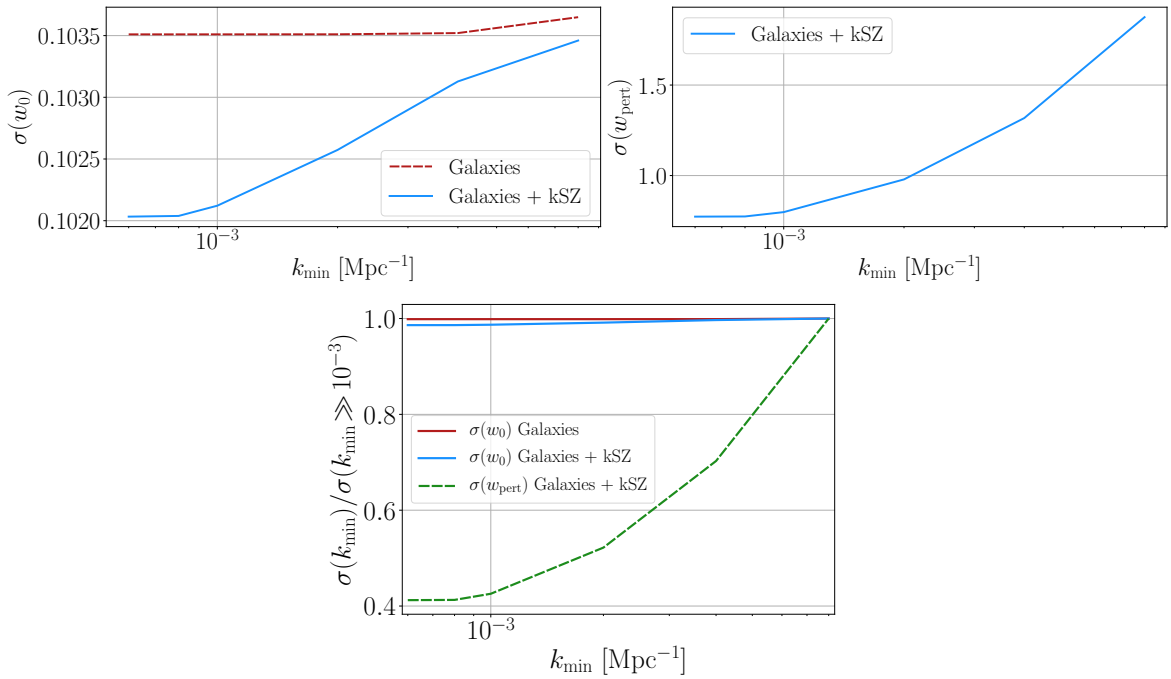

Figure 6.5: Forecasts for the anticipated experimental specifications of the CMB-S4 and LSST surveys. *(Upper left)* Constraints on the dark energy equation of state w_0 from combination of CMB with galaxies and kSZ reconstructed velocities discussed in the text. The galaxy observables are shown to dominate the constraints on, w_0 while improvements afforded by the kSZ reconstruction is marginal (on the percent level). *(Upper right)* Constraints on the dark energy perturbation parameter $w_{\rm pert}$ introduced in the text quantifying the influence of dark energy clustering on matter fluctuations and structure growth on large scales. The benefit of kSZ reconstruction is demonstrated with the increase in the detection significance on vary large scales. *Bottom plot* contains the same information as the upper two plots, shown together for better comparison.

noise that satisfy

$$N_\ell = \Delta_T^2 \exp\left[\frac{\ell(\ell+1)\theta^2_{\rm FWHM}}{8\ln 2}\right], \tag{6.35}$$

where $\{\Delta_T, \theta_{\rm FWHM}\}$ is $\{1.0\mu$K-arcmin$, 1.5$-arcmin$\}$ for CMB-S4.

Information contained in the two-point functions of the halo and mass-density fields (which is approximated to be Gaussian) can be utilised given the signal and noise covariance matrices, that can be written as

$$\boldsymbol{S} = \begin{pmatrix} P_{vv} & P_{vh} \\ P_{vh} & P_{hh} \end{pmatrix} \quad \text{and} \quad \boldsymbol{N} = \begin{pmatrix} N^{\rm rec}_{vv} & 0 \\ 0 & N_{hh} \end{pmatrix}, \tag{6.36}$$

where $N_{vv}^{\rm rec}$ is the velocity reconstruction noise from the kSZ measurement, $N_{hh} = 1/\bar{n}_h$ is the shot-noise from the galaxy-survey, and the total covariance is defined as $\boldsymbol{C}(k,z) = \boldsymbol{S}(k,z) + \boldsymbol{N}(k,z)$. The Fisher matrix for some redshift bin z_i is

$$F_{ab} = \frac{V}{2}\int_{\vec{k}} \mathrm{Tr}\left[\partial_a \boldsymbol{C}(\vec{k})\boldsymbol{C}(\vec{k})^{-1}\partial_b \boldsymbol{C}(\vec{k})\boldsymbol{C}(\vec{k})^{-1}\right] + F_{ab}^{\rm CMB}\,, \tag{6.37}$$

where V is the volume of the large-scale structure survey and sets the longest k-mode accessible to the reconstruction, i.e. $k_{\rm min} = \pi/V^{1/3}$ and $F_{\alpha\beta}^{\rm CMB}$ is the contribution of the CMB temperature and polarisation (lensed and including the contribution of kSZ on the temperature spectra variance) to the Fisher matrix. The integral $\int_{\vec{k}}$ is over the phase space accessible to the observation.

Table 6.3: Cosmology model parameters and biases b_v, b_G, b_1, which are respectively, the optical depth bias, the galaxy bias and the non-linear galaxy bias. We take the galaxy bias $b_g(z)$ as a function of redshift, and set it equal to $\dagger = \{1.0588, 1.3718, 1.7882, 2.2232, 2.7408\}$, for the redshift bins discussed in the text, respectively. We set the fiducial value of all the parameters θ_{XY} discussed in the text to zero.

Parameter	$10^9 A_s$	n_s	$\Omega_b h^2$	$\Omega_c h^2$	h	τ
Fiducial value	2.2	0.9645	0.02225	0.1198	0.673	0.06
Parameter	$\theta_{\{XY\}}$	w_0	c_s	$b_v(z)$	$b_{\rm G}(z)$	$b_1(z)$
Fiducial value	0	-1.0	1.0	1	$\dagger$	0

As we are interested in isolating the constraining power of observations on the dark energy perturbations, we add a number of arbitrary parameters to our model to remove the constraining power of the CMB, the density field g, and the reconstructed remote radial velocity field v, on w_0. These observables are otherwise sensitive to the background (scale-invariant) cosmology. We add $\theta_{XY}\mathrm{d}\tilde{P}_{XY}/\mathrm{d}w_0$ to the derivatives of the observables, $\boldsymbol{C}_{,a}$ for $\{XY\} = \{gg, gv, vv\}$ as well as $\theta_{XY}\mathrm{d}C_\ell^{XY}/\mathrm{d}w_0$ for $\{XY\} = \{TT, TE, EE\}$ to the CMB where $\tilde{P}_{XY}$ is the theory prediction for the galaxy and velocity spectra in the absence of dark energy clustering. We define the residual dark energy equation of state parameter as $w_{\rm pert}$ which quantifies the influence of dark energy perturbations on the cosmological observables.

The model parameters and the corresponding fiducial values are described in Table 6.3. Note we consider a different set of bias parameters compared to Table 6.1 as we are considering large scale density fluctuations as signal, not the number counts. We use survey

specifications of *Planck* survey on large scales $\ell > 50$, and CMB-S4 otherwise, including lensing and the kSZ effect which add to the CMB noise on small scales. We use galaxy number counts from LSST 'gold-sample'-like survey and reconstructed velocities from cross-correlating LSST with CMB-S4. After isolating constraints on dark energy perturbations from the Fisher matrix like we described above, we find the error on the dark energy equation of state as $\sigma(w_{\rm pert}) \simeq 0.75$ for the synchronous gauge predictions with fiducial values of $\{w_0, c_s\}$ set equal to $\{-1.0, 1.0\}$, using CMB, galaxy density and kSZ reconstructed velocity fields and taking into account the effect of photo-z errors and excluding redshift space distortions (RSDs) from the analysis.[4] We also find the error on $w_{\rm pert}$ to be largely insensitive to the fiducial value of w_0 around -1. For fiducial cosmologies with $w_0 \neq -1$ we also evaluate the detection significance of CMB-S4 and LSST surveys of the dark energy speed of sound c_s, and find $c_s/\sigma_{c_s} < 1$ for allowed values of w_0 inside the range $0 \leq c_s \leq 1$, supporting our statement from earlier regarding the difficulty of measuring c_s directly.

Note, of course, that these measurements are impacted by the photo-z errors and the RSDs. The photo-z errors can reduce the constraining power on galaxy bias parameters (b_G and b_1) up to $\sim$50 percent in a redshift-dependent way, as well as leading to similarly worse constraints on H_0 and w_0. When taken into account and can be modelled accurately, RSDs can contribute to breaking degeneracies between H_0 and w_0, reducing the errors on these parameters up to $\sim$30 percent. Note that when isolating the constraining power of the scale-dependent growth in the Fisher matrix, we assume the added derivatives are impacted by the photo-z errors in an identical way as the observables. We exclude RSDs from our analysis and leave a more detailed consideration to an upcoming work.

In Figure 6.5 we demonstrate the constraining power of sample-variance cancellation on large scales through using kSZ reconstructed velocity fields. We note that while the dark energy equation of state parameter w_0 is well constrained by the galaxy power spectrum with marginal (percent level) improvements from kSZ reconstruction for CMB-S4 and LSST experiments, the constraining power of these experiments on the isolated effect of dark energy perturbations (captured with the parameter $w_{\rm pert}$) see significant improvement on large scales from kSZ constraints on the growth of structure. We note that measurements of galaxies alone fail to detect dark energy perturbations once the constraining power of the galaxy power spectrum is removed from the Fisher matrix as we discussed, while the effect of RSDs, once taken into account, can potentially be used to constrain $w_{\rm pert}$.[5]

[4] RSDs appear when relating the line-of-sight position $\vec{x}$ in real-space to the redshift space position $\vec{s}$ due to the velocity dependence of the latter (i.e. $\vec{s} = \vec{x} + \vec{v} \cdot \hat{\mathbf{n}}/\mathscr{H}$).

[5] We find, however, that even in the case of perfect RSD reconstruction, galaxy surveys still provide over an order of magnitude worse precision than that afforded from the kSZ measurements.

We evaluate the detection significance of the dark energy perturbations for various different experimental specifications in Figure 6.6. We find modest improvements from increasing the CMB survey quality, i.e. its rms noise level, parametrized by Δ_T, and the beam size suggesting the near future experiments will be more dominantly shot-noise limited, while removing the effects of weak gravitational lensing as well as the kSZ from the CMB temperature variance and significant improvements to CMB survey quality can potentially improve the detection significance of dark energy perturbations.

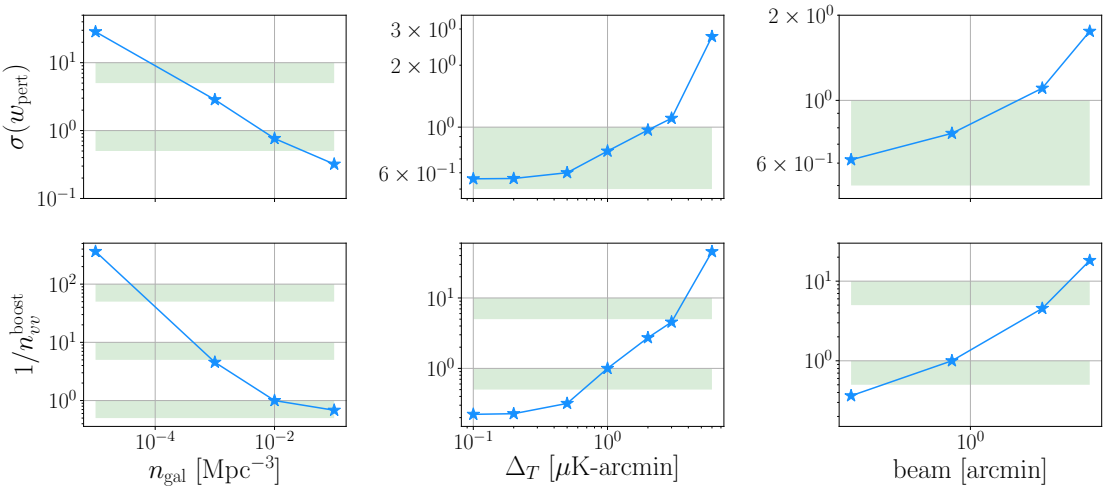

Figure 6.6: Constraints on the dark energy perturbations parameter $w_{\rm pert}$, defined in the text, for a variety of experimental specifications. From left to right, columns correspond to changing the galaxy density of the galaxy survey $n_{\rm gal}$, the CMB noise amplitude Δ_T and the CMB beam size. The upper rows show the error on $w_{\rm pert}$ while lower rows correspond to the change in the reconstructed noise on the velocity fields with the appropriate change in the experimental specifications, normalised to the reconstruction noise for an experiment with specifications matching CMB-S4 and LSST. The improvement on detection significance depends more significantly on the galaxy density, indicating the observations are shot noise dominated.

6.7 Discussion

6.7.1 Compensated isocurvature perturbations

In the above sections, we have shown that by measuring the scale-dependent galaxy bias with the sample variance cancellation technique using kSZ tomography from upcoming CMB experiments and galaxy-surveys, constraining the correlated CIP amplitude at order one at high significance will be possible in the near future. We also considered a curvaton model of

inflation and demonstrated that our method will be able to constrain the CIP amplitude and the local non-Gaussianity predicted by this model at high significance.

As our understanding of the fundamental characteristics of the Universe advances, we might find it generally useful to know whether baryon and CDM fluctuations trace the total matter, or whether CIPs produced at early times correspond to a significant source of fluctuations in the Universe. From a phenomenological perspective, better constraints on the CIPs may rule out generic models of many field inflation, for example, or allow for less ambiguous measurements of early Universe signatures, such as primordial non-Gaussianity which may be degenerate with the CIPs. Constraints from the CMB measurements currently allow for CIPs to be up to a few orders of magnitude larger than the adiabatic fluctuations [337], while forecasts that use the upcoming CMB and galaxy surveys alone suggest it will still be hard to rule out scenarios where CIPs dominate over adiabatic fluctuations, or to distinguish between the different CIP scenarios discussed above, for example, with high significance. With an order of magnitude improvement on CIP constraints, here, we have been able to show that these issues may be resolved by measuring the galaxy-bias through sample-variance cancellation using the reconstructed remote dipole field from kSZ tomography.

In addition to the kSZ effect considered in this Chapter, one can also consider cross-correlating with other tracers of large-scale structure such as the remote quadrupole field from measurements of the polarized Sunyaev Zel'dovich effect, e.g. [358, 260, 270, 248, 271], and the transverse velocity fields from the moving lens effect, e.g. [227, 15, 275]. Including these effects in our forecasts, we do not see a significant improvement upon the constraints presented in this work, although we note that using these effects without kSZ can still considerably improve upon past constraints as well as potentially providing a good consistency test. We leave considering additional probes of large-scale structure, such as galaxy-galaxy lensing, to future work.

Our study focused on isocurvature perturbations modes that are correlated with the adiabatic fluctuations, as predicted by the curvaton models we consider. In principle, CIPs can be partially correlated (or uncorrelated) with the adiabatic perturbations. In relation to the galaxy-bias studied here, uncorrelated CIPs result in a halo over-density that is not fully correlated with matter over-density, inducing a so-called 'stochastic' halo-bias on large scales [359]. The stochastic halo-bias can arise in many field models of inflation, for example, where the small-scale matter power may get redistributed in the presence of an additional field that do not contribute to the curvature fluctuations, and is not correlated with the gravitational potential. In these cases, the bias inferred from the cross-correlations of the halo over-density and matter over-density will differ from the bias inferred from halo

auto-correlations, where the latter will see a boost compared to the former, which will be unaffected from uncorrelated fluctuations. The sample-variance cancellation method we use with the kSZ tomography will fail to detect the contribution from a stochastic contribution, as it utilises the cross-correlations of the remote dipole field (an unbiased tracer of the matter over-density) and the galaxy over-density, in order to constrain the scale-dependent galaxy-bias. Moreover, any uncorrelated bias contributes as noise to this measurement, further worsening the significance of our constraints. It is thus hard to imagine taking advantage of the sample-variance cancellation in the case of uncorrelated CIPs. Nevertheless, depending on the scale dependence of the uncorrelated modes, it may still be possible to get competitive constraints on the CIP amplitude from measurement of the scale-dependent galaxy-bias using galaxy number-counts only, for example, compared to using CMB and BAO reconstruction alone, as can be seen from Table 6.2. We leave a more detailed study of the stochastic bias to future work.

Lastly, we note that the current competitive studies of the scale-dependent galaxy-bias such as the one afforded by photometric quasar searches report stringent constraints on local non-Gaussianity, e.g. $-49 < f_{\rm NL} < 31$ [360], which can be translated into similar constraints on the CIP amplitude, A, by comparing the contribution to the transfer function of the intrinsic galaxy perturbations from local non-Gaussianity and the CIPs. We find that these contributions are similar at $\sim \mathcal{O}(1)$, suggesting that photometric quasar studies can already improve on current CMB constraints significantly. We leave a more careful analysis to an upcoming work.

Advances in the precision of small-scale cosmology measurements from the near-future CMB and galaxy surveys will provide new opportunities to study the fundamental nature of the Universe on largest scales. We have used kSZ reconstruction and sample-variance cancellation in order to constrain correlated compensated isocurvature fluctuations on large scales and showed that our method will improve the detection significance by over an order of magnitude.

6.7.2 Dark energy perturbations

We have evaluated the prospects of detecting dark energy perturbations from the growth of large scale structure, using galaxy measurements and the method of kSZ reconstruction which allow over an order of magnitude increase in detection significance through sample variance cancellation. We defined a simple technique to isolate the Fisher information on the

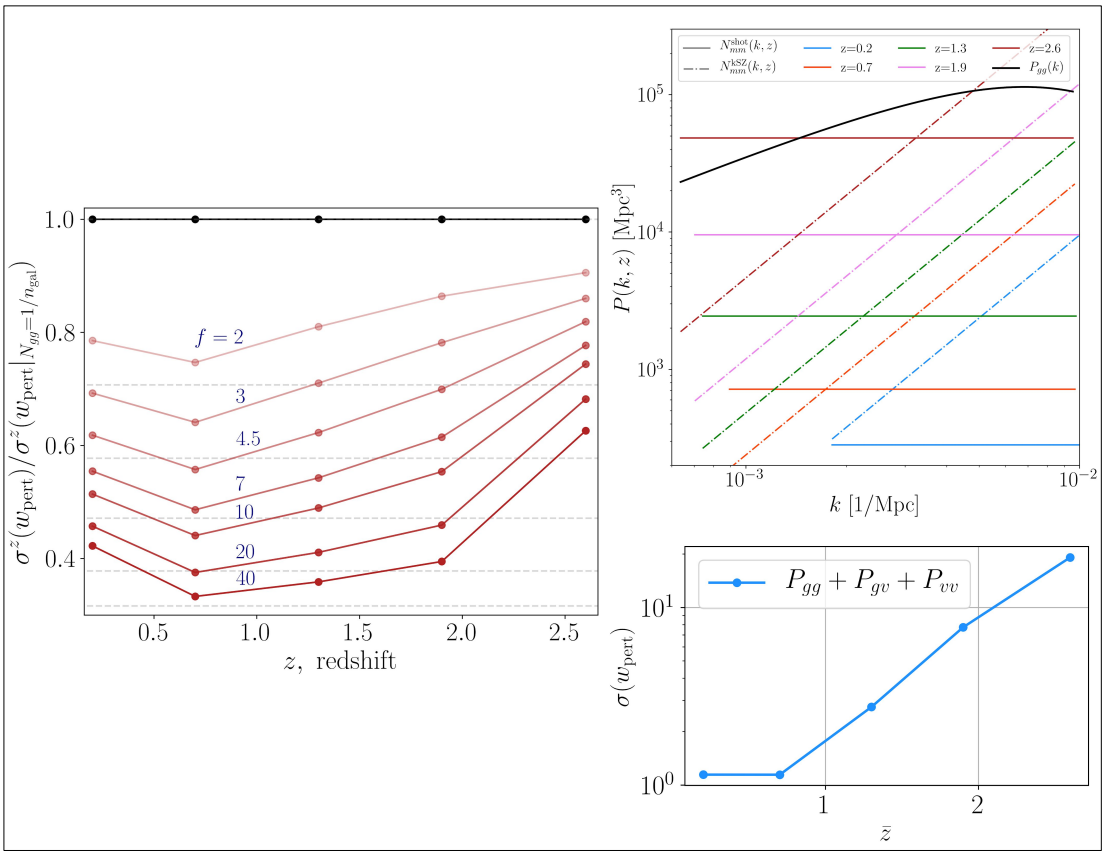

Figure 6.7: Plots describe details of the forecast we perform in this section for the dark energy perturbations parameter $w_{\rm pert}$. *Bottom right* plot shows the error on $w_{\rm pert}$ from each redshift bin. It is evident from this plot that the SNR on the perk energy perturbations will peak at nearest redshift bins, where dark energy dominates. *Upper right* plot compares the forecasted noise from the upcoming LSST galaxy survey with the reconstruction noise on the density perturbations afforded by the kSZ measurement. Plot shows that for all redshift bins except the nearest bin shot noise dominates over the kSZ reconstruction noise. Shot noise is shown to be the dominant limiting factor of the constraints on $w_{\rm pert}$. *Left* plot relate to the discussion in Section 6.7.2 on improving the constraints on $w_{\rm pert}$ by mass binning the galaxy catalog. We show the fractional improvement of the error on $w_{\rm pert}$ parameter for different redshift and different mass-binning, varying from 2 to 40. We discuss the anticipated measurement precision on the halo masses with upcoming experiments in Section 6.7.2.

influence of dark energy perturbations and clustering on large scales from the the background cosmology.

On the residual $w_{\rm pert}$ parameter we defined in Section 6.6, we find the error $\sigma(w_{\rm pert}) \simeq 0.75$ for experimental specifications matching the upcoming CMB-S4 and LSST surveys, suggesting that a non-ambiguous detection of dark energy perturbations with small $\delta w_0 := 1 + w_0$ and small $w_{\rm pert}$ may be difficult. Note, however, that in our analysis we assumed galaxy shot-noise on all scales. Sample variance cancellation technique we employ, constraining the

relation between the density and the velocity fields on large-scales, is impacted from this shot noise. In fact for the upcoming high-fidelity CMB experiments like CMB-S4, we find the errors on $w_{\rm pert}$ are dominated by the shot noise on all redshift bins. It follows that reducing the shot noise on largest scales could increase the detection significance of our cross-correlation measurement. An important understanding for reducing galaxy shot-noise on large scales was achieved in e.g. [361–363], where the authors show by weighting central halo galaxies by halo mass, the resulting shot noise can be reduced dramatically (orders of magnitude) for the upcoming surveys. This is understood to be due to the local mass and momentum conservation of halo on small scales, subject to non-linear evolution, which dictates a k^4 behaviour as $k \to 0$, hence different than the largely assumed k^0 shot-noise [361]. Note that procedure we described here is equivalent to mass-binning a halo catalogue. We estimate dividing the galaxy catalogues to around 20 mass bins, which correspond to a logarithmic scatter in mass around $\sigma_M/M \sim 0.5$, will be likely with the anticipated mass-accuracy of the upcoming experiments [293, 292]. Taking into account the fractional reduction estimates for 20 mass bins and anticipated LSST galaxy density, we find errors on the dark energy perturbations will reach $\sigma(w_{\rm pert}) \sim 0.4$. Note a further factor $1/\sqrt{2}$ reduction is anticipated using the mass-scatter matrix defined in [362]. We demonstrate these results in Figure 6.7.

Despite the fact that dark energy is the dominant contributor to the energy density in our Universe, we know next to nothing about its microphysics. The revolutionary advancements in our cosmological understanding afforded mainly by the CMB experiments in the past decade strongly sharpened our knowledge about the background dynamics of dark energy. Current data is in excellent agreement with $w_0 = -1$. Even small deviations from $w_0 = -1$, however, would allow an extremely rich phenomenology of new physics, which can potentially be probed by measuring dark energy perturbations. Constraining dark energy perturbations still evade our observational tools. In particular the forecasted sensitivity of the upcoming experiments to the dark energy speed of sound c_s suggest the necessity of searching for alternative probes that may detect the microphysics of dark energy in a non-ambitious way. The method we described in this Chapter serves to contribute to this search and provide guidance regarding the direction forward with the upcoming ambitious cosmology experiments. Our findings suggest detection of the perturbation characteristics of dark energy will be difficult and potentially require combining variety of methods and observables.

Finally, unlike the case of non-Gaussianity, for example, where multi-field inflationary models can predict large values of bispectra amplitudes; it is harder to imagine dark energy clustering under GR with small deviations from $w = -1$ could produce large perturbations on large scales due to smallness of initial fluctuations and the $1/(1-3w_0)$ suppression

factor, which will be larger compared to density fluctuations. Discussing dark energy models that can potentially produce more significant clustering is upcoming work, and is beyond the scope of this thesis. Note that the scale dependence of growth rate is also sensitive to modifications to GR. Various classes of Horndesky models, for example, predict $f(k)$ different than the ΛCDM prediction [364]. I will explore the sensitivity of the upcoming experiments to these scenarios in an upcoming work.

Chapter 7

Delensing for parameter inference

I introduced weak gravitational lensing of the CMB in Sections 2.7.1 and 4.3. In particular in Section 4.3 I described the effects on the CMB temperature and polarisation spectra, following on the lines of [13]. In this chapter I begin by re-iterating some of the pedagogical statements from earlier, before focusing on the mitigation of the gravitational lensing from the CMB: a procedure called *delensing*. Using the quadratic lensing reconstruction estimator to evaluate the deflection field reconstruction noise; I introduce an all-orders delensed auto- and cross-spectra estimators for T, E, B fields, after building the scientific case for delensing. I then follow with a description of the iterative delensing procedure before concluding with a discussion on my upcoming work on the subject.

This Chapter includes material from my ongoing work with Daniel Green, Joel Meyers and Alex van Engelen. The goal of the related project is to extend the work in [307] to full-sky and provide a publicly available, modular, easy-to-use, fast and stable delensing software that calculates the delensed spectra to all-orders in lensing potential and on full-sky, as well as all lensing-reconstruction noise covariances on full-sky with the quadratic estimator. The novel calculations coded for the software include the delensed spectra estimates discussed below in Section 7.3 and lensing-reconstruction estimator covariances described in Section 7.3 and introduced in detail in Appendix A.2.

I coded the mentioned software as an extension to the `CLASS` Boltzmann solver and performed the relevant full-sky calculations in this Chapter and in Appendix A.2. This upcoming public software is imagined to be a part of the lensing and delensing forecasting pipelines that are being built for upcoming CMB experiments including Simons Observatory and CMB-S4. The code will be complemented with a forecasting paper following up

on [307], which will showcase the software and contribute to the science case of delensing CMB beyond the B-modes.

7.1 Introduction

As I discussed in the earlier chapters, weak gravitational lensing of the CMB can be measured from deflections of the observed temperature and polarisation anisotropies on small scales. Upcoming surveys such as the Simons Observatory and CMB-S4 will achieve an unprecedented accuracy at detecting the effect of gravitational lensing and will significantly improve the current measurements of the distribution of matter between our telescopes and the last-scattering surface. The distribution of matter in the Universe is a central cosmological observable containing significant information about the characteristics of the primordial Universe and the growth of structure.

The lensing potential, defined in Eq. (4.8), is sensitive to cosmological parameters and is a valuable signal. The effect of lensing on the CMB, however, is often regarded as a nuisance as it worsens the measurement accuracy of the baryon acoustic oscillations (BAOs) peak locations, for example, by having a smearing effect (discussed in Section 4.3) on the correlation structure. As discussed earlier, lensing also converts E-modes to B-modes adding significant confusion on the primordial gravitational-wave searches.

Removing the effect of lensing from the CMB maps and/or the power spectra (delensing) aims to remap the lensed CMB photons onto their undeflected positions in the sky by means of reconstructing a deflection estimate $\vec{\alpha}^{\rm obs}(\hat{\mathbf{n}})$ and using this to delens. Delensing has been studied most extensively for improving the prospects of primordial gravity-wave detection through the measurement of B-modes [e.g. 365–369], while the broader use of delensing on the E-mode polarisation as well as the temperature maps has been demonstrated in the recent literature [e.g. 307, 370–373, 310].

At leading order in perturbation theory, delensing can be written simply as,

$$T^{\rm d}(\hat{\mathbf{n}}) = T^{\rm obs}(\hat{\mathbf{n}} - \vec{\alpha}(\hat{\mathbf{n}})) \simeq T^{\rm obs}(\hat{\mathbf{n}}) - \vec{\alpha}^{\rm obs}(\hat{\mathbf{n}}) \cdot \boldsymbol{\nabla} T^{\rm obs}(\hat{\mathbf{n}}) \,, \tag{7.1}$$

where $T^{\rm obs}$ and $\vec{\alpha}^{\rm obs}$ are the observed temperature and the deflection maps respectively and $T^{\rm d}$ is the delensed CMB temperature map. This perturbative approximation, however, is less accurate on small scales where lensing can dominate over the primary CMB. Motivated with improving the delensing accuracy, I introduce in Section 7.3.1 a non-perturbative delensing

method for the CMB temperature and polarization. First I make the science case for delensing beyond the B-modes.

7.2 Case for delensing

A main goal of delensing is the mitigation of the effect of lensing on the CMB spectra. One of the main applications, for example, is reducing the variance of the B-modes. The primordial B-mode polarisation is a direct probe of the inflationary gravitational wave signal, and is an important scientific target for many upcoming cosmological surveys. Delensing is particularly necessary for the small values of tensor-to-scalar ratio which amount to lower gravitational wave signal, potentially dominated by lensing-generated power on large-scales. The scientific case for delensing the B-modes has been made extensively in the literature [e.g. 365–369]. Here, I discuss potential benefits of delensing maps of E-mode polarisation and temperature.

7.2.1 CMB acoustic peak locations

The radiation content of the Universe has a significant effect on the CMB at small scales and has a dominant influence on the expansion rate of the Universe and on the fluctuations in the gravitational potential at early times. This makes CMB a very powerful tool to probe the expansion history as well as the physics of light particles beyond the Standard Model (SM).

Accurate measurements of the CMB peak locations, in particular, are essential for determining a multitude of cosmological parameters including the Hubble constant H_0, as well as the effective number of weakly-coupled light degrees of freedom, $N_{\rm eff}$. As was discussed in Section 4.3, gravitational lensing smooths out the CMB peaks by convolving the unlensed CMB spectra with the lensing potential, hence correlating otherwise uncorrelated modes in temperature and E-mode polarisation. This decreases (increases) the power at the peaks (troughs), reducing the measurement accuracy of the peak locations. Lensing can also shift the peak locations if the maxima or minima are asymmetric around their extremum. For the upcoming surveys, delensing can hence potentially allow significant improvements in sensitivity to these parameters by mitigating these effects.

In particular, delensing has been shown to be very important for the accurate $N_{\rm eff}$ measurements expected in the near future [307]. It is well understood that the amplitude and the phase of the acoustic oscillations are modulated by light relics [374, 375] through their gravitational influence. The deviations from the SM prediction of $N_{\rm eff} = 3.046$ [376], often

parametrised with $\Delta N_{\rm eff}$, amount to a quintessential probe of light particle content of the Universe. A non-zero $\Delta N_{\rm eff}$ can be produced in various ways (see e.g. [205], for a review). Combined with other probes of beyond SM physics, measurements of $\Delta N_{\rm eff}$ can provide strong constrains on different particle physics models, as well as providing strong constraints on the reheating temperature and physics of BBN.

Furthermore, the CMB peak locations are most directly affected by the angular size of the sound horizon at recombination. The angular size is defined as $\theta_s := r_{\rm rec}/D_A^\star$, where $z_{\rm rec}$ is the redshift z at recombination, $r_{\rm rec} := r_s(z_{\rm rec})$ for $r_s(z)$, the comoving size of the sound horizon, and D_A is the comoving angular diameter distance to the recombination. The angular size is constrained by the locations of the peaks (not their amplitude) and it is one of the most robustly measured parameters from the CMB surveys. Since lensing smooths the peak locations, delensing has been shown to be most beneficial for the precise determination of θ_s [e.g. 307].

The angular size θ_s measured from the CMB can be used with the calibrated CMB peak morphology at recombination in order to infer the comoving angular diameter distance to recombination, D_A. The sound horizon at recombination is determined by the particle content of the Universe which is also inferred from data. This inferred angular diameter distance is the redshift integral of the Hubble time, i.e.

$$D_A = \int_0^z {\rm d}z'/H(z')\,, \tag{7.2}$$

which, along with the inferred matter density, can be used to determine the Hubble constant today, H_0. As it heavily depends on the angular size, θ_s (and hence the BAO peak locations), delensing also provides an improved measurement of H_0.

7.2.2 CMB damping Tail

Measurements of the damping tail probe a large dynamic range in the CMB and improve constraints on the primordial helium fraction, Y_p, and the effective number of relativistic species, $N_{\rm eff}$, for example. In particular, deviations from the standard ΛCDM paradigm with additional degrees of freedom can significantly impact the CMB damping tail. For example, inflationary models with multiple degrees of freedom can produce isocurvature (entropy) fluctuations [e.g. 124, 125, 364, 178, 377, 378], where the relative mixture of different species become independent degrees of freedom, affecting the otherwise adiabatic CMB perturbations. Similar effects can also be sourced by cosmic defects [379, 380], which can produce observable and distinct fluctuations.

In addition to $N_{\rm eff}$ discussed above, another valuable probe of the light relic content of the Universe is the primordial helium fraction Y_p. The helium fraction is sensitive to the radiation density and the neutrino distribution during BBN. Importantly, effects of $N_{\rm eff}$ and Y_p on the damping tail are largely degenerate: increasing either leads to an increased damping of the power spectrum at fixed θ_s.

The relation between $N_{\rm eff}$ and the damping tail can be understood from

$$\frac{\theta_D}{\theta_s} \propto H_\star^{1/2} \leftrightarrow N_{\rm eff}\,, \tag{7.3}$$

where θ_D is the damping scale, θ_s is the angular size of the sound horizon at recombination and $H_\star$ is the Hubble parameter at the time or recombination. Because θ_s is very well measured, changes in the expansion rate history, which was dominated by the density in radiation at early times; directly affects the damping tail of the power-spectrum. This suggests a change in $H_\star$ would be compensated by a change in the damping scale of the CMB. Since $H_\star$ is controlled by the radiation content, measurement of the damping tail largely drive the constraints on $N_{\rm eff}$.

Furthermore, the helium abundance has a similar effect on the damping scale. Since helium recombines earlier than hydrogen, changing the amount of helium changes the abundance of available electrons between the time of helium and hydrogen recombinations, in turn changing the diffusion length via the relation,

$$Y_p \propto \frac{1}{n_e(t_\star)} \propto \lambda_c = \frac{1}{n_e \sigma_T a}\,. \tag{7.4}$$

It follows that more helium (at fixed baryon density) leads to fewer free electrons during hydrogen recombination, leading to larger diffusion length for photons and less power in the CMB damping tail.

This suggests that the effect of $N_{\rm eff}$ on the peak locations can be isolated by marginalising over Y_p, and that delensing the peak locations could allow for breaking the degeneracy between the $N_{\rm eff}$ and Y_p, improving their measurement accuracies.

7.2.3 Lensing potential reconstruction

While CMB distortions due to weak gravitational lensing obscure information regarding the early Universe as discussed above, the lensing field itself carries information about the distribution of the matter in the Universe. The distribution of matter in turn contains

information about the primordial fluctuations and their evolution in time, and is sensitive to the properties of neutrinos and dark energy. Hence reconstructing the map of the lensing potential from measurements of CMB, for example, is a major goal of modern cosmology. The relevant scientific program also involves calculating its power-spectrum and using its cross-correlations with the other large-scale structure observables, such as galaxy distributions, for parameter inference.

The power spectrum of the lensing map is a powerful probe of the growth of structure on large scales and high redshifts, and is very sensitive to parameters such as the total mass of neutrinos, $\sum m_\nu$. Delensing leads to improved reconstruction-noise on the lensing map and facilitates a better measurement of lensing, leading to better measurements of parameters that affect the lensing power spectrum.

Furthermore, the high-fidelity lensing maps that will be available from the upcoming CMB surveys will be highly correlated with the galaxy clustering data, which will be observed with the upcoming surveys of large-scale structure. Since the related cross-correlation coefficient can be as large as $\sim 95\%$, it will be possible to use the cross-correlations between the lensing field and the large-scale structure to break various degeneracies and improve cosmological parameter constraints e.g. [215]. For these purposes, it be possible to utilise sample variance cancellation techniques to determine cosmological parameters [313]. The benefit of the cross-correlations has been highlighted recently in e.g. [215], where authors found cross-correlations of CMB-S4 with the upcoming LSS surveys can provide impressive constraints on the matter amplitude $\sigma_8(z)$, the halo bias parameter and the amplitude of local non-Gaussianity, $f_{\rm NL}$. Through improving the lensing reconstruction, delensing will allow for better cross-correlation measurements.

7.3 Formalism

7.3.1 All-orders delensing on the full sky

In this section I discuss calculations from my ongoing project with Joel Meyers, Dan Green and Alex van Engelen where we calculate the delensed CMB maps, $T^{\rm d}$, $E^{\rm d}$, $B^{\rm d}$, for temperature, E- and B-mode polarisation, respectively, following a similar procedure to that introduced in [307]. We extend the earlier work on the flat sky to the full sky. As in [307], we demand the following conditions to be met from our procedure:

- Delensing should be accurate in the limit where the noise vanishes, e.g. $T^{\rm d}(\hat{\mathbf{n}}) \simeq T(\hat{\mathbf{n}})$.

- As per lensing, the delensing procedure must not add or remove power from the CMB map.
- Maps should be filtered to minimize the impact of experimental noise on the observables.

We apply filtering *before* delensing to avoid using noisy modes on the CMB and also the lensing reconstruction. Our lensing reconstruction method is an efficient implementation of lensing-reconstruction for all quadratic combinations of T, E, and B, extending what was done in [381] for just TT and EB.

Given an observed temperature map $T^{\rm obs}(\hat{\mathbf{n}})$ and an observed lensing deflection map $\alpha^{\rm obs}(\hat{\mathbf{n}})$, the estimate of the delensed temperature map can be written, for example,

$$T^{\rm d}(\hat{\mathbf{n}}) = \bar{h} \star T^{\rm obs}(\hat{\mathbf{n}}) + h \star T^{\rm obs}(\hat{\mathbf{n}} - g \star \alpha^{\rm obs}(\hat{\mathbf{n}}))\,, \tag{7.5}$$

where $(\star)$ refers to a convolution and $\bar{h}$, h and g are filters that will be chosen to satisfy the conditions discussed above.

The lensed all-sky correlation functions have been calculated in [382]. The correlation function for the CMB anisotropies is

$$\begin{aligned}\tilde{\xi}^{TT}(\beta) &= \langle \Theta(\hat{\mathbf{n}}_1')\Theta(\hat{\mathbf{n}}_2')\rangle \\ &= \sum_{\ell m} C_\ell^{TT}{}_{\ell m}(\hat{\mathbf{n}}_1') Y^*_{\ell m}(\hat{\mathbf{n}}_2')\rangle \\ &= \sum_{\ell m m'} C_\ell^{TT}{}_{\ell} d^\ell_{mm'}(\beta)\langle Y_{\ell m}(\theta_1,\phi_1) Y_{\ell m}(\theta_2,\phi_2)\rangle,\end{aligned} \tag{7.6}$$

where θ_i and ϕ_i are polar angles associated with the unit vector $\hat{\mathbf{n}}_i$, β is the angle between two directions, $\hat{\mathbf{n}}_1 \cdot \hat{\mathbf{n}}_2 = \cos\beta$ and $d^\ell_{mm'}(\beta) := D^\ell_{mm'}(0,\beta,0)$ are the reduced Wigner functions representing the Eulerian rotation of the harmonic at some deflected position $\hat{\mathbf{n}}$. The average over spherical (in brackets) is over possible realisations of the lensing defection field defined earlier $\vec{\alpha}(\theta,\phi)$ and reduces to integrals over the averaged differences between deflection angles projected onto Fourier wave-vectors on two sphere in the form

$$\tilde{\xi}^{TT}(\beta) \simeq \sum_\ell \frac{2\ell+1}{4\pi} C_\ell^{TT} \sum_{mm'} i^{m-m'} d^\ell_{mm'} \frac{1}{(2\pi)^2} \int \mathrm{d}\phi_{\vec{L}} \mathrm{d}\phi_{\vec{L}'} e^{i(m\phi_{\vec{L}} - m'\phi'_{\vec{L}'}} \left\langle e^{i(\vec{L}\cdot\vec{\alpha}_1 - \vec{L}'\cdot\vec{\alpha}_2)} \right\rangle, \tag{7.7}$$

where we used the spherical harmonic expansion

$${}_sY_{\ell m}(\theta,\phi)^m (-i)^s \sqrt{\frac{2\ell+1}{4\pi}} \frac{e^{-is\phi}}{2\pi} \int_0^{2\pi} \mathrm{d}\phi_{\vec{L}} e^{i\vec{L}\cdot\vec{\alpha}} e^{i(m+s)\phi_{\vec{L}}}\,, \tag{7.8}$$

with $\vec{L} := (L+1/2)(\cos\phi_{\vec{L}}, \sin\phi_{\vec{L}})$. The ensemble average in Eq. 7.7 can be separated into a 'diagonal' contribution coming from the contraction of the diagonal elements in the deflection angle, $C_{\rm gl}(\beta)$, and a 'trace-free' part, $C_{\rm gl,2}(\beta)$ which is subdominant. We will define these explicitly below. The lensed correlation functions for the temperature and polarization take the form,

$$\tilde{\xi}^{TT} \simeq \sum_\ell \frac{2\ell+1}{4\pi} C_\ell^{TT} \Big[X^2_{000} d^\ell_{00} + \frac{8}{\ell(\ell+1)} C_{\rm gl,2} X'^2_{000} d^\ell_{1-1} + C^2_{\rm gl,2} \left(X'^2_{000} d^\ell_{00} + X^2_{220} d^\ell_{2-2} \right) \Big] , \tag{7.9}$$

$$\tilde{\xi}^{TE} \simeq \sum_\ell C_\ell^{TE} \Bigg\{ X_{022} X_{000} d^\ell_{20} + \frac{2 C_{\rm gl,2} X'_{000}}{\sqrt{\ell(\ell+1)}} (X_{121} d^\ell_{11} + X_{132} d^\ell_{3-1}) + \frac{1}{2} C^2_{\rm gl,2} \left[(2 X'_{022} X'_{000} + X^2_{220}) d^\ell_{20} + X_{220} X_{242} d^\ell_{4-2} \right] \Bigg\} , \tag{7.10}$$

$$\tilde{\xi}_- \simeq \sum_\ell \frac{2\ell+1}{4\pi} (C^E_\ell - C^B_\ell) \Bigg\{ X^2_{022} d^\ell_{2-2} + C_{\rm gl,2} (X^2_{121} d^\ell_{1-1} + X^2_{132} d^\ell_{3-3}) + \frac{1}{2} C^2_{\rm gl,2} \left[2 (X'_{022})^2 d^\ell_{2-2} + X^2_{220} d^\ell_{00} + X^2_{242} d^\ell_{4-4} \right] \Bigg\} , \tag{7.11}$$

and

$$\tilde{\xi}_+ \simeq \sum_\ell \frac{2\ell+1}{4\pi} (C^E_\ell + C^B_\ell) \Big\{ X^2_{022} d^\ell_{22} + 2 C_{\rm gl,2} X_{132} X_{121} d^\ell_{31} + C^2_{\rm gl,2} \left[(X'_{022})^2 d^\ell_{22} + X_{242} X_{220} d^\ell_{40} \right] \tag{7.12}$$

where

$$X_{000} = e^{-\ell(\ell+1)\sigma^2/4} \tag{7.13}$$

$$X_{220} = \frac{1}{4} \sqrt{(\ell+2)(\ell-1)\ell(\ell+1)} e^{-(\ell(\ell+1)-2)\sigma^2/4} , \tag{7.14}$$

and

$$\sigma^2(\beta) = C_{\rm gl}(0) - C_{\rm gl}(\beta) \tag{7.15}$$

$$C_{\rm gl}(\beta) = \sum_\ell \frac{2\ell+1}{4\pi}\ell(\ell+1)C_\ell^{\phi\phi} d^\ell_{11}(\beta) \tag{7.16}$$

$$C_{\rm gl,2}(\beta) = \sum_\ell \frac{2\ell+1}{4\pi}\ell(\ell+1)C_\ell^{\phi\phi} d^\ell_{-11}(\beta)\,. \tag{7.17}$$

Note that on the expressions above we in fact make a simplifying (perturbative) assumption bringing down the term $C_{\rm gl,2}$ down from the exponential. As shown in Ref. [307] (and discussed in the literature [382, e.g.]), these off-diagonal contributions in α_{ij} are subdominant compared to the $C_{\rm gl} := \langle\vec{\alpha}(\hat{\mathbf{n}})\cdot\vec{\alpha}(\hat{\mathbf{n}}')\rangle$.

Following the same procedure discussed in [307], I calculate the expressions for delensed all-sky correlations functions to all-orders in the lensing potential. Note that one of the ways the delensed spectra differs from the lensed spectra is the 2 additional terms due to our rigorous filtering choice: we apply two filters to data, h_ℓ and $\bar{h}_\ell$ to satisfy the conditions we defined in bullet-points above and as defined in [307]. These lead to terms proportional to $\{|h_\ell|^2, |h_\ell\bar{h}_\ell|, |\bar{h}_\ell|^2\}$ which dominate the signal in the high-, middle- and low-ℓ ranges, respectively. These are,

$$\begin{aligned}
\xi^{TT,\rm d} = \sum_\ell \frac{2\ell+1}{4\pi}\Bigg(& |\bar{h}_\ell|^2\tilde{C}_\ell^{TT} \\
&+2\bar{h}_\ell h_\ell C_\ell^{TT}\Bigg[(X^{\bar{h}h}_{000})^2 d^\ell_{00} + \frac{8}{\ell(\ell+1)}C^{\bar{h}h}_{\rm gl,2}(X^{\bar{h}h\,\prime}_{000})^2 d^\ell_{1-1} \\
&\qquad +(C^{h^2}_{\rm gl,2})^2\left((X^{\bar{h}h\,\prime}_{000})^2 d^\ell_{000} + (X^{\bar{h}h}_{220})^2 d^\ell_{2-2}\right)\Bigg] \\
&+|h_\ell|^2 C_\ell^{TT}\Bigg[(X^{h^2}_{000})^2 d^\ell_{00} + \frac{8}{\ell(\ell+1)}C^{h^2}_{\rm gl,2}(X^{h^2\,\prime}_{000})^2 d^\ell_{1-1} \\
&\qquad +(C^{h^2}_{\rm gl,2})^2\left((X^{h^2\,\prime}_{000})^2 d^\ell_{00} + (X^{h^2}_{220})^2 d^\ell_{2-2}\right)\Bigg]\Bigg)
\end{aligned} \tag{7.18}$$

$$
\begin{aligned}
\tilde{\xi}^{TE,\mathrm{d}} = \sum_\ell \frac{2\ell+1}{4\pi} \Bigg(& \bar{h}\bar{h}^P \tilde{C}_\ell^{TE} \\
& + (h\bar{h}^P + \bar{h}h^P) C_\ell^{TE} \Bigg[X_{022}^{h\bar{h}} X_{000}^{h\bar{h}} d_{20}^\ell + \frac{2C_{\mathrm{gl},2}^{h\bar{h}} X_{000}^{h\bar{h}\,\prime}}{\sqrt{\ell(\ell+1)}} (X_{121}^{h\bar{h}} d_{11}^\ell + X_{132}^{h\bar{h}} d_{3-1}^\ell) \\
& \qquad + \frac{1}{2} (C_{\mathrm{gl},2}^{h\bar{h}})^2 \left[(2X_{022}^{h\bar{h}\,\prime} X_{000}^{h\bar{h}\,\prime} + (X_{220}^{h\bar{h}})^2) d_{20}^\ell + X_{220}^{h\bar{h}} X_{242}^{h\bar{h}} d_{4-2}^\ell \right] \Bigg] \\
& + (h_\ell h_\ell^P) C_\ell^{TE} \Bigg\{ X_{022}^{h^2} X_{000}^{h^2} d_{20}^\ell + \frac{2C_{\mathrm{gl},2}^{h^2} X_{000}^{h^2\,\prime}}{\sqrt{\ell(\ell+1)}} (X_{121}^{h^2} d_{11}^\ell + X_{132}^{h^2} d_{3-1}^\ell) \\
& \qquad + \frac{1}{2} (C_{\mathrm{gl},2}^{h^2})^2 \left[(2X_{022}^{h^2\,\prime} X_{000}^{h^2\,\prime} + (X_{220}^{h^2})^2) d_{20}^\ell + X_{220}^{h^2} X_{242}^{h^2} d_{4-2}^\ell \right] \Bigg\} \Bigg)
\end{aligned}
\tag{7.19}
$$

$$
\begin{aligned}
\tilde{\xi}_-^{\mathrm{d}} = \sum_\ell \frac{2\ell+1}{4\pi} \Bigg(& \bar{h}\bar{h}^P (\tilde{C}_\ell^E - \tilde{C}_\ell^B) \\
& + (h\bar{h}^P + \bar{h}h^P)(C_\ell^E - C_\ell^B) \Bigg\{ (X_{022}^{h\bar{h}})^2 d_{2-2}^\ell + C_{\mathrm{gl},2}^{h\bar{h}} ((X_{121}^{h\bar{h}})^2 d_{1-1}^\ell + (X_{132}^{h\bar{h}})^2 d_{3-3}^\ell) \\
& \qquad + \frac{1}{2} (C_{\mathrm{gl},2}^{h\bar{h}})^2 \left[2(X_{022}^{h\bar{h}\,\prime})^2 d_{2-2}^\ell + (X_{220}^{h\bar{h}})^2 d_{00}^\ell + (X_{242}^{h\bar{h}})^2 d_{4-4}^\ell \right] \Bigg\} \\
& + h_\ell h_\ell^P (C_\ell^E - C_\ell^B) \Bigg\{ (X_{022}^{h^2})^2 d_{2-2}^\ell + C_{\mathrm{gl},2}^{h^2} ((X_{121}^{h^2})^2 d_{1-1}^\ell + (X_{132}^{h^2})^2 d_{3-3}^\ell) \\
& \qquad + \frac{1}{2} (C_{\mathrm{gl},2}^{h^2})^2 \left[2(X_{022}^{h^2\,\prime})^2 d_{2-2}^\ell + (X_{220}^{h^2})^2 d_{00}^\ell + (X_{242}^{h^2})^2 d_{4-4}^\ell \right] \Bigg\} \Bigg)
\end{aligned}
\tag{7.20}
$$

$$\begin{aligned}\tilde{\xi}_+^{\rm d} = \sum_\ell \frac{2\ell+1}{4\pi}\Bigg(&\bar{h}\bar{h}^P(\tilde{C}_\ell^E+\tilde{C}_\ell^B)\\ &+(h\bar{h}^P+\bar{h}h^P)(C_\ell^E+C_\ell^B)\Bigg\{(X_{022}^{h\bar{h}})^2 d_{22}^\ell + 2C_{{\rm gl},2}^{h\bar{h}} X_{132}^{h\bar{h}} X_{121}^{h\bar{h}} d_{31}^\ell\\ &\qquad + C_{{\rm gl},2}^2\left[({X'_{022}}^{h\bar{h}})^2 d_{22}^\ell + X_{242}^{h\bar{h}} X_{220}^{h\bar{h}} d_{40}^\ell\right]\Bigg\}\\ &+(hh^P+hh^P)(C_\ell^E+C_\ell^B)\Bigg\{(X_{022}^{h^2})^2 d_{22}^\ell + 2C_{{\rm gl},2}^{h^2} X_{132}^{h^2} X_{121}^{h^2} d_{31}^\ell\\ &\qquad + C_{{\rm gl},2}^2\left[({X'_{022}}^{hh^P})^2 d_{22}^\ell + X_{242}^{hh^P} X_{220}^{hh^P} d_{40}^\ell\right]\Bigg\}\Bigg)\end{aligned} \tag{7.21}$$

where

$$h_\ell = \frac{C_\ell^{TT}}{C_\ell^{TT}+N_\ell^{TT}} \tag{7.22}$$

$$\bar{h}_\ell = \sqrt{1-h_\ell^2(1-e^{-\ell(\ell+1)C_{\rm gl}^{\rm obs}(0)/2})} - h_\ell e^{-\ell(\ell+1)C_{\rm gl}^{\rm obs}(0)/4} \tag{7.23}$$

and

$$X_{000}^{\bar{h}h} = e^{-\ell(\ell+1)[\sigma^2(\beta)]^{\bar{h}h}/4} \tag{7.24}$$

$$X_{000}^{h^2} = e^{-\ell(\ell+1)[\sigma^2(\beta)]^{h^2}/4} \tag{7.25}$$

$$X_{210}^{\bar{h}h} = \frac{1}{4}\sqrt{(\ell+2)(\ell+1)\ell(\ell-1)}e^{-(\ell(\ell+1)-2)[\sigma^2(\beta)]^{\bar{h}h}/4} \tag{7.26}$$

$$X_{220}^{h^2} = \frac{1}{4}\sqrt{(\ell+2)(\ell+1)\ell(\ell-1)}e^{-(\ell(\ell+1)-2)[\sigma^2(\beta)]^{h^2}/4} \tag{7.27}$$

where

$$[\sigma^2(\beta)]^{\bar{h}h} = (C_{\rm gl}(0)-C_{\rm gl}(\beta)) - (C_{\rm gl}^{\rm cross}(0)-C_{\rm gl}^{\rm cross}(\beta)) + \frac{1}{2}C_{\rm gl}^{\rm obs}(0) \tag{7.28}$$

$$[\sigma^2(\beta)]^{h^2} = (C_{\rm gl}(0)-C_{\rm gl}(\beta)) - 2(C_{\rm gl}^{\rm cross}(0)-C_{\rm gl}^{\rm cross}(\beta)) + (C_{\rm gl}^{\rm obs}(\beta)-C_{\rm gl}^{\rm obs}(\beta)) \tag{7.29}$$

and

$$C^{\bar{h}h}_{\mathrm{gl},2}(\beta) = C_{\mathrm{gl},2}(\beta) - C^{\mathrm{cross}}_{\mathrm{gl},2}(\beta) \tag{7.30}$$

$$C^{h^2}_{\mathrm{gl},2} = C_{\mathrm{gl},2}(\beta) - 2C^{\mathrm{cross}}_{\mathrm{gl},2}(\beta) + C^{\mathrm{obs}}_{\mathrm{gl},2}(\beta) \tag{7.31}$$

$$C^{\mathrm{obs}}_{\mathrm{gl}}(\beta) = \sum_{\ell} \frac{2\ell+1}{4\pi} \ell(\ell+1)|g_\ell|^2 C^{\phi\phi,\mathrm{obs}}_{\ell} d^{\ell}_{11}(\beta) \tag{7.32}$$

$$C^{\mathrm{obs}}_{\mathrm{gl},2}(\beta) = \sum_{\ell} \frac{2\ell+1}{4\pi} \ell(\ell+1)|g_\ell|^2 C^{\phi\phi,\mathrm{obs}}_{\ell} d^{\ell}_{-11}(\beta) \tag{7.33}$$

$$C^{\mathrm{cross}}_{\mathrm{gl}}(\beta) = \sum_{\ell} \frac{2\ell+1}{4\pi} \ell(\ell+1) g_\ell C^{\phi\phi,\mathrm{cross}}_{\ell} d^{\ell}_{11}(\beta) \tag{7.34}$$

$$C^{\mathrm{cross}}_{\mathrm{gl},2}(\beta) = \sum_{\ell} \frac{2\ell+1}{4\pi} \ell(\ell+1) g_\ell C^{\phi\phi,\mathrm{cross}}_{\ell} d^{\ell}_{-11}(\beta) \tag{7.35}$$

where I defined

$$\tilde{C}^{\phi\phi}_{\ell} := C^{\phi\phi}_{\ell} + N^{\phi\phi}_{\ell} \,. \tag{7.36}$$

Delensed power spectra can now be calculated by performing an integral over the angular separation β and using Wigner d-matrices as

$$C^{\mathrm{d},TT}_{\ell} = 2\pi \int_{-1}^{1} \xi^{\mathrm{d},TT}(\beta) d^{\ell}_{00}(\beta) \mathrm{d}\cos\beta \,, \tag{7.37}$$

$$C^{\mathrm{d},TE}_{\ell} = 2\pi \int_{-1}^{1} \xi^{\mathrm{d},TE}(\beta) d^{\ell}_{20}(\beta) \mathrm{d}\cos\beta \,, \tag{7.38}$$

$$C^{\mathrm{d},EE}_{\ell} - C^{\mathrm{d},BB}_{\ell} = 2\pi \int_{-1}^{1} \xi^{\mathrm{d},-}(\beta) d^{\ell}_{22}(\beta) \mathrm{d}\cos\beta \,, \tag{7.39}$$

$$C^{\mathrm{d},EE}_{\ell} + C^{\mathrm{d},BB}_{\ell} = 2\pi \int_{-1}^{1} \xi^{\mathrm{d},-}(\beta) d^{\ell}_{22}(\beta) \mathrm{d}\cos\beta \,. \tag{7.40}$$

The minimum-variance reconstruction-noise quadratic estimator depends on the experimental specifications and can be calculated by combining all measured quadratic estimators from the T, E and B maps as

$$N^{\phi\phi,\mathrm{mv}}_{L} = \frac{1}{\sum_{\alpha\beta} (N_L^{-1})^{\alpha\beta}} \,, \tag{7.41}$$

where

$$N^{ab}_{\ell} = (2\ell+1) \left[\sum_{\ell_1\ell_2} \frac{|f^{\alpha}_{\ell_1\ell\ell_2}|^2}{c_N \tilde{C}^{aa}_{\ell_1} \tilde{C}^{bb}_{\ell_2}} \right]^{-1} \tag{7.42}$$

for $\alpha = \{ab\}$ and $\{ab\} =$ TT, EE, BE, TB, BB spectra, where $c_N = 2$ for the {TT, EE, BB} spectra and $c_N = 1$ for the {BE,TE} spectra. Also note here I use a different notation from some parts of this thesis, where I define observed spectra as $\tilde{C}_\ell^{aa} := C_\ell^{aa} + N_\ell^{aa}$. I provide novel calculations for the full-sky estimator covariances defined in Eq. 7.42 in Appendix A.2.

I demonstrate the performance of delensing given experimental specifications appropriate to Simons Observatory (SO) and CMB-S4 (S4) in Figure 7.1.

7.3.2 Iterative Delensing

The delensed spectra of the CMB can be used to calculate an improved lensing reconstruction noise. Until convergence, repeated application of delensing on the CMB spectra, with improved noise at each iteration, would increase the signal-to-noise ratio of the lensing measurement. Note that at this point it is useful to draw the distinction between the iterative maximum-likelihood method introduced in [383] (and sometimes referred as 'the iterative method' in the literature); and the iterative technique I discuss here, where I use the quadratic lensing-reconstruction estimator. The former maximum-likelihood lensing reconstruction method is known to be potentially more optimal, especially at low noise levels, then the latter analytic estimator I discuss here. The quadratic estimators, nevertheless, have the advantage of being simpler (and often much faster) to calculate. This makes quadratic estimators very attractive for purposes like making extensive Fisher forecasts in the anticipation of upcoming data. Hence in this section I discuss an iterative (all-orders) delensing technique with the quadratic lensing-reconstruction estimator, as done in [381].

This iterative delensing procedure is shown schematically in Fig. 7.3. I use observed CMB spectra of temperature and polarisation and a spectrum of the observed deflection field. Since I am considering internal delensing with the CMB spectra here, our observed deflection field is the minimum-variance reconstruction with the quadratic estimator. I use the observed spectra and the lensing reconstruction to calculate our estimate for the delensed observables. I use the delensed observables to repeat the minimum-variance lensing reconstruction and obtain an improved lensing reconstruction with lower minimum-variance lensing-reconstruction noise. I use the improved lensing reconstruction and the delensed spectra to calculate improved delensed observables. I repeat this process until convergence.

The iterative delensing with the quadratic lensing-reconstruction estimator is not a novel procedure, especially for delensing with external estimators, as discussed in [381]. Generally, however, delensing forecasts (in the literature) iterate only over the $C_\ell^{BB,\mathrm{d}}$ spectra and the EB- and the TB- variances of the minimum-variance quadratic estimator, as defined in Eq. (7.41).

The improvement in the quality of delensing from iteration can be seen in Fig. 7.2. While this improvement is dominated by the improvement in the EB-variance via iterating $C_\ell^{BB,\mathrm{d}}$; iterating the CMB temperature as well as the E-mode polarisation and the corresponding variances can provide a non-trivial improvement on the lensing reconstruction noise even for the upcoming CMB experiments like CMB-S4, as can be seen in the bottom-right plot in Fig. 7.1.

7.4 Discussion

The discussion in this Chapter draws from the science case for my upcoming work with Joel Meyers, Daniel Green and Alex van Engelen where we perform extensive Fisher forecasts using the full-sky all-orders delensing estimator, as introduced in Section 7.3.1. As discussed earlier, in this upcoming work we produce detailed forecasts on aforementioned cosmological parameters sensitive to lensing and share a publicly available delensing software intended to be integrated into developing analysis pipelines for the upcoming CMB experiments such as Simons Observatory and CMB-S4. Calculations and the coding are complete; and the code is extensively tested to be stable. We are in the process of writing our science papers. As discussed throughout this section, however, our findings suggest our more rigorous implementation of delensing provide only marginal improvements for cosmological parameter inference for the upcoming CMB experiment specifications, when compared to earlier studies [e.g. 307]. Experiments with higher sensitivity, such as the proposed CMB-HD, can potentially make the case of iterative delensing with temperature and E-mode polarisation maps stronger. It is also evident, nevertheless, that stable calculations with all-orders delensing estimators on the full-sky will improve the forecasting quality of the lensing and delensing analysis pipelines of the upcoming CMB experiments.

Irrespective of the improvements afforded by extending the notation from flat-sky to full-sky, CMB experiments will be highly sensitive to lensing. This leads to significantly improved constraints on cosmological parameters from delensing all spectra (as opposed to only B-modes) . As discussed in Section 7.2, delensing recovers BAO peak features, improves the measurement of the damping tail, and improves the measurement of the lensing potential. Lensing-induced covariances can also be largely removed by delensing [e.g. 307, 384]. Regarding parameter constraints, most significant improvements occur for the parameters that are directly sensitive to the peak locations, such as θ_s and the Hubble parameter. I

have also discussed the value of delensing for $N_{\rm eff}$ forecasts. In particular, I described the degeneracy of $N_{\rm eff}$ and Y_p on the damping tail. Better measurements of peak locations improves $N_{\rm eff}$ constraints because neutrinos shift the BAO peaks due to their influence on the metric beyond the BAO scale. Improving the damping tail by delensing also improves the constraints on $N_{\rm eff}$ by better measurement of the degenerate Y_p parameter as discussed above.

Going beyond forecasting, our discussion and recent studies [e.g. 307, 371–373, 310] suggest delensing may be necessary for future likelihood analysis with data. When increasing the realism of our statements, however, it is valuable to revisit the approximations I make throughout this section. First, I consider idealised temperature and polarisation noise for the CMB experiments. In reality the CMB noise anticipated from SO or CMB-S4, for example, will be impacted by the residual foregrounds, in particular the tSZ effect. The noise forecasts for these experiments are publicly available and will be used in our upcoming analysis. Second, the real data might well violate some of the assumptions I make in calculating the simple analytic predictions in Section 7.3. Third, the iterative delensing with internal data sets is known to introduce an additional bias which may be difficult to mitigate. I now discuss these latter two issues briefly.

Our estimates of the delensed spectra introduced in Section 7.3 rely on few approximations. First, as can be seen from our estimate of the delensed temperature map at zero noise limit, $T^d(\hat{\mathbf{n}}) = \tilde{T}(\hat{\mathbf{n}} - \vec{\alpha}(\hat{\mathbf{n}}))$, our delensed estimate $T^d(\hat{\mathbf{n}})$ fails to recover the unlensed temperature map due to non-zero gradients, up to an error of order $\mathscr{O}((\vec{\alpha}(\hat{\mathbf{n}}) \cdot \vec{\nabla})\vec{\alpha}(\hat{\mathbf{n}}))$. It has been shown in [307], however, that the error on the unlensed spectra estimate due to ignoring these terms is around two orders of magnitude smaller compared to the effect of lensing at leading order in perturbation theory introduced in Section 4.3. Hence, in order to derive the expressions in Section 7.3, I assume $(\vec{\alpha}(\hat{\mathbf{n}}) \cdot \vec{\nabla})\vec{\alpha}(\hat{\mathbf{n}}) \ll \vec{\alpha}$. Another important approximation required to make the all-orders description calculable, of course, is the Gaussianity of the lensing potential [382]. This approximation is widely accepted as well-motivated and supported by the current experimental constraints. As I introduced in Section 4.3, lensing field is the line integral of matter fluctuations on the photon trajectory. The relevant integrands peak at redshifts around $z \sim 2$ and on large scales where perturbations are linear and Gaussian, latter statement supported in the literature [see, e.g. 385–388].

Furthermore, delensing with internal data sets, as I discuss here, is known to introduce additional biases to the delensed fields [e.g, 389]. In particular if the maps that are being delensed are overlapping or the same with maps that are used to reconstruct the deflection field, the reconstructed deflection field would no longer independent of the CMB. This would drive the delensed spectra and the covariance away from their unbiased values. Developing

techniques to remove the internal CMB delensing bias is an active field of research [see e.g. 390, 391, 388, 371, 392, 393]. Calculation of the internal delensing bias and its effect on our estimators is beyond the scope of this chapter. Note, however, I expect internal delensing bias to degrade the statistical power of our method. Moreover, that the iterative delensing procedure discussed here may also influence the internal delensing bias, potentially escalating the degradation at each iteration step. I leave a more detailed analysis to our upcoming work.

Finally, note that lensing also induces additional power-spectrum covariances, reducing the measurement quality of CMB observations. Recent studies show delensing can potentially significantly reduce the effect of lensing on the covariances and have important implications for non-Gaussianity searches (see e.g. [384]). Calculating analytic all-orders expressions for the delen sed spectra covariances is potentially an arduous task and is outside the scope of our ongoing project.[1]

[1]Note, however, that the analytic approximation to the power-spectra covariances, introduced in Ref. [394], is often used in the literature and argued to be good fit to simulations (see the discussion in e.g. [307], for example).

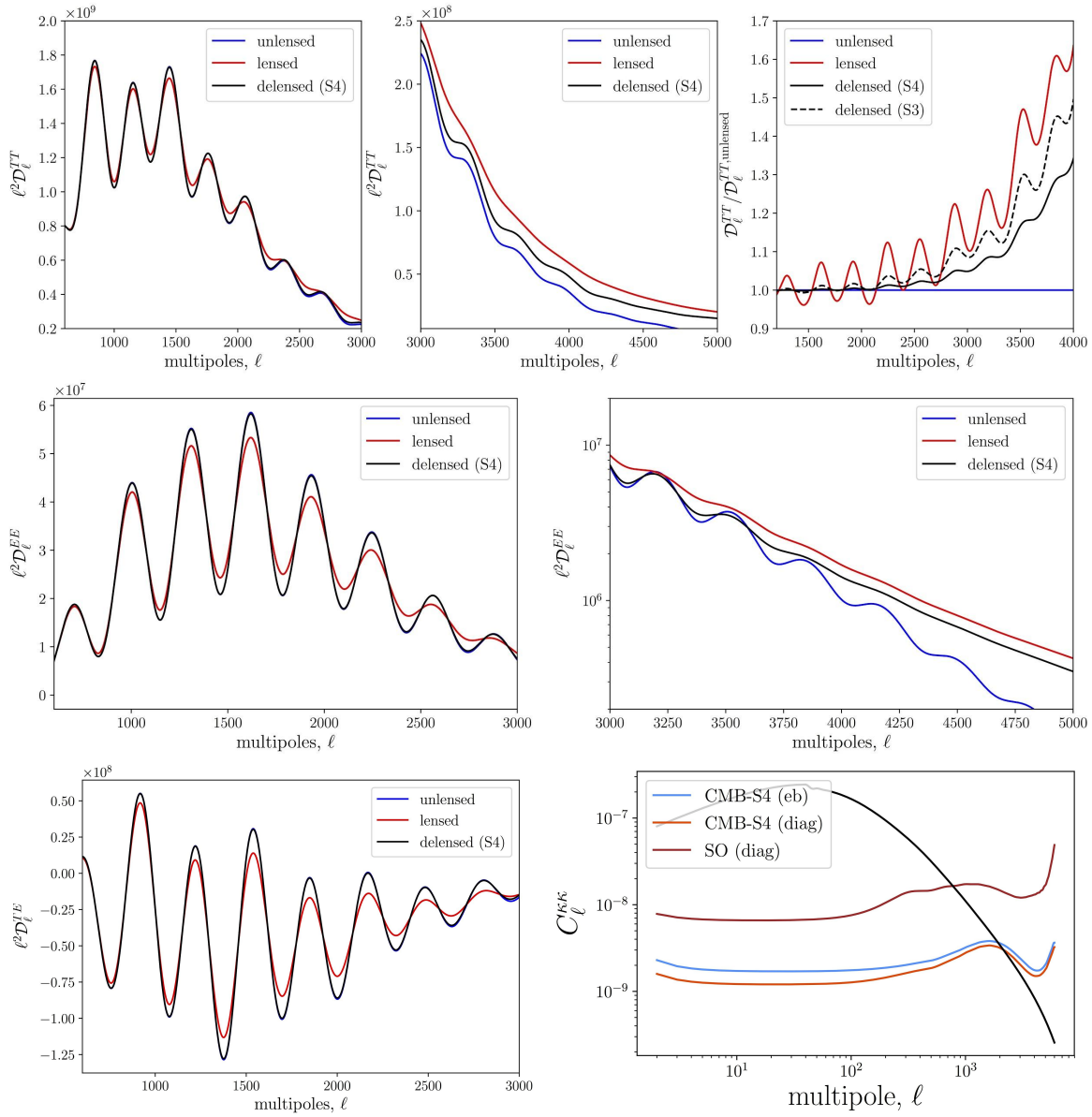

Figure 7.1: Delensed CMB temperature and polarisation auto- and cross-spectra shown alongside the lensing reconstruction noise. Upmost plots show the lensed, unlensed and delensed spectra, the latter calculated with CMB-S4 (S4) and SO (S3) experimental specifications. Delensing is shown to recover the smoothed structure on most of the acoustic peaks up to large numbers of multipoles. On smaller scales, delensing with S4 experimental specifications recovers some significant fraction of the damping tail up to scales $\ell \gtrsim 4000$. Improvement with a less accurate experiment such as S3 is also evident but shown to be less than compared to S4. On the middle plots, similar improvements are shown for the polarisation spectra. The acoustic peaks and the damping tail is largely recovered using a S4-like experiment up to multipoles around $\ell \sim 3000$. Similar observations also apply for the cross-power between temperature and the polarisation. The bottom plot shows the lensing-reconstruction noise. The improvement when comparing an S4 to an S3 type experiment is evident. Also shown the difference between the EB-only delensing and delesing with all spectra [approximating the off-diagonal covariances, i.e. weights with $\alpha \neq \beta$ in Eq. (7.42), zero].

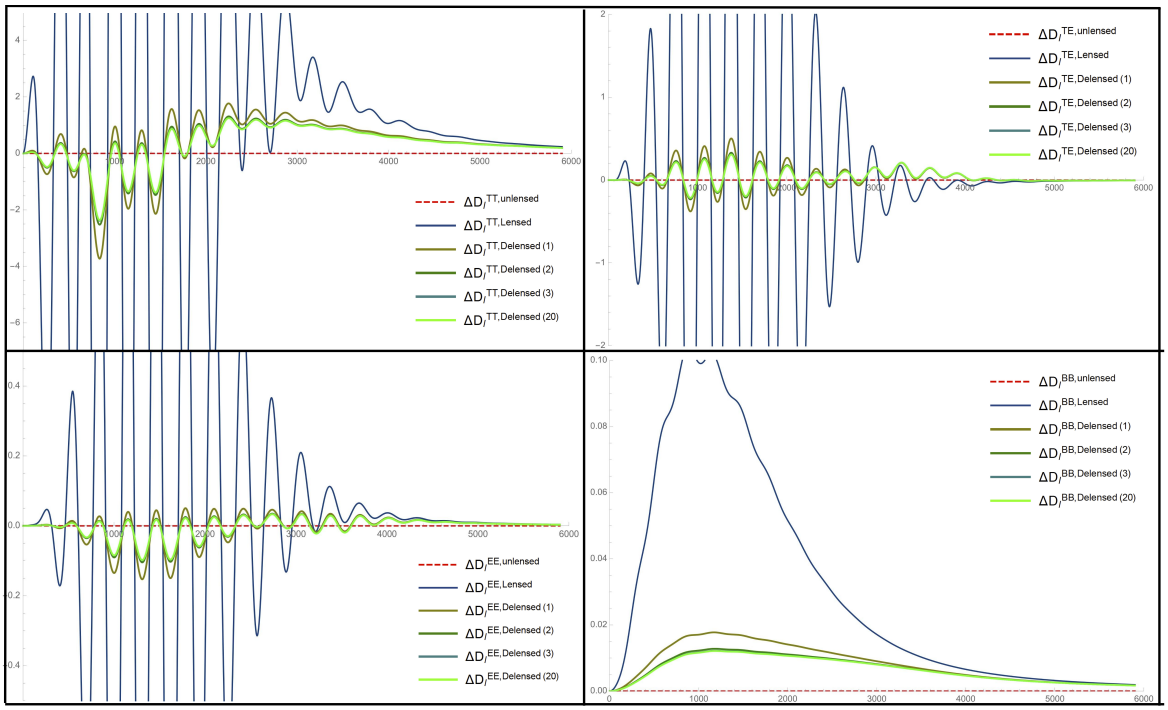

Figure 7.2: Fractional difference between the lensed spectra and the delensed spectra are shown. The y-axes are $\Delta D_\ell^{XY,\mathrm{spec}} := [C_\ell^{XY,\mathrm{unlensed}} - C_\ell^{XY,\mathrm{spec}}]/C_\ell^{XY,\mathrm{spec}}$, where $\{XY\} = \{TT, TE, EE, BB\}$ and $\mathrm{spec} = \{\mathrm{unlensed}, \mathrm{lensed}, \mathrm{delensed}\ (n_{\mathrm{iter}})\}$ where I define $n_{\mathrm{iter}} = \{1, 2, 3, 20\}$ as the number of iterations. The x-axes are in ℓ, multipoles. In all cases the iterated delensed spectra converge at a large number $n_{\mathrm{iter}} \simeq 20$.

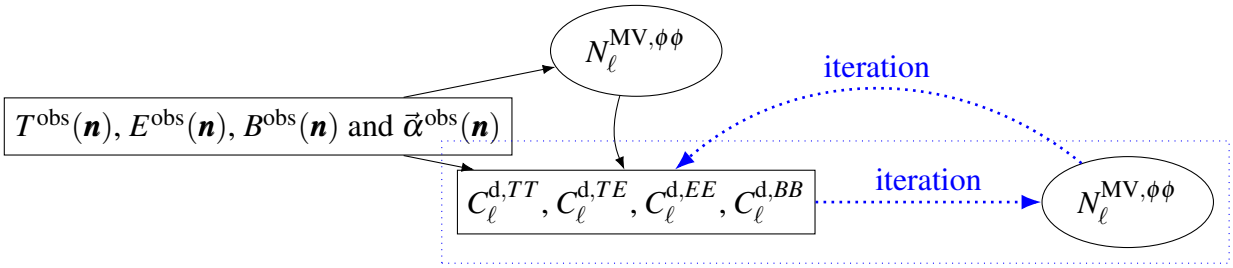

Figure 7.3: Schematic plot of the iterative delensing procedure. The observed CMB maps of temperature and polarisation is used with the observed maps of the deflection field in order to calculate the minimum-variance lensing reconstruction noise. These maps are then used together with the lensing reconstruction noise to calculate the delensed CMB temperature and polarisation spectra. Delensed CMB spectra can be used to calculate an improved lensing reconstruction noise, which can in turn be utilized to re-calculate the delensed CMB spectra. The latter step can be repeated until the calculate spectra converges to the best possible estimate of the delensed CMB.

Chapter 8

Upcoming work: Probing CIPs with the 21cm

In this section I discuss my ongoing work on probing CIPs (see Section 6.4) with the 21cm hydrogen line signal from the cosmic dawn era ($z \simeq 15-20$). This signal is subject to a large BAO effect due to large relative velocities between the DM and baryons following recombination. I discussed the effect in Section 2.7.2 and expand on that discussion below. This work is part of an ongoing science program I am building for utilising this signature for the purpose of probing fundamental physics. This project involves collaborations with Marc Kamionkowski, Bikash Dinda, Julian Munoz and Tom Binnie. Except for the discussion in Section 8.6, I have written all of the text. I have also lead the conceptualisation, as well as produced the presented results and plots. The text in Section 8.6 is compiled with inputs from Tom Binnie, who also contributed to the project by providing survey-specific configuration files I used to generate noise forecasts for the 21cm hydrogen-line experiments: HERA and SKA-1low. I discuss these more in detail in what follows.

8.1 Introduction

Measurements of the 21cm hydrogen-line provides a unique window into the cosmic-dawn era when the first stars were formed ($z \simeq 15-20$). During these early times the typical mass of collapsed baryonic objects fall near the critical mass below which gas pressure prevents their collapse. The abundance of Lyman-α photons that excite the hyperfine transition in neutral hydrogen and allow it to absorb 21cm photons from the cosmic microwave background (CMB) will depend on the collapse-fraction of baryons and is directly impacted by effects

that alter early structure growth such as local modulations of relative densities of dark matter (DM) and baryons due to bulk compensated isocurvature perturbations (CIPs) I study in this chaper.

The standard cosmological paradigm (ΛCDM) with single-field inflation predicts adiabatic initial conditions with inhomogeneities in DM, baryons, neutrinos, and photons all uniquely determined by the primordial curvature perturbations. More general theories with multiple degrees of freedom, however, can source non-adiabatic (isocurvature) perturbations, where the relative mixture of DM, baryons, neutrinos, and photons become independent degrees of freedom. While measurements of the CMB and galaxy distributions put tight constraints on most forms of isocurvature, a specific form of isocurvature is difficult to constrain from CMB and galaxy-surveys alone: CIPs. CIPs are fluctuations of baryons and DM that leave the total matter perturbations unchanged and adiabatic. Since CMB is only sensitive to the total matter fluctuations at the leading order, CIPs avoid stringent constraints from measurements of the CMB alone, allowing for CIPs to have an amplitude orders of magnitude larger than the adiabatic modes [331–338, 17]. A detection of CIPs can provide insight into both the number of primordial fields that contribute to the observed density fluctuations, as well as their decay channels, e.g. [345, 395].

Regardless of whether adiabatic or isocurvature, primordial fluctuations seed the rich large-scale structure of matter we observe in our Universe. As matter clusters under gravity, however, its components can behave very differently. While the majority of matter is collisionless, dark and cold, a fraction of it are baryons which couple to photons before the recombination at redshift $z \simeq 1100$, giving rise to the Baryon Acoustic Oscillations (BAOs) observed from the CMB and galaxy-surveys. The same physics also induces a bulk relative velocity between DM and baryons [396–402, 398, 403–406]. More recently, it was shown in [66, 407] that for reasonable models of epochs up to the end of reionization, detecting a velocity-induced acoustic feature, so called Velocity Acoustic Oscillations (VAOs), may be possible from the measurement of 21cm hydrogen-line with the upcoming experiments such as HERA [408] or SKA-low [409, 410]. The VAO feature provides an effective probe of the early Universe physics that affect the relative behaviour of DM and baryons.

As I discussed earlier in Chapter 2.7.2, unlike the matter power-spectrum (where the effect of BAO is small), the VAO feature is $\mathcal{O}(1)$ in the 21cm power-spectrum [407]. Furthermore, as is the case for the BAO feature in the CMB and LSS observables, some characteristics of the VAOs are unaffected by the complicated local physics related to various feedback mechanisms which play a role during the epoch of reionization, and can be utilised to constrain effects that have a coherent impact on the observables on large-scales, such as

CIPs. In this chapter I discuss the detection significance of CIPs from measurement of the 21cm hydrogen line. This chaper is organised as follows. In Section 2.7.2 I discuss the 21cm hydrogen-line and the effect of VAOs on the brightness temperature power-spectrum. In Section 8.3 I discuss the sensitivity of the 21cm hydrogen-line spectra on the effect of CIPs. I evaluate the detection significance of CIPs using both the full shape of the power spectra as well as change in the VAO scale. For the latter I introduce as a robust measure without using the amplitude information directly. I discuss various sources of complication in Section 8.5 and conclude with discussion in Section 8.7. I describe our noise calculations in Section 8.6.

8.2 21cm simulations

I calculate the observable signal using the semi-numerical simulations provided by `21cmvFAST`[1], which is built upon `21cmFAST`[2]. Initial conditions for density and velocity fields are set at $z = 300$ with a Gaussian random field in Lagrangian space, before being evolved with the Zel'dovich approximation [411] to match the mean collapse fraction for the conditional Sheth-Tormen halo mass function [412]. The sources embedded in each halo are assumed to emit photons at a rate proportional to the increase of the total collapsed halo mass. In each cell, the excursion set formalism is used to estimate the mean number of sources contributing to the gas temperature from the surroundings. $T_{\rm S}$ is calculated from Compton scattering [413] of the Lyman-α background and the inhomogeneous heating history of the gas (through a combination of X-rays and collisional coupling). Please see [414] for more detail on this calculation.

I produce realisations of the 21cm signal in 2000Mpc boxes on 1200^3 grids of cubes, which are assumed to be a 'snapshot' of the Universe at a given redshfit (we call these 'coeval' cubes) for each observed frequency. I simulate many coeval cubes at the respective redshift from an initial (random) density field given by appropriate transfer functions for matter and relative velocities in order to evaluate the mean and variance of the anticipated power spectra.

[1] github/JulianBMunoz/21cmvFAST
[2] github.com/andreimesinger/21cmFAST

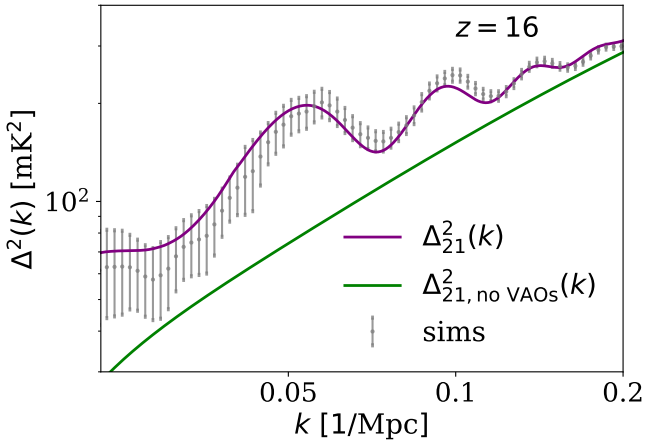

Figure 8.1: The 21cm hydrogen-line signal at $z = 16$, shown including and excluding the effect of VAOs, and for moderate foregrounds calculated using `21cmvFAST` [66]. Error bars (same for both lines, shown in the figure for the signal including VAOs only for brevity) are Poisson errors from our simulations.

8.3 CIPs and their effects on observables

8.3.1 Compensated isocurvature perturbations (CIPs)

CIPs were introduced in Section 6.4. Different from the discussion in that section, however, I now focus on uncorrelated CIPs and parametrise them with a scale-invariant power-spectrum as studied in e.g. [335]. For *uncorrelated* CIPs, cross-correlations cannot be utilised to improve the signal-to-noise, resulting in significantly more pessimistic detection prospects. It is hence important to add to the list of independent ways of measuring uncorrelated CIPs.

More generally, since the primordial CIPs could be sourced by the gravitational potential in the early Universe, they can constitute to a significant source of density differences between baryons and DM on large scales. These observational signatures of primordial CIPs are largely protected from complicated non-linear physics due to the equivalence principle, which dictate that it is difficult for local interactions to produce coherent effects on large scales.

8.3.2 CIP reconstruction from the 21cm hydrogen-line

The dominant effect of CIPs on the 21cm power-spectrum is modulating its amplitude by locally altering the baryon density which the brightness temperature depends directly via the baryon-collapse fraction. This is a linear-order effect and have been studied in the literature,

see e.g. Ref. [332]. I show the effect of CIPs on the 21cm power-spectrum amplitude in Figure 8.2. Differently from CMB and LSS observables, the direct dependence of the 21cm amplitude to baryon fraction provides a unique and potentially powerful probe of CIPs.

I evaluate the detection significance of CIPs in the absence of modelling uncertainties and for a fixed cosmology, assuming a 21cm hydrogen-line survey can locally test the observed spectra against the effect of CIPs inside different boxes of size smaller than our simulation box and the survey (voxels). I use the separate universes approximation in each voxel. The large scale CIP fluctuations in Fourier space can then be estimated from the Fourier transform of the locally measured CIP amplitude $\Delta(\vec{X})$. From the measurement of the effect on the full shape (FS) of the 21cm hydrogen-line power spectra (see upper plot in Figure 8.2), the Fisher error on the local the CIP amplitude, $\Delta_{\rm fid}$ can be calculated at some redshift z as,

$$\sigma^{-2}_{\Delta,\rm FS}(z) = \frac{1}{\Delta^2_{\rm fid}} \sum_{k-\rm bins} \left(\frac{\delta\Delta^2_{21,\rm CIP}(k,z)}{\Delta^{2,\rm obs}_{21}(k,z)} \right)^2 , \tag{8.1}$$

where the k range and the mode count is determined by the experiment sensitivity, and the voxel size. $\Delta^{2,\rm obs}_{21}(k,z)$ includes both the experiment noise and sample variance. I calculate the anticipated experimental noise for HERA and SKA-low using the software `21cmSense`[3] [415–417], which I describe in Appendix 8.6.

I assume sufficiently many voxels can be utilised for constraining CIPs; and the effect of dividing the survey volume to smaller parts can be captured by writing the reconstructed CIP field as a convolution of the true field, $\Delta(\vec{k})$, with a tophat window function in real space, which takes the form,

$$W(kr) := \frac{3}{(kr)^2}[\sin(kr) - kr\cos(kr)] , \tag{8.2}$$

in Fourier space.The reconstruction noise of CIP fluctuations in Fourier space in the full survey volume can be found as

$$N^{\rm rec}_{\Delta\Delta}(k,z) := \Lambda(z)\,[W(kr)]^{-2} , \tag{8.3}$$

where $\Lambda(z) = \sigma^2_\Delta(z) V_{\rm box}$ is approximately independent of the box volume. Finally, I define the scale-invariant CIP power spectra as

$$P_{\Delta\Delta}(k,z) := A_{\rm CIP} k^{-3} . \tag{8.4}$$

[3] github.com/jpober/21cmSense

The error on $A_{\rm CIP}$ can then be calculated as

$$\sigma_{A_{\rm CIP}}^{-2} = \frac{1}{A_{\rm CIP}^2} \sum_{k-\rm modes} \left(\frac{P_{\Delta\Delta}(k,z)}{N_{\Delta\Delta}^{\rm rec}(k,z)} \right)^2 , \tag{8.5}$$

where $\sum_{k-\rm modes} := V_{\rm bin} \sum_k {\rm d}k k^2/(2\pi^2)$ and $V_{\rm bin}$ is the survey volume inside the redshift bin. I take 8 redshift bins centred within the redshift range $z \in [10, 24]$ with redshift bin size $\Delta z = 2$. The detection signal-to-noise can be written as ${\rm SNR} = A_{\rm CIP}/\sigma_{A_{\rm CIP}}$. I show forecasts on the CIP amplitude in Figure 8.3 using the CIPs' effect on the power-spectra, inside smaller sub-volumes (or voxels) of size varying within the range $r_{\rm box} \in [150{\rm Mpc}, 1500{\rm Mpc}]$, along with constraints from utilising the VAO reconstruction alone, which I discuss next.

I find in Figure 8.3 that even the first generation 21cm surveys such as HERA and SKA-low can provide constraining power comparable to a cosmic variance limited (CVL) CMB experiment, if inference from the FS power-spectra can be utilised.

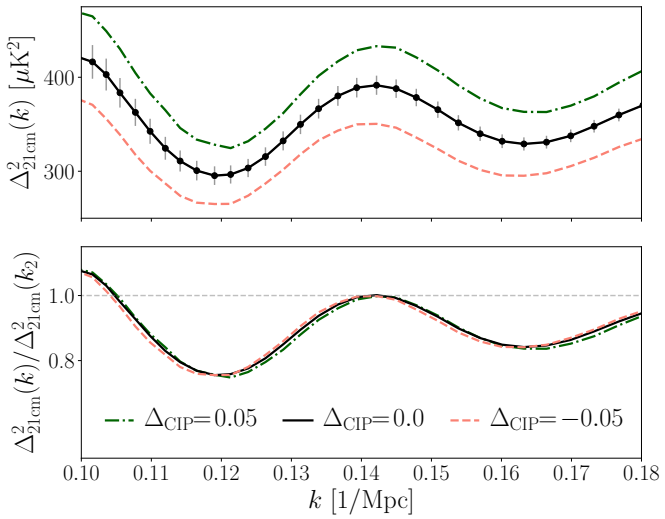

Figure 8.2: The effect of locally varying baryon-DM ratio and the speed of sound c_s of the baryon-photon plasma due to CIPs on the VAO signature, at redshift $z=16$, and calculated with low foreground assumption using `21cmvFAST` software. The black solid lines show the 21cm-hydrogen line brightness temperature power spectrum with zero CIP amplitude, $\Delta=0$. The green dash-dotted (salmon dashed) lines show the power-spectra in a universe with $\Delta=0.05\,(-0.05)$. Upper plot shows the spectra where the effect of the local variation of baryon density can be seen from the significant modulation of the spectra amplitude. Lower plot shows the spectra normalised at the location of the second displayed peak, $k = k_2$, highlighting the shift in the VAO peak locations due to varying c_s induced by varying baryon-DM ratio.

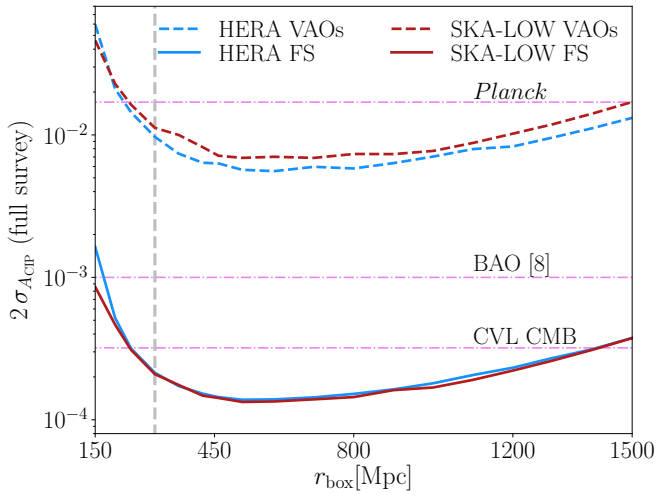

Figure 8.3: The detection significance for the CIP fluctuations from the ongoing HERA and upcoming SKA-low surveys, shown as a function of the voxel size in comoving Mpc at redshifts $z = 16$. Results are from simulations with moderate baryonic-feedback levels `21cmSense`. The *Planck* and cosmic variance limited (CVL) constraints from CMB were calculated in [335]. The BAO constraints from a galaxy survey were discussed in [338] (note these constraints are for *correlated* CIP fluctuations hence more optimistic than those I consider here). I find VAO measurements from HERA and SKA-low (labeled HERA VAOs and SKA-low VAOs) may provide robust (see text) constraints on the CIP fluctuations, improving upon *Planck*. Potentially utilising the local modulations to the full-shape (HERA FS and SKA-low FS) of the power-spectrum may go beyond the ongoing galaxy surveys and reach the fidelity of the CVL CMB experiments.

Table 8.1: The 95% confidence level upper-limit forecasts for the CIP amplitude $A_{\rm CIP}$ using the VAO scale measurement, insensitive to the 21cm power-spectrum amplitude, as described in Section 8.3.3, for various baryonic feedback scenarios, using experimental specifications for the ongoing HERA experiment and the upcoming SKA-LOW for various foreground levels (see Appendices).

HERA	Feedback		
Foregrounds	Low	Moderate	High
Pessimistic	8.03×10^{-3}	9.21×10^{-3}	9.68×10^{-3}
Moderate	4.90×10^{-3}	5.60×10^{-3}	5.20×10^{-3}
Optimistic	4.62×10^{-6}	5.10×10^{-5}	3.90×10^{-5}
SKA-LOW	Feedback		
Foregrounds	Low	Moderate	High
Pessimistic	9.05×10^{-2}	1.90×10^{-1}	1.60×10^{-1}
Moderate	4.90×10^{-3}	6.90×10^{-3}	4.60×10^{-3}
Optimistic	4.62×10^{-6}	5.35×10^{-6}	4.74×10^{-6}

Table 8.2: Similar to Table 8.1, using the full shape (FS) of the 21cm power-spectra.

HERA	Feedback		
Foregrounds	Low	Moderate	High
Pessimistic	1.48×10^{-4}	2.13×10^{-4}	1.78×10^{-4}
Moderate	9.81×10^{-5}	1.38×10^{-4}	1.15×10^{-4}
Optimistic	6.87×10^{-6}	8.91×10^{-6}	8.18×10^{-6}
SKA-LOW	Feedback		
Foregrounds	Low	Moderate	High
Pessimistic	2.27×10^{-3}	3.65×10^{-3}	3.12×10^{-3}
Moderate	9.25×10^{-5}	1.33×10^{-4}	1.16×10^{-4}
Optimistic	3.40×10^{-7}	4.29×10^{-7}	4.53×10^{-7}

8.3.3 Robust CIP reconstruction

In reality, however, local CIP measurements from the 21cm will be biased due to our poor understanding of the underlying astrophysical feedback processes and will be degenerate with various astrophysical parameters which contribute a large model uncertainty to the measurement of the amplitude of the 21cm signal. Such degeneracies can potentially be surmounted by external measurements of observables that depend on similar astrophysical processes or by careful modelling, in which case the model parameters need to be marginalised, weakening the constraining power of the 21cm observations on the effect of CIPs from the amplitude. Hence it is valuable to evaluate the prospects of detecting CIPs without directly depending on the amplitude of the 21cm power-spectrum, providing a measure potentially robust against the uncertainties of foreground and feedback scenarios.

I consider the effect of CIPs on the local 21cm power-spectrum amplitude as an approximately scale-invariant boost, which I parametrise by a fiducial value, $\delta A_{21}^{\rm CIP}$. In addition, local variations of baryon density also change the VAO scale due to spatial modulations of the sound speed of the baryon-photon fluid and induce a shift in the phase of the VAO peak locations (since oscillations in the DM and baryons are out of phase with each other). As discussed above, these spatial variations in baryon-DM ratio due to CIPs can be measured by dividing the 21cm survey into voxels and measuring the local value of CIPs from the VAO scale, for example, and using the separate-universe approximation inside each box. Here, I estimate the isolated effect on the VAO scale and phase by marginalizing over the 21cm power-spectrum amplitude, $\delta A_{21}^{\rm CIP}$. I discuss the effect of CIPs on the VAO scale in more detail in Section 8.4.

I calculate the error on the local CIP amplitude by defining a Fisher matrix with 2 parameters of the form

$$F_{\alpha\beta} = \sum_{k-\text{bins}} \text{Tr}\left[\left(\partial_\alpha \mathbf{C}\right)\mathbf{C}^{-1}\left(\partial_\beta \mathbf{C}\right)\mathbf{C}^{-1}\right], \tag{8.6}$$

where $\alpha, \beta \in \{\Delta(X), \delta A_{21}^{\text{CIP}}\}$ and $\mathbf{C} = \Delta_{21}^{2,\text{obs}}(k,z)$. I calculate the error on the local CIP amplitude as

$$\sigma_{\Delta\Delta} = \sqrt{F^{-1}_{\Delta\Delta}}, \tag{8.7}$$

which I find to be around an order of magnitude larger than that provided by the FS power-spectra. Since I assume the constraints in this section are provided by the VAOs, I refer to these results as the 'VAO constraints' on the CIPs. Lastly, as before, I use Eqns. (8.3) and (8.5) to evaluate the prospects of detecting the CIP effect over the full survey volume.

In Figure 8.3, I compare our results in this section with the constraints from the FS discussed earlier. I find using the full statistical power of the 21cm power-spectrum measurement, upcoming experiments such as HERA and SKA-low may provide higher detection significance to CIPs then compared to cosmic-variance-limited (CVL) BAO and CMB measurements for moderate feedback and foreground scenarios. Using constraints only from the measurement of the VAO feature, however, the prospects of detecting CIPs will be lower, while nevertheless improving upon *Planck*.

8.4 CIP reconstruction from the VAO scale

8.4.1 VAO scale and the CIPs

As discussed in Section 8.3.3, CIPs locally induce spatial modulations of the sound speed due to changing baryon and DM densities. This affects the VAO scale. In this section I evaluate the detection prospect of CIPs from measuring the local variations on the VAO scale by modelling the smooth part of the power-spectrum and isolating the VAO contribution.

In order to calculate the error on local CIP amplitude from measurements of the VAO scale, I assume the total VAO detection SNR can be recast as the error on the VAO scale $\varepsilon\, r_{\text{VAO}}/\sigma_{r_{\text{VAO}}}$ with some efficiency parameter ε. The fidelity of the VAO scale measurement will depend on the modelling uncertainties of the non-oscillatory part of the 21cm signal and can be evaluated by various template fitting methods used extensively in the literature for

the BAO scale measurement from galaxy surveys. I discuss these later in Section 8.4.2, and leave a more involved analysis to future work.

CIPs locally modulate the sound speed of the baryon-photon fluid as $c_s \to \alpha(\vec{X})\, c_s$, where similar to e.g. [338], I Taylor expand $\alpha(\vec{X})$ in the limit $\Delta(\vec{X}) \ll 1$ as

$$\alpha(\vec{X}) \simeq 1 + \frac{\Delta(\vec{X})}{C}, \tag{8.8}$$

where $C \simeq -5.33$ [338]. The relevant observable is the local modulation of the VAO scale, $r_{\rm VAO} \to \alpha(\vec{X})\, r_{\rm VAO}$, which can be related to the separation between two peaks in Fourier space, for example, approximately as $k_{\rm VAO} \simeq 2\pi / r_{\rm VAO}$, where $r_{\rm VAO} \simeq 150$Mpc for ΛCDM with *Planck* best fit parameters. Hence the SNR on the CIP amplitude measured in a voxel (using separate universe approximation) differs from the SNR of the VAOs by a factor of C^{-1}.

Having assumed the SNR of the VAO measurement is equal to the inverse of the fractional error on the VAO scale, I can write

$$\sigma_{r_{\rm VAO}}^{-2} = \frac{1}{r_{\rm VAO}^2} \sum_{k-{\rm bins}} \left[\frac{\delta\Delta^2_{21,{\rm VAOs}}(k,z)}{\Delta^{2,{\rm obs}}_{21}(k,z)} \right]^2, \tag{8.9}$$

where I defined $\delta\Delta^2_{21,{\rm VAOs}}(k,z)$ as the difference between the 21cm power-spectra calculated with and without the effect of VAOs. The observed 21cm signal in the denominator includes sample variance, experimental noise and the 21cm spectra excluding VAOs. I then relate the local VAO SNR to the SNR on the CIP amplitude as $\sigma_{r_{\rm VAO}} / r_{\rm VAO} \simeq C^{-1} \sigma_\Delta$, and calculate the CIP reconstruction noise as defined in Eq. (8.3).

I find, setting $\varepsilon = 1$, the constraints from the VAO scale measurement matches very well the method described in Section 8.3.3 where I had marginalized over the amplitude of the 21cm power-spectrum.

8.4.2 The fidelity of the VAO reconstruction

Above I assumed the SNR on the VAO measurement can be related to the SNR on the VAO scale with some efficiency factor ε. While $\varepsilon \simeq 1$ may probably be a good approximation in the high SNR regime, for the upcoming experiments where VAOs may only be detected to few σ significance (and with the large astrophysical model uncertainties present in the calculation of non-oscillatory part of the 21cm signal), the constraints on the VAO scale $r_{\rm VAO}$ may be poorer. A relatively robust assessment of the detection prospects of the VAO scale could

be achieved by modelling the non-oscillatory part of the 21cm signal by some higher-order polynomial, and perform a maximum-likelihood analysis of these model parameters along with Alcock-Patchinsky (AP) parameters, as was done in [66], for example. I leave a more detailed assessment of the AP parameter reconstruction from the VAO signal to a future study.

8.5 Local modulations of BAOs from other effects

So far I assumed only CIPs modulate baryon-DM fraction in the 21cm signal spatially. In reality there can be a multitude of effects that impact the BAO scale, either by inducing biases locally, or contributing to noise on the global CIP signal.

Regions corresponding to under- and over-densities due to very long-wavelength modes (with $k \ll 2\pi/r_{\rm VAO}$) of matter perturbation can mimic closed or open universes, which could vary the BAO scale and the cosmological parameters locally. Note, however, for the uncorrelated CIPs I consider in this chaper, I expect the long-wavelength matter fluctuations will not introduce a bias to our measurement of the power-spectra. These fluctuations may nevertheless contribute a noise to our calculation comparable to the galaxy shot noise. More generally, I anticipate the ΛCDM priors from cosmological measurements will dominate the (cosmological) parameter constraints locally, allowing our assumption of fixed cosmology to be sufficiently robust for our purposes in this chaper.

Furthermore, short wavelength fluctuations $k \gtrsim 2\pi/r_{\rm VAO}$ can also contribute to the noise on the BAO measurement in each voxel by locally stretching or shrinking galaxies. This can potentially contribute to lowering the SNR by boosting the local error on the CIP measurement.

8.6 `21cmSense`: Telescope sensitivity estimation

Foreground mitigation for the cosmological 21cm signal is performed either via wedge suppression or avoidance[4]. 21CMSENSE [415–417] is a python module designed to estimate the noise power spectra when a given telescope array observed the 21cm signal via foreground avoidance.

[4]Please see [418, 419] for detailed description of the EoR window and foreground wedge.

In every u-v bin[5] the noise is calculated as,

$$\delta^2_{\rm uv}(\mathbf{k}) \approx X^2 Y \frac{\mathbf{k}^3}{2\pi^2} \frac{\Omega_{\rm Eff}}{2t_0} T^2_{\rm sys}, \tag{8.10}$$

where X^2Y is a scalar conversion from an observed solid angle (or effective beam, $\Omega_{\rm Eff}$) to a comoving distance [420]. The system temperature ($T_{\rm sys}$) can be calculated as $T_{\rm sys}(z) = T_{\rm rx}(z) + T_{\rm gal}(z)$, where $T_{\rm rx}(z) = 0.1T_{\rm gal}(z) + 40{\rm K}$ is the receiver temperature and $T_{\rm gal}(z) = T_{408}(408{\rm MHz}/\nu(z))^{2.75}$ is the contribution from our own galaxy at a frequency ν with $T_{408} = 25{\rm K}$ [410, 421]. t_0 is the total observation time.

Assuming Gaussian errors on cosmic variance, I express the total uncertainty with an inversely weighted sum across all the k modes as

$$\delta\Delta^2_{21}(k) = \left\{ \sum_i \frac{1}{[\delta^2_{{\rm uv},i}(k) + \Delta^2_{21}(k)]^2} \right\}^{-\frac{1}{2}}, \tag{8.11}$$

where the index, i, represents multiple measurements of the same frequency from redundant baselines within the array. This is therefore the total noise, including both sample variance and thermal noise.

`21cmSense` can implement foreground-wedge avoidance with three levels of severity:

- *Pessimistic* - baselines are added incoherently. No k modes are included from within the horizon wedge (and buffer zone);
- *Moderate* - all baselines are added coherently. No k modes are included from the horizon wedge (and buffer zone);
- *Optimistic* - All baselines in the primary field of view (no buffer zone) are added coherently.

To reiterate, I can write the foreground wedge simply as

$$k_\parallel = a + bk_\perp\,, \tag{8.12}$$

[5]Different from traditional telescopes, a radio interferometer does not produce sky-images directly. A radio interferometer instead measures the Fourier transform of the distribution of sky brightness in a plane that is perpendicular to the line of sight. The coordinates on this plane (for some particular baseline) are labelled u and v, and are taken at a distance from the origin corresponding to the length of the baseline, measured in wavelengths.

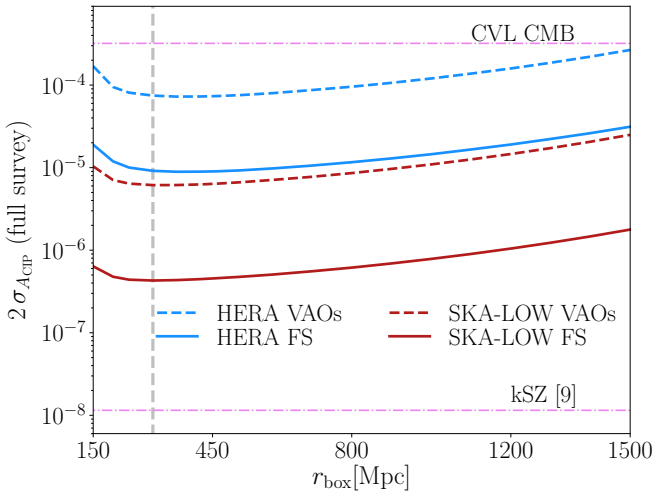

Figure 8.4: The detection significance for the CIP fluctuations from the ongoing HERA and upcoming SKA-low surveys, similar to Figure 8.3 except for the *optimistic* foreground-wedge assumption. The kSZ constraints are calculated in Ref. [17].

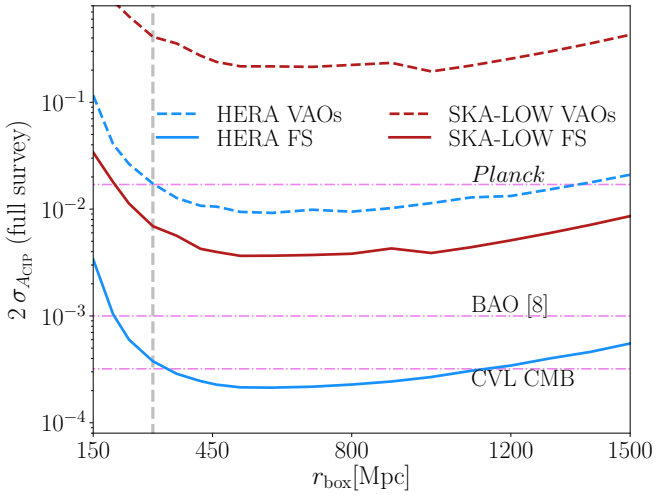

Figure 8.5: The detection significance for the CIP fluctuations from the ongoing HERA and upcoming SKA-low surveys, similar to Figure 8.3 except for the *pessimistic* foreground-wedge assumption

where $k_{\parallel}$ and $k_{\perp}$ are the Fourier modes projected on the line-of-side and the transverse plane respectively; b depends on the instrument beam, bandwidth and underlying cosmology; a is the user=defined buffer zone. Typically in the *Pessimistic* or *Moderate* case $a = 0.1h\text{Mpc}^{-1}$, meaning modes below the line (in Equation 8.12) are rejected as they are likely contaminated by foregrounds. I show the CIP forecasts from Section 8.3 with optimistic and pessimistic foreground-wedges in Figures 8.4 and 8.5, respectively.

I apply 21CMSENSE to two telescopes. Firstly, for SKA I use the specification of SKA1-low. Only the core 225 stations are used as the small baselines generate 21cm sensitivity for high redshift observations. Including longer baselines significantly slows computation and adds negligible precision to the measurement at the redshifts used in this work. Each station[6] has diameter of 35 m giving SKA a core collecting area of 374444 m^2 accross a total bandwidth ranging $[50, 350]$ MHz. SKA is simulated for 6 hours per night for a tracked scan (different fields for 1 hour each) and as a drift scan.

Secondly, I consider HERA [422, 423], with stations located in a filled hexagonal grid (11 along each side). Each station is 14 m in diameter giving a total collecting area of 50,953 m^2 across a total bandwidth ranging $[50, 250]$ MHz. The antennae are taken to be at $T_{rx} = 100$K. HERA is operated in drift scan mode for 6 hours per night.

Both instruments observe for 1080 hours and both instruments have the bandwidth taken as 8 MHz (centred on the frequency relating to the redshift of each coeval simulation box).

8.7 Discussion

In this chaper, I have utilised the constraining power of the 21cm temperature brightness measurements to evaluate the detection prospects of CIPs. I evaluated the detection significance of CIPs from measurements of both the total change in the power-spectra as well as the varying VAO scale, in local voxels of varying size. I have shown that the ongoing HERA and upcoming SKA-low experiments may be able to measure the uncorrelated CIP amplitude up to a precision comparable to the CMB and LSS experiments.

Upcoming novel observational opportunities will allow significant advances in our understanding of the fundamental properties of the Universe. Among others, characteristics of relative baryon and DM fluctuations prove valuable for probing deviations from adiabaticity that may be sourced by fundamental physics during the early Universe. Constraining CIPs may rule out models of multi-field inflation, or allow less ambiguous measurements of early Universe signatures such as primordial non-Gaussianity.

The uncorrelated CIPs considered in this chaper are difficult to constrain on large scales since the sample variance cancellation techniques (as done in [17], for example) cannot be utilised in this case to increase the detection significance. Hence, adding to the number of independent measurements is generally valuable. The current constraints on uncorrelated CIP fluctuations afforded by *Planck* and galaxy surveys still allow for the CIP amplitude

[6] Station locations are taken from skatelescope.org/key-documents

to be significantly larger than the adiabatic fluctuations we measure in the Universe. As discussed in the text, constraints provided by the upcoming 21cm experiments may have the potential to improve current constraints by orders of magnitude in the next decade.

Chapter 9

Anisotropy of the GW background with PTAs

In this final Chapter I digress and discuss my work with Marc Kamionkowsi and Andrew Jaffe on evaluating the prospects for detecting the statistical anisotropy of the stochastic gravitational wave background, anticipated to be produced by super massive black hole binaries. This astrophysical signal is anticipated to be detected by pulsar timing arrays (PTAs), sets of pulsars which are analyzed to search for correlated signatures in their pulse arrival times. In this chapter I discuss our work in [424] where we used a formalism more common in the study of cosmological fluctuations in order to evaluate the minimum level of statistical anisotropy that can be detected by the ongoing PTA experiment. I have essentially contributed to the conceptualisation of the project, as well as the text, the analysis and the calculation and presentation of the results. All of these items (except for the production of plots and the numerical calculations) also saw significant contributions from Marc Kamionkowski and Andrew Jaffe. The purpose of this chapter is not to provide a rigorous and pedagogical discussion of the relevant gravitational wave signal or the experimental specifications of pulsar timing arrays. The chapter aims mainly to provide a simple and straight forward conceptual analysis of the prospects of detecting deviations from statistical anisotropy with the gravitational wave signal in order to potentially guide the community towards profitable directions (or away from pessimistic ones).

9.1 Introduction

A longstanding effort [425–430] to detect a stochastic gravitational-wave background with pulsar-timing arrays consists now of three major efforts—the Parkes Pulsar Timing Array (PPTA) [431, 432], North American Nanohertz Observatory for Gravitational Waves (NANOGrav) [433], and the European Pulsar Timing Array (EPTA) [434]–that collaborate through an International Pulsar Timing Array (IPTA) [435]. The effects of gravitational waves on the arrival times of pulses from pulsars [436, 437] produce a characteristic angular correlation [438] in the pulsar-timing residuals. Signals at the frequencies $\sim$ 1nHz are expected from the mergers of supermassive-black-hole binaries [439, 440]. There are also prospects to use complementary information from stellar astrometry [441–445] as the apparent position of distant stars will oscillate with a characteristic pattern on the sky due to GWs.

It is still not understood, though, whether the local GW signal due to SMBH mergers will be the type of stochastic background that arises as the sum of a large number of cosmological sources, or whether it will be dominated by just a handful—or even just one—source [446–450]. Roughly speaking, if there are $\sim N$ Poisson sources contributing to the signal, then the amplitude of anisotropy in the GW background should be $\sim N^{-1/2}$. A first obvious step, after the initial detection of a gravitational-wave signal, will therefore be to seek the anisotropy in the background that may arise from a finite number of sources. Exotic sources might also lead to anisotropy [451].

Prior work [452–454] has developed tools to characterize and seek with PTAs anisotropy in the GW background that were then implemented in a null search [455]. This anisotropy was characterized (as it is here also) in terms of an uncorrelated and unpolarized background of gravitational waves with a direction-dependent intensity parametrized in terms of spherical-harmonic expansion of the intensity. Here we re-derive anisotropy-detection tools using mathematical objects (bipolar spherical harmonics; BiPoSHs [456–458]) developed for analogous problems in the study of the cosmic microwave background. The analysis here provides some simplifications and insights and also intuitive estimates for the smallest detectable signals. We provide numerical results for the smallest detectable dipole-anisotropy amplitude as a function of the signal-to-noise with which the isotropic signal is detected and as a function of the number of pulsars in the array. We restrict our attention to PTAs but describe how the detectability will be augmented with the inclusion of astrometry.

This chapter is organized as follows: In Section 9.2 we describe the idealized observables that we model. In Section 9.3 we review the standard Hellings-Downs correlation function

(and its harmonic-space equivalent, the timing-residual power spectrum) used to detect the GW background. Section 9.4 introduces the bipolar-spherical-harmonic formalism and describes how to infer the BiPoSH amplitudes from the observables. Section 9.5 describes the model of an uncorrelated anisotropic background we consider here (and considered in Refs. [453, 454]) and calculates the BiPoSH coefficients for the model in terms of the model's anisotropy parameters g_{LM}. Section 9.6 derives minimum-variance estimators for the spherical-harmonic coefficients g_{LM} that parametrize the anisotropy and the variances $(\Delta g_{LM})^2$ with which they can be measured. Section 9.7 evaluates the smallest detectable anisotropy beginning with a dipole and then generalizing to anisotropies of higher-order multipole moment and then the anisotropy due to a beam of uncorrelated unpolarized gravitational waves from a specific direction. Section 9.8 describes how the previous results, obtained for a single timing-residual map, are generalized to incorporate the multiple maps that may be obtained from time-domain information. We discuss the extension to astrometry and make closing remarks in Section 9.9.

9.2 Harmonic and real-space angular observables

PTA measurements are characterized by the temporal evolution of the timing residuals and the dependence of the observables as a function of position on the sky. Here we focus primarily on the angular structure. To simplify, we speak here of the "timing residuals" $z(\hat{n})$ measured in a PTA as a function of position $\hat{n}$ on the sky. These "timing residuals," in a more complete analysis, will be obtained from some convolution of the timing residuals (TRs) with a time-sequence window function (and there may well be a number of such timing residuals that are obtained from convolutions of the full timing-residual data with different time-sequence window functions—more on this in Section 9.8). Strictly speaking, therefore, each appearance of a GW power spectrum $P_h(k)$ in the expressions below should be replaced by $P_h(k)\,[W(k)]^2$ where $W(k)$ is an appropriate time-domain window function.

Any such timing residual $z(\hat{n})$ can be expanded

$$z(\hat{n}) = \sum_{\ell=2}^{\infty} \sum_{m=-\ell}^{\ell} z_{\ell m} Y_{\ell m}(\hat{n}), \tag{9.1}$$

in terms of spherical harmonics $Y_{\ell m}(\hat{n})$, which constitute a complete orthonormal basis for scalar functions on the two-sphere. The expansion coefficients are obtained from the inverse

transform,

$$z_{\ell m} = \int d^2\hat{n}\, z(\hat{n})\, Y^*_{\ell m}(\hat{n}). \tag{9.2}$$

The sum in Eq. (9.1) is only over $\ell \geq 2$, as the transverse-traceless gravitational waves that propagate in general relativity give rise only to timing-residual patterns with $\ell \geq 2$. We assume that the timing residuals (convolved with a time-sequence window function) are real, and so $z^*_{\ell m} = (-1)^m z_{\ell,-m}$. [1] Note that specification of $z(\hat{n})$ is equivalent to specification of $z_{\ell m}$ and *vice versa*—they are two different ways to describe the same observables.

9.3 Power spectrum and correlation function

A gravitational wave with polarization tensor h_{ab} induces a fluctuation in the observed pulsar's pulse frequency, $\delta\nu/\nu$ in the form

$$\frac{\delta\nu}{\nu} = -H^{ab}[h_{ab}(t_{\rm e}, x_{\rm e}) - h_{ab}(t_{\rm p} - D/c, x_{\rm p})]\,, \tag{9.3}$$

where H^{ab} is some geometrical projection that depends on the direction of the gravitational wave with respect to earth and the pulsar, D is the distance of the gravitational wave source to earth, $t_{\rm e}$ and $x_{\rm e}$ are the time and position evaluated at Earth. $t_{\rm p}$ and $x_{\rm p}$ are the time and position at the pulsar. The shift in frequency can be interpreted as a net shift in frequency (i.e. a redshift) and are called 'timing residuals'. The timing residuals $z(\hat{n}, \hat{k})$ arising from a gravitational wave moving in direction $\hat{k}$ are given by [459–462]

$$z(\hat{n}; \hat{k}) = \frac{n^a n^b h_{ab}}{2(1 + \hat{k}\cdot\hat{n})}\,. \tag{9.4}$$

Strictly speaking, the timing residuals are observed as a function of time, but the angular pattern here is that after those time-domain data have been convolved with a time-domain window function so that the resulting map $z(\hat{n})$ is then real.

As discussed in Refs. [463, 445] (and below), the rotationally-invariant observed power spectrum $C_\ell \propto \sum_m |z_{\ell m}|^2/(2\ell+1)$ for this plane wave is

$$C_\ell \propto \frac{(\ell-2)!}{(\ell+2)!}. \tag{9.5}$$

[1] In time-frequency Fourier space, $z(f)$ would be complex, but satisfy a similar reality condition.

Since Eq. (9.4) is a scalar and linear in h_{ab}, the timing residuals from *any* collection of plane waves—i.e., any gravitational-wave signal—will have the power spectrum of Eq. (9.5).[2] If the timing residuals $z(\hat{n})$ arise from a realization of a statistically isotropic gravitational-wave background, then the spherical-harmonic coefficients $z_{\ell m}$ of the observed $z(\hat{n})$ map will satisfy

$$\langle z_{\ell m} z^*_{\ell' m'} \rangle = C_\ell \, \delta_{\ell\ell'} \delta_{mm'}, \tag{9.6}$$

where the angle brackets denote the average over all realizations of the gravitational-wave background, and $\delta_{\ell\ell'}$ and $\delta_{mm'}$ are Kronecker deltas. Eq. (9.6) states that if the GW background is statistically isotropic then all of the $z_{\ell m}$ are uncorrelated and that each $z_{\ell m}$ is some number selected from a distribution of variance C_ℓ. The resulting map, $z(\hat{n})$, is then real after convolution with the appropriate time-domain window function.

The timing-residual power spectrum is related to the rotationally-invariant two-point autocorrelation function [454],

$$C(\Theta) = \langle z(\hat{n}) z(\hat{m}) \rangle_{\hat{n}\cdot\hat{m}=\cos\Theta} = \sum_\ell \frac{2\ell+1}{4\pi} C_\ell P_\ell(\cos\Theta); \tag{9.7}$$

i.e., the product of the timing residuals in two different directions separated by an angle Θ, averaged over all such pairs of directions. The two-point autocorrelation function from a stochastic GW background is the classic Hellings-Downs curve,

$$C(\Theta) \propto (1/2)(1-x)\log\left[\frac{1}{2}(1-x)\right] - \frac{1}{6}\left[\frac{1}{2}(1-x)\right] + \frac{1}{3}, \tag{9.8}$$

where $x = \cos\Theta$. Again, the two-point autocorrelation function has this form regardless of whether the GW background is statistically isotropic or otherwise.

Since the power spectrum C_ℓ and two-point autocorrelation function $C(\Theta)$ do not depend on whether the background is isotropic or otherwise, the natural first step in any effort to detect a GW background is to establish from the data that these are nonzero. Formulas to derive C_ℓ from (idealized) data are provided below.

[2] It is mathematically possible—e.g., from a standing wave composed of two identical gravitational waves moving in opposite directions— to get a different ℓ dependence, but hard to imagine how any astrophysical scenario could produce a power spectrum, that differs.

9.4 Bipolar spherical harmonics

There is, however, far more information in a map $z(\hat{n})$ (or equivalently, its set of $z_{\ell m}$) than that provided by the timing-residual power spectrum and Hellings-Downs correlation. The most general correlation between any two $z_{\ell m}$s can be written (see, e.g., Ref. [464, 465]),

$$\begin{aligned}\langle z_{\ell m} z^*_{\ell' m'} \rangle &= C_\ell \delta_{\ell\ell'} \delta_{mm'} \\ &\quad + \sum_{L=1}^{\infty} \sum_{M=-L}^{L} (-1)^{m'} \langle \ell\, m\, \ell',\, -m' | LM \rangle A^{LM}_{ll'},\end{aligned} \tag{9.9}$$

where C_ℓ is the (isotropic) power spectrum introduced above, $\langle \ell\, m\, \ell'\, m' | LM \rangle$ are Clebsch-Gordan coefficients, and the $A^{LM}_{ll'}$ are BiPoSH coefficients. Note that the power spectrum C_ℓ can be identified as $(-1)^\ell A^{00}_{\ell\ell}/\sqrt{2\ell+1}$.

As Eq. (9.7) indicates, the Hellings-Downs curve $C(\Theta)$ considers information obtained only from the angular separation Θ between two directions $\hat{n}$ and $\hat{m}$, but disregards any information about the specific directions $\hat{n}$ and $\hat{m}$. This additional information is parametrized with BiPoSHs in terms of BiPoSH coefficients $A^{LM}_{\ell\ell'}$ that characterize departures from statistical isotropy. If there is a dipolar power anisotropy (higher flux of GWs from one direction than from the opposite direction), it is characterized by the $L = 1$ (dipolar) BiPoSHs, and the different $M = 0, \pm 1$ components provide the spherical-tensor representation of the dipole. A quadrupolar power asymmetry (e.g., as might arise if there were GWs coming from the $\pm\hat{z}$ direction) are characterized by the $L = 2$ BiPoSH coefficients, and so forth.

9.4.1 Measurement of BiPoSH coefficients

We suppose that the "data" come in the form of a collection of measured values $z^{\rm data}_{\ell m} = z_{\ell m} + z^{\rm noise}_{\ell m}$ each of which has a contribution $z_{\ell m}$ from the signal and another $z^{\rm noise}_{\ell m}$ from measurement noise. We assume that the noise in each $z^{\rm noise}_{\ell m}$ are uncorrelated and that each $z_{\ell m}$ has a variance N^{zz} (which we further assume to be ℓ-independent – the white-noise power spectrum – a good approximation if the timing-residual noises in all pulsars are comparable).

Estimators for the BiPoSH coefficients are then obtained from

$$\widehat{A^{LM}_{ll'}} = \sum_{mm'} z^{\rm data}_{lm} z^{*\,\rm data}_{l'm'} (-1)^{m'} \langle l\, m\, l',\, -m' | LM \rangle. \tag{9.10}$$

This estimator has a variance, under the null hypothesis (for even $L+\ell+\ell'$) [464],

$$\left\langle \left| \widehat{A^{LM}_{ll'}} \right|^2 \right\rangle = (1+\delta_{\ell\ell'}) C_\ell^{\rm data} C_{\ell'}^{\rm data}, \tag{9.11}$$

where $C_\ell^{\rm data} = C_\ell + N^{zz}$ is the power spectrum of the map, which includes the signal and the noise. The $\delta_{ll'}$ arises since the root-variance to a variance of a Gaussian distribution is $\sqrt{2}$ times the variance. We will see below that we need consider only combinations with even $\ell+\ell'+L$. If the map $z(\hat{n})$ is real, then $A^{LM}_{\ell\ell'} = A^{LM}_{\ell'\ell}$ (for even $\ell+\ell'+L$), and the estimators $\widehat{A^{LM}_{\ell\ell'}}$ and $\widehat{A^{LM}_{\ell'\ell}}$ are the same. The covariance between any two other different $\widehat{A^{LM}_{\ell\ell'}}$ vanishes.

By setting $L=0$ and identifying $C_\ell = (-1)^\ell A^{00}_{\ell\ell}/\sqrt{2\ell+1}$, we recover the power-spectrum estimator,

$$\widehat{C_\ell} = \sum_{m=-\ell}^{\ell} \frac{|z^{\rm data}_{\ell m}|^2}{2\ell+1} - N^{zz}, \tag{9.12}$$

which has a variance

$$\left\langle (\Delta C_\ell)^2 \right\rangle = \frac{2}{2\ell+1} \left(C_\ell^{\rm data} \right)^2. \tag{9.13}$$

Under the null hypothesis of no gravitational-wave background (to be distinguished from the null hypothesis of a gravitational-wave background that is isotropic), $C_\ell^{\rm data} = N^{zz}$. This result will be used in Eq. (9.25) below.

9.5 Model and BiPoSH Coefficients

We now focus on understanding the ℓ,ℓ' dependence of the BiPoSH coefficients $A^{LM}_{\ell\ell'}$. To do so, we must understand the dependence of the observable $z(\hat{n})$ on the gravitational-wave background.

9.5.1 Model of anisotropic background

In order to link measurements of the timing residuals to an underlying gravitational wave background, we need a model for the statistics of that background. Although there are an infinitude of ways the background can depart from statistical isotropy, we consider (as did

Refs. [453, 454]) here those that can be parametrized as

$$\left\langle h_s(\vec{k}) h^*_{s'}(\vec{k}') \right\rangle = \frac{1}{4}\delta_{ss'}(2\pi)^3\delta_D(\vec{k}-\vec{k}')P_h(k) \times \left[1+\sum_{L>0}\sum_{M=-L}^{L} g_{LM}Y_{LM}(\hat{k})\right], \tag{9.14}$$

where $h_s(\vec{k})$ is the amplitude of the gravitational-wave mode with wavevector $\vec{k}$ and polarization $s = +, \times$. With the Dirac delta function in this parametrization, we are still preserving the assumption that different Fourier modes are uncorrelated. We are also assuming that the frequency dependence of the GW background is the same in all directions[3] and that the $+$ and $\times$ modes are still equally populated (i.e., that the background is unpolarized). The sum over spherical harmonics allows, however, for the most general angular dependence of the gravitational-wave flux, parametrized by spherical-harmonic coefficients g_{LM}. Here, the gravitational-wave power spectrum is $P_h(k)$, and an isotropic background is recovered for $g_{LM} \to 0$ for all $L > 0$. In this model, the g_{LM} are the spherical harmonic coefficients of the map of total gravitational-wave power.

Since the term in the brackets in Eq. (9.14) must be positive, the spherical-harmonic coefficients are restricted to be $g_{L0} \leq \sqrt{4\pi/(2L+1)}$, and a roughly similar bound applies to $\sqrt{2}\,\mathrm{Re}\,g_{LM}$ and $\sqrt{2}\,\mathrm{Im}\,g_{LM}$ for $M \neq 0$.

9.5.2 Resulting timing-residual BiPoSH coefficients (and angular power spectrum)

We now calculate the BiPoSH amplitude that arises from a GW background of the form in Eq. (9.14), based on its imprint, Eq. (9.4). If the GW direction is taken to be $\hat{k} = \hat{z}$, then this becomes

$$z(\hat{n};\hat{k}=\hat{z}) = h_+(1-\cos\theta)\cos 2\phi + h_\times(1-\cos\theta)\sin 2\phi, \tag{9.15}$$

where h_+ and $h_\times$ (both most generally complex) are the amplitudes of the $+$ and $\times$ polarizations.

[3] This restriction is irrelevant, given that the angular pattern induced by a gravitational wave is independent of the GW frequency.

This plane wave is described by spherical-harmonic coefficients,

$$\begin{aligned} z_{\ell m}(\hat{z}) &= z_\ell \left[h_+ (\delta_{m2} + \delta_{m,-2}) + i h_\times (\delta_{m2} - \delta_{m,-2}) \right] \\ &= z_\ell \left[(h_+ + i h_\times)\delta_{m2} + (h_+ - i h_\times)\delta_{m,-2} \right], \end{aligned} \tag{9.16}$$

where we defined

$$z_\ell \equiv (-1)^\ell \sqrt{\frac{4\pi(2\ell+1)(\ell-2)!}{(\ell+2)!}}. \tag{9.17}$$

From this result, we can construct the spherical-harmonic coefficients for a plane wave in any other direction. To do so, we write

$$z(\hat{n};\hat{k}) = \sum_{\ell m m'} Y_{\ell m}(\hat{n}) D^{(l)}_{m m'}(\phi_k, \theta_k, 0) z_{\ell m'}(\hat{z}), \tag{9.18}$$

where $D^{(\ell)}_{m m'}(\phi_k, \theta_k, 0)$ are the Wigner rotation functions.[4] We thus infer, given Eq. (9.16), which restricts the m' sum to ± 2, that a gravitational wave moving in the $\hat{k}$ direction imprints a pulsar-timing-residual pattern described by spherical-harmonic coefficients,

$$\begin{aligned} z_{\ell m}(\hat{k}) &= \sum_{m'} D^{(\ell)}_{m m'}(\phi_k, \theta_k, 0) z_{\ell m'}(\hat{z}) \\ &= z_\ell \left[(h_+ + i h_\times) D^{(\ell)}_{m2} + (h_+ - i h_\times) D^{(\ell)}_{m,-2} \right], \end{aligned} \tag{9.19}$$

where h_+ and $h_\times$ are the GW amplitudes for this wave, and the arguments of the rotation matrices are $(\phi_k, \theta_k, 0)$.

Given this result, we can now calculate the BiPoSH coefficients for a direction-dependent power spectrum of the form given in Eq. (9.14). We start by noting that a given gravitational-wave pattern is described by a set of amplitudes $h_+(\vec{k})$ and $h_\times(\vec{k})$ for each possible wavevector $\vec{k}$. The spherical-harmonic coefficients induced by this gravitational-wave pattern are

$$z_{\ell m} = \sqrt{2} z_\ell \int \frac{d^3k}{(2\pi)^3} \left[h_R(\vec{k}) D^{(\ell)}_{m2} + h_L(\vec{k}) D^{(\ell)}_{m,-2} \right], \tag{9.20}$$

[4] Strictly speaking, this rotation most generally involves three Euler rotations. We will always choose, however, the $+$ and $\times$ polarizations to align with the $\hat{\theta}$-$\hat{\phi}$ directions. The rotation thus involves first a rotation about the $\hat{z}$ direction by the azimuthal angle ϕ_k of $\hat{k} = (\theta_k, \phi_k)$ and then another rotation by the polar angle θ_k.

where $h_R(\vec{k}) = 2^{-1/2}(h_+ + ih_\times)(\vec{k})$ and $h_L(\vec{k}) = 2^{-1/2}(h_+ - ih_\times)(\vec{k})$. The correlation between any two spherical-harmonic coefficients is therefore

$$\begin{aligned}\langle z_{\ell m} z^*_{\ell' m'} \rangle &= z_\ell z_{\ell'} \int \frac{d^3k}{(2\pi)^3} P_h(k) \left[1 + \sum_{LM} g_{LM} Y_{LM}(\hat{k}) \right] \\ &\quad \times \left[D^{(\ell)}_{m2}(\hat{k}) \left(D^{(\ell')}_{m'2}(\hat{k}) \right)^* \right. \\ &\quad \left. + D^{(\ell)}_{m,-2}(\hat{k}) \left(D^{(\ell')}_{m',-2}(\hat{k}) \right)^* \right]. \end{aligned} \tag{9.21}$$

After performing the integral over directions $\hat{k}$ we find an expression for $\langle z_{\ell m} z^*_{\ell' m'} \rangle$ of the form Eq. (9.9) with

$$C_\ell = \frac{z_\ell^2}{2\ell + 1} I, \tag{9.22}$$

and

$$A^{LM}_{\ell\ell'} = (-1)^{\ell - \ell'} (4\pi)^{-1/2} g_{LM} z_\ell z_{\ell'} H^L_{\ell\ell'} I, \tag{9.23}$$

where

$$H^L_{\ell\ell'} \equiv \begin{pmatrix} \ell & \ell' & L \\ 2 & -2 & 0 \end{pmatrix}, \tag{9.24}$$

in terms of Wigner-3j symbols, and we defined $I \equiv [4\pi/(2\pi)^3] \int k^2 \, dk \, P_h(k)$. The two terms in Eq. (9.21) cancel if $\ell + \ell' + L$ is odd, and so $A^{LM}_{\ell\ell'}$ is nonzero only for even $\ell + \ell' + L$. There are two interesting features of Eq. (9.23). First, the ℓ dependence appears only in the factors $z_\ell z_{\ell'} H^L_{\ell\ell'}$; as we will see below, this will allow us to write an optimal estimator for the anisotropy coefficients g_{LM}. Second, the power spectrum and BiPoSH coefficients both depend in the same way on the power spectrum $P_h(k)$.

9.6 Minimum-variance estimators of anisotropy

9.6.1 Isotropic signal-to-noise

Before evaluating the smallest detectable anisotropy, we write the power spectrum in terms of the signal-to-noise ratio (SNR) with which the isotropic signal is detected; this will be useful below. To do so, we recall that the variance with which any given C_ℓ can be measured is $[2/(2\ell + 1)](N^{zz})^2$. The signal-to-noise ratio SNR from a measurement that accesses

multipole moments up to $\ell_{\rm max}$ is then given by (see Ref. [463] for a derivation)

$$(\mathrm{SNR})^2 = \sum_{\ell=2}^{\ell_{\rm max}} \frac{(2\ell+1)}{2} \left(\frac{C_\ell}{N^{zz}}\right)^2 \tag{9.25}$$

and by using Eq. (9.22), we find $I^2 \simeq [1.17(\mathrm{SNR})N^{zz}]^2$ in the limit $\ell_{\rm max} \to \infty$, which turns out to be remarkably accurate for any finite $\ell_{\rm max} \geq 3$ given the very rapid decay of the summand with ℓ. We can thus fix the gravitational-wave amplitude I in terms of the signal-to-noise ratio with which the isotropic signal has been established, and the noise term, which will cancel in the estimator variance calculation below.[5]

9.6.2 BiPoSH estimators and variance

The observables that we seek to obtain from the data are the anisotropy amplitudes g_{LM}. Each estimator $\widehat{A^{LM}_{\ell\ell'}}$ provides an estimator,

$$(\widehat{g_{LM}})_{\ell\ell'} = (-1)^{\ell-\ell'}\sqrt{4\pi}\frac{\widehat{A^{LM}_{\ell\ell'}}}{z_\ell z_{\ell'} H^L_{\ell\ell'} I}, \tag{9.26}$$

for g_{LM}. The variance of each of these estimators is (for $L+\ell+\ell'$ even),

$$\begin{aligned}(\Delta g_{LM})^2_{\ell\ell'} &= \frac{4\pi(1+\delta_{\ell\ell'})C^{\rm data}_\ell C^{\rm data}_{\ell'}}{z^2_\ell z^2_{\ell'}(H^L_{\ell\ell'})^2 I^2} \\ &= \frac{8\pi^3}{27}\frac{(1+\delta_{\ell\ell'})C^{\rm data}_\ell C^{\rm data}_{\ell'}}{\left(z_\ell z_{\ell'} H^L_{\ell\ell'}\right)^2 (\mathrm{SNR})^2 (N^{zz})^2}.\end{aligned} \tag{9.27}$$

We then combine all the estimators $(\widehat{g_{LM}})_{\ell\ell'}$ with inverse-variance weighting to obtain the minimum-variance estimator[6],

$$\widehat{g_{LM}} = \frac{\sum_{\ell\ell'}(\widehat{g_{LM}})_{\ell\ell'}(\Delta g_{LM})^{-2}_{\ell\ell'}}{\sum_{\ell\ell'}(\Delta g_{LM})^{-2}_{\ell\ell'}}. \tag{9.28}$$

Note that the sums here are only over $\ell\ell'$ pairs that have even $\ell+\ell'+L$, $|\ell-\ell'| \leq L \leq \ell+\ell'$, and $\ell, \ell' \leq \ell_{\rm max}$. Given the reality of $z(\hat{n})$, we sum only over $\ell' \geq \ell$ to avoid double counting the contributions from $A^{LM}_{\ell\ell'}$ and $A^{LM}_{\ell'\ell}$. The variance $(\Delta g_{LM})^2$ with which g_{LM} can be measured

[5] Eq. (9.25) also indicates that $\gtrsim 93\%$ of the total signal to noise in the detection of the GW signal comes from the quadrupole.

[6] The statistical independence of the different $\ell\ell'$ estimators is discussed further in the third-to-last paragraph.

is the inverse of the denominator; i.e.,

$$(\Delta g_{LM})^{-2} = \frac{27}{16\pi^3}\sum_{\ell\ell'}\frac{\left[H^L_{\ell\ell'}z_\ell z_{\ell'}(\mathrm{SNR})N^{zz}\right]^2}{(C_\ell+N^{zz})(C_{\ell'}+N^{zz})}. \tag{9.29}$$

In this equation, the sum is now over *all* ℓ-ℓ' pairs with $|\ell-\ell'|\leq L\leq \ell+\ell'$, $\ell+\ell'+L$ even, and $\ell,\ell'\leq \ell_{\rm max}$, which we obtain by using $1+\delta_{\ell\ell'}=2$ for $\ell=\ell'$ and then including both $\ell>\ell'$ and $\ell<\ell'$ and dividing by 2 [465]. We can then use

$$C_\ell = \frac{3}{\pi}\sqrt{\frac{3}{2}}\frac{z_\ell^2}{2\ell+1}N^{zz}(\mathrm{SNR}), \tag{9.30}$$

to obtain for the SNR $\to\infty$ limit,

$$(\Delta g_{LM})^{-2} = \frac{1}{8\pi}\sum_{\ell\ell'}(2\ell+1)(2\ell'+1)(H^L_{\ell\ell'})^2, \quad \text{as SNR}\to\infty. \tag{9.31}$$

The smallest g_{LM} that can be distinguished at the $\sim 3\sigma$ level from the null hypothesis $g_{LM}=0$ is then $g_{LM,\rm min}\simeq 3(\Delta g_{LM})$.

9.7 Smallest detectable anisotropies

9.7.1 Results for dipole anisotropy

We now illustrate with the dipole $L=1$. To do so, we note that the only nonvanishing ℓ-ℓ' pairs are those with $\ell'=\ell\pm 1$. We then choose to take $\ell'=\ell+1$ and multiply by two and use $(H^{L=1}_{\ell,\ell+1})^2=(\ell+3)(\ell-1)/[(\ell+1)(2\ell+1)(2\ell+3)]$ to obtain

$$\begin{aligned} g_{1M,\rm min} &= 3\left[\sum_{\ell=2}^{\ell_{\rm max}-1}\frac{54}{\pi}\frac{(\mathrm{SNR})^2}{\ell^2(\ell+1)^3(\ell+2)^2}\right. \\ &\quad \left.\times\frac{1}{(1+C_\ell/N^{zz})\,(1+C_{\ell+1}/N^{zz})}\right]^{-1/2}. \end{aligned} \tag{9.32}$$

We take the sum on ℓ up to $\ell_{\rm max}-1$ so that the maximum $\ell'=\ell+1$ corresponds to the largest multipole $\ell_{\rm max}$ that is measured.

We then set $\ell_{\rm max}\simeq N_p^{1/2}$, where N_p is the number of pulsars, if these pulsars are distributed roughly uniformly on the sky; the sensitivity to higher-ℓ modes will be exponentially reduced. We then plot in Fig. 9.1 the smallest detectable (at the $\gtrsim 3\sigma$ confidence level) dipole-

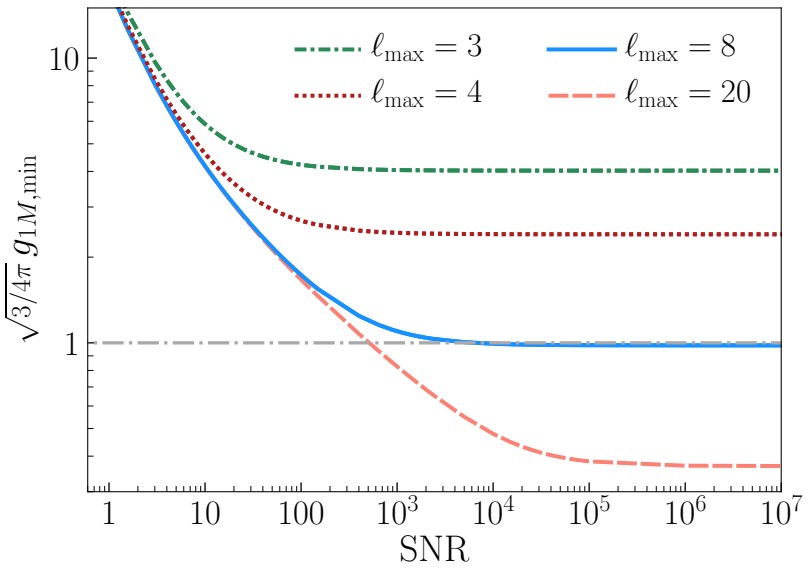

Figure 9.1: The smallest detectable (at the 3σ level) dipole-anisotropy coefficient g_{1M} (multiplied by $\sqrt{3/4\pi}$). Results are shown as a function of the signal-to-noise ratio for the isotropic GW signal and for several values of the maximum timing-residual multipole moment $\ell_{\rm max}$ (which is $\ell_{\rm max} \simeq \sqrt{N_p}$ in terms of the number N_p of pulsars).

anisotropy amplitude g_{1M} as a function of the signal-to-noise ratio SNR with which the isotropic signal is detected and for different numbers of pulsars. The results can be understood by noting that Eq. (9.32) becomes, in the SNR $\to \infty$ limit and in the limit $\ell_{\rm max} \gg 1$,

$$g_{1M,\rm min} \sim \frac{6\sqrt{2\pi}}{\ell_{\rm max}}, \qquad \text{as SNR} \to \infty. \tag{9.33}$$

However, this asymptotic limit is reached only for very large SNR, given the very rapid decrease of C_ℓ/N^{zz} with ℓ. In more physical terms, the anisotropy is inferred through correlations between spherical-harmonic modes of different ℓ, and so individual modes of higher ℓ must be measured with high signal-to-noise. The steep dropoff of C_ℓ with ℓ (each of the seven $\ell = 3$ moments has a signal-to-noise that is smaller by a factor of 5 than that for each quadrupole moment) requires that the isotropic signal (which is very heavily dominated by the quadrupole) be detected with very high significance. In the low-SNR limit, Eq. (9.32) is approximated,

$$g_{1M,\rm min} \sim \frac{28}{\rm SNR}, \qquad \text{as SNR} \to 0; \tag{9.34}$$

given the rapid decrease of the summand with ℓ in this low-SNR limit, this result is obtained for any $\ell_{\rm max} \geq 3$. In practice, this SNR $\to 0$ limit is somewhat academic (and optimistic), as the factor $C_{\ell=2}/N^{zz}$ in the denominator of the summand in Eq. (9.32) is already 1.8 for

SNR = 3. Thus, the numerical result is a bit larger, even for SNR = 3, than indicated by Eq. (9.34). The numerical results in Fig. 9.1 then indicate that the scaling with higher SNR is more like $(\mathrm{SNR})^{-1/2}$ rather than $(\mathrm{SNR})^{-1}$ at higher SNR, and that the SNR $\to \infty$ limit (the "pulsar-number–limited regime") is achieved for SNR $\gtrsim 1000$. This can be understood by noting that, for example, the C_ℓ/N^{zz} in the denominator of the summand in Eq. (9.32) does not reach unity until the signal-to-noise ratio grows, for $\ell = 4$, to SNR $\gtrsim 60$, and for $\ell = 8$, to SNR $\gtrsim 1500$. This then shows that the benefit of $\gtrsim 16$ ($\gtrsim 64$) pulsars for this particular measurement is limited until the GW signal is detected at SNR $\gtrsim 60$ ($\gtrsim 1500$).

If we wanted first to simply establish the existence of a dipole, without specifying its direction, then our observable would be the overall dipole amplitude,

$$d = \sqrt{\frac{3}{4\pi}}\left[\sum_M |g_{1M}|^2\right]^{1/2}, \tag{9.35}$$

where we have included the factor of $\sqrt{4\pi}$ so that $d \leq 1$. The SNR with which this can be established is then $\sqrt{3}$ times that with which any individual g_{1M} can be measured, and so the smallest detectable (at 3σ) dipole has an amplitude

$$\begin{aligned} d_{\rm min} &\simeq \frac{8}{\mathrm{SNR}}, \qquad \text{as} \quad \mathrm{SNR} \to 0, \\ d_{\rm min} &\simeq \frac{4}{\ell_{\rm max}}, \qquad \text{as} \quad \mathrm{SNR} \to \infty, \end{aligned} \tag{9.36}$$

again noting that the SNR $\to 0$ limit is likely overly optimistic for SNR $\gtrsim 3$ and the SNR $\to \infty$ limit is valid for $\ell_{\rm max} \gg 1$.

9.7.2 Higher L modes

The results for higher L of the smallest detectable g_{LM} are easily obtained by numerical evaluation of Eq. (9.31) and shown for different $\ell_{\rm max}$ and (SNR) in Fig. 9.2. The qualitative dependence of the results are similar to those for $g_{1M,\rm min}$, although the sensitivity to higher-L anisotropies is reduced a bit (e.g., by about 50% for $L = 5$) relative to the dipole sensitivity.

9.7.3 A gravitational-wave beam

Suppose that a gravitational-wave signal has been detected and that we wish to determine the fraction of the local gravitational-wave energy density coming from a specific direction.

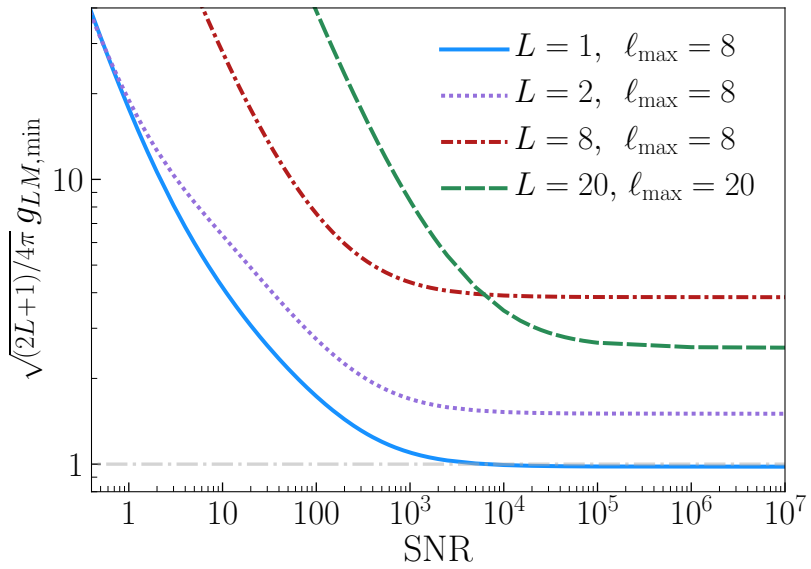

Figure 9.2: The smallest detectable anisotropy coefficient g_{LM}, for $L = \{1,2,8,20\}$, as a function of the total SNR with which the isotropic GW signal is detected. Results are provided for $\ell_{\rm max} = \{8,8,8,20\}$ respectively for the different L.

To be more precise suppose that we model the gravitational-wave signal as an isotropic uncorrelated background plus a flux of gravitational waves all coming from some specific direction (e.g., the direction of some specific SMBH binary candidate), which we take to be in the $\hat{z}$ direction, that makes up a fraction f of the local GW energy density. This situation is described by anisotropy coefficients $g_{LM} = \sqrt{4\pi} f \sqrt{2L+1}\delta_{M0}$. The minimum-variance estimator for the amplitude f is then obtained by summing the minimum-variance estimators for g_{L0} (scaled by $\sqrt{4\pi}$), with inverse-variance weighting. In Fig. 9.3, we plot the smallest f using the results above for $g_{LM,\rm min}$ for $L \leq 8$, detectable with measurements of g_{LM} up to $L = 8$, as a function of SNR from a single map and find it approaches $f_{\rm min} \simeq 0.1$ in the SNR $\gtrsim 1000$ regime. It may be possible, however, to improve the sensitivity to a specific gravitational-wave point source if the signal is characterized by more than the incoherent flux assumed here.

9.8 Multiple maps

So far, we have assumed that there is a single timing-residual map $z(\hat{n})$ obtained by convolving the time-domain data with a single window function. Suppose, however, that the time-domain data are convolved with n_w different time-domain window functions that have negligible overlap in frequency space (or in phase). For example, if we were to have measurements

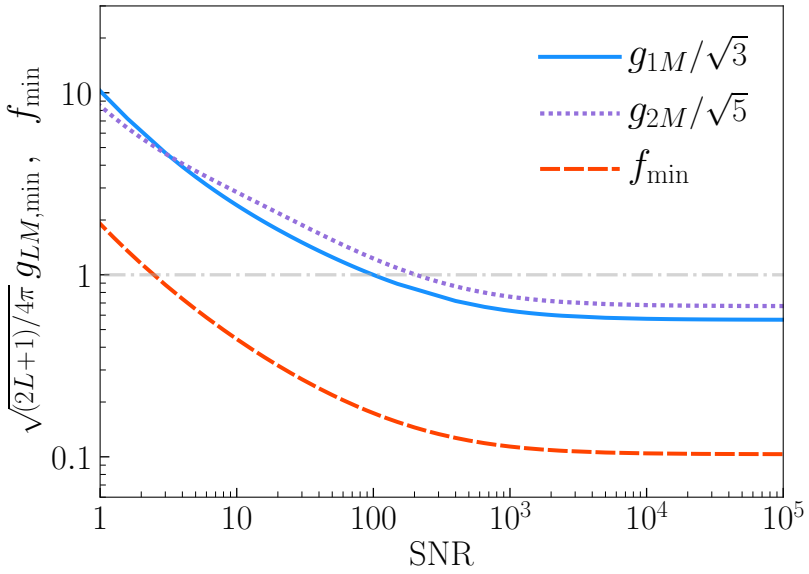

Figure 9.3: For $\ell_{\rm max} = 8$, the smallest detectable dipole-anisotropy amplitude d (which is $3^{-1/2}$ times the $g_{1M,\rm min}$ plotted in Fig. 9.1), and the smallest detectable quadrupole-anisotropy amplitude, shown together with the smallest detectable (again, at 3σ) beam amplitude f obtained with measurements of g_{L0} up to L=8 is $f_{\rm min} \simeq 0.1$ in the high SNR limit.

performed, every two weeks for ~ 10 years, yielding ~ 250 measurements for each pulsar, the time-domain window functions could be taken to be the ~ 250 different time-domain Fourier modes. In this case, we will have $n_w \sim 250$ statistically independent timing-residual maps $z^i(\hat{n})$, with $i = 1, 2, \ldots, n_w$. If the Hellings-Downs power spectrum is detected with signal-to-noise ratio $({\rm SNR})_i$ in each individual map i, then the signal-to-noise ratio (squared) for the entire experiment, after co-adding all the information, will be $({\rm SNR})^2 = \sum_i ({\rm SNR})_i^2$.

The optimal estimator for any given g_{LM} is then obtained by adding (with inverse-variance weighting) the estimators $\widehat{g^i_{LM}}$ from each map i; i.e., we augment Eq. (9.29) with an additional sum over i and replace the SNR, the power spectrum C_ℓ, and noise power spectrum N^{zz} by those—$({\rm SNR})_i$, C^i_ℓ, and N^{zz}_i—associated with the ith map:

$$(\Delta g_{LM})^{-2} = \frac{27}{16\pi^3} \sum_i \sum_{\ell\ell'} \frac{(H^L_{\ell\ell'} z_\ell z_{\ell'} ({\rm SNR})_i N^{zz}_i)^2}{(C^i_\ell + N^{zz}_i)(C^i_{\ell'} + N^{zz}_i)}. \tag{9.37}$$

The SNR, power spectrum, and noise power spectrum for each map are related by

$$C^i_\ell = \frac{3}{\pi} \sqrt{\frac{3}{2}} \frac{z^2_\ell}{2\ell+1} N^{zz}_i ({\rm SNR})_i, \tag{9.38}$$

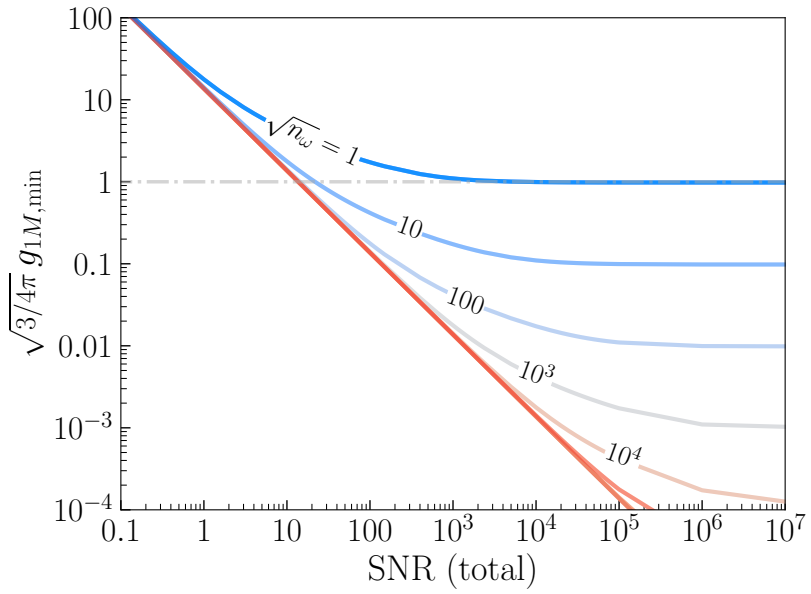

Figure 9.4: The smallest detectable dipole coefficient $g_{1M,\min}$ as a function of the *total* signal-to-noise for $\ell_{\max} = 8$. The different curves show results obtained for different numbers of statistically independent maps n_ω, *assuming that the total SNR is distributed equally among all these maps*.

In the SNR $\to 0$ limit, these replacements result (given $\sum_i (\mathrm{SNR})_i^2 = (\mathrm{SNR})^2$) in the same anisotropy sensitivity as inferred for a single map in this limit in Eq. (9.34). If, however, the signal-to-noise ratio SNR_i in some number $n_{\rm high}$ of maps is high enough (e.g., $(\mathrm{SNR})_i \gtrsim 60$ for $N_p = 16$ or $(\mathrm{SNR})_i \gtrsim 1500$ for $N_p = 64$) that pulsar-number–limited regime is reached *in each individual map*, then the sensitivity to anisotropy can be improved by a factor $\sqrt{n_{\rm high}}$ relative to that, Eq. (9.33), as shown in Fig. 9.4. It must be kept in mind that the improvement shown in Fig. 9.4 possible with additional maps is achieved *only if the total SNR is split evenly among all of these many maps*.

The remaining question, then, is how the total signal-to-noise is distributed among the maps. In the best-case scenario, it will be distributed equally among the n_w maps. If so, then sensitivity to anisotropy could be improved, in principle, by the factor $\sqrt{n_w}$ over that in Eq. (9.33), as shown in Fig. 9.4. This improvement would require, however, that the *total* signal-to-noise be $\sim \sqrt{n_w}$ larger than that (SNR $\gtrsim 60$ for $N_p = 16$ and SNR $\gtrsim 1500$ for $N_p \gtrsim 64$) for a single map.

Given the likely (given the most promising astrophysical scenarios) decrease of the signal with GW frequency, however, the signal-to-noise will probably be dominated by a small subset of the maps (those at the lowest frequencies). If so, then $n_{\rm high}$ may be far smaller than n_w, and the sensitivity, from multiple maps, to anisotropy will be only marginally improved over the single-map estimate in Eq. (9.33).

9.9 Discussion

We have discussed the search for anisotropy in a PTA-detected gravitational-wave signal in terms of bipolar spherical harmonics for idealized measurements parametrized in terms of the number of pulsars (assumed to be uniformly distributed on the sky) and the signal-to-noise ratio (SNR) with which the isotropic signal is established. We focussed our attention first on the case of a single timing-residual map $z(\hat{n})$ (obtained from the convolution of the data with a single time-domain window function) and then discussed the generalization to multiple maps (which take into account more of the time-domain information).

We considered a search for anisotropy in an uncorrelated and unpolarized GW background in which the anisotropy is independent of GW frequency. In this case, the anisotropy is parametrized entirely in terms of spherical-harmonic coefficients g_{LM}. We derived the optimal estimators for these g_{LM} for idealized measurements in which N_p pulsars are distributed roughly uniformly on the sky and the same timing-residual noise in each pulsar. We then obtain the variance with which each g_{LM} can be determined; this variance is expressed in terms of the signal-to-noise with which the isotropic signal is detected and in terms of the number of pulsars.

The main qualitative upshot of the analysis is that the isotropic signal will have to be established very well before there is any possibility to detect anisotropy. The reason stems from the the fact that the anisotropy is obtained (for odd L) through cross-correlation of spherical-harmonic modes $z_{\ell m}$ of the timing-residual map of different ℓ and from the fact (inferred from Eq. (9.25)) that 94% of the $(\mathrm{SNR})^2$ for the isotropic signal comes from $\ell = 2$, with only 6% coming from higher modes. Our numerical results in Fig. 9.1 show that with a single map it will require the isotropic signal to be established with SNR $\gtrsim 1000$ before even the maximal dipole anisotropy can be distinguished, at the 3σ level, from a statistically isotropic background. This would, moreover, require $\gtrsim 60$ pulsars spread uniformly over the sky. The sensitivity to a dipole signal can be improved with more pulsars and/or (as Fig. 9.4 shows) with multiple maps, constructed with different statistically-independent time-domain window functions. This latter improvement can be achieved, however, only if the signal-to-noise is spread evenly among these different maps. Fig. 9.2 indicate the additional challenge facing a search for higher-order anisotropy.

When discussing the prospects to detect anisotropy, we must be careful to state clearly the question we are trying to answer. Here we have focused on the sensitivity to departures from *statistical isotropy* parametrized in terms of spherical-harmonic coefficients g_{LM}, under the null hypothesis of a statistically-isotropic background. This sensitivity is limited not only

by measurement noise, but also by cosmic variance. In our null hypothesis of a statistically isotropic signal, the spherical-harmonic coefficients $z_{\ell m}$ for the map are selected, in the limit of no-noise measurements, from a distribution with variance C_ℓ. Departures from statistical isotropy show up, roughly speaking, in terms of disparities between the amplitudes of the different m modes for a given ℓ. The conclusion of our analysis is that this is difficult to establish given the variance C_ℓ under the null hypothesis.

A measurement that is consistent with *statistical isotropy* may still well exhibit some evidence that the local GW background is a realization that exhibits anisotropy. Suppose, for example, that we had precise measurement of the five timing-residual quadrupole moments z_{2m} and found that the z_{22} and $z_{2,-2}$ components were significantly larger than the other three quadrupole moments. Our calculation [obtained by evaluating Eq. (9.31) with only the $\ell = \ell' = 2$ term] indicates that it would be impossible to infer from this measurement any departure from statistical isotropy. Still, if such a result were observed, it would indicate that the local GW signal is coming primarily from the $\pm\hat{z}$ direction. If there was indeed a strong candidate GW source (e.g., a SMBH-binary candidate) in the $\hat{z}$ direction, then this observation would provide some evidence that the GW signal was coming predominantly from that source.

Our initial calculations explored the detectability of anisotropy from a single timing-residual map obtained by convolving the data with a single time-domain window function. If, however, multiple maps that explore different GW frequency ranges can be obtained, then there are prospects to co-add the anisotropy estimators from those maps to improve upon the pulsar-number limit that arises from a single map. Significant improvement in this way requires, however, that the $z_{\ell m}$ are measured with high SNR in multiple maps.

We also considered the prospects to measure the fraction f of the local GW intensity that comes from a given direction. We conclude also that measurement of f will be similarly challenging: For example, we found a value $f_{\rm min} \simeq 0.1$ for the smallest detectable fraction for a survey with 64 pulsars with SNR $\gtrsim 1000$ for the isotropic signal. This calculation leaves out ingredients (e.g., timing, polarization, and source evolution) that, if included in the analysis, might improve the ability to localize a point source. Still, the rough conclusions and scalings of the sensitivities with SNR and pulsar number should translate to those for a more complete point-source search.

We also note, for possible comparison with previous work in configuration space [452–454], that a sky described by BiPoSHs $A^{LM}_{ll'}$ has a two-point correlation function,

$$C(\hat{n},\hat{m}) = C(\Theta) + \sum_{\ell\ell' LM} A^{LM}_{ll'}\, \{Y_\ell(\hat{n}) \otimes Y_{\ell'}(\hat{m})\}_{LM}, \tag{9.39}$$

where

$$\{Y_\ell(\hat{n}) \otimes Y_{\ell'}(\hat{m})\}_{LM} = \sum_{mm'} \langle \ell m \ell' m' | LM \rangle \, Y_{\ell m}(\hat{n}) Y_{\ell' m'}(\hat{m}), \tag{9.40}$$

are the BiPoSHs. These BiPoSHs constitute a complete orthonormal basis for functions of $\hat{n}$ and $\hat{m}$ in terms of total-angular-momentum states labeled by quantum numbers L and M composed of angular momentum states with l and l'; they are an alternative to the outer product of the $\{l,m\}$ and $\{l',m'\}$ bases. It should be possible to identify these bipolar spherical harmonics to the anisotropic correlation functions worked out in Refs. [453–455], but we leave this exercise to future work.

The analysis presented here should be straightforwardly generalized to astrometric GW searches, e.g. [442]. As shown in Ref. [445], the E-mode map from an astrometic survey provides the same information as a timing-residual map. Therefore, everything said here about a timing-residual map can be applied equally to the E-mode map. The higher density of stellar astrometric sources on the sky may ultimately allow higher $\ell_{\rm max}$ but the advantage of this higher $\ell_{\rm max}$ for anisotropy searches can be capitalized upon only with a sufficiently high SNR. The B modes in the astrometry map can provide additional statistically independent information and, when combined with the E modes and/or timing residuals, can conceivably improve the sensitivity to anisotropy by a factor of $\sqrt{2}$.

The numerical results we find for the sensitivity to anisotropy may be optimistic, given the idealizations assumed here. Uneven distribution of pulsars on the sky and/or pulsar-to-pulsar variations in the timing-residual noises will degrade the sensitivity. There is another, more subtle, caveat: The estimator in Eq. (9.28), and the expression, Eq. (9.29), for its variance, are derived under the assumption that the different $\widehat{A^{LM}_{\ell\ell'}}$ are statistically independent. Although the covariance between any two different $\widehat{A^{LM}_{\ell\ell'}}$ vanishes (except for those with $\ell \leftrightarrow \ell'$), they are *not* statistically independent. The variance will thus most generally be a bit larger, and the sensitivity to anisotropy a bit degraded. We anticipate, though, that for the low-L values considered here that this will be a relatively small (perhaps $\sim 10\%$) effect, although this should be evaluated further with Monte Carlo simulations of isotropic GW signals.

We hope that the approach developed here provides a conceptually straightforward way to understand the search for anisotropy in the GW background and aids in the development of observational/analysis strategies for the PTA search for gravitational waves. It will be interesting in future work to compare the results here to those obtained from detailed simulations of the PTA analysis pipeline, as well as with those inferred from a fully Bayesian approach (see similar applications for the cosmic microwave background [466, 467], for example). It will also be interesing to extend the analysis here to seek anisotropies in the

polarization of the GW background, as parametrized, for example, by GW Stokes parameters [468], or anisotropies in the frequency dependence of the GW background. In the former work, authors compare the statistics of the GW Stokes parameters (spin 4) and concentrate on the isotropic spectra and cross-spectra, similar to this work, which builds a bridge between the two formalisms in terms of the statistical anisotropy of the amplitude fields that, as mentioned above, is a generalization of the power anisotropy.

In this work we have considered ideal measurements in which GW-induced redshifts are measured as a function of position on the sky (with uniform sensitivity over the entire sky) and as a function of time (with uniform sampling/sensitivity). In this case, the harmonic-space basis is a cross product of spherical harmonics (for the sky) and Fourier modes for the time domain. In this idealized case, each (spherical-harmonic)–(time-domain Fourier mode) is statistically independent, for the GW background we are considering (i.e., that specified in Eq. (9.14)). In practice, incomplete/irregular sky coverage, nonuniform timing-residual noise, and irregularities in the observation times destroy this elegant diagonalization. Techniques have been developed to deal with the cross-correlations induced by these imperfections on the idealized eigenmodes. For example, one can deal with real-space correlations, as done in prior work (e.g., Refs. [453–455]). Another option is to work with experiment-specific signal-to-noise eigenmodes (e.g., as were developed in Ref. [469]). Most generally, these imperfections will reduce the sensitivity to isotropic signals and/or anisotropy in the signal relative to those obtained here, assuming ideal measurements, although more detailed specification of the experiment is required to evaluate precisely the reduction in sensitivity.

Appendix A

Technical calculations

A.1 Moving lens effect angular reconstruction

In this section I show some of the intermediate steps that I omitted from calculations discussed in Section 5.5. The numerator of the signal $\tan\varphi$ [introduced in Section 5.5] can be written as

$$\begin{aligned}\alpha &= \int_{\text{template}} \mathrm{d}^2\vec{r}\sin\varphi \sum_{i,\text{halos}} \Psi_{u,i}(r)\Theta^{\text{ml}}(\vec{r}) \\ &= \int_{\text{template}} \mathrm{d}^2\vec{r}\sin\varphi\cos(\varphi-\varphi_0)\int_{\text{patch}}\mathrm{d}^2\vec{R}\int_{z-\text{bin}}\mathrm{d}z\int_{\text{catalog}}\mathrm{d}M \\ &\qquad\times\left[\bar{N}_c(m_*,z)\,\chi^2\frac{\mathrm{d}z}{\mathrm{d}\chi}n(M,z)A(M,z)\,\Psi_u(r)\mathscr{M}_u(r)\right].\end{aligned} \tag{A.1}$$

The denominator differs by a cosine

$$\begin{aligned}\beta &= \int_{\text{template}} \mathrm{d}^2\vec{r}\cos\varphi \sum_{i,\text{halos}} \Psi_{u,i}(r)\Theta^{\text{ml}}(\vec{r}) \\ &= \int_{\text{template}} \mathrm{d}^2\vec{r}\cos\varphi\cos(\varphi-\varphi_0)\int_{\text{patch}}\mathrm{d}^2\vec{R}\int_{z-\text{bin}}\mathrm{d}z\int_{\text{catalog}}\mathrm{d}M \\ &\qquad\times\left[\bar{N}_c(m_*,z)\,\chi^2\frac{\mathrm{d}z}{\mathrm{d}\chi}n(M,z)A(M,z)\,\Psi_u(r)\mathscr{M}_u(r)\right].\end{aligned} \tag{A.2}$$

Errors can be calculated using a relation similar to Eq. (5.28), with the CMB component without the moving lens effect instead, and performing the average over the realisations of

the CMB as,

$$\begin{aligned}
\sigma_\alpha^2 &= \int_{\text{template}} \mathrm{d}^2\vec{r}\sin\varphi\,\mathrm{d}^2\vec{r}'\sin\varphi' \\
&\qquad \times \sum_{i,j,\text{halos}} \Psi_{i,u}(r)\Psi^*_{j,u}(r')\langle\tilde{\Theta}(\vec{R}_i+\vec{r})\tilde{\Theta}^*(\vec{R}_j+\vec{r}')\rangle \\
&= \int_{\text{template}} \mathrm{d}^2\vec{r}\sin\varphi\,\mathrm{d}^2\vec{r}'\sin\varphi' \sum_{i,j,\text{halos}} \Psi_{i,u}(r)\Psi^*_{j,u}(r') \\
&\qquad \times\left[\iint \frac{\mathrm{d}^2\vec{L}}{(2\pi)^2}\frac{\mathrm{d}^2\vec{L}'}{(2\pi)^2} C_L^{\tilde{\Theta}\tilde{\Theta}}\delta^2(\vec{L}+\vec{L}')e^{-i\vec{L}\cdot(\vec{R}_i+\vec{r})-i\vec{L}'\cdot(\vec{R}_j+\vec{r}')}\right] \\
&= \int_{\text{template}} \mathrm{d}^2\vec{r}\sin\varphi\,\mathrm{d}^2\vec{r}'\sin\varphi' \sum_{i,j,\text{halos}} \Psi_{i,u}(r)\Psi^*_{j,u}(r') \\
&\qquad \times\left[\int \frac{\mathrm{d}^2\vec{L}}{(2\pi)^2} C_L^{\tilde{\Theta}\tilde{\Theta}} e^{-i\vec{L}\cdot(\vec{R}_i+\vec{r}-\vec{R}_j-\vec{r}')}\right] \\
&= \int_{\text{template}} r\mathrm{d}r\,r\mathrm{d}r' \sum_{i,j,\text{halos}} \Psi_{i,u}(r)\Psi^*_{j,u}(r')\int \frac{\mathrm{d}^2\vec{L}}{(2\pi)^2} C_L^{\tilde{\Theta}\tilde{\Theta}} e^{-i\vec{L}\cdot(\vec{R}_i-\vec{R}_j)} \\
&\qquad \times\left[\iint \mathrm{d}\varphi\mathrm{d}\varphi' e^{-irL\cos(\varphi-\varphi_0)+ir'L'\cos(\varphi'-\varphi_0)}\right] \\
&= \int_{\text{template}} r\mathrm{d}r\,r\mathrm{d}r' \sum_{i,j,\text{halos}} \Psi_{i,u}(r)\Psi^*_{j,u}(r')\int \frac{\mathrm{d}^2\vec{L}}{(2\pi)^2} C_L^{\tilde{\Theta}\tilde{\Theta}} e^{-i\vec{L}\cdot(\vec{R}_i-\vec{R}_j)} \\
&\qquad \times\left[(2\pi\sin\varphi_0)^2 J_1(Lr)J_1(Lr')\right],
\end{aligned} \tag{A.3}$$

and the error on β differs by a cosine and take the form,

$$\begin{aligned}
\sigma_\alpha^2 &= \int_{\text{template}} \mathrm{d}^2\vec{r}\cos\varphi\,\mathrm{d}^2\vec{r}'\cos\varphi' \\
&\qquad \times \sum_{i,j,\text{halos}} \Psi_{i,u}(r)\Psi^*_{j,u}(r')\langle\tilde{\Theta}(\vec{R}_i+\vec{r})\tilde{\Theta}^*(\vec{R}_j+\vec{r}')\rangle \\
&= \int_{\text{template}} r\mathrm{d}r\,r\mathrm{d}r' \sum_{i,j,\text{halos}} \Psi_{i,u}(r)\Psi^*_{j,u}(r')\int \frac{\mathrm{d}^2\vec{L}}{(2\pi)^2} C_L^{\tilde{\Theta}\tilde{\Theta}} e^{-i\vec{L}\cdot(\vec{R}_i-\vec{R}_j)} \\
&\qquad \times\left[(2\pi\cos\varphi_0)^2 J_1(Lr)J_1(Lr')\right],
\end{aligned} \tag{A.4}$$

where we defined $L = |\vec{L}|$ where $\vec{L}$ is conjugate to the radial displacement on the patch. We write the sum over the halos as,

$$\sum_{i,j,\text{halos}} \Psi_{i,u}(r)\Psi^*_{j,u}(r') = \iint_{z-\text{bin}} \chi^2\chi'^2 \mathrm{d}\chi\, \mathrm{d}\chi' \iint_{\text{catalog}} \mathrm{d}M\mathrm{d}M' n(M,\chi)n(M,\chi') \times \left[\Psi_u(r,M,\chi)\Psi^*_u(r',M',\chi') \iint_{\text{patch}} \mathrm{d}^2\vec{R}_i \mathrm{d}^2\vec{R}_j\right], \tag{A.5}$$

and use the equality,

$$\begin{aligned}\iint_{\text{patch}} \mathrm{d}^2\vec{R}_i \mathrm{d}^2\vec{R}_j e^{-i\vec{L}\cdot(\vec{R}_i-\vec{R}_j)} &= 4\pi^2 \iint_{\text{patch}} R_i R_j \mathrm{d}R_i \mathrm{d}R_j J_0(LR_i)J_0(LR_j) \\ &= \frac{4\pi^2}{L^2}\left[R_{\max}J_1(R_{\max}L) - R_{\min}J_1(R_{\min}L)\right],\end{aligned} \tag{A.6}$$

in Eqs.(A.3) and (A.4) to get our results in Section 5.5.

A.2 Full-sky lensing estimator covariances

Below I show full-sky expressions for lensing-noise reconstruction with the quadratic estimator using Wigner 3d-matrices. These are results of my calculations and are coded for an upcoming delensing software I discuss in Section 7 which aims to provide accurate delensed CMB spectra and lensing reconstruction noise estimates with the quadratic estimator. These equations complement those shown in 7.3.1.

Table A.1: The optimal full-sky CMB weak-lensing estimator normalisations from [470].

α	$f^{\alpha}_{\ell_1\ell\ell_2}$	parity
TT	$C^{\rm TT}_{\ell_1}F^0_{\ell_2\ell\ell_1} + C^{\rm TT}_{\ell_2}F^0_{\ell_1\ell\ell_2}$	-
TE	$C^{\rm TE}_{\ell_1}F^2_{\ell_2\ell\ell_1} + C^{\rm TE}_{\ell_2}F^0_{\ell_1\ell\ell_2}$	even
EE	$C^{\rm EE}_{\ell_1}F^2_{\ell_2\ell\ell_1} + C^{\rm EE}_{\ell_2}F^2_{\ell_1\ell\ell_2}$	even
TB	$iC^{\rm TE}_{\ell_1}F^2_{\ell_2\ell\ell_1}$	odd
EB	$i\left(C^{\rm EE}_{\ell_1}F^2_{\ell_2\ell\ell_1} - C^{\rm BB}_{\ell_2}F^2_{\ell_1\ell\ell_2}\right)$	odd
BB	$C^{\rm BB}_{\ell_1}F^2_{\ell_2\ell\ell_1} + C^{\rm BB}_{\ell_2}F^0_{\ell_1\ell\ell_2}$	even

We will define $F^s_{\ell_1\ell_2\ell_3}$ as [381],

$$F^s_{\ell_1\ell_2\ell_3} = -\sqrt{\frac{(2\ell_1+1)(2\ell_2+1)(2\ell_3+1)\ell_3(\ell_3+1)}{16\pi}} \times \left[\sqrt{(\ell_2-s)(\ell_2+s+1)}\begin{pmatrix}\ell_1 & \ell_2 & \ell_3\\ -s & s+1 & -1\end{pmatrix} + \sqrt{(\ell_2+s)(\ell_2-s+1)}\begin{pmatrix}\ell_1 & \ell_2 & \ell_3\\ -s & s-1 & +1\end{pmatrix}\right], \tag{A.7}$$

and use the following identities,

$$\int_{-1}^{1} \mathrm{d}(\cos\theta)\, d^{\ell_1}_{s_1 s_1'}(\theta) d^{\ell_2}_{s_2 s_2'}(\theta) d^{\ell_3}_{s_3 s_3'}(\theta) = 2\begin{pmatrix}\ell_1 & \ell_2 & \ell_3\\ s_1 & s_2 & s_3\end{pmatrix}\begin{pmatrix}\ell_1 & \ell_2 & \ell_3\\ s_1' & s_2' & s_3'\end{pmatrix}, \tag{A.8}$$

$$\begin{pmatrix}\ell_2 & \ell_3 & \ell_1\\ s_2 & s_3 & s_1\end{pmatrix} = \begin{pmatrix}\ell_1 & \ell_2 & \ell_3\\ s_1 & s_2 & s_3\end{pmatrix}, \tag{A.9}$$

$$\begin{pmatrix}\ell_2 & \ell_1 & \ell_3\\ s_2 & s_1 & s_3\end{pmatrix} = (-1)^{\ell_1+\ell_2+\ell_3}\begin{pmatrix}\ell_1 & \ell_2 & \ell_3\\ s_1 & s_2 & s_3\end{pmatrix}, \tag{A.10}$$

$$\begin{pmatrix}\ell_1 & \ell_2 & \ell_3\\ -s_1 & -s_2 & -s_3\end{pmatrix} = (-1)^{\ell_1+\ell_2+\ell_3}\begin{pmatrix}\ell_1 & \ell_2 & \ell_3\\ s_1 & s_2 & s_3\end{pmatrix}. \tag{A.11}$$

Also note

$$F^s_{\ell_2\ell\ell_1} = F^s_{\ell_1\ell_2\ell} \quad \text{and} \quad d^{\ell}_{m,m'} = d^{\ell}_{-m',-m} = (-1)^{m'-m} d^{\ell}_{m',m}\,. \tag{A.12}$$

The reconstruction-noise of the quadratic estimator has the form

$$N^{ab}_{\ell} = (2\ell+1)\left[\sum_{\ell_1\ell_2} \frac{|f^{\alpha}_{\ell_1\ell\ell_2}|^2}{c_N \tilde{C}^{aa}_{\ell_1}\tilde{C}^{bb}_{\ell_2}}\right]^{-1} \tag{A.13}$$

for $\alpha = \{ab\}$ and $\{ab\} = $ TT, EE, BE, TB, BB spectra, where $c_N = 2$ for the {TT, EE, BB} spectra and $c_N = 1$ for the {BE,TE} spectra. Also note here we use a different notation, where we define observed spectra as $\tilde{C}^{aa}_{\ell} := C^{aa}_{\ell} + N^{aa}_{\ell}$. For the TE spectrum lensing noise reconstruction takes the from

$$N^{\mathrm{TE}}_{\ell} = (2\ell+1)\left[\sum_{\ell_1\ell_2} \frac{\tilde{C}^{\mathrm{TT}}_{\ell_2}\tilde{C}^{\mathrm{EE}}_{\ell_1}|f^{\mathrm{TE}}_{\ell_1\ell\ell_2}|^2 - (-1)^{\ell+\ell_1+\ell_2} C^{\mathrm{TE}}_{\ell_1} C^{\mathrm{TE}}_{\ell_2} f^{\mathrm{TE}\star}_{\ell_2\ell\ell_1} f^{\mathrm{TE}}_{\ell_1\ell\ell_2}}{\tilde{C}^{\mathrm{TT}}_{\ell_1}\tilde{C}^{\mathrm{TT}}_{\ell_2}\tilde{C}^{\mathrm{EE}}_{\ell_1}\tilde{C}^{\mathrm{EE}}_{\ell_2} - \left(C^{\mathrm{TE}}_{\ell_1} C^{\mathrm{TE}}_{\ell_2}\right)^2}\right]^{-1}. \tag{A.14}$$

Using these equalities we calculate the useful terms for variance.

For $N_\ell^{TT;TT}$, we find

$$C^{\rm TT}_{\ell_1} F^0_{\ell_2\ell\ell_1} + C^{\rm TT}_{\ell_2} F^0_{\ell_1\ell\ell_2} = C^{\rm TT}_{\ell_1} F^0_{\ell_1\ell_2\ell} + C^{\rm TT}_{\ell_2} F^0_{\ell_2\ell_1\ell}\,, \tag{A.15}$$

$$\left[C^{\rm TT}_{\ell_1} F^0_{\ell_2\ell_1\ell} + C^{\rm TT}_{\ell_2} F^0_{\ell_1\ell_2\ell}\right]^2 = (C^{\rm TT}_{\ell_1} F^0_{\ell_2\ell_1\ell})^2 + 2C^{\rm TT}_{\ell_1} C^{\rm TT}_{\ell_2} F^0_{\ell_2\ell_1\ell} F^0_{\ell_1\ell_2\ell} + (C^{\rm TT}_{\ell_2} F^0_{\ell_1\ell_2\ell})^2 \tag{A.16}$$

$$\begin{aligned}\left[C^{\rm TT}_{\ell_1} F^0_{\ell_2\ell_1\ell} + C^{\rm TT}_{\ell_2} F^0_{\ell_1\ell_2\ell}\right]^2 =\ & \frac{(2\ell_1+1)(2\ell_2+1)\ell(\ell+1)(2\ell+1)}{32\pi} \\ & \times \Bigg(2\ell_1(\ell_1+1)(C^{\rm TT}_{\ell_1})^2 \left[\int {\rm d}\cos\theta \left(d^{\ell_2}_{00} d^{\ell_1}_{11} d^{\ell_3}_{11} + d^{\ell_1}_{00} d^{\ell_2}_{1-1} d^{\ell_3}_{1-1}\right)\right] \\ & + 2\sqrt{\ell_1(\ell_1+1)}\sqrt{\ell_2(\ell_2+1)} C^{\rm TT}_{\ell_1} C^{\rm TT}_{\ell_2} \left[\int {\rm d}\cos\theta \left(d^{\ell_1}_{01} d^{\ell_2}_{01} d^{\ell_3}_{11} - d^{\ell_1}_{01} d^{\ell_2}_{01} d^{\ell_3}_{1-1}\right)\right]\Bigg)\,.\end{aligned} \tag{A.17}$$

For $N_\ell^{EE;EE}$, we find

$$\begin{aligned}|f^{\rm EE}_{\ell_1\ell\ell_2}|^2 &= \left[C^{\rm EE}_{\ell_1} F^2_{\ell_2\ell_1\ell} + C^{\rm EE}_{\ell_2} F^2_{\ell_1\ell_2\ell}\right]^2 \quad , \text{even} \\ &= \left[C^{\rm EE}_{\ell_1}\left(\frac{F^2_{\ell_2\ell_1\ell} + F^{-2}_{\ell_2\ell_1\ell}}{2}\right) + C^{\rm EE}_{\ell_2}\left(\frac{F^2_{\ell_1\ell_2\ell} + F^{-2}_{\ell_1\ell_2\ell}}{2}\right)\right]^2 \\ &= \frac{1}{4}\Big[(C^{\rm EE}_{\ell_1} F^2_{\ell_2\ell_1\ell})^2 + (C^{\rm EE}_{\ell_1} F^{-2}_{\ell_2\ell_1\ell})^2 + 2(C^{\rm EE}_{\ell_1} C^{\rm EE}_{\ell_1} F^2_{\ell_2\ell_1\ell} F^{-2}_{\ell_2\ell_1\ell}) \\ &\quad + (C^{\rm EE}_{\ell_2} F^2_{\ell_1\ell_2\ell})^2 + (C^{\rm EE}_{\ell_2} F^{-2}_{\ell_1\ell_2\ell})^2 + 2(C^{\rm EE}_{\ell_2} C^{\rm EE}_{\ell_2} F^2_{\ell_1\ell_2\ell} F^{-2}_{\ell_1\ell_2\ell}) \\ &\quad + 2(C^{\rm EE}_{\ell_1} C^{\rm EE}_{\ell_2} F^2_{\ell_2\ell_1\ell} F^2_{\ell_1\ell_2\ell}) + 2(C^{\rm EE}_{\ell_1} C^{\rm EE}_{\ell_2} F^2_{\ell_2\ell_1\ell} F^{-2}_{\ell_1\ell_2\ell}) \\ &\quad + 2(C^{\rm EE}_{\ell_1} C^{\rm EE}_{\ell_2} F^{-2}_{\ell_2\ell_1\ell} F^2_{\ell_1\ell_2\ell}) + 2(C^{\rm EE}_{\ell_1} C^{\rm EE}_{\ell_2} F^{-2}_{\ell_2\ell_1\ell} F^{-2}_{\ell_1\ell_2\ell})\Big]\,,\end{aligned} \tag{A.18}$$

Putting Eq. (A.18) in place, the lensing noise reconstruction for the EE spectra takes the form

$$\begin{aligned}N^{\rm EE}_\ell = \Big(\frac{\pi\ell(\ell+1)}{16}\int_{-1}^{+1} {\rm d}\cos\theta\ \Big[& 4\left(\zeta^{\rm EE}_{22}\zeta^{\rm EE}_{33} + \zeta^{\rm EE}_{22}\zeta^{\rm EE}_{11} + 2\zeta^{\rm EE}_{2-2}\zeta^{\rm EE}_{3-1}\right) d^\ell_{11} \\ & +4\left(\zeta^{\rm EE}_{2-2}\zeta^{\rm EE}_{3-3} + \zeta^{\rm EE}_{2-2}\zeta^{\rm EE}_{1-1} + 2\zeta^{\rm EE}_{22}\zeta^{\rm EE}_{31}\right) d^\ell_{1-1} \\ & -4\left(\zeta^{\rm EE}_{3-2}\zeta^{\rm EE}_{3-2} + \zeta^{\rm EE}_{2-1}\zeta^{\rm EE}_{2-1} + 2\zeta^{\rm EE}_{32}\zeta^{\rm EE}_{21}\right) d^\ell_{11} \\ & +4\left(\zeta^{\rm EE}_{32}\zeta^{\rm EE}_{32} + \zeta^{\rm EE}_{21}\zeta^{\rm EE}_{21} - 2\zeta^{\rm EE}_{3-2}\zeta^{\rm EE}_{2-1}\right) d^\ell_{1-1}\Big]\Big)^{-1}\,,\end{aligned} \tag{A.19}$$

where

$$\zeta^{\alpha\beta}_{3\pm1} := \sum_\ell \tfrac{2\ell+1}{4\pi} \frac{\left(\tilde{C}_\ell^{\alpha\beta}\right)^2}{C_\ell^{\alpha\beta}+N_\ell^{\alpha\beta}} \sqrt{(\ell+2)(\ell-1)(\ell-2)(\ell+3)} d^\ell_{3\pm1} \tag{A.20}$$

$$\zeta^{\alpha\beta}_{3\pm3} := \sum_\ell \tfrac{2\ell+1}{4\pi} \frac{\left(\tilde{C}_\ell^{\alpha\beta}\right)^2}{C_\ell^{\alpha\beta}+N_\ell^{\alpha\beta}} (\ell-2)(\ell+3) d^\ell_{3\pm3} \tag{A.21}$$

$$\zeta^{\alpha\beta}_{1\pm1} := \sum_\ell \tfrac{2\ell+1}{4\pi} \frac{\left(\tilde{C}_\ell^{\alpha\beta}\right)^2}{C_\ell^{\alpha\beta}+N_\ell^{\alpha\beta}} (\ell+2)(\ell-1) d^\ell_{1\pm1} \tag{A.22}$$

$$\zeta^{\alpha\beta}_{2\pm2} := \sum_\ell \tfrac{2\ell+1}{4\pi} \frac{1}{C_\ell^{\alpha\beta}+N_\ell^{\alpha\beta}} d^\ell_{2\pm2} \tag{A.23}$$

$$\zeta^{\alpha\beta}_{3\pm2} := \sum_\ell \tfrac{2\ell+1}{4\pi} \frac{\tilde{C}_\ell^{\alpha\beta}}{C_\ell^{\alpha\beta}+N_\ell^{\alpha\beta}} \sqrt{(\ell_2-2)(\ell_2+3)} d^\ell_{3\pm2} \tag{A.24}$$

$$\zeta^{\alpha\beta}_{2\pm1} := \sum_\ell \tfrac{2\ell+1}{4\pi} \frac{\tilde{C}_\ell^{\alpha\beta}}{C_\ell^{\alpha\beta}+N_\ell^{\alpha\beta}} \sqrt{(\ell_2+2)(\ell_2-1)} d^\ell_{2\pm1} \,. \tag{A.25}$$

Note that in order to calculate $N_\ell^{BB;BB}$, we simply change EE→BB.

For $N_\ell^{EB;EB}$, we find

$$\begin{aligned}
|f^{\rm EB}_{\ell_1\ell\ell_2}|^2 &= \left[C^{\rm EE}_{\ell_1} F^2_{\ell_2\ell_1\ell} - C^{\rm BB}_{\ell_2} F^2_{\ell_1\ell_2\ell}\right]^2 \quad , \text{ odd} \\
&= \left[C^{\rm EE}_{\ell_1}\left(\frac{F^2_{\ell_2\ell_1\ell} - F^{-2}_{\ell_2\ell_1\ell}}{2}\right) - C^{\rm BB}_{\ell_2}\left(\frac{F^2_{\ell_1\ell_2\ell} - F^{-2}_{\ell_1\ell_2\ell}}{2}\right)\right]^2 \\
&= \frac{1}{4}\Big[(C^{\rm EE}_{\ell_1} F^2_{\ell_2\ell_1\ell})^2 + (C^{\rm EE}_{\ell_1} F^{-2}_{\ell_2\ell_1\ell})^2 - 2(C^{\rm EE}_{\ell_1} C^{\rm EE}_{\ell_1} F^2_{\ell_2\ell_1\ell} F^{-2}_{\ell_2\ell_1\ell}) \\
&\quad + (C^{\rm BB}_{\ell_2} F^2_{\ell_1\ell_2\ell})^2 + (C^{\rm BB}_{\ell_2} F^{-2}_{\ell_1\ell_2\ell})^2 - 2(C^{\rm BB}_{\ell_2} C^{\rm BB}_{\ell_2} F^2_{\ell_1\ell_2\ell} F^{-2}_{\ell_1\ell_2\ell}) \\
&\quad - C^{\rm EE}_{\ell_1} C^{\rm BB}_{\ell_2}(F^2_{\ell_2\ell_1\ell} F^2_{\ell_1\ell_2\ell} + F^2_{\ell_1\ell_2\ell} F^2_{\ell_2\ell_1\ell}) + C^{\rm EE}_{\ell_1} C^{\rm BB}_{\ell_2}(F^2_{\ell_2\ell_1\ell} F^{-2}_{\ell_1\ell_2\ell} + F^{-2}_{\ell_1\ell_2\ell} F^2_{\ell_2\ell_1\ell}) \\
&\quad + C^{\rm EE}_{\ell_1} C^{\rm BB}_{\ell_2}(F^{-2}_{\ell_2\ell_1\ell} F^2_{\ell_1\ell_2\ell} + F^2_{\ell_1\ell_2\ell} F^{-2}_{\ell_2\ell_1\ell}) - C^{\rm EE}_{\ell_1} C^{\rm BB}_{\ell_2}(F^{-2}_{\ell_2\ell_1\ell} F^{-2}_{\ell_1\ell_2\ell} + F^{-2}_{\ell_1\ell_2\ell} F^{-2}_{\ell_2\ell_1\ell})\Big] \,.
\end{aligned} \tag{A.26}$$

Note that in the case $C_\ell^{\rm BB}=0$ only the first line above is non-zero which gives the expression found in [381]. Using the equalities in Eq. (A.28) we get

$$\begin{aligned}
N_\ell^{\rm EB} = \Big(&\frac{\pi\ell(\ell+1)}{4}\int_{-1}^{+1} {\rm d}\cos\theta \\
\big[&\left(\zeta_{22}^{\rm BB}\zeta_{33}^{\rm EE}+\zeta_{22}^{\rm BB}\zeta_{11}^{\rm EE}-2\zeta_{2-2}^{\rm BB}\zeta_{3-1}^{\rm EE}\right.\\
&\left.+\zeta_{22}^{\rm EE}\zeta_{33}^{\rm BB}+\zeta_{22}^{\rm EE}\zeta_{11}^{\rm BB}-2\zeta_{2-2}^{\rm EE}\zeta_{3-1}^{\rm BB}\right)d_{11}^\ell\\
-&\left(\zeta_{2-2}^{\rm EE}\zeta_{3-3}^{\rm BB}+\zeta_{2-2}^{\rm EE}\zeta_{1-1}^{\rm BB}-2\zeta_{22}^{\rm EE}\zeta_{31}^{\rm BB}\right.\\
&\left.+\zeta_{2-2}^{\rm BB}\zeta_{3-3}^{\rm EE}+\zeta_{2-2}^{\rm BB}\zeta_{1-1}^{\rm EE}-2\zeta_{22}^{\rm BB}\zeta_{31}^{\rm EE}\right)d_{1-1}^\ell\\
+&\left(\zeta_{3-2}^{\rm EE/BB}\zeta_{3-2}^{\rm BB/EE}+\zeta_{2-1}^{\rm EE/BB}\zeta_{2-1}^{\rm BB/EE}-\zeta_{32}^{\rm EE/BB}\zeta_{21}^{\rm BB/EE}-\zeta_{32}^{\rm BB/EE}\zeta_{21}^{\rm EE/BB}\right)d_{11}^\ell\\
+&\left(\zeta_{32}^{\rm EE/BB}\zeta_{32}^{\rm BB/EE}+\zeta_{21}^{\rm EE/BB}\zeta_{21}^{\rm BB/EE}+\zeta_{3-2}^{\rm EE/BB}\zeta_{2-1}^{\rm BB/EE}+\zeta_{3-2}^{\rm BB}\zeta_{2-1}^{\rm EE/BB}\right)d_{1-1}^\ell\,,
\end{aligned} \tag{A.27}$$

where

$$\zeta_{3\pm2}^{\alpha\alpha/\beta\beta} := \sum_\ell \tfrac{2\ell+1}{4\pi}\tfrac{\tilde{C}_\ell^{\alpha\alpha}}{C_\ell^{\beta\beta}+N_\ell^{\beta\beta}}\sqrt{(\ell_2-2)(\ell_2+3)}d_{3\pm2}^\ell \tag{A.28}$$

$$\zeta_{2\pm1}^{\alpha\alpha/\beta\beta} := \sum_\ell \tfrac{2\ell+1}{4\pi}\tfrac{\tilde{C}_\ell^{\alpha\alpha}}{C_\ell^{\beta\beta}+N_\ell^{\beta\beta}}\sqrt{(\ell_2+2)(\ell_2-1)}d_{2\pm1}^\ell\,. \tag{A.29}$$

For $N_\ell^{TE;TE}$, we find

$$\begin{aligned}
|f_{\ell_1\ell\ell_2}^{\rm TE}|^2 &= \left[C_{\ell_1}^{\rm TE}F_{\ell_2\ell\ell_1}^2+C_{\ell_2}^{\rm TE}F_{\ell_1\ell\ell_2}^0\right]^2 \quad \text{even}\\
&= \left[C_{\ell_1}^{\rm TE}\left(\frac{F_{\ell_1\ell_2\ell}^2+F_{\ell_1\ell_2\ell}^{-2}}{2}\right)+C_{\ell_2}^{\rm TE}F_{\ell_2\ell_1\ell}^0\right]^2\\
&= \frac{1}{4}\Big[(C_{\ell_1}^{\rm TE}F_{\ell_2\ell_1\ell})^2+(C_{\ell_1}^{\rm TE}F_{\ell_2\ell_1\ell}^{-2})^2+2(C_{\ell_1}^{\rm TE}C_{\ell_1}^{\rm TE}F_{\ell_2\ell_1\ell}^2F_{\ell_2\ell_1\ell}^{-2})\\
&\quad +2C_{\ell_1}^{\rm TE}C_{\ell_2}^{\rm TE}(F_{\ell_2\ell_1\ell}^2F_{\ell_1\ell_2\ell}^0+F_{\ell_1\ell_2\ell}^0F_{\ell_2\ell_1\ell}^2)\\
&\quad +2C_{\ell_1}^{\rm TE}C_{\ell_2}^{\rm TE}(F_{\ell_2\ell_1\ell}^{-2}F_{\ell_1\ell_2\ell}^0+F_{\ell_1\ell_2\ell}^0F_{\ell_2\ell_1\ell}^{-2})+4(C_{\ell_2}^{\rm TE}F_{\ell_1\ell_2\ell}^0)^2\Big]
\end{aligned} \tag{A.30}$$

We will use the following approximation [470],

$$g_{\ell_1\ell_2}^{\rm TE} = \frac{f_{\ell_1\ell\ell_2}^{\rm TE}}{C_{\ell_1}^{\rm TT}C_{\ell_2}^{\rm EE}}, \tag{A.31}$$

hence

$$N_\ell^{\rm TE} = \ell(\ell+1)(2\ell+1)\left[\sum_{\ell_1\ell_2} g_{\ell_1\ell_2}^{\rm TE}(\ell)f_{\ell_1\ell\ell_2}^{\rm TE}\right]^{-1}. \tag{A.32}$$

The expression for $N_\ell^{\rm TE}$ becomes

$$\begin{aligned} N_\ell^{\rm TE} = \Big(\frac{\pi\ell(\ell+1)}{8}\int_{-1}^{+1} {\rm d}\cos\theta \;\Big[&+2\left(\zeta_{22}^{\rm TE}\zeta_{11}^{\rm TE/TT}+\zeta_{22}^{\rm TE}\zeta_{33}^{\rm TE}+2\zeta_{2-2}^{\rm TE}\zeta_{3-1}^{\rm TE}\right)d_{11}^\ell \\ &+2\left(\zeta_{2-2}^{\rm TE}\zeta_{1-1}^{\rm TE/TT}+\zeta_{2-2}^{\rm TE}\zeta_{3-3}+2\zeta_{22}^{\rm TE}\zeta_{31}^{\rm TE}\right)d_{1-1}^\ell \\ &+8\left(\zeta_{21}^{\rm TE}\zeta_{01}^{\rm TE}-\zeta_{2-1}^{\rm TE}\zeta_{30}^{\rm TE}\right)d_{11}^\ell \\ &+8\left(\zeta_{2-1}^{\rm TE}\zeta_{01}^{\rm TE}-\zeta_{21}^{\rm TE}\zeta_{30}^{\rm TE}\right)d_{1-1}^\ell \\ &+8\left(\zeta_{00}^{\rm TE}\zeta_{11}^{\rm TE/TT}d_{11}^\ell+\zeta_{00}^{\rm TE}\zeta_{1-1}^{\rm TE/TT}d_{1-1}^\ell\right)\Big]\Big)^{-1}, \end{aligned} \tag{A.33}$$

where for convenience we defined

$$\zeta_{3\pm1}^{{\rm TE},\ell} := \sum_\ell \frac{2\ell+1}{4\pi}\sqrt{(\ell-1)(\ell+2)(\ell-2)(\ell+3)}\frac{(\tilde{C}_\ell^{\rm TE})^2}{C_\ell^{\rm TT}+N_\ell^{\rm TT}}d_{3\pm1}^\ell \tag{A.34}$$

$$\zeta_{1\pm1}^{{\rm TE}/\alpha,\ell} := \sum_\ell \frac{2\ell+1}{4\pi}(\ell+2)(\ell-1)\frac{(\tilde{C}_\ell^{\rm TE})^2}{C_\ell^{\alpha}+N_\ell^{\alpha}}d_{1\pm1}^\ell \tag{A.35}$$

$$\zeta_{2\pm2}^{{\rm TE},\ell} := \sum_\ell \frac{2\ell+1}{4\pi}\frac{1}{C_\ell^{\rm EE}+N_\ell^{\rm EE}}d_{2\pm2}^\ell \tag{A.36}$$

$$\zeta_{00}^{{\rm TE},\ell} := \sum_\ell \frac{2\ell+1}{4\pi}\frac{1}{C_\ell^{\rm TT}+N_\ell^{\rm TT}}d_{00}^\ell \tag{A.37}$$

$$\zeta_{3\pm3}^{{\rm TE},\ell} := \sum_\ell \frac{2\ell+1}{4\pi}(\ell-2)(\ell+3)\frac{(\tilde{C}_\ell^{\rm TE})^2}{C_\ell^{\rm TT}+N_\ell^{\rm TT}}d_{3\pm3}^\ell \tag{A.38}$$

$$\zeta_{\pm10}^{{\rm TE},\ell} := \sum_\ell \frac{2\ell+1}{4\pi}\sqrt{(\ell+2)(\ell-1)}\frac{\tilde{C}_\ell^{\rm TE}}{C_\ell^{\rm TT}+N_\ell^{\rm TT}}d_{\pm10}^\ell \tag{A.39}$$

$$\zeta_{2\pm1}^{{\rm TE},\ell} := \sum_\ell \frac{2\ell+1}{4\pi}\sqrt{\ell(\ell+1)}\frac{\tilde{C}_\ell^{\rm TE}}{C_\ell^{\rm EE}+N_\ell^{\rm EE}}d_{2\pm1}^\ell \tag{A.40}$$

$$\zeta_{30}^{{\rm TE},\ell} := \sum_\ell \frac{2\ell+1}{4\pi}C_\ell^{\rm TE}\sqrt{(\ell-2)(\ell+3)}\frac{\tilde{C}_\ell^{\rm TE}}{C_\ell^{\rm TT}+N_\ell^{\rm TT}}d_{30}^\ell \tag{A.41}$$

For $N_\ell^{TB;TB}$, we find

$$g_{\ell_1\ell_2}^{\rm TB}f_{\ell_1\ell\ell_2}^{\rm TB} = \frac{1}{4}\frac{(\tilde{C}_{\ell_1}^{\rm TE})^2}{C_{\ell_1}^{\rm TT}C_{\ell_2}^{\rm BB}}\left[\left(F_{\ell_2\ell_1\ell}^2-F_{\ell_2\ell_1\ell}^{-2}\right)\left(F_{\ell_2\ell_1\ell}^2-F_{\ell_2\ell_1\ell}^{-2}\right)\right]. \tag{A.42}$$

Defining for convenience

$$\zeta^{\mathrm{TB},\ell}_{2\pm2} := \sum_\ell \frac{2\ell+1}{4\pi}\frac{1}{C^{\mathrm{BB}}_\ell} d^\ell_{2\pm2} \tag{A.43}$$

$$\zeta^{\mathrm{TB},\ell}_{3\pm1} := \sum_\ell \frac{2\ell+1}{4\pi}\sqrt{(\ell+2)(\ell-2)(\ell-1)(\ell+3)}\frac{(\tilde{C}^{\mathrm{TE}}_\ell)^2}{C^{\mathrm{TT}}_\ell} d^\ell_{3\pm1} \tag{A.44}$$

$$\zeta^{\mathrm{TB},\ell}_{3\pm3} := \sum_\ell \frac{2\ell+1}{4\pi}(\ell-2)(\ell+3)\frac{(\tilde{C}^{\mathrm{TE}}_\ell)^2}{C^{\mathrm{TT}}_\ell} d^\ell_{3\pm3} \tag{A.45}$$

$$\zeta^{\mathrm{TB},\ell}_{1\pm1} := \sum_\ell \frac{2\ell+1}{4\pi}(\ell-1)(\ell+2)\frac{(\tilde{C}^{\mathrm{TE}}_\ell)^2}{C^{\mathrm{TT}}_\ell} d^\ell_{1\pm1}\,. \tag{A.46}$$

The expression for N^{TB}_ℓ becomes

$$N^{\mathrm{TB}}_\ell = \Big(\frac{\pi\ell(\ell+1)}{8}\int_{-1}^{+1}\mathrm{d}\cos\theta\ \big[+2\left(\zeta^{\mathrm{TB}}_{22}\zeta^{\mathrm{TB}}_{11}+\zeta^{\mathrm{TB}}_{22}\zeta^{\mathrm{TB}}_{33}-2\zeta^{\mathrm{TB}}_{2-2}\zeta^{\mathrm{TB}}_{3-1}\right)d^\ell_{11} \\ -2\left(\zeta^{\mathrm{TB}}_{2-2}\zeta^{\mathrm{TB}}_{1-1}+\zeta^{\mathrm{TB}}_{2-2}\zeta^{\mathrm{TB}}_{3-3}-2\zeta^{\mathrm{TB}}_{22}\zeta^{\mathrm{TB}}_{31}\right)d^\ell_{1-1}\,\big]\Big)^{-1}. \tag{A.47}$$

For $N_\ell^{TE;EE}$, we find

$$
\begin{aligned}
&\sum_{\ell_1\ell_2}\{g^{\mathrm{TE}*}_{\ell_1\ell_2}[C^{\mathrm{TE}}_{\ell_1}C^{\mathrm{EE}}_{\ell_2}\left(g^{\mathrm{EE}}_{\ell_1\ell_2}+g^{\mathrm{EE}}_{\ell_2\ell_1}\right)\}\\
&=\frac{C^{\mathrm{TE}}_{\ell_1}C^{\mathrm{EE}}_{\ell_2}}{8}\times\left(\tilde{C}^{\mathrm{EE}}_{\ell_1}\left[2\tilde{C}^{\mathrm{TE}}_{\ell_1}\left(F^{2}_{\ell_2\ell_1\ell}+F^{-2}_{\ell_2\ell_1\ell}\right)^2+4\tilde{C}^{\mathrm{TE}}_{\ell_2}\left(F^{0}_{\ell_1\ell_2\ell}F^{2}_{\ell_2\ell_1\ell}+F^{0}_{\ell_1\ell_2\ell}F^{-2}_{\ell_2\ell_1\ell}\right)\right]\right)\\
&\qquad\times\left(\tilde{C}^{\mathrm{EE}}_{\ell_2}\left[2\tilde{C}^{\mathrm{TE}}_{\ell_1}\left(F^{2}_{\ell_2\ell_1\ell}F^{2}_{\ell_1\ell_2\ell}+F^{2}_{\ell_2\ell_1\ell}F^{-2}_{\ell_1\ell_2\ell}+F^{-2}_{\ell_2\ell_1\ell}F^{2}_{\ell_1\ell_2\ell}+F^{-2}_{\ell_2\ell_1\ell}F^{-2}_{\ell_1\ell_2\ell}\right)\right.\right.\\
&\qquad\qquad\left.\left.+4\tilde{C}^{\mathrm{TE}}_{\ell_2}\left(F^{0}_{\ell_1\ell_2\ell}F^{2}_{\ell_1\ell_2\ell}+F^{0}_{\ell_1\ell_2\ell}F^{-2}_{\ell_1\ell_2\ell}\right)\right]\right)\\
&=\frac{1}{4}\int_{-1}^{+1}\mathrm{d}\cos\theta\,\left[\left(\zeta^{\mathrm{TE;EE}}_{22}\zeta^{\mathrm{TE;EE}}_{33}+\zeta^{\mathrm{TE;EE}}_{22}\zeta^{\mathrm{TE;EE}}_{11,(1)}+2\zeta^{\mathrm{TE;EE}}_{2-2}\zeta^{\mathrm{TE;EE}}_{3-1,(1)}\right)d^{\ell}_{11}\right.\\
&\qquad+\left(\zeta^{\mathrm{TE;EE}}_{2-2}\zeta^{\mathrm{TE;EE}}_{3-3}+\zeta^{\mathrm{TE;EE}}_{2-2}\zeta^{\mathrm{TE;EE}}_{1-1,(1)}+2\zeta^{\mathrm{TE;EE}}_{22}\zeta^{\mathrm{TE;EE}}_{31,(1)}\right)d^{\ell}_{1-1}\\
&\qquad+2\left(\zeta^{\mathrm{TE;EE}}_{01}\zeta^{\mathrm{TE;EE}}_{21}-\zeta^{\mathrm{TE;EE}}_{30}\zeta^{\mathrm{TE;EE}}_{2-1}\right)d_{11}\\
&\qquad+2\left(\zeta^{\mathrm{TE;EE}}_{01}\zeta^{\mathrm{TE;EE}}_{2-1}-\zeta^{\mathrm{TE;EE}}_{30}\zeta^{\mathrm{TE;EE}}_{21}\right)d_{1-1}\\
&\qquad-\left(\zeta^{\mathrm{TE;EE}}_{3-2,(\alpha)}\zeta^{\mathrm{TE;EE}}_{3-2,(\beta)}+\zeta^{\mathrm{TE;EE}}_{2-1,(\alpha)}\zeta^{\mathrm{TE;EE}}_{2-1,(\beta)}+\zeta^{\mathrm{TE;EE}}_{32,(\alpha)}\zeta^{\mathrm{TE;EE}}_{21,(\alpha)}+\zeta^{\mathrm{TE;EE}}_{21,(\beta)}\zeta^{\mathrm{TE;EE}}_{32,(\beta)}\right)d_{11}\\
&\qquad+\left(\zeta^{\mathrm{TE;EE}}_{32,(\alpha)}\zeta^{\mathrm{TE;EE}}_{32,(\beta)}+\zeta^{\mathrm{TE;EE}}_{21,(\alpha)}\zeta^{\mathrm{TE;EE}}_{21,(\beta)}-\zeta^{\mathrm{TE;EE}}_{3-2,(\alpha)}\zeta^{\mathrm{TE;EE}}_{2-1,(\alpha)}-\zeta^{\mathrm{TE;EE}}_{2-1,(\beta)}\zeta^{\mathrm{TE;EE}}_{3-2,(\beta)}\right)d_{1-1}\\
&\qquad+2\left(\zeta^{\mathrm{TE;EE}}_{20}\zeta^{\mathrm{TE;EE}}_{1-1,(2)}+\zeta^{\mathrm{TE;EE}}_{20}\zeta^{\mathrm{TE;EE}}_{31,(2)}\right)d_{11}\\
&\qquad\left.+2\left(\zeta^{\mathrm{TE;EE}}_{20}\zeta^{\mathrm{TE;EE}}_{11,(2)}+\zeta^{\mathrm{TE;EE}}_{20}\zeta^{\mathrm{TE;EE}}_{3-1,(2)}\right)d_{1-1}\,,\right.
\end{aligned}
\tag{A.48}
$$

where

$$\zeta^{\mathrm{TE;EE}}_{2\pm2} = \sum_\ell \frac{2\ell+1}{4\pi}\frac{1}{C^{\mathrm{EE}}_\ell} d_{2\pm2} \tag{A.49}$$

$$\zeta^{\mathrm{TE;EE}}_{3\pm3} = \sum_\ell \frac{(2\ell+1)(\ell-2)(\ell+3)}{4\pi}\frac{C^{\mathrm{TE}}_\ell \tilde{C}^{\mathrm{EE}}_\ell \tilde{C}^{\mathrm{TE}}_\ell}{C^{\mathrm{TT}}_\ell C^{\mathrm{EE}}_\ell} d_{3\pm3} \tag{A.50}$$

$$\zeta^{\mathrm{TE;EE}}_{3\pm1,(1)} = \sum_\ell \frac{(2\ell+1)\sqrt{(\ell+2)(\ell-1)(\ell-2)(\ell+3)}}{4\pi}\frac{C^{\mathrm{TE}}_\ell \tilde{C}^{\mathrm{EE}}_\ell \tilde{C}^{\mathrm{TE}}_\ell}{C^{\mathrm{TT}}_\ell C^{\mathrm{EE}}_\ell} d_{3\pm1} \tag{A.51}$$

$$\zeta^{\mathrm{TE;EE}}_{1\pm1,(1)} = \sum_\ell \frac{(2\ell+1)(\ell+2)(\ell-1)}{4\pi}\frac{C^{\mathrm{TE}}_\ell \tilde{C}^{\mathrm{EE}}_\ell \tilde{C}^{\mathrm{TE}}_\ell}{C^{\mathrm{TT}}_\ell C^{\mathrm{EE}}_\ell} d_{1\pm1} \tag{A.52}$$

$$\zeta^{\mathrm{TE;EE}}_{01} = \sum_\ell \frac{(2\ell+1)\sqrt{(\ell+2)\ell}}{4\pi}\frac{C^{\mathrm{TE}}_\ell \tilde{C}^{\mathrm{EE}}_\ell}{C^{\mathrm{EE}}_\ell C^{\mathrm{TT}}_\ell} d_{01} \tag{A.53}$$

$$\zeta^{\mathrm{TE;EE}}_{30} = \sum_\ell \frac{(2\ell+1)\sqrt{(\ell-2)(\ell+3)}}{4\pi}\frac{C^{\mathrm{TE}}_\ell \tilde{C}^{\mathrm{EE}}_\ell}{C^{\mathrm{EE}}_\ell C^{\mathrm{TT}}_\ell} d_{30} \tag{A.54}$$

$$\zeta^{\mathrm{TE;EE}}_{2\pm1} = \sum_\ell \frac{(2\ell+1)\ell(\ell+1)}{4\pi}\frac{\tilde{C}^{\mathrm{TE}}_\ell}{C^{\mathrm{EE}}_\ell} d_{2\pm1} \tag{A.55}$$

$$\zeta^{\mathrm{TE;EE}}_{2\pm1,(\alpha)} = \sum_\ell \frac{(2\ell+1)\sqrt{\ell+2(\ell-1)}}{4\pi}\frac{\tilde{C}^{\mathrm{EE}}_\ell}{C^{\mathrm{EE}}_\ell} d_{2\pm1} \tag{A.56}$$

$$\zeta^{\mathrm{TE;EE}}_{3\pm2,(\alpha)} = \sum_\ell \frac{(2\ell+1)\sqrt{(\ell-2)(\ell+3)}}{4\pi}\frac{C^{\mathrm{TE}}_\ell \tilde{C}^{\mathrm{TE}}_\ell}{C^{\mathrm{EE}}_\ell C^{\mathrm{TT}}_\ell} d_{3\pm2} \tag{A.57}$$

$$\zeta^{\mathrm{TE;EE}}_{2\pm1,(\beta)} = \sum_\ell \frac{(2\ell+1)(\ell+2)(\ell-1)}{4\pi}\frac{C^{\mathrm{TE}}_\ell \tilde{C}^{\mathrm{TE}}_\ell}{C^{\mathrm{EE}}_\ell C^{\mathrm{TT}}_\ell} d_{2\pm1} \tag{A.58}$$

$$\zeta^{\mathrm{TE;EE}}_{3\pm2,(\beta)} = \sum_\ell \frac{(2\ell+1)\sqrt{(\ell-2)(\ell+3)}}{4\pi}\frac{\tilde{C}^{\mathrm{EE}}_\ell}{C^{\mathrm{EE}}_\ell} d_{3\pm2} \tag{A.59}$$

$$\zeta^{\mathrm{TE;EE}}_{20} = \sum_\ell \frac{2\ell+1}{4\pi}\frac{C^{\mathrm{TE}}_\ell \tilde{C}^{\mathrm{EE}}_\ell}{C^{\mathrm{TT}}_\ell C^{\mathrm{EE}}_\ell} d_{20} \tag{A.60}$$

$$\zeta^{\mathrm{TE;EE}}_{1\pm1,(2)} = \sum_\ell \frac{(2\ell+1)\sqrt{\ell(\ell+1)(\ell+2)(\ell-1)}}{4\pi}\frac{\tilde{C}^{\mathrm{TE}}_\ell}{C^{\mathrm{EE}}_\ell} d_{1\pm1} \tag{A.61}$$

$$\zeta^{\mathrm{TE;EE}}_{3\pm1,(2)} = \sum_\ell \frac{(2\ell+1)\sqrt{\ell(\ell+1)(\ell-2)(\ell+3)}}{4\pi}\frac{\tilde{C}^{\mathrm{TE}}_\ell}{C^{\mathrm{EE}}_\ell} d_{3\pm1} \tag{A.62}$$

For $N_\ell^{TT;TE}$, we find

$$
\begin{aligned}
&\sum_{\ell_1\ell_2}\{g^{\mathrm{TT}*}_{\ell_1\ell_2}(C^{\mathrm{TT}}_{\ell_1}C^{\mathrm{TE}}_{\ell_2}g^{\mathrm{EE}}_{\ell_1\ell_2}+C^{\mathrm{TE}}_{\ell_1}C^{\mathrm{TT}}_{\ell_2}g^{\mathrm{EE}}_{\ell_2\ell_1})]\}\\
&=\frac{1}{2C^{\mathrm{TT}}_{\ell_1}C^{\mathrm{TT}}_{\ell_2}}\left[\frac{C^{\mathrm{TE}}_{\ell_2}}{C^{\mathrm{EE}}_{\ell_2}}\left(\tilde{C}^{TT}_{\ell_1}\left[\frac{\tilde{C}^{\mathrm{TE}}_{\ell_1}}{2}\left(F^0_{\ell_2\ell_1\ell}F^2_{\ell_2\ell_1\ell}+F^0_{\ell_2\ell_1\ell}F^{-2}_{\ell_2\ell_1\ell}\right)+\tilde{C}^{\mathrm{TE}}_{\ell_2}\left(F^0_{\ell_2\ell_1\ell}F^0_{\ell_1\ell_2\ell}\right)\right]\right.\right.\\
&\qquad\left.\left.\tilde{C}^{TT}_{\ell_2}\left[\frac{\tilde{C}^{\mathrm{TE}}_{\ell_1}}{2}\left(F^0_{\ell_1\ell_2\ell}F^2_{\ell_2\ell_1\ell}+F^0_{\ell_1\ell_2\ell}F^{-2}_{\ell_2\ell_1\ell}\right)+\tilde{C}^{\mathrm{TE}}_{\ell_2}\left(F^0_{\ell_1\ell_2\ell}F^0_{\ell_1\ell_2\ell}\right)\right]\right)\right.\\
&\qquad+\frac{C^{\mathrm{TE}}_{\ell_1}}{C^{\mathrm{EE}}_{\ell_1}}\left(\tilde{C}^{TT}_{\ell_1}\left[\frac{\tilde{C}^{\mathrm{TE}}_{\ell_2}}{2}\left(F^0_{\ell_2\ell_1\ell}F^2_{\ell_1\ell_2\ell}+F^0_{\ell_2\ell_1\ell}F^{-2}_{\ell_1\ell_2\ell}\right)+\tilde{C}^{\mathrm{TE}}_{\ell_1}\left(F^0_{\ell_2\ell_1\ell}F^0_{\ell_2\ell_1\ell}\right)\right]\right.\\
&\qquad\left.\left.\left.\tilde{C}^{TT}_{\ell_2}\left[\frac{\tilde{C}^{\mathrm{TE}}_{\ell_2}}{2}\left(F^0_{\ell_1\ell_2\ell}F^2_{\ell_1\ell_2\ell}+F^0_{\ell_1\ell_2\ell}F^{-2}_{\ell_1\ell_2\ell}\right)+\tilde{C}^{\mathrm{TE}}_{\ell_1}\left(F^0_{\ell_1\ell_2\ell}F^0_{\ell_2\ell_1\ell}\right)\right]\right)\right]\\
&=\frac{1}{2}\int_{-1}^{+1}\mathrm{d}\cos\theta\ \left[\left(\zeta^{\mathrm{TT;TE}}_{20}\zeta^{\mathrm{TT;TE}}_{1-1,(1)}+\zeta^{\mathrm{TT;TE}}_{20}\zeta^{\mathrm{TT;TE}}_{31}-2\zeta^{\mathrm{TT;TE}}_{01,(1)}\zeta^{\mathrm{TT;TE}}_{01,(2)}\right)d^\ell_{11}\right.\\
&\qquad+\left(\zeta^{\mathrm{TT;TE}}_{20}\zeta^{\mathrm{TT;TE}}_{11,(1)}+\zeta^{\mathrm{TT;TE}}_{20}\zeta^{\mathrm{TT;TE}}_{3-1}\ +2\zeta^{\mathrm{TT;TE}}_{01,(1)}\zeta^{\mathrm{TT;TE}}_{01,(2)}\right)d^\ell_{1-1}\\
&\qquad+\left(\zeta^{\mathrm{TT;TE}}_{01,(3)}\zeta^{\mathrm{TT;TE}}_{21}-\zeta^{\mathrm{TT;TE}}_{30}\zeta^{\mathrm{TT;TE}}_{2-1}\ +2\zeta^{\mathrm{TT;TE}}_{00,(1)}\zeta^{\mathrm{TT;TE}}_{11,(2)}\right)d^\ell_{11}\\
&\qquad\left.+\left(\zeta^{\mathrm{TT;TE}}_{01,(3)}\zeta^{\mathrm{TT;TE}}_{2-1}-\zeta^{\mathrm{TT;TE}}_{30}\zeta^{\mathrm{TT;TE}}_{21}\ +2\zeta^{\mathrm{TT;TE}}_{00,(1)}\zeta^{\mathrm{TT;TE}}_{1-1,(2)}\right)d^\ell_{1-1}\right.
\end{aligned}
\tag{A.63}
$$

where

$$\zeta_{20}^{\mathrm{TT;TE}} = \sum_\ell \frac{2\ell+1}{4\pi} \frac{C_\ell^{\mathrm{TE}}}{C_\ell^{\mathrm{EE}} C_\ell^{\mathrm{TT}}} d_{20} \tag{A.64}$$

$$\zeta_{1\pm1,(1)}^{\mathrm{TT;TE}} = \sum_\ell \frac{(2\ell+1)\sqrt{\ell(\ell+1)(\ell+2)(\ell-1)}}{4\pi} \frac{\tilde{C}_\ell^{\mathrm{TT}} \tilde{C}_\ell^{\mathrm{TE}}}{C_\ell^{\mathrm{TT}}} d_{1\pm1} \tag{A.65}$$

$$\zeta_{3\pm1}^{\mathrm{TT;TE}} = \sum_\ell \frac{(2\ell+1)\sqrt{\ell(\ell+1)(\ell-2)(\ell+3)}}{4\pi} \frac{\tilde{C}_\ell^{\mathrm{TT}} \tilde{C}_\ell^{\mathrm{TE}}}{C_\ell^{\mathrm{TT}}} d_{3\pm1} \tag{A.66}$$

$$\zeta_{01,(3)}^{\mathrm{TT;TE}} = \sum_\ell \frac{(2\ell+1)\sqrt{\ell(\ell+2)}}{4\pi} \frac{\tilde{C}_\ell^{\mathrm{TE}}}{C_\ell^{\mathrm{TT}}} d_{01} \tag{A.67}$$

$$\zeta_{2\pm1}^{\mathrm{TT;TE}} = \sum_\ell \frac{(2\ell+1)(\ell+2)(\ell-1)}{4\pi} \frac{C_\ell^{\mathrm{TE}} \tilde{C}_\ell^{\mathrm{TT}}}{C_\ell^{\mathrm{TT}} C_\ell^{\mathrm{EE}}} d_{2\pm1} \tag{A.68}$$

$$\zeta_{30}^{\mathrm{TT;TE}} = \sum_\ell \frac{(2\ell+1)\sqrt{(\ell-2)(\ell+3)}}{4\pi} \frac{\tilde{C}_\ell^{\mathrm{TE}}}{C_\ell^{\mathrm{TT}}} d_{30} \tag{A.69}$$

$$\zeta_{01,(1)}^{\mathrm{TT;TE}} = \sum_\ell \frac{(2\ell+1)\sqrt{\ell(\ell+1)}}{4\pi} \frac{C_\ell^{\mathrm{TE}} \tilde{C}_\ell^{\mathrm{TE}}}{C_\ell^{\mathrm{TT}} C_\ell^{\mathrm{EE}}} d_{01} \tag{A.70}$$

$$\zeta_{01,(2)}^{\mathrm{TT;TE}} = \sum_\ell \frac{(2\ell+1)\sqrt{\ell(\ell+1)}}{4\pi} \frac{\tilde{C}_\ell^{\mathrm{TT}}}{C_\ell^{\mathrm{TT}}} d_{01} \tag{A.71}$$

$$\zeta_{00,(1)}^{\mathrm{TT;TE}} = \sum_\ell \frac{2\ell+1}{4\pi} \frac{1}{C_\ell^{\mathrm{TT}}} d_{01} \tag{A.72}$$

$$\zeta_{1\pm1,(2)}^{\mathrm{TT;TE}} = \sum_\ell \frac{(2\ell+1)\ell(\ell+1)}{4\pi} \frac{C_\ell^{\mathrm{TE}} \tilde{C}_\ell^{\mathrm{TT}} \tilde{C}_\ell^{\mathrm{TE}}}{C_\ell^{\mathrm{TT}} C_\ell^{\mathrm{EE}}} d_{01} \tag{A.73}$$

For $N_\ell^{TT;EE}$, we find

$$\begin{aligned}
&\sum_{\ell_1\ell_2}\{g^{\mathrm{TT}*}_{\ell_1\ell_2}C^{\mathrm{TE}}_{\ell_1}C^{\mathrm{TE}}_{\ell_2}\left(g^{\mathrm{EE}}_{\ell_1\ell_2}+g^{\mathrm{EE}}_{\ell_2\ell_1}\right)\}\\
&=\frac{C^{\mathrm{TE}}_{\ell_1}C^{\mathrm{TE}}_{\ell_2}}{2C^{\mathrm{TT}}_{\ell_1}C^{\mathrm{TT}}_{\ell_2}C^{\mathrm{EE}}_{\ell_1}C^{\mathrm{EE}}_{\ell_2}}\left[\tilde{C}^{\mathrm{TT}}_{\ell_1}\tilde{C}^{\mathrm{EE}}_{\ell_1}\left(F^0_{\ell_2\ell_1\ell}F^2_{\ell_2\ell_1\ell}+F^0_{\ell_2\ell_1\ell}F^{-2}_{\ell_2\ell_1\ell}\right)\right.\\
&\qquad\left.\tilde{C}^{\mathrm{TT}}_{\ell_1}\tilde{C}^{\mathrm{EE}}_{\ell_2}\left(F^0_{\ell_2\ell_1\ell}F^2_{\ell_1\ell_2\ell}+F^0_{\ell_2\ell_1\ell}F^{-2}_{\ell_1\ell_2\ell}\right)\right]\\
&=\frac{1}{2}\int_{-1}^{+1}\mathrm{d}\cos\theta\ \left[\left(\zeta^{\mathrm{TT;TE}}_{20}\zeta^{\mathrm{TT;TE}}_{1-1}+\zeta^{\mathrm{TT;TE}}_{20}\zeta^{\mathrm{TT;TE}}_{31}\right)d^\ell_{11}\right.\\
&\qquad+\left(\zeta^{\mathrm{TT;TE}}_{20}\zeta^{\mathrm{TT;TE}}_{11}+\zeta^{\mathrm{TT;TE}}_{20}\zeta^{\mathrm{TT;TE}}_{3-1}\right)d^\ell_{1-1}\\
&\qquad+\left(\zeta^{\mathrm{TT;TE}}_{01}\zeta^{\mathrm{TT;TE}}_{21}-\zeta^{\mathrm{TT;TE}}_{30}\zeta^{\mathrm{TT;TE}}_{2-1}\right)d^\ell_{11}\\
&\qquad+\left.\left(\zeta^{\mathrm{TT;TE}}_{01}\zeta^{\mathrm{TT;TE}}_{2-1}-\zeta^{\mathrm{TT;TE}}_{30}\zeta^{\mathrm{TT;TE}}_{21}\right)d^\ell_{1-1}\right.
\end{aligned}\tag{A.74}$$

where

$$\zeta^{\mathrm{TT;EE}}_{20}=\sum_\ell\frac{2\ell+1}{4\pi}\frac{C^{\mathrm{TE}}_\ell}{C^{\mathrm{EE}}_\ell C^{\mathrm{TT}}_\ell}d_{20}\tag{A.75}$$

$$\zeta^{\mathrm{TT;EE}}_{1\pm1}=\sum_\ell\frac{(2\ell+1)\sqrt{\ell(\ell+1)(\ell+2)(\ell-1)}}{4\pi}\frac{C^{\mathrm{TE}}_\ell\tilde{C}^{\mathrm{TT}}_\ell\tilde{C}^{\mathrm{EE}}_\ell}{C^{\mathrm{TT}}_\ell C^{\mathrm{EE}}_\ell}d_{1\pm1}\tag{A.76}$$

$$\zeta^{\mathrm{TT;EE}}_{3\pm1}=\sum_\ell\frac{(2\ell+1)\sqrt{\ell(\ell+1)(\ell-2)(\ell+3)}}{4\pi}\frac{C^{\mathrm{TE}}_\ell\tilde{C}^{\mathrm{TT}}_\ell\tilde{C}^{\mathrm{EE}}_\ell}{C^{\mathrm{TT}}_\ell C^{\mathrm{EE}}_\ell}d_{3\pm1}\tag{A.77}$$

$$\zeta^{\mathrm{TT;EE}}_{01}=\sum_\ell\frac{(2\ell+1)sqrt\ell(\ell+2)}{4\pi}\frac{C^{\mathrm{TE}}_\ell\tilde{C}^{\mathrm{EE}}_\ell}{C^{\mathrm{TT}}_\ell C^{\mathrm{EE}}_\ell}d_{01}\tag{A.78}$$

$$\zeta^{\mathrm{TT;EE}}_{2\pm1}=\sum_\ell\frac{(2\ell+1)(\ell+2)(\ell-1)}{4\pi}\frac{C^{\mathrm{TE}}_\ell\tilde{C}^{\mathrm{TT}}_\ell}{C^{\mathrm{TT}}_\ell C^{\mathrm{EE}}_\ell}d_{2\pm1}\tag{A.79}$$

$$\zeta^{\mathrm{TT;EE}}_{30}=\sum_\ell\frac{(2\ell+1)\sqrt{(\ell-2)(\ell+3)}}{4\pi}\frac{C^{\mathrm{TE}}_\ell\tilde{C}^{\mathrm{TT}}_\ell}{C^{\mathrm{TT}}_\ell C^{\mathrm{EE}}_\ell}d_{30}\tag{A.80}$$

For $N_\ell^{TB;EB}$ we find

$$\begin{aligned}
&\sum_{\ell_1\ell_2} g^{\mathrm{TB}*}_{\ell_1\ell_2}\left(C^{\mathrm{TE}}_{\ell_1}C^{\mathrm{BB}}_{\ell_2}g^{\mathrm{EB}}_{\ell_1\ell_2}\right)\\
&=\sum_{\ell_1\ell_2}\frac{C^{\mathrm{TE}}_{\ell_1}\tilde{C}^{\mathrm{TE}}_{\ell_1}}{C^{\mathrm{TT}}_{\ell_1}C^{\mathrm{EE}}_{\ell_1}C^{\mathrm{BB}}_{\ell_2}}\left[\frac{\tilde{C}^{\mathrm{EE}}_{\ell_1}}{4}\left(F^2_{\ell_2\ell_1\ell}-F^{-2}_{\ell_2\ell_1\ell}\right)^2-\frac{\tilde{C}^{\mathrm{BB}}_{\ell_2}}{4}\left(F^2_{\ell_2\ell_1\ell}F^2_{\ell_1\ell_2\ell}-F^2_{\ell_2\ell_1\ell}F^{-2}_{\ell_1\ell_2\ell}-F^{-2}_{\ell_2\ell_1\ell}F^2_{\ell_1\ell_2\ell}+F^{-2}_{\ell_2\ell_1\ell}F^2_{\ell_1\ell_2\ell}\right)\right]\\
&=\frac{1}{4}\int_{-1}^{+1}\mathrm{d}\cos\theta\ \Big[\left(\zeta^{\mathrm{TB;EB}}_{22}\zeta^{\mathrm{TB;EB}}_{33}+\zeta^{\mathrm{TB;EB}}_{22}\zeta^{\mathrm{TB;EB}}_{11,(1)}-2\zeta^{\mathrm{TB;EB}}_{2-2}\zeta^{\mathrm{TB;EB}}_{3-1,(1)}\right)d^\ell_{11}\\
&\quad-\left(\zeta^{\mathrm{TB;EB}}_{2-2}\zeta^{\mathrm{TB;EB}}_{3-3}+\zeta^{\mathrm{TB;EB}}_{2-2}\zeta^{\mathrm{TB;EB}}_{1-1,(1)}-2\zeta^{\mathrm{TB;EB}}_{22}\zeta^{\mathrm{TB;EB}}_{31,(1)}\right)d^\ell_{1-1}\\
&\quad+(-1)^{(\ell_1+\ell_2+\ell:\mathrm{odd})}\left(\zeta^{\mathrm{TB;EB}}_{3-2,(\alpha)}\zeta^{\mathrm{TB;EB}}_{3-2,(\beta)}+\zeta^{\mathrm{TB;EB}}_{2-1,(\alpha)}\zeta^{\mathrm{TB;EB}}_{2-1,(\beta)}-\zeta^{\mathrm{TB;EB}}_{32,(\alpha)}\zeta^{\mathrm{TB;EB}}_{21,(\alpha)}-\zeta^{\mathrm{TB;EB}}_{21,(\beta)}\zeta^{\mathrm{TB;EB}}_{32,(\beta)}\right)d_{11}\\
&\quad+(-1)^{(\ell_1+\ell_2+\ell:\mathrm{odd})}\left(\zeta^{\mathrm{TB;EB}}_{32,(\alpha)}\zeta^{\mathrm{TB;EB}}_{32,(\beta)}+\zeta^{\mathrm{TB;EB}}_{21,(\alpha)}\zeta^{\mathrm{TB;EB}}_{21,(\beta)}+\zeta^{\mathrm{TB;EB}}_{3-2,(\alpha)}\zeta^{\mathrm{TB;EB}}_{2-1,(\alpha)}+\zeta^{\mathrm{TB;EB}}_{2-1,(\beta)}\zeta^{\mathrm{TB;EB}}_{3-2,(\beta)}\right)d_{1-1}
\end{aligned}\tag{A.81}$$

where

$$\zeta^{\mathrm{TB;EB}}_{2\pm2}=\sum_\ell\frac{2\ell+1}{4\pi}\frac{1}{C^{\mathrm{BB}}_\ell}d_{2\pm2}\tag{A.82}$$

$$\zeta^{\mathrm{TB;EB}}_{3\pm3}=\sum_\ell\frac{(2\ell+1)\times(\ell-2)\times(\ell+3)}{4\pi}\frac{C^{\mathrm{TE}}_\ell\tilde{C}^{\mathrm{TE}}_\ell\tilde{C}^{\mathrm{EE}}_\ell}{C^{\mathrm{TT}}_\ell C^{\mathrm{EE}}_\ell}d_{3\pm3}\tag{A.83}$$

$$\zeta^{\mathrm{TB;EB}}_{3\pm1,(1)}=\sum_\ell\frac{(2\ell+1)\times\sqrt{(\ell+2)\times(\ell-1)\times(\ell-2)\times(\ell+3)}}{4\pi}\frac{C^{\mathrm{TE}}_\ell\tilde{C}^{\mathrm{TE}}_\ell\tilde{C}^{\mathrm{EE}}_\ell}{C^{\mathrm{TT}}_\ell C^{\mathrm{EE}}_\ell}d_{3\pm1}\tag{A.84}$$

$$\zeta^{\mathrm{TB;EB}}_{1\pm1,(1)}=\sum_\ell\frac{(2\ell+1)\times(\ell+2)\times(\ell-1)}{4\pi}\frac{C^{\mathrm{TE}}_\ell\tilde{C}^{\mathrm{TE}}_\ell\tilde{C}^{\mathrm{EE}}_\ell}{C^{\mathrm{TT}}_\ell C^{\mathrm{EE}}_\ell}d_{1\pm1}\tag{A.85}$$

$$\zeta^{\mathrm{TB;EB}}_{2\pm1,(\alpha)}=\sum_\ell\frac{(2\ell+1)\times(\ell+2)\times(\ell-1)}{4\pi}\frac{\tilde{C}^{\mathrm{BB}}_\ell}{C^{\mathrm{BB}}_\ell}d_{2\pm1}\tag{A.86}$$

$$\zeta^{\mathrm{TB;EB}}_{3\pm2,(\alpha)}=\sum_\ell\frac{(2\ell+1)\times\sqrt{(\ell-2)\times(\ell+3)}}{4\pi}\frac{C^{\mathrm{TE}}_\ell\tilde{C}^{\mathrm{TE}}_\ell}{C^{\mathrm{TT}}_\ell C^{\mathrm{EE}}_\ell}d_{3\pm2}\tag{A.87}$$

$$\zeta^{\mathrm{TB;EB}}_{2\pm1,(\beta)}=\sum_\ell\frac{(2\ell+1)\times(\ell+2)\times(\ell-1)}{4\pi}\frac{C^{\mathrm{TE}}_\ell\tilde{C}^{\mathrm{TE}}_\ell}{C^{\mathrm{TT}}_\ell C^{\mathrm{EE}}_\ell}d_{2\pm1}\tag{A.88}$$

$$\zeta^{\mathrm{TB;EB}}_{3\pm2,(\beta)}=\sum_\ell\frac{(2\ell+1)\times\sqrt{(\ell-2)\times(\ell+3)}}{4\pi}\frac{\tilde{C}^{\mathrm{BB}}_\ell}{C^{\mathrm{BB}}_\ell}d_{3\pm2}\tag{A.89}$$

Appendix B

kSZ bias with the transverse velocities

In Chapter 6 I introduced the kSZ effect as a probe of fundamental physics. The cosmology that can be extracted from the kSZ measurements, however, is limited by the uncertainty on the distribution of the ionised electron gas and its cross-correlation with the underlying density fluctuations accessible to galaxy surveys, for example. This effect is called the 'optical dept degeneracy' in kSZ reconstruction.

In this Appendix I explore a possible method to constrain the optical depth bias by an unbiased external measurement of transverse velocity field (potentially will be made possible by the moving-lens effect measurements). I expand on one point made in Chapter 5 regarding the potential astrophysics applications of the moving-lens effect measurement.

The idea explored here is as follows: the underlying 3-velocity field is pure-gradient on very large-scales (as expected in standard considerations of initial conditions). This means that while we can potentially have three observational degrees of freedom afforded by combined measurements of the kSZ and the moving lens effects, for example, the number of independent equations are reduced by one constraint equation, setting the curl component to zero. This indices that while the true unbiased velocity fields should give zero curl, a biased measurement of a velocity component (e.g. the radial velocities measured by the kSZ effect) would lead the reconstructed 3-velocity *away* from zero curl. The measured unbiased transverse velocity components can then be used to constrain this deviation in the reconstructed 3-velocity field.

I have made the conceptualisation and the calculations of this study. The idea had first came to light in discussions with Kendrick Smith.

B.1 Spurious 3-velocity curl from velocity bias

Estimates for the large-scale radial velocities $\hat{v}_r^{\rm kSZ}$ from kinematic Sunyaev Zel'dovich (kSZ) effect are biased due to uncertainties in the galaxy-electron cross-correlations in the from

$$\langle \hat{v}_r^{\rm kSZ}(\mathbf{k}) \rangle = b_v v_r(\mathbf{k}) \tag{B.1}$$

where b_v is called the velocity bias and $v_r(\mathbf{k})$ is the radial part of the true three-dimensional velocity in Fourier space. We define the velocity field with *local* unit coordinates as

$$\mathbf{v}(\mathbf{r}) = v_r(\mathbf{r})\ \hat{\mathbf{r}}(\theta,\phi) + v_\theta(\mathbf{r})\ \hat{\boldsymbol{\theta}}(\theta,\phi) + v_\phi(\mathbf{r})\ \hat{\boldsymbol{\phi}}(\theta,\phi)\,,$$

or equivalently,

$$\begin{aligned} v_r(\mathbf{r}) &= \mathbf{v}(\mathbf{r})\cdot\hat{\mathbf{r}}(\theta,\phi)\,,\\ v_\theta(\mathbf{r}) &= \mathbf{v}(\mathbf{r})\cdot\hat{\boldsymbol{\theta}}(\theta,\phi)\,,\\ v_\phi(\mathbf{r}) &= \mathbf{v}(\mathbf{r})\cdot\hat{\boldsymbol{\phi}}(\theta,\phi)\,, \end{aligned} \tag{B.2}$$

where

$$\begin{aligned} \hat{\mathbf{r}} &= \sin\theta\cos\phi\ \hat{\mathbf{x}} + \sin\theta\sin\phi\ \hat{\mathbf{y}} + \cos\theta\ \hat{\mathbf{z}}\\ \hat{\boldsymbol{\theta}} &= \cos\theta\cos\phi\ \hat{\mathbf{x}} + \cos\theta\sin\phi\ \hat{\mathbf{y}} - \sin\theta\ \hat{\mathbf{z}}\\ \hat{\boldsymbol{\phi}} &= -\sin\phi\ \hat{\mathbf{x}} + \cos\phi\ \hat{\mathbf{y}}\,, \end{aligned} \tag{B.3}$$

are (unit) vector fields. I will omit showing the angular dependence of the unit vectors in what follows. Similarly, we locally define the components of the velocity vector in Fourier space $\tilde{\mathbf{v}}(\mathbf{k})$ as

$$\begin{aligned} v_r(\mathbf{r}) &= \int \frac{\mathrm{d}^3\mathbf{k}}{(2\pi)^3}\ (\tilde{\mathbf{v}}(\mathbf{k})\cdot\hat{\mathbf{r}})\ e^{i\mathbf{k}\cdot\mathbf{r}}\\ v_\theta(\mathbf{r}) &= \int \frac{\mathrm{d}^3\mathbf{k}}{(2\pi)^3}\ \left(\tilde{\mathbf{v}}(\mathbf{k})\cdot\hat{\boldsymbol{\theta}}\right)\ e^{i\mathbf{k}\cdot\mathbf{r}}\\ v_\phi(\mathbf{r}) &= \int \frac{\mathrm{d}^3\mathbf{k}}{(2\pi)^3}\ \left(\tilde{\mathbf{v}}(\mathbf{k})\cdot\hat{\boldsymbol{\phi}}\right)\ e^{i\mathbf{k}\cdot\mathbf{r}} \end{aligned} \tag{B.4}$$

where

$$\tilde{v_r}(\mathbf{k}) = \tilde{\mathbf{v}}(\mathbf{k})\cdot\hat{\mathbf{r}},\quad \tilde{v_\theta}(\mathbf{k}) = \tilde{\mathbf{v}}(\mathbf{k})\cdot\hat{\boldsymbol{\theta}}\ \ \tilde{v_\phi}(\mathbf{k}) = \tilde{\mathbf{v}}(\mathbf{k})\cdot\hat{\boldsymbol{\phi}}\,,$$

are the Fourier transforms of the components $v_r(\mathbf{r})$, $v_\theta(\mathbf{r})$, $v_\phi(\mathbf{r})$, and I will omit the tilde on the Fourier transforms in the remainder of these notes.

The *true* three-dimensional velocity is pure gradient on large scales hence it satisfies $\mathbf{v}(\mathbf{k}) = i\hat{\mathbf{k}}v(\mathbf{k})$, or equivalently $\mathbf{v}(\mathbf{k}) = \nabla v(\mathbf{k})/k$ where $k = |\mathbf{k}|$, since we consider scalar perturbations only. The Helmholtz decomposition of a vector field to curl-free and divergence-free components, which we use throughout these notes, is defined as

$$\mathbf{v}(\mathbf{r}) = -\nabla_{\mathbf{r}} v(\mathbf{r}) + \nabla_{\mathbf{r}} \times \mathbf{A}(\mathbf{r}) \tag{B.5}$$

where $\nabla_{\mathbf{r}}$ is the three dimensional gradient, and

$$\mathbf{A}^a(\mathbf{r}) = -i \int \frac{\mathrm{d}^3\mathbf{k}}{(2\pi)^3} \frac{[\mathbf{k} \times \mathbf{v}(\mathbf{k})]^a}{k^2} e^{i\mathbf{k}\cdot\mathbf{r}}\,, \tag{B.6}$$

$$v(\mathbf{r}) = -i \int \frac{\mathrm{d}^3\mathbf{k}}{(2\pi)^3} \frac{\mathbf{k} \cdot \mathbf{v}(\mathbf{k})}{k^2} e^{i\mathbf{k}\cdot\mathbf{r}}\,, \tag{B.7}$$

and

$$\mathbf{v}^a(\mathbf{k}) = \int \frac{\mathrm{d}^3\mathbf{k}}{(2\pi)^3} \mathbf{v}^a(\mathbf{r}) e^{i\mathbf{k}\cdot\mathbf{r}}\,, \tag{B.8}$$

such that the in Fourier space, the velocity can be written as

$$\mathbf{v}(\mathbf{k}) = i\mathbf{k}\left[i\frac{\mathbf{k}\cdot\mathbf{v}(\mathbf{k})}{k^2}\right] - i\mathbf{k}\times\left[i\frac{\mathbf{k}\times\mathbf{v}(\mathbf{k})}{k^2}\right]. \tag{B.9}$$

Now let us consider the scenario where we have unbiased measurements of the transverse velocities

$$\hat{\mathbf{v}}_\perp(\mathbf{k}) = \hat{v}_\theta(\mathbf{k})\hat{\boldsymbol{\theta}} + \hat{v}_\phi(\mathbf{k})\hat{\boldsymbol{\phi}}\,,$$

hence $\langle\hat{v}_\theta\rangle = v_\theta$ and $\langle\hat{v}_\phi\rangle = v_\phi$, and a biased measurement of the radial component as shown in Eq. (B.1). The non-unity bias parameter will modify the three-dimensional velocity by $\Delta\mathbf{v}(\mathbf{k}) = (b_v - 1)v_r(\mathbf{k})\hat{\mathbf{r}}$, which introduces a curl contribution that can be calculated in the form

$$\mathbf{v}^C(\mathbf{k}) = -i\mathbf{k}\times\left[i\frac{\mathbf{k}\times\Delta\mathbf{v}(\mathbf{k})}{k^2}\right]. \tag{B.10}$$

The resulting curl component of the velocity at some local point in space can be found straightforwardly using

$$\begin{aligned}\mathbf{k}\times\mathbf{v}(\mathbf{k}) = &\left(k_\theta v_\phi(\mathbf{k}) - k_\phi v_\theta(\mathbf{k})\right)\hat{\mathbf{r}}\\ &+\left(k_\phi v_r(\mathbf{k}) - k_r v_\phi(\mathbf{k})\right)\hat{\boldsymbol{\theta}}\\ &+\left(k_r v_\theta(\mathbf{k}) - k_\theta v_r(\mathbf{k})\right)\hat{\boldsymbol{\phi}}\,,\end{aligned} \tag{B.11}$$

where note for the true velocity field $[\mathbf{k}\times\mathbf{v}(\mathbf{k})]^a = 0$, and

$$\mathbf{k}\times\Delta\mathbf{v}(\mathbf{k}) = k_\phi(b_v-1)v_r(\mathbf{k})\hat{\boldsymbol{\theta}} + k_\theta(b_v-1)v_r(\mathbf{k})\hat{\boldsymbol{\phi}}\,,$$

which gives,

$$\mathbf{v}^C(\mathbf{k}) = \left[\frac{k_r}{k^2}(b_v-1)v_r(\mathbf{k})\right]\left[k_\phi\hat{\boldsymbol{\theta}} + k_\theta\hat{\boldsymbol{\phi}}\right]\,, \tag{B.12}$$

where k_r, k_θ, k_ϕ are the locally defined radial, $\hat{\boldsymbol{\theta}}$ and $\hat{\boldsymbol{\phi}}$ components of the wavenumber respectively, i.e. $\mathbf{k} = k_r\,\hat{\mathbf{r}} + k_\theta\,\hat{\boldsymbol{\theta}} + k_\phi\,\hat{\boldsymbol{\phi}}$, and we used the fact that the true velocity field $\mathbf{v}$ is pure gradient satisfying the equality

$$v_r(\mathbf{k})/k_r = v_\theta(\mathbf{k})/k_\theta = v_\phi(\mathbf{k})/k_\phi\,. \tag{B.13}$$

We will be interested in the transverse-projected gradient and curl and components, the latter given in Eq. (B.12). Note the curl component induced by the non-unity b_v is identical to the transverse velocity component of the three-dimensional pure-gradient velocity field up-to a scale-dependent coefficient. The contribution to the gradient part of the transverse velocity is

$$\begin{aligned}\Delta\mathbf{v}^G_\perp(\hat{\mathbf{n}}) &= -(\nabla_{\mathbf{r}})_\perp\int\frac{\mathrm{d}^3\mathbf{k}}{(2\pi)^3}\frac{\mathbf{k}\cdot\Delta\mathbf{v}(\mathbf{k})}{k^2}e^{ik\hat{\mathbf{k}}\cdot\hat{\mathbf{n}}\chi}\\ &= -\nabla\int\frac{\mathrm{d}^3\mathbf{k}}{(2\pi)^3}v(\mathbf{k})\frac{(\hat{\mathbf{k}}\cdot\hat{\mathbf{n}})^2}{\chi k}e^{ik\hat{\mathbf{k}}\cdot\hat{\mathbf{n}}\chi}\,,\end{aligned} \tag{B.14}$$

where $(\nabla_{\mathbf{r}})_\perp$ is the three dimensional gradient projected onto the two-sphere, $\nabla = (\partial/\partial\theta)\hat{\boldsymbol{\theta}} + (\sin\theta)^{-1}(\partial/\partial\phi)\hat{\boldsymbol{\phi}}$ is the gradient on the 2-sphere and used the familiar notation $\hat{\mathbf{n}} := \hat{\mathbf{r}}$. In what follows I omit showing the factor of $\Delta b_v = (b_v - 1)$ multiplying the right-hand side.

Note that we can expand the exponential as

$$e^{ikr\hat{\mathbf{k}}\cdot\hat{\mathbf{n}}} = \sum_{\ell m} 4\pi i^{\ell} j_{\ell}(kr) Y^{\star}_{\ell m}(\hat{\mathbf{k}}) Y_{\ell m}(\hat{\mathbf{n}})\,.$$

and can use the fact that $2/3[P_2(\hat{\mathbf{n}}\cdot\hat{\mathbf{k}}) - 1/2] = (\hat{\mathbf{n}}\cdot\hat{\mathbf{k}})^2$ with the relation

$$P_{\ell}(\hat{\mathbf{n}}\cdot\hat{\mathbf{k}}) = \frac{4\pi}{2\ell+1} \sum_{m=-\ell}^{\ell} Y^{\star}_{\ell m}(\hat{\mathbf{n}}) Y_{\ell m}(\hat{\mathbf{k}})\,,$$

which allows us to write

$$\begin{aligned}\Delta\mathbf{v}^{G}_{\perp}(\hat{\mathbf{n}}) = -\nabla \sum_{LM} 4\pi i^{\ell} \int \frac{\mathrm{d}^3\mathbf{k}}{(2\pi)^3} \frac{v(\mathbf{k})}{k\chi} j_{\ell}(k\chi) \\ \times \left[\frac{2}{3}\left(\frac{4\pi}{5}\sum_{m'} Y^{\star}_{2m'}(\hat{\mathbf{n}}) Y_{2m'}(\hat{\mathbf{k}}) - \frac{1}{2}\right) Y^{\star}_{LM}(\hat{\mathbf{k}}) Y_{LM}(\hat{\mathbf{n}})\right]\end{aligned} \tag{B.15}$$

B.2 The effect on ϒ

We can expand the transverse velocity field in a form that will prove useful in what follows, as

$$\mathbf{v}^{a}_{\perp}(\hat{\mathbf{n}}) = \nabla^{a}\Upsilon(\hat{\mathbf{n}}) + \varepsilon^{a}_{b}\nabla^{b}\varpi(\hat{\mathbf{n}})\,, \tag{B.16}$$

where $\nabla^{a}\Upsilon(\hat{\mathbf{n}}) = \left[\mathbf{v}_{\perp} + \Delta\mathbf{v}^{G}_{\perp}\right]^{a}(\mathbf{n})$ and ε_{ab} is the 2-dimensional levi-civita tensor. We defined some useful spherical harmonic relations in Eqns. (6.5) and (6.6). We get for the correction to the pure gradient velocity,

$$\begin{aligned}(\delta\Upsilon)_{\ell m} = \sum_{LM} 4\pi i^{\ell} \int \frac{\mathrm{d}^3\mathbf{k}}{(2\pi)^3} \frac{v(\mathbf{k})}{k\chi} j_{\ell}(k\chi) \\ \times \left[F_{LM\ell m}(\hat{\mathbf{k}}) - \frac{1}{3}\delta_{\ell L}\delta_{mM}\right] Y^{\star}_{LM}(\hat{\mathbf{k}})\end{aligned} \tag{B.17}$$

where

$$F_{LM\ell m}(\hat{\mathbf{k}}) = \frac{8\pi}{15}\sqrt{\frac{5(2L+1)(2\ell+1)}{4\pi}} \times \sum_{m'} \begin{pmatrix} 2 & L & \ell \\ -m' & M & -m \end{pmatrix} \begin{pmatrix} 2 & L & \ell \\ 0 & 0 & 0 \end{pmatrix} Y_{2m'}(\hat{\mathbf{k}}) \tag{B.18}$$

Contracting the $\hat{\mathbf{k}}$ dependent spherical harmonics and doing the $\sum_{mm'}$ sum, we find,

$$\boxed{(\delta\Upsilon)_{\ell m} = -4\pi i^{\ell}\int \frac{\mathrm{d}^3\mathbf{k}}{(2\pi)^3}\frac{v(\mathbf{k})}{k\chi}Y^{\star}_{\ell m}(\hat{\mathbf{k}}) \times \left(\frac{2}{3}\frac{\mathrm{d}^2 j_\ell(k\chi)}{k^2\mathrm{d}\chi^2} + \left[\frac{2\ell^2-2\ell+1/2}{(2\ell+3)(2\ell-1)} + \frac{1}{3}\right] j_\ell(k\chi)\right).} \tag{B.19}$$

We are interested in the signal $\langle \delta\Upsilon_{\ell m}\delta\Upsilon^{\star}_{\ell m}\rangle = C_\ell^{\delta\Upsilon\delta\Upsilon}\delta_{\ell\ell'}\delta_{mm'}$. We show this spectra in Fig. B.1.

B.3 The effect on ϖ

Calculating $\varpi(\hat{\mathbf{n}})$ is more involved. We begin by noting $\varepsilon_b^1\nabla^b\varpi(\hat{\mathbf{n}}) = -(\sin\theta)^{-1}(\partial/\partial\phi)\varpi(\hat{\mathbf{n}})$ and $\varepsilon_b^2\nabla^b\varpi(\hat{\mathbf{n}}) = (\partial/\partial\theta)\varpi(\hat{\mathbf{n}})$ and using the derived curl contribution to the transverse velocity in Eq. (B.12), we write

$$\int \frac{\mathrm{d}^3\mathbf{k}}{(2\pi)^3}(\mathbf{v}^C(\mathbf{k})\cdot\hat{\boldsymbol{\theta}})e^{ikr\hat{\mathbf{k}}\cdot\hat{\mathbf{n}}} = -\sum_{\ell m}\varpi_{\ell m}\frac{1}{\sin\theta}\frac{\partial Y_{\ell m}(\hat{\mathbf{n}})}{\partial\phi}, \tag{B.20}$$

$$\int \frac{\mathrm{d}^3\mathbf{k}}{(2\pi)^3}(\mathbf{v}^C(\mathbf{k})\cdot\hat{\boldsymbol{\phi}})e^{ikr\hat{\mathbf{k}}\cdot\hat{\mathbf{n}}} = -\sum_{\ell m}\varpi_{\ell m}\frac{\partial Y_{\ell m}(\hat{\mathbf{n}})}{\partial\theta}, \tag{B.21}$$

where $\mathbf{v}^C(\mathbf{k})\cdot\hat{\boldsymbol{\theta}} = (\hat{\mathbf{k}}\cdot\hat{\boldsymbol{\phi}})(\hat{\mathbf{k}}\cdot\hat{\mathbf{n}})^2 v(\mathbf{k})$ and $\mathbf{v}^C(\mathbf{k})\cdot\hat{\boldsymbol{\phi}} = (\hat{\mathbf{k}}\cdot\hat{\boldsymbol{\theta}})(\hat{\mathbf{k}}\cdot\hat{\mathbf{n}})^2 v(\mathbf{k})$.

We now define *vector* spherical harmonics defined as $\mathbf{\Phi}_{\ell m}(\hat{\mathbf{n}}) = \mathbf{r} \times \nabla_{\mathbf{r}} Y_{\ell m}(\hat{\mathbf{n}})$ which projected on two sphere give $(1/r)(\star\nabla)Y_{\ell m}(\hat{\mathbf{n}})$, and we use the equality

$$(\star\nabla)\varpi(\hat{\mathbf{n}}) = \sum_{\ell m} \varpi_{\ell m}(\star\nabla)Y_{\ell m}(\hat{\mathbf{n}}) \tag{B.22}$$

where $(\star\nabla) = -\nabla_\phi\ \hat{\boldsymbol{\theta}} + \nabla_\theta\ \hat{\boldsymbol{\phi}}$ is the curl on two sphere, and we will use

$$\int \mathrm{d}^2\hat{\mathbf{n}}\ \mathbf{\Phi}_{\ell m}(\hat{\mathbf{n}}) \cdot \mathbf{\Phi}^\star_{\ell' m'}(\hat{\mathbf{n}}) = \ell(\ell+1)\delta_{\ell\ell'}\delta_{m'm}\,.$$

We can isolate the coefficients $\varpi_{\ell m}$ in Eq. (B.22) by multiplying by the vector spherical harmonic $\mathbf{\Phi}^\star_{\ell' m'}$ integrating over the angle $\mathrm{d}^2\hat{\mathbf{n}}$. Corresponding expression is equivalent to the Fourier transform of the curl component of the transverse velocity in Eq. (B.12) multiplied by $\mathbf{\Phi}^\star_{\ell m}$ and integrated over $\mathrm{d}^2\hat{\mathbf{n}}$. Note also that the unit basis fields can be written as $(\sin\theta)^{-1}(\partial/\partial\phi)\hat{\mathbf{n}} = \hat{\boldsymbol{\phi}}$ and $(\partial/\partial\theta)\hat{\mathbf{n}} = \hat{\boldsymbol{\theta}}$ and that $\hat{\mathbf{k}}$ do not depend on angles θ and ϕ associated to $\hat{\mathbf{n}}$. We can now write

$$\begin{aligned}
&\ell(\ell+1)\varpi_{\ell m} = \\
&-\sum_{LM} 4\pi i^L \int \mathrm{d}^2\hat{\mathbf{n}} \int \frac{\mathrm{d}^3\mathbf{k}}{(2\pi)^3} \frac{j_L(k\chi)}{\chi} Y^\star_{LM}(\hat{\mathbf{k}}) Y_{LM}(\hat{\mathbf{n}}) \\
&\quad \times \frac{v(\mathbf{k})}{3} \left[\frac{\partial}{\partial\phi}\left[(\hat{\mathbf{n}}\cdot\hat{\mathbf{k}})^3\right] \left(\frac{\partial Y_{\ell m}(\hat{\mathbf{n}})}{\sin^2\theta\,\partial\phi} \right)^\star \right. \\
&\qquad\qquad \left. + \frac{\partial}{\partial\theta}\left[(\hat{\mathbf{n}}\cdot\hat{\mathbf{k}})^3\right] \left(\frac{\partial Y_{\ell m}(\hat{\mathbf{n}})}{\partial\theta} \right)^\star \right].
\end{aligned} \tag{B.23}$$

which has the form of the angular integral,

$$\int \mathrm{d}^2\hat{\mathbf{n}}\ Y_{LM}(\hat{\mathbf{n}}) \left[(\star\nabla)Y^\star_{\lambda m'}(\hat{\mathbf{n}}) \cdot (\star\nabla)Y^\star_{\ell m}(\hat{\mathbf{n}}) \right] \Big|_{\lambda=\{1,3\}}\,, \tag{B.24}$$

and note that $(\hat{\mathbf{n}}\cdot\hat{\mathbf{k}})^3 = [2P_3(\hat{\mathbf{n}}\cdot\hat{\mathbf{k}}) + 3P_1(\hat{\mathbf{n}}\cdot\hat{\mathbf{k}})]/5$ and $(\partial/\partial\phi)Y_{\ell m}(\hat{\mathbf{n}}) = imY_{\ell m}(\hat{\mathbf{n}})$. We begin by introducing

$$\begin{aligned}
P_3(\hat{\mathbf{n}}\cdot\hat{\mathbf{k}}) &= \sum_{m'} Y^\star_{3m'}(\hat{\mathbf{n}}) Y_{3m'}(\hat{\mathbf{k}}) \\
P_1(\hat{\mathbf{n}}\cdot\hat{\mathbf{k}}) &= \sum_{m'} Y^\star_{1m'}(\hat{\mathbf{n}}) Y_{1m'}(\hat{\mathbf{k}})\,,
\end{aligned} \tag{B.25}$$

where I note that the summed indices m', upon expanding, will be the *same* for both of the P_3 terms in the second and third lines of Eq. (B.23) as well as the indices for P_1 terms. This is because these are coming from the same transverse velocity *vector* and the expansion is actually performed on the vector, not separately.

We can perform an integration by parts on the terms in the second and third lines and can transform the integrals in Eq. (B.23) into a summation of three terms whose angular integral looks like

$$\begin{aligned}
&\int \mathrm{d}^2\hat{\mathbf{n}} Y_{LM}(\hat{\mathbf{n}}) Y^{\star}_{\lambda m'}(\hat{\mathbf{n}}) \\
&\times \left[\frac{1}{\sin\theta}\frac{\partial}{\partial\theta}\left(\sin\theta\frac{\partial}{\partial\theta}\right) - \frac{1}{\sin^2\theta}\frac{\partial^2}{\partial\phi^2}\right] Y^{\star}_{\ell m}(\hat{\mathbf{n}}) \\
&= \ell(\ell+1)\int \mathrm{d}^2\hat{\mathbf{n}}\, Y_{LM}(\hat{\mathbf{n}}) Y^{\star}_{\lambda m'}(\hat{\mathbf{n}}) Y^{\star}_{\ell m}(\hat{\mathbf{n}})
\end{aligned} \tag{B.26}$$

where $\lambda = \{1,3\}$ and the L^2 operator acts separately on all spherical harmonics. We can now write

$$\begin{aligned}
\ell(\ell+1)\varpi_{\ell m} = &-\sum_{LM}\frac{4\pi i^L}{3}\int\frac{\mathrm{d}^3\mathbf{k}}{(2\pi)^3}\frac{j_L(k\chi)}{\chi}Y^{\star}_{LM}(\hat{\mathbf{k}})v(\mathbf{k}) \\
\times\Bigg(&\sum_{m'}\frac{4\pi}{35}[(3)(4)+\ell(\ell+1)+L(L+1)]\sqrt{\frac{7(2\ell+1)(2L+1)}{4\pi}}\begin{pmatrix}3 & \ell & L\\ -m' & -m & M\end{pmatrix}\begin{pmatrix}3 & \ell & L\\ 0 & 0 & 0\end{pmatrix}Y^{\star}_{3m'}(\hat{\mathbf{k}}) \\
&+\sum_{m'}\frac{6\pi}{15}[(1)(2)+\ell(\ell+1)+L(L+1)]\sqrt{\frac{3(2\ell+1)(2L+1)}{4\pi}}\begin{pmatrix}1 & \ell & L\\ -m' & -m & M\end{pmatrix}\begin{pmatrix}1 & \ell & L\\ 0 & 0 & 0\end{pmatrix}Y^{\star}_{1m'}(\hat{\mathbf{k}})\Bigg)
\end{aligned} \tag{B.27}$$

We now use the equalities

$$\begin{aligned}
&Y^{\star}_{LM}(\hat{\mathbf{k}})Y_{3m'}(\hat{\mathbf{k}}) \\
&\quad= \sum_{L'M'}(-1)^{L+3+L'}\sqrt{\frac{7(2L+1)(2L'+1)}{4\pi}}\,, \\
&\quad\quad\begin{pmatrix}L & 3 & L'\\ -M & m' & M'\end{pmatrix}\begin{pmatrix}L & 3 & L'\\ 0 & 0 & 0\end{pmatrix}Y^{\star}_{L'M'}(\hat{\mathbf{k}})
\end{aligned} \tag{B.28}$$

$$
\begin{aligned}
&Y^{\star}_{LM}(\hat{\mathbf{k}})Y_{1m'}(\hat{\mathbf{k}}) \\
&\quad = \sum_{L'M'}(-1)^{L+1+L'}\sqrt{\frac{3(2L+1)(2L'+1)}{4\pi}} \\
&\quad \begin{pmatrix} L & 1 & L' \\ -M & m' & M' \end{pmatrix}\begin{pmatrix} L & 1 & L' \\ 0 & 0 & 0 \end{pmatrix} Y^{\star}_{L'M'}(\hat{\mathbf{k}})
\end{aligned}
\tag{B.29}
$$

and do the the $\sum_{Mm'}$ summations after inserting the above expressions into Eq. (B.34). We use

$$
\begin{aligned}
&\sum_{Mm'}\begin{pmatrix} 3 & L & \ell \\ m' & -M & m \end{pmatrix}\begin{pmatrix} 3 & L & L' \\ m' & -M & M' \end{pmatrix} \\
&\qquad = (2\ell+1)^{-1}\delta_{L'\ell}\delta_{M'm}\,,
\end{aligned}
\tag{B.30}
$$

(B.31)

and

$$
\begin{aligned}
&\sum_{Mm'}\begin{pmatrix} 1 & L & \ell \\ m' & -M & m \end{pmatrix}\begin{pmatrix} 1 & L & L' \\ m' & -M & M' \end{pmatrix} \\
&\qquad = (2\ell+1)^{-1}\delta_{L'\ell}\delta_{M'm}\,,
\end{aligned}
\tag{B.32}
$$

(B.33)

to get

$$
\begin{aligned}
\ell(\ell+1)\varpi_{\ell m} = -\sum_{L}\frac{4\pi i^{L}}{15}\int\frac{\mathrm{d}^3\mathbf{k}}{(2\pi)^3}\frac{j_L(k\chi)}{\chi}v(\mathbf{k})(2L+1)Y^{\star}_{\ell m}(\hat{\mathbf{k}}) \\
\times\left\{\Big[(3)(4)+\ell(\ell+1)+L(L+1)\Big]\begin{pmatrix} 3 & \ell & L \\ 0 & 0 & 0 \end{pmatrix}^2\right. \\
\left.+\frac{3}{2}\Big[(1)(2)+\ell(\ell+1)+L(L+1)\Big]\begin{pmatrix} 1 & \ell & L \\ 0 & 0 & 0 \end{pmatrix}^2\right\}
\end{aligned}
\tag{B.34}
$$

such that,

$$
\boxed{\ell(\ell+1)\varpi_{\ell m} = -16\pi i^{\ell+1}\int\frac{\mathrm{d}^3\mathbf{k}}{(2\pi)^3}\frac{\beta_\ell(k\chi)}{\chi}v(\mathbf{k})Y^{\star}_{\ell m}(\hat{\mathbf{k}})}\,,
\tag{B.35}
$$

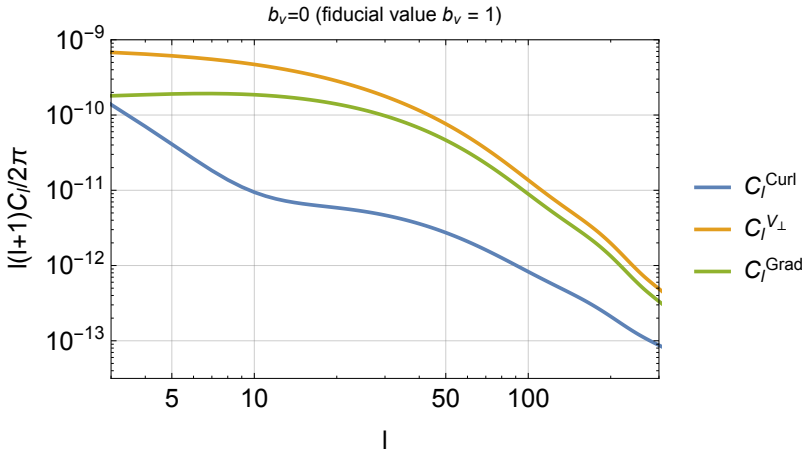

Figure B.1: Plot shows the spectra of the field contributions that are purely curl, $C_\ell^{\varpi\varpi}$ and that are purely gradient, $C_\ell^{\delta\Upsilon\delta\Upsilon}$, in the presence of non-unity bias, shown here for $b_v = 0$. Also plotted, the pure-gradient transverse velocity potential $C_\ell^{\Upsilon\Upsilon}$, all for the redshift bin $z = [1.0, 1.25]$.

where

$$\beta_\ell(k\chi)a_\ell(k\chi)j_\ell(k\chi) + b_\ell(k\chi)\frac{\mathrm{d}j_\ell(k\chi)}{k\mathrm{d}\chi}\,. \tag{B.36}$$

The terms $a_\ell(k\chi)$ and $b_\ell(k\chi)$ are complicated functions of ℓ and factors of $k\chi$ that at the moment do not give further insight on the results. We will be interested with the power spectra of the curl term, $\langle\varpi_{\ell m}\varpi_{\ell' m'}\rangle = C_\ell^{\varpi\varpi}\delta_{\ell\ell'}\delta_{mm'}$ where it is easy to see that the isotropy is satisfied from Eq. (B.35).

B.4 Optical dept bias constraints with transverse velocities

We find the error on the velocity bias $\sigma(b_v)/b_v$ from the $\hat{\Upsilon}$ reconstruction will satisfy

$$\sigma(b_v)/b_v \sim \mathscr{O}(10\ \mathrm{SNR}_{\hat{\Upsilon}}^{-1})\,, \tag{B.37}$$

where SNR is the signal-to-noise ratio on the gradient part of the transverse velocities $\hat{\Upsilon}$ estimated from measurements. From the moving lens effect cross-correlations with a density survey, we have found the SNR $\simeq 50$, giving an error of ~ 0.2, not really competitive with the FRB results, see Figure 3 of [323]. Note also the signal from the curl component, one

gets,

$$\sigma(b_v)/b_v \lesssim \mathscr{O}(\mathrm{SNR}_{\hat{\varpi}}^{-1})\,. \tag{B.38}$$

However, if we can reconstruct the large-scale velocity field from a more precise experiment, such as a large-scale structure surveys with much higher SNR, perhaps one should achieve some compatible results.

Bibliography

[1] S. Weinberg, *Cosmology*. OUP Oxford, 2008.

[2] S. Dodelson, *Modern cosmology*. Elsevier, 2003.

[3] V. Mukhanov, *Physical Foundations of Cosmology*. Cambridge University Press, Oxford, 2005.

[4] P. J. E. Peebles, *The large-scale structure of the universe*. 1980.

[5] W. Hu, *Concepts in CMB anisotropy formation*, vol. 470, p. 207. 1996. arXiv:astro-ph/9511130.

[6] W. Hu and S. Dodelson, "Cosmic Microwave Background Anisotropies," *Ann. Rev. Astron. Astrophys.* **40** (2002) 171–216, arXiv:astro-ph/0110414.

[7] D. Baumann, "Inflation," in *Physics of the large and the small, TASI 09, proceedings of the Theoretical Advanced Study Institute in Elementary Particle Physics, Boulder, Colorado, USA, 1-26 June 2009*, pp. 523–686. 2011. arXiv:0907.5424 [hep-th]. http://inspirehep.net/record/827549/files/arXiv:0907.5424.pdf.

[8] D. Baumann, "Primordial Cosmology," *PoS* **TASI2017** (2018) 009, arXiv:1807.03098 [hep-th].

[9] A. Challinor and H. Peiris, "Lecture notes on the physics of cosmic microwave background anisotropies," in *American Institute of Physics Conference Series*, M. Novello and S. Perez, eds., vol. 1132 of *American Institute of Physics Conference Series*, pp. 86–140. May, 2009. arXiv:0903.5158 [astro-ph.CO].

[10] W. Hu, "Lecture Notes on CMB Theory: From Nucleosynthesis to Recombination," arXiv:0802.3688 [astro-ph].

[11] J. Renk, P. Stroeker, S. Bloor, H. S. C., *et al.*, "CosmoBit: A GAMBIT module for computing cosmological observables and likelihoods,".

[12] S. C. Hotinli, J. Frazer, A. H. Jaffe, J. Meyers, L. C. Price, and E. R. M. Tarrant, "Effect of reheating on predictions following multiple-field inflation," *Phys. Rev. D* **97** no. 2, (2018) 023511, arXiv:1710.08913 [astro-ph.CO].

[13] A. Lewis and A. Challinor, "Weak gravitational lensing of the cmb," *Phys. Rept.* **429** (2006) 1–65, arXiv:astro-ph/0601594 [astro-ph].

[14] N. Aghanim, S. Majumdar, and J. Silk, "Secondary anisotropies of the CMB," *Rept. Prog. Phys.* **71** (2008) 066902, arXiv:0711.0518 [astro-ph].

[15] S. C. Hotinli, J. Meyers, N. Dalal, A. H. Jaffe, M. C. Johnson, J. B. Mertens, M. Münchmeyer, K. M. Smith, and A. van Engelen, "Transverse Velocities with the Moving Lens Effect," *Phys. Rev. Lett.* **123** no. 6, (2019) 061301, arXiv:1812.03167 [astro-ph.CO].

[16] S. C. Hotinli, M. C. Johnson, and J. Meyers, "Optimal filters for the moving lens effect," arXiv:2006.03060 [astro-ph.CO].

[17] S. C. Hotinli, J. B. Mertens, M. C. Johnson, and M. Kamionkowski, "Probing correlated compensated isocurvature perturbations using scale-dependent galaxy bias," *Phys. Rev.* **D100** no. 10, (2019) 103528, arXiv:1908.08953 [astro-ph.CO].

[18] G. F. Smoot, C. L. Bennett, A. Kogut, E. L. Wright, *et al.*, "Structure in the COBE Differential Microwave Radiometer First-Year Maps," **396** (Sept., 1992) L1.

[19] **WMAP** Collaboration, D. Spergel *et al.*, "First year Wilkinson Microwave Anisotropy Probe (WMAP) observations: Determination of cosmological parameters," *Astrophys. J. Suppl.* **148** (2003) 175–194, arXiv:astro-ph/0302209.

[20] **Planck** Collaboration, P. Ade *et al.*, "Planck 2013 results. XVI. Cosmological parameters," *Astron. Astrophys.* **571** (2014) A16, arXiv:1303.5076 [astro-ph.CO].

[21] **Supernova Search Team** Collaboration, A. G. Riess *et al.*, "Observational evidence from supernovae for an accelerating universe and a cosmological constant," *Astron. J.* **116** (1998) 1009–1038, arXiv:astro-ph/9805201.

[22] **Supernova Cosmology Project** Collaboration, S. Perlmutter *et al.*, "Measurements of Ω and Λ from 42 high redshift supernovae," *Astrophys. J.* **517** (1999) 565–586, arXiv:astro-ph/9812133.

[23] **2DFGRS** Collaboration, M. Colless *et al.*, "The 2dF Galaxy Redshift Survey: Spectra and redshifts," *Mon. Not. Roy. Astron. Soc.* **328** (2001) 1039, arXiv:astro-ph/0106498.

[24] **SDSS** Collaboration, C. Stoughton *et al.*, "The Sloan Digital Sky Survey: Early Data Release," *Astron. J.* **123** (2002) 485–548.

[25] **BOSS** Collaboration, S. Alam *et al.*, "The clustering of galaxies in the completed SDSS-III Baryon Oscillation Spectroscopic Survey: cosmological analysis of the DR12 galaxy sample," *Mon. Not. Roy. Astron. Soc.* **470** no. 3, (2017) 2617–2652, arXiv:1607.03155 [astro-ph.CO].

[26] A. Friedman, "Über die krümmung des raumes," *Zeitschrift für Physik* **10** no. 1, (1922) 377–386. https://doi.org/10.1007/BF01332580.

[27] G. Lemaître, "L'Univers en expansion," *Annales de la Société Scientifique de Bruxelles* **53** (Jan., 1933) 51.

[28] H. P. Robertson, "Kinematics and World-Structure III.," **83** (May, 1936) 257.

[29] A. G. Walker, "On Milne's Theory of World-Structure," *Proceedings of the London Mathematical Society* **42** (Jan., 1937) 90–127.

[30] A. Einstein, "Die Grundlage der allgemeinen Relativitätstheorie," *Annalen der Physik* **354** no. 7, (Jan., 1916) 769–822.

[31] D. J. Fixsen, "The Temperature of the Cosmic Microwave Background," **707** no. 2, (Dec., 2009) 916–920, arXiv:0911.1955 [astro-ph.CO].

[32] J. M. Bardeen, "Gauge Invariant Cosmological Perturbations," *Phys. Rev. D* **22** (1980) 1882–1905.

[33] H. Kodama and M. Sasaki, "Cosmological Perturbation Theory," *Prog. Theor. Phys. Suppl.* **78** (1984) 1–166.

[34] V. F. Mukhanov, H. A. Feldman, and R. H. Brandenberger, "Theory of cosmological perturbations," **215** no. 5-6, (June, 1992) 203–333.

[35] C.-P. Ma and E. Bertschinger, "Cosmological perturbation theory in the synchronous and conformal Newtonian gauges," *Astrophys. J.* **455** (1995) 7–25, arXiv:astro-ph/9506072.

[36] K. A. Malik and D. Wands, "Cosmological perturbations," *Phys. Rept.* **475** (2009) 1–51, arXiv:0809.4944 [astro-ph].

[37] **Planck** Collaboration, N. Aghanim *et al.*, "Planck 2018 results. VI. Cosmological parameters," arXiv:1807.06209 [astro-ph.CO].

[38] J. M. Bardeen, P. J. Steinhardt, and M. S. Turner, "Spontaneous Creation of Almost Scale - Free Density Perturbations in an Inflationary Universe," *Phys.Rev.* **D28** (1983) 679.

[39] S. Weinberg, "Adiabatic modes in cosmology," *Phys.Rev.* **D67** (2003) 123504, arXiv:astro-ph/0302326 [astro-ph].

[40] P. Meszaros, "The behaviour of point masses in an expanding cosmological substratum," *Astron. Astrophys.* **37** (1974) 225–228.

[41] A. A. Starobinsky, "Relict Gravitation Radiation Spectrum and Initial State of the Universe. (In Russian)," *JETP Lett.* **30** (1979) 682–685.

[42] A. A. Starobinsky, "A New Type of Isotropic Cosmological Models Without Singularity," *Phys.Lett.* **B91** (1980) 99–102.

[43] D. Kazanas, "Dynamics of the Universe and Spontaneous Symmetry Breaking," *Astrophys.J.* **241** (1980) L59–L63.

[44] K. Sato, "First Order Phase Transition of a Vacuum and Expansion of the Universe," *Mon.Not.Roy.Astron.Soc.* **195** (1981) 467–479.

[45] A. H. Guth, "The Inflationary Universe: A Possible Solution to the Horizon and Flatness Problems," *Phys.Rev.* **D23** (1981) 347–356.

[46] V. F. Mukhanov and G. V. Chibisov, "Quantum Fluctuation and Nonsingular Universe. (In Russian)," *JETP Lett.* **33** (1981) 532–535.

[47] S. Hawking, "The Development of Irregularities in a Single Bubble Inflationary Universe," *Phys.Lett.* **B115** (1982) 295.

[48] A. H. Guth and S. Pi, "Fluctuations in the New Inflationary Universe," *Phys.Rev.Lett.* **49** (1982) 1110–1113.

[49] A. A. Starobinsky, "Dynamics of Phase Transition in the New Inflationary Universe Scenario and Generation of Perturbations," *Phys.Lett.* **B117** (1982) 175–178.

[50] **Planck** Collaboration, P. A. R. Ade *et al.*, "Planck 2015 results. XX. Constraints on inflation," arXiv:1502.02114 [astro-ph.CO].

[51] J. Martin, C. Ringeval, and V. Vennin, "Encyclopædia Inflationaris," **5-6** (2014) 75–235, arXiv:1303.3787 [astro-ph.CO].

[52] E. Silverstein and A. Westphal, "Monodromy in the CMB: Gravity Waves and String Inflation," **78** (2008) 106003, arXiv:0803.3085 [hep-th].

[53] L. McAllister, E. Silverstein, and A. Westphal, "Gravity Waves and Linear Inflation from Axion Monodromy," **82** (2010) 046003, arXiv:0808.0706 [hep-th].

[54] N. Kaloper, A. Lawrence, and L. Sorbo, "An Ignoble Approach to Large Field Inflation," **1103** (2011) 023, arXiv:1101.0026 [hep-th].

[55] L. Kofman, A. D. Linde, and A. A. Starobinsky, "Towards the theory of reheating after inflation," *Phys. Rev.* **D56** (1997) 3258–3295, arXiv:hep-ph/9704452 [hep-ph].

[56] R. Allahverdi, R. Brandenberger, F.-Y. Cyr-Racine, and A. Mazumdar, "Reheating in Inflationary Cosmology: Theory and Applications," *Ann. Rev. Nucl. Part. Sci.* **60** (2010) 27–51, arXiv:1001.2600 [hep-th].

[57] M. A. Amin, M. P. Hertzberg, D. I. Kaiser, and J. Karouby, "Nonperturbative dynamics of reheating after inflation: A review," *International Journal of Modern Physics D* **24** (Dec., 2015) 1530003, arXiv:1410.3808 [hep-ph].

[58] A. R. Liddle and D. H. Lyth, "The Cold dark matter density perturbation," *Phys. Rept.* **231** (1993) 1–105, arXiv:astro-ph/9303019 [astro-ph].

[59] A. R. Liddle and S. M. Leach, "How long before the end of inflation were observable perturbations produced?," *Phys. Rev.* **D68** (2003) 103503, arXiv:astro-ph/0305263 [astro-ph].

[60] D. J. Fixsen, "The Temperature of the Cosmic Microwave Background," **707** no. 2, (Dec, 2009) 916–920, arXiv:0911.1955 [astro-ph.CO].

[61] R. Sachs and A. Wolfe, "Perturbations of a cosmological model and angular variations of the microwave background," *Astrophys. J.* **147** (1967) 73–90.

[62] S. R. Furlanetto, S. P. Oh, and F. H. Briggs, "Cosmology at low frequencies: The 21 cm transition and the high-redshift Universe," **433** no. 4-6, (Oct., 2006) 181–301, arXiv:astro-ph/0608032 [astro-ph].

[63] A. Fialkov, R. Barkana, A. Pinhas, and E. Visbal, "Complete history of the observable 21 cm signal from the first stars during the pre-reionization era," **437** no. 1, (Jan., 2014) L36–L40, arXiv:1306.2354 [astro-ph.CO].

[64] R. Barkana and A. Loeb, "The physics and early history of the intergalactic medium," *Reports on Progress in Physics* **70** no. 4, (Apr., 2007) 627–657, arXiv:astro-ph/0611541 [astro-ph].

[65] A. Loeb and S. Furlanetto, *The First Galaxies in the Universe*. Princeton University Press, 2013.

[66] J. B. Muñoz, "A Standard Ruler at Cosmic Dawn," *Phys. Rev. Lett.* **123** no. 13, (2019) 131301, arXiv:1904.07868 [astro-ph.CO].

[67] A. Meiksin, M. J. White, and J. Peacock, "Baryonic signatures in large scale structure," *Mon. Not. Roy. Astron. Soc.* **304** (1999) 851–864, arXiv:astro-ph/9812214.

[68] H.-J. Seo and D. J. Eisenstein, "Baryonic acoustic oscillations in simulated galaxy redshift surveys," *Astrophys. J.* **633** (2005) 575–588, arXiv:astro-ph/0507338.

[69] D. J. Eisenstein, H.-j. Seo, E. Sirko, and D. Spergel, "Improving Cosmological Distance Measurements by Reconstruction of the Baryon Acoustic Peak," *Astrophys. J.* **664** (2007) 675–679, arXiv:astro-ph/0604362.

[70] E. V. Linder and R. N. Cahn, "Parameterized beyond-Einstein growth," *Astroparticle Physics* **28** no. 4-5, (Dec., 2007) 481–488, arXiv:astro-ph/0701317 [astro-ph].

[71] Y.-S. Song and W. J. Percival, "Reconstructing the history of structure formation using redshift distortions," **2009** no. 10, (Oct., 2009) 004, arXiv:0807.0810 [astro-ph].

[72] E.-M. Mueller, W. Percival, E. Linder, S. Alam, G.-B. Zhao, A. G. Sánchez, F. Beutler, and J. Brinkmann, "The clustering of galaxies in the completed SDSS-III Baryon Oscillation Spectroscopic Survey: constraining modified gravity," **475** no. 2, (Apr., 2018) 2122–2131, arXiv:1612.00812 [astro-ph.CO].

[73] D. Baumann, A. Nicolis, L. Senatore, and M. Zaldarriaga, "Cosmological Non-Linearities as an Effective Fluid," *JCAP* **07** (2012) 051, arXiv:1004.2488 [astro-ph.CO].

[74] J. J. M. Carrasco, M. P. Hertzberg, and L. Senatore, "The Effective Field Theory of Cosmological Large Scale Structures," *JHEP* **09** (2012) 082, arXiv:1206.2926 [astro-ph.CO].

[75] L. Senatore, "Bias in the Effective Field Theory of Large Scale Structures," *JCAP* **11** (2015) 007, arXiv:1406.7843 [astro-ph.CO].

[76] L. Senatore and M. Zaldarriaga, "The IR-resummed Effective Field Theory of Large Scale Structures," *JCAP* **02** (2015) 013, arXiv:1404.5954 [astro-ph.CO].

[77] T. Baldauf, L. Mercolli, and M. Zaldarriaga, "Effective field theory of large scale structure at two loops: The apparent scale dependence of the speed of sound," *Phys. Rev. D* **92** no. 12, (2015) 123007, arXiv:1507.02256 [astro-ph.CO].

[78] J. J. M. Carrasco, S. Foreman, D. Green, and L. Senatore, "The Effective Field Theory of Large Scale Structures at Two Loops," *JCAP* **07** (2014) 057, arXiv:1310.0464 [astro-ph.CO].

[79] A. Perko, L. Senatore, E. Jennings, and R. H. Wechsler, "Biased Tracers in Redshift Space in the EFT of Large-Scale Structure," arXiv:1610.09321 [astro-ph.CO].

[80] V. Assassi, D. Baumann, D. Green, and M. Zaldarriaga, "Renormalized Halo Bias," *JCAP* **08** (2014) 056, arXiv:1402.5916 [astro-ph.CO].

[81] M. Lewandowski, A. Perko, and L. Senatore, "Analytic Prediction of Baryonic Effects from the EFT of Large Scale Structures," *JCAP* **05** (2015) 019, arXiv:1412.5049 [astro-ph.CO].

[82] P. McDonald and A. Roy, "Clustering of dark matter tracers: generalizing bias for the coming era of precision LSS," **2009** no. 8, (Aug., 2009) 020, arXiv:0902.0991 [astro-ph.CO].

[83] H.-J. Seo, J. Eckel, D. J. Eisenstein, K. Mehta, M. Metchnik, N. Padmanabhan, P. Pinto, R. Takahashi, M. White, and X. Xu, "High-precision Predictions for the Acoustic Scale in the Nonlinear Regime," **720** no. 2, (Sept., 2010) 1650–1667, arXiv:0910.5005 [astro-ph.CO].

[84] K. T. Mehta, H.-J. Seo, J. Eckel, D. J. Eisenstein, M. Metchnik, P. Pinto, and X. Xu, "Galaxy Bias and Its Effects on the Baryon Acoustic Oscillation Measurements," **734** no. 2, (June, 2011) 94, arXiv:1104.1178 [astro-ph.CO].

[85] N. Padmanabhan, X. Xu, D. J. Eisenstein, R. Scalzo, A. J. Cuesta, K. T. Mehta, and E. Kazin, "A 2 per cent distance to z = 0.35 by reconstructing baryon acoustic oscillations - I. Methods and application to the Sloan Digital Sky Survey," **427** no. 3, (Dec., 2012) 2132–2145, arXiv:1202.0090 [astro-ph.CO].

[86] N. S. Sugiyama and D. N. Spergel, "How does non-linear dynamics affect the baryon acoustic oscillation?," *JCAP* **02** (2014) 042, arXiv:1306.6660 [astro-ph.CO].

[87] **BOSS** Collaboration, A. Font-Ribera *et al.*, "Quasar-Lyman α Forest Cross-Correlation from BOSS DR11 : Baryon Acoustic Oscillations," **1405** (2014) 027, arXiv:1311.1767 [astro-ph.CO].

[88] J. E. Bautista *et al.*, "Measurement of baryon acoustic oscillation correlations at $z = 2.3$ with SDSS DR12 Lyα-Forests," *Astron. Astrophys.* **603** (2017) A12, arXiv:1702.00176 [astro-ph.CO].

[89] H. du Mas des Bourboux *et al.*, "Baryon acoustic oscillations from the complete SDSS-III Lyα-quasar cross-correlation function at $z = 2.4$," *Astron. Astrophys.* **608** (2017) A130, arXiv:1708.02225 [astro-ph.CO].

[90] N. E. Chisari *et al.*, "Modelling baryonic feedback for survey cosmology," *Open J. Astrophys.* (2019) , arXiv:1905.06082 [astro-ph.CO].

[91] E. Semboloni, H. Hoekstra, J. Schaye, M. P. van Daalen, and I. G. McCarthy, "Quantifying the effect of baryon physics on weak lensing tomography," **417** no. 3, (Nov., 2011) 2020–2035, arXiv:1105.1075 [astro-ph.CO].

[92] A. J. Mead, J. A. Peacock, C. Heymans, S. Joudaki, and A. F. Heavens, "An accurate halo model for fitting non-linear cosmological power spectra and baryonic feedback models," **454** no. 2, (Dec., 2015) 1958–1975, arXiv:1505.07833 [astro-ph.CO].

[93] A. Heavens, A. Refregier, and C. Heymans, "Intrinsic correlation of galaxy shapes: implications for weak lensing measurements," **319** no. 2, (Dec., 2000) 649–656, arXiv:astro-ph/0005269 [astro-ph].

[94] P. Catelan, M. Kamionkowski, and R. D. Blandford, "Intrinsic and extrinsic galaxy alignment," **320** no. 1, (Jan., 2001) L7–L13, arXiv:astro-ph/0005470 [astro-ph].

[95] C. Heymans *et al.*, "CFHTLenS tomographic weak lensing cosmological parameter constraints: Mitigating the impact of intrinsic galaxy alignments," **432** (2013) 2433, arXiv:1303.1808 [astro-ph.CO].

[96] M. A. Troxel and M. Ishak, "The intrinsic alignment of galaxies and its impact on weak gravitational lensing in an era of precision cosmology," **558** (Feb., 2015) 1–59, arXiv:1407.6990 [astro-ph.CO].

[97] H. Hildebrandt, M. Viola, C. Heymans, S. Joudaki, K. Kuijken, *et al.*, "KiDS-450: cosmological parameter constraints from tomographic weak gravitational lensing," **465** no. 2, (Feb., 2017) 1454–1498, arXiv:1606.05338 [astro-ph.CO].

[98] H.-J. Huang, T. Eifler, R. Mandelbaum, and S. Dodelson, "Modelling baryonic physics in future weak lensing surveys," **488** no. 2, (Sept., 2019) 1652–1678, arXiv:1809.01146 [astro-ph.CO].

[99] M. Kilbinger, L. Fu, C. Heymans, and F. o. Simpson, "CFHTLenS: combined probe cosmological model comparison using 2D weak gravitational lensing," **430** no. 3, (Apr., 2013) 2200–2220, arXiv:1212.3338 [astro-ph.CO].

[100] M. A. Troxel, N. MacCrann, J. Zuntz, T. F. Eifler, E. Krause, S. Dodelson, D. Gruen, J. Blazek, O. Friedrich, S. Samuroff, J. Prat, L. F. Secco, C. Davis, A. Ferté, D. J., and DES Collaboration, "Dark Energy Survey Year 1 results: Cosmological constraints from cosmic shear," **98** no. 4, (Aug., 2018) 043528, arXiv:1708.01538 [astro-ph.CO].

[101] A. G. Riess *et al.*, "A 2.4% Determination of the Local Value of the Hubble Constant," *Astrophys. J.* **826** no. 1, (2016) 56, arXiv:1604.01424 [astro-ph.CO].

[102] A. G. Riess, S. Casertano, W. Yuan, L. M. Macri, and D. Scolnic, "Large Magellanic Cloud Cepheid Standards Provide a 1% Foundation for the Determination of the Hubble Constant and Stronger Evidence for Physics beyond ΛCDM," *Astrophys. J.* **876** no. 1, (2019) 85, arXiv:1903.07603 [astro-ph.CO].

[103] W. L. Freedman, B. F. Madore, D. Hatt, T. J. Hoyt, I. S. Jang, R. L. Beaton, C. R. Burns, M. G. Lee, A. J. Monson, J. R. Neeley, M. M. Phillips, J. A. Rich, and M. Seibert, "The Carnegie-Chicago Hubble Program. VIII. An Independent Determination of the Hubble Constant Based on the Tip of the Red Giant Branch," **882** no. 1, (Sept., 2019) 34, arXiv:1907.05922 [astro-ph.CO].

[104] D. M. Scolnic, D. O. Jones, A. Rest, Y. C. Pan, R. Chornock, R. J. Foley, M. E. Huber, R. Kessler, G. Narayan, A. G. Riess, and et al., "The complete light-curve sample of spectroscopically confirmed sne ia from pan-starrs1 and cosmological constraints from the combined pantheon sample," **859** no. 2, (May, 2018) 101, arXiv:1710.00845. http://dx.doi.org/10.3847/1538-4357/aab9bb.

[105] A. Conley, J. Guy, M. Sullivan, N. Regnault, *et al.*, "Supernova Constraints and Systematic Uncertainties from the First Three Years of the Supernova Legacy Survey," **192** no. 1, (Jan., 2011) 1, arXiv:1104.1443 [astro-ph.CO].

[106] L. Hui and P. B. Greene, "Correlated fluctuations in luminosity distance and the importance of peculiar motion in supernova surveys," **73** no. 12, (June, 2006) 123526, arXiv:astro-ph/0512159 [astro-ph].

[107] P. L. Kelly, M. Hicken, D. L. Burke, K. S. Mand el, and R. P. Kirshner, "Hubble Residuals of Nearby Type Ia Supernovae are Correlated with Host Galaxy Masses," **715** no. 2, (June, 2010) 743–756, arXiv:0912.0929 [astro-ph.CO].

[108] R. Kessler and D. Scolnic, "Correcting Type Ia Supernova Distances for Selection Biases and Contamination in Photometrically Identified Samples," **836** no. 1, (Feb., 2017) 56, arXiv:1610.04677 [astro-ph.CO].

[109] T. M. Davis, S. R. Hinton, C. Howlett, and J. Calcino, "Can redshift errors bias measurements of the Hubble Constant?," **490** no. 2, (Dec., 2019) 2948–2957, arXiv:1907.12639 [astro-ph.CO].

[110] **SDSS** Collaboration, M. Betoule *et al.*, "Improved cosmological constraints from a joint analysis of the SDSS-II and SNLS supernova samples," *Astron. Astrophys.* **568** (2014) A22, arXiv:1401.4064 [astro-ph.CO].

[111] D. Scolnic *et al.*, "The Complete Light-curve Sample of Spectroscopically Confirmed SNe Ia from Pan-STARRS1 and Cosmological Constraints from the Combined Pantheon Sample," *Astrophys. J.* **859** no. 2, (2018) 101, arXiv:1710.00845 [astro-ph.CO].

[112] M. J. Mortonson, H. V. Peiris, and R. Easther, "Bayesian Analysis of Inflation: Parameter Estimation for Single Field Models," **83** (2011) 043505, arXiv:1007.4205.

[113] R. Easther and H. V. Peiris, "Bayesian Analysis of Inflation II: Model Selection and Constraints on Reheating," **85** (2012) 103533, arXiv:1112.0326.

[114] J. Norena, C. Wagner, L. Verde, H. V. Peiris, and R. Easther, "Bayesian Analysis of Inflation III: Slow Roll Reconstruction Using Model Selection," **86** (2012) 023505, arXiv:1202.0304.

[115] L. C. Price, J. Frazer, J. Xu, H. V. Peiris, and R. Easther, "MultiModeCode: An efficient numerical solver for multifield inflation," *JCAP* **1503** no. 03, (2015) 005, arXiv:1410.0685.

[116] M. Grana, "Flux compactifications in string theory: A Comprehensive review," *Phys. Rept.* **423** (2006) 91–158, arXiv:hep-th/0509003 [hep-th].

[117] M. R. Douglas and S. Kachru, "Flux compactification," *Rev. Mod. Phys.* **79** (2007) 733–796, arXiv:hep-th/0610102 [hep-th].

[118] F. Denef, M. R. Douglas, and S. Kachru, "Physics of String Flux Compactifications," *Ann. Rev. Nucl. Part. Sci.* **57** (2007) 119–144, arXiv:hep-th/0701050 [hep-th].

[119] F. Denef, "Les Houches Lectures on Constructing String Vacua," in *String theory and the real world: From particle physics to astrophysics. Proceedings, Summer School in Theoretical Physics, 87th Session, Les Houches, France, July 2-27, 2007*, pp. 483–610. 2008. arXiv:0803.1194 [hep-th]. http://inspirehep.net/record/780946/files/arXiv:0803.1194.pdf.

[120] J. Meyers and N. Sivanandam, "Non-Gaussianities in Multifield Inflation: Superhorizon Evolution, Adiabaticity, and the Fate of fnl," *Phys.Rev.* **D83** (2011) 103517, arXiv:1011.4934 [astro-ph.CO].

[121] J. Meyers and N. Sivanandam, "Adiabaticity and the Fate of Non-Gaussianities: The Trispectrum and Beyond," *Phys.Rev.* **D84** (2011) 063522, arXiv:1104.5238 [astro-ph.CO].

[122] D. Seery, D. J. Mulryne, J. Frazer, and R. H. Ribeiro, "Inflationary perturbation theory is geometrical optics in phase space," *JCAP* **1209** (2012) 010, arXiv:1203.2635 [astro-ph.CO].

[123] J. Elliston, D. J. Mulryne, D. Seery, and R. Tavakol, "Evolution of fNL to the adiabatic limit," *JCAP* **1111** (2011) 005, arXiv:1106.2153 [astro-ph.CO].

[124] D. Polarski and A. A. Starobinsky, "Isocurvature perturbations in multiple inflationary models," *Phys. Rev.* **D50** (1994) 6123–6129, arXiv:astro-ph/9404061 [astro-ph].

[125] J. Garcia-Bellido and D. Wands, "Metric perturbations in two field inflation," *Phys. Rev.* **D53** (1996) 5437–5445, arXiv:astro-ph/9511029 [astro-ph].

[126] D. Langlois, "Correlated adiabatic and isocurvature perturbations from double inflation," *Phys. Rev.* **D59** (1999) 123512, arXiv:astro-ph/9906080 [astro-ph].

[127] S. Weinberg, "Can non-adiabatic perturbations arise after single-field inflation?," *Phys.Rev.* **D70** (2004) 043541, arXiv:astro-ph/0401313 [astro-ph].

[128] S. Weinberg, "Non-Gaussian Correlations Outside the Horizon," *Phys.Rev.* **D78** (2008) 123521, arXiv:0808.2909 [hep-th].

[129] S. Dodelson and L. Hui, "A Horizon ratio bound for inflationary fluctuations," *Phys. Rev. Lett.* **91** (2003) 131301, arXiv:astro-ph/0305113 [astro-ph].

[130] L. Alabidi and D. H. Lyth, "Inflation models and observation," *JCAP* **0605** (2006) 016, arXiv:astro-ph/0510441 [astro-ph].

[131] P. Adshead, R. Easther, J. Pritchard, and A. Loeb, "Inflation and the Scale Dependent Spectral Index: Prospects and Strategies," *JCAP* **1102** (2011) 021, arXiv:1007.3748 [astro-ph.CO].

[132] J. Martin, C. Ringeval, and V. Vennin, "Observing Inflationary Reheating," *Phys. Rev. Lett.* **114** no. 8, (2015) 081303, arXiv:1410.7958 [astro-ph.CO].

[133] S. Weinberg, "Must cosmological perturbations remain non-adiabatic after multi-field inflation?," *Phys.Rev.* **D70** (2004) 083522, arXiv:astro-ph/0405397 [astro-ph].

[134] S. Weinberg, "Non-Gaussian Correlations Outside the Horizon II: The General Case," *Phys.Rev.* **D79** (2009) 043504, arXiv:0810.2831 [hep-ph].

[135] J. Meyers, "Non-Gaussian Correlations Outside the Horizon in Local Thermal Equilibrium," arXiv:1212.4438 [astro-ph.CO].

[136] M. Bucher, K. Moodley, and N. Turok, "The General primordial cosmic perturbation," *Phys. Rev.* **D62** (2000) 083508, arXiv:astro-ph/9904231 [astro-ph].

[137] G. Leung, E. R. M. Tarrant, C. T. Byrnes, and E. J. Copeland, "Reheating, Multifield Inflation and the Fate of the Primordial Observables," *JCAP* **1209** (2012) 008, arXiv:1206.5196 [astro-ph.CO].

[138] G. Leung, E. R. M. Tarrant, C. T. Byrnes, and E. J. Copeland, "Influence of Reheating on the Trispectrum and its Scale Dependence," *JCAP* **1308** (2013) 006, arXiv:1303.4678 [astro-ph.CO].

[139] J. Meyers and E. R. M. Tarrant, "Perturbative Reheating After Multiple-Field Inflation: The Impact on Primordial Observables," *Phys. Rev.* **D89** no. 6, (2014) 063535, arXiv:1311.3972 [astro-ph.CO].

[140] J. Frazer, "Predictions in multifield models of inflation," *JCAP* **1401** (2014) 028, arXiv:1303.3611 [astro-ph.CO].

[141] D. I. Kaiser and E. I. Sfakianakis, "Multifield Inflation after Planck: The Case for Nonminimal Couplings," *Phys. Rev. Lett.* **112** no. 1, (2014) 011302, arXiv:1304.0363 [astro-ph.CO].

[142] R. Easther, J. Frazer, H. V. Peiris, and L. C. Price, "Simple predictions from multifield inflationary models," *Phys. Rev. Lett.* **112** (2014) 161302, arXiv:1312.4035 [astro-ph.CO].

[143] D. Wenren, "Tilt and Tensor-to-Scalar Ratio in Multifield Monodromy Inflation," arXiv:1405.1411 [hep-th].

[144] L. C. Price, H. V. Peiris, J. Frazer, and R. Easther, "Gravitational wave consistency relations for multifield inflation," *Phys. Rev. Lett.* **114** no. 3, (2015) 031301, arXiv:1409.2498 [astro-ph.CO].

[145] L. C. Price, H. V. Peiris, J. Frazer, and R. Easther, "Designing and testing inflationary models with Bayesian networks," arXiv:1511.00029 [astro-ph.CO].

[146] M. Dias, J. Frazer, and M. C. D. Marsh, "Simple emergent power spectra from complex inflationary physics," arXiv:1604.05970 [astro-ph.CO].

[147] M. Dias, J. Frazer, and M. c. D. Marsh, "Seven Lessons from Manyfield Inflation in Random Potentials," arXiv:1706.03774 [astro-ph.CO].

[148] T. Bjorkmo and M. C. D. Marsh, "Manyfield Inflation in Random Potentials," arXiv:1709.10076 [astro-ph.CO].

[149] V. Vennin, H. Assadullahi, H. Firouzjahi, M. Noorbala, and D. Wands, "Critical Number of Fields in Stochastic Inflation," arXiv:1604.06017 [astro-ph.CO].

[150] P. B. Greene, L. Kofman, A. D. Linde, and A. A. Starobinsky, "Structure of resonance in preheating after inflation," *Phys. Rev.* **D56** (1997) 6175–6192, arXiv:hep-ph/9705347 [hep-ph].

[151] K. Enqvist, A. Jokinen, A. Mazumdar, T. Multamäki, and A. Väihkönen, "Non-Gaussianity from preheating," *Physical Review Letters* **94** no. 16, (Apr., 2005) 161301, astro-ph/0411394.

[152] J. R. Bond, A. V. Frolov, Z. Huang, and L. Kofman, "Non-Gaussian Spikes from Chaotic Billiards in Inflation Preheating," *Phys. Rev. Lett.* **103** (2009) 071301, arXiv:0903.3407 [astro-ph.CO].

[153] K. Kohri, D. H. Lyth, and C. A. Valenzuela-Toledo, "Preheating and the non-gaussianity of the curvature perturbation," *JCAP* **1002** (2010) 023, arXiv:0904.0793 [hep-ph]. [Erratum: JCAP1009,E01(2011)].

[154] A. M. Green and K. A. Malik, "Primordial black hole production due to preheating," *Phys. Rev.* **D64** (2001) 021301, arXiv:hep-ph/0008113 [hep-ph].

[155] B. A. Bassett and S. Tsujikawa, "Inflationary preheating and primordial black holes," *Phys. Rev.* **D63** (2001) 123503, arXiv:hep-ph/0008328 [hep-ph].

[156] M. Y. Khlopov, "Primordial black holes," *Research in Astronomy and Astrophysics* **10** (June, 2010) 495–528, arXiv:0801.0116.

[157] D. Battefeld and S. Kawai, "Preheating after N-flation," *Phys. Rev.* **D77** (2008) 123507, arXiv:0803.0321 [astro-ph].

[158] D. Battefeld, T. Battefeld, and J. T. Giblin, "On the Suppression of Parametric Resonance and the Viability of Tachyonic Preheating after Multi-Field Inflation," *Phys. Rev.* **D79** (2009) 123510, arXiv:0904.2778 [astro-ph.CO].

[159] J. Braden, L. Kofman, and N. Barnaby, "Reheating the Universe After Multi-Field Inflation," *JCAP* **1007** (2010) 016, arXiv:1005.2196 [hep-th].

[160] M. P. DeCross, D. I. Kaiser, A. Prabhu, C. Prescod-Weinstein, and E. I. Sfakianakis, "Preheating after Multifield Inflation with Nonminimal Couplings, I: Covariant Formalism and Attractor Behavior," *ArXiv e-prints* (Oct., 2015) , arXiv:1510.08553.

[161] D. S. Salopek and J. R. Bond, "Nonlinear evolution of long wavelength metric fluctuations in inflationary models," *Phys. Rev.* **D42** (1990) 3936–3962.

[162] M. Sasaki and E. D. Stewart, "A General analytic formula for the spectral index of the density perturbations produced during inflation," *Prog. Theor. Phys.* **95** (1996) 71–78, arXiv:astro-ph/9507001 [astro-ph].

[163] M. Sasaki and T. Tanaka, "Superhorizon scale dynamics of multiscalar inflation," *Prog. Theor. Phys.* **99** (1998) 763–782, arXiv:gr-qc/9801017 [gr-qc].

[164] D. Wands, K. A. Malik, D. H. Lyth, and A. R. Liddle, "A New approach to the evolution of cosmological perturbations on large scales," *Phys. Rev.* **D62** (2000) 043527, arXiv:astro-ph/0003278 [astro-ph].

[165] D. H. Lyth, K. A. Malik, and M. Sasaki, "A General proof of the conservation of the curvature perturbation," *JCAP* **0505** (2005) 004, arXiv:astro-ph/0411220 [astro-ph].

[166] M. A. Amin, M. P. Hertzberg, D. I. Kaiser, and J. Karouby, "Nonperturbative Dynamics Of Reheating After Inflation: A Review," *Int. J. Mod. Phys.* **D24** (2014) 1530003, arXiv:1410.3808 [hep-ph].

[167] Y. Shtanov, J. H. Traschen, and R. H. Brandenberger, "Universe reheating after inflation," *Phys.Rev.* **D51** (1995) 5438–5455, arXiv:hep-ph/9407247 [hep-ph].

[168] L. Kofman, A. D. Linde, and A. A. Starobinsky, "Reheating after inflation," *Phys.Rev.Lett.* **73** (1994) 3195–3198, arXiv:hep-th/9405187 [hep-th].

[169] J. H. Traschen and R. H. Brandenberger, "Particle Production During Out-of-equilibrium Phase Transitions," *Phys.Rev.* **D42** (1990) 2491–2504.

[170] D. H. Lyth and D. Wands, "Generating the curvature perturbation without an inflaton," *Phys.Lett.* **B524** (2002) 5–14, arXiv:hep-ph/0110002 [hep-ph].

[171] D. H. Lyth and Y. Rodriguez, "The Inflationary prediction for primordial non-Gaussianity," *Phys.Rev.Lett.* **95** (2005) 121302, arXiv:astro-ph/0504045 [astro-ph].

[172] M. Sasaki, J. Valiviita, and D. Wands, "Non-Gaussianity of the primordial perturbation in the curvaton model," *Phys.Rev.* **D74** (2006) 103003, arXiv:astro-ph/0607627 [astro-ph].

[173] M. Kawasaki, T. Kobayashi, and F. Takahashi, "Non-Gaussianity from Curvatons Revisited," *Phys.Rev.* **D84** (2011) 123506, arXiv:1107.6011 [astro-ph.CO].

[174] M. Kawasaki, T. Kobayashi, and F. Takahashi, "Non-Gaussianity from Axionic Curvaton," *JCAP* **1303** (2013) 016, arXiv:1210.6595 [astro-ph.CO].

[175] J. Fonseca and D. Wands, "Primordial non-Gaussianity from mixed inflaton-curvaton perturbations," *JCAP* **1206** (2012) 028, arXiv:1204.3443 [astro-ph.CO].

[176] A. D. Linde and V. F. Mukhanov, "Nongaussian isocurvature perturbations from inflation," *Phys.Rev.* **D56** (1997) 535–539, arXiv:astro-ph/9610219 [astro-ph].

[177] K. Enqvist and M. S. Sloth, "Adiabatic CMB perturbations in pre - big bang string cosmology," *Nucl.Phys.* **B626** (2002) 395–409, arXiv:hep-ph/0109214 [hep-ph].

[178] D. H. Lyth, C. Ungarelli, and D. Wands, "The Primordial density perturbation in the curvaton scenario," *Phys.Rev.* **D67** (2003) 023503, arXiv:astro-ph/0208055 [astro-ph].

[179] V. Vennin, K. Koyama, and D. Wands, "Encyclopædia curvatonis," *JCAP* **1511** (2015) 008, arXiv:1507.07575 [astro-ph.CO].

[180] H. Assadullahi, J. Valiviita, and D. Wands, "Primordial non-Gaussianity from two curvaton decays," *Phys. Rev.* **D76** (2007) 103003, arXiv:0708.0223 [hep-ph].

[181] D. Salopek, J. Bond, and J. M. Bardeen, "Designing Density Fluctuation Spectra in Inflation," *Phys.Rev.* **D40** (1989) 1753.

[182] T. S. Bunch and P. C. W. Davies, "Quantum Field Theory in de Sitter Space: Renormalization by Point Splitting," *Proc. Roy. Soc. Lond.* **A360** (1978) 117–134.

[183] **Planck** Collaboration, P. A. R. Ade *et al.*, "Planck 2015 results. XIII. Cosmological parameters," *Astron. Astrophys.* **594** (2016) A13, arXiv:1502.01589 [astro-ph.CO].

[184] A. R. Liddle, A. Mazumdar, and F. E. Schunck, "Assisted inflation," *Phys. Rev.* **D58** (1998) 061301, arXiv:astro-ph/9804177 [astro-ph].

[185] S. Dimopoulos, S. Kachru, J. McGreevy, and J. G. Wacker, "N-flation," *JCAP* **0808** (2008) 003, arXiv:hep-th/0507205 [hep-th].

[186] R. Easther and L. McAllister, "Random matrices and the spectrum of N-flation," *JCAP* **0605** (2006) 018, arXiv:hep-th/0512102 [hep-th].

[187] T. Battefeld and R. Easther, "Non-Gaussianities in Multi-field Inflation," *JCAP* **0703** (2007) 020, arXiv:astro-ph/0610296 [astro-ph].

[188] D. Battefeld and T. Battefeld, "Non-Gaussianities in N-flation," *JCAP* **0705** (2007) 012, arXiv:hep-th/0703012 [hep-th].

[189] S. A. Kim and A. R. Liddle, "Nflation: observable predictions from the random matrix mass spectrum," *Phys. Rev.* **D76** (2007) 063515, arXiv:0707.1982 [astro-ph].

[190] S. A. Kim and A. R. Liddle, "Nflation: multi-field inflationary dynamics and perturbations," *Phys. Rev.* **D74** (2006) 023513, arXiv:astro-ph/0605604 [astro-ph].

[191] J. Ellis, M. Fairbairn, and M. Sueiro, "Rescuing Quadratic Inflation," *JCAP* **1402** (2014) 044, arXiv:1312.1353 [astro-ph.CO].

[192] T. C. Bachlechner, M. Dias, J. Frazer, and L. McAllister, "Chaotic inflation with kinetic alignment of axion fields," *Phys. Rev.* **D91** no. 2, (2015) 023520, arXiv:1404.7496 [hep-th].

[193] M. Kawasaki, K. Kohri, and N. Sugiyama, "Cosmological Constraints on Late-time Entropy Production," *Physical Review Letters* **82** (May, 1999) 4168–4171, astro-ph/9811437.

[194] M. Kawasaki, K. Kohri, and N. Sugiyama, "MeV-scale reheating temperature and thermalization of the neutrino background," **62** no. 2, (July, 2000) 023506, astro-ph/0002127.

[195] R. J. Hardwick and C. T. Byrnes, "Bayesian evidence of the post-Planck curvaton," *JCAP* **1508** no. 08, (2015) 010, arXiv:1502.06951 [astro-ph.CO].

[196] V. Vennin, K. Koyama, and D. Wands, "Inflation with an extra light scalar field after Planck," *JCAP* **1603** no. 03, (2016) 024, arXiv:1512.03403 [astro-ph.CO].

[197] R. J. Hardwick, V. Vennin, K. Koyama, and D. Wands, "Constraining Curvatonic Reheating," *JCAP* **1608** no. 08, (2016) 042, arXiv:1606.01223 [astro-ph.CO].

[198] J. Martin, C. Ringeval, and V. Vennin, "How Well Can Future CMB Missions Constrain Cosmic Inflation?," *JCAP* **1410** no. 10, (2014) 038, arXiv:1407.4034 [astro-ph.CO].

[199] M. Drewes, "What can the CMB tell about the microphysics of cosmic reheating?," *JCAP* **1603** no. 03, (2016) 013, arXiv:1511.03280 [astro-ph.CO].

[200] J. Martin, C. Ringeval, and V. Vennin, "Information Gain on Reheating: the One Bit Milestone," *Phys. Rev.* **D93** no. 10, (2016) 103532, arXiv:1603.02606 [astro-ph.CO].

[201] N. Bartolo, E. Komatsu, S. Matarrese, and A. Riotto, "Non-Gaussianity from inflation: Theory and observations," *Phys. Rept.* **402** (2004) 103–266, arXiv:astro-ph/0406398 [astro-ph].

[202] J. M. Maldacena, "Non-Gaussian features of primordial fluctuations in single field inflationary models," *JHEP* **05** (2003) 013, arXiv:astro-ph/0210603 [astro-ph].

[203] P. Creminelli and M. Zaldarriaga, "Single field consistency relation for the 3-point function," *JCAP* **0410** (2004) 006, arXiv:astro-ph/0407059 [astro-ph].

[204] **Simons Observatory** Collaboration, J. Aguirre *et al.*, "The Simons Observatory: Science goals and forecasts," arXiv:1808.07445 [astro-ph.CO].

[205] **CMB-S4** Collaboration, K. N. Abazajian *et al.*, "CMB-S4 Science Book, First Edition," arXiv:1610.02743 [astro-ph.CO].

[206] The Dark Energy Survey Collaboration, "The Dark Energy Survey," *ArXiv Astrophysics e-prints* (Oct., 2005) , astro-ph/0510346.

[207] **LSST Science, LSST Project** Collaboration, P. A. Abell *et al.*, "LSST Science Book, Version 2.0" arXiv:0912.0201 [astro-ph.IM].

[208] R. K. Sachs and A. M. Wolfe, "Perturbations of a Cosmological Model and Angular Variations of the Microwave Background," **147** (Jan., 1967) 73.

[209] M. J. Rees and D. W. Sciama, "Large-scale Density Inhomogeneities in the Universe," **217** (Feb., 1968) 511–516.

[210] Ya. B. Zeldovich and R. A. Sunyaev, "The Interaction of Matter and Radiation in a Hot-Model Universe," *Astrophys. Space Sci.* **4** (1969) 301–316.

[211] R. A. Sunyaev and Ya. B. Zeldovich, "The Interaction of matter and radiation in the hot model of the universe," *Astrophys. Space Sci.* **7** (1970) 20–30.

[212] R. A. Sunyaev and Ya. B. Zeldovich, "The Observations of relic radiation as a test of the nature of X-Ray radiation from the clusters of galaxies," *Comments Astrophys. Space Phys.* **4** (1972) 173–178.

[213] R. A. Sunyaev and Ya. B. Zeldovich, "Microwave background radiation as a probe of the contemporary structure and history of the universe," *Ann. Rev. Astron. Astrophys.* **18** (1980) 537–560.

[214] S. Y. Sazonov and R. A. Sunyaev, "Microwave polarization in the direction of galaxy clusters induced by the CMB quadrupole anisotropy," *Mon. Not. Roy. Astron. Soc.* **310** (1999) 765–772, arXiv:astro-ph/9903287 [astro-ph].

[215] M. Schmittfull and U. Seljak, "Parameter constraints from cross-correlation of CMB lensing with galaxy clustering," *Phys. Rev.* **D97** no. 12, (2018) 123540, arXiv:1710.09465 [astro-ph.CO].

[216] A.-S. Deutsch, E. Dimastrogiovanni, M. Fasiello, M. C. Johnson, and M. Münchmeyer, "Primordial gravitational wave phenomenology with polarized Sunyaev Zel'dovich tomography," *Phys. Rev.* **D100** no. 8, (2019) 083538, arXiv:1810.09463 [astro-ph.CO].

[217] M. Münchmeyer, M. S. Madhavacheril, S. Ferraro, M. C. Johnson, and K. M. Smith, "Constraining local non-Gaussianities with kSZ tomography," arXiv:1810.13424 [astro-ph.CO].

[218] J. I. Cayuso and M. C. Johnson, "Towards testing CMB anomalies using the kinetic and polarized Sunyaev-Zel'dovich effects," *Phys. Rev. D* **101** no. 12, (2020) 123508, arXiv:1904.10981 [astro-ph.CO].

[219] Z. Pan and M. C. Johnson, "Forecasted constraints on modified gravity from Sunyaev Zel'dovich tomography," arXiv:1906.04208 [astro-ph.CO].

[220] M. Ballardini, W. L. Matthewson, and R. Maartens, "Constraining primordial non-Gaussianity using two galaxy surveys and CMB lensing," *Mon. Not. Roy. Astron. Soc.* **489** no. 2, (2019) 1950–1956, arXiv:1906.04730 [astro-ph.CO].

[221] M. Birkinshaw, "The Sunyaev-Zel'dovich effect," *Phys. Rept.* **310** (1999) 97–195, arXiv:astro-ph/9808050.

[222] R. G. Crittenden and N. Turok, "Looking for Lambda with the Rees-Sciama effect," *Phys. Rev. Lett.* **76** (1996) 575, arXiv:astro-ph/9510072.

[223] M. Kamionkowski, "Matter microwave correlations in an open universe," *Phys. Rev. D* **54** (1996) 4169–4170, arXiv:astro-ph/9602150.

[224] W. Hu, "Dark synergy: Gravitational lensing and the CMB," *Phys. Rev. D* **65** (2002) 023003, arXiv:astro-ph/0108090.

[225] M. Rees and D. Sciama, "Large scale Density Inhomogeneities in the Universe," *Nature* **217** (1968) 511–516.

[226] U. Seljak, "Rees-Sciama effect in a CDM universe," *Astrophys. J.* **460** (1996) 549, arXiv:astro-ph/9506048.

[227] M. Birkinshaw and S. F. Gull, "A test for transverse motions of clusters of galaxies," **302** (Mar., 1983) 315–317.

[228] S. Chandrasekhar, "Radiative transfer," *New York: Dover, 1960* (1960) .

[229] A. S. Kompaneets, "The Establishment of Thermal Equilibrium between Quanta and Electrons," *Soviet Journal of Experimental and Theoretical Physics* **4** no. 5, (May, 1957) 730–737.

[230] E. Roebber and G. Holder, "The Polarization Signature of Local Bulk Flows," *Astrophys. J.* **781** no. 2, (2014) 98, arXiv:1306.5248 [astro-ph.CO].

[231] W. R. Coulton *et al.*, "Non-Gaussianity of secondary anisotropies from ACTPol and Planck," *JCAP* **09** (2018) 022, arXiv:1711.07879 [astro-ph.CO].

[232] S. Bhattacharya, D. Nagai, L. Shaw, T. Crawford, and G. P. Holder, "Bispectrum of the Sunyaev-Zel'dovich Effect," **760** no. 1, (Nov., 2012) 5, arXiv:1203.6368 [astro-ph.CO].

[233] T. Crawford *et al.*, "A Measurement of the Secondary-CMB and Millimeter-wave-foreground Bispectrum using 800 deg^2 of South Pole Telescope Data," *Astrophys. J.* **784** (2014) 143, arXiv:1303.3535 [astro-ph.CO].

[234] J. C. Hill and B. D. Sherwin, "Cosmological constraints from moments of the thermal Sunyaev-Zel'dovich effect," **87** no. 2, (Jan., 2013) 023527, arXiv:1205.5794 [astro-ph.CO].

[235] **ACT** Collaboration, J. Hill *et al.*, "The Atacama Cosmology Telescope: A Measurement of the Thermal Sunyaev-Zeldovich One-Point PDF," arXiv:1411.8004 [astro-ph.CO].

[236] **Planck** Collaboration, N. Aghanim *et al.*, "Planck 2015 results. XXII. A map of the thermal Sunyaev-Zeldovich effect," *Astron. Astrophys.* **594** (2016) A22, arXiv:1502.01596 [astro-ph.CO].

[237] L. Thiele, J. C. Hill, and K. M. Smith, "Accurate analytic model for the thermal Sunyaev-Zel'dovich one-point probability distribution function," *Phys. Rev. D* **99** no. 10, (2019) 103511, arXiv:1812.05584 [astro-ph.CO].

[238] M. J. Wilson, B. D. Sherwin, J. C. Hill, *et al.*, "Atacama Cosmology Telescope: A measurement of the thermal Sunyaev-Zel'dovich effect using the skewness of the CMB temperature distribution," **86** no. 12, (Dec., 2012) 122005, arXiv:1203.6633 [astro-ph.CO].

[239] J. E. Carlstrom, G. P. Holder, and E. D. Reese, "Cosmology with the Sunyaev-Zel'dovich effect," *Ann. Rev. Astron. Astrophys.* **40** (2002) 643–680, arXiv:astro-ph/0208192.

[240] E. Komatsu and U. Seljak, "The Sunyaev-Zel'dovich angular power spectrum as a probe of cosmological parameters," *Mon. Not. Roy. Astron. Soc.* **336** (2002) 1256, arXiv:astro-ph/0205468.

[241] R. A. Battye and J. Weller, "Constraining cosmological parameters using Sunyaev-Zel'dovich cluster surveys," *Phys. Rev. D* **68** (2003) 083506, arXiv:astro-ph/0305568.

[242] G. Voit, "Tracing cosmic evolution with clusters of galaxies," *Rev. Mod. Phys.* **77** (2005) 207–258, arXiv:astro-ph/0410173.

[243] D. Nagai, A. V. Kravtsov, and A. Vikhlinin, "Effects of Galaxy Formation on Thermodynamics of the Intracluster Medium," **668** no. 1, (Oct., 2007) 1–14, arXiv:astro-ph/0703661 [astro-ph].

[244] N. Battaglia, J. R. Bond, C. Pfrommer, and J. L. Sievers, "On the Cluster Physics of Sunyaev-Zel'dovich and X-Ray Surveys. I. The Influence of Feedback, Non-thermal Pressure, and Cluster Shapes on Y-M Scaling Relations," **758** no. 2, (Oct., 2012) 74, arXiv:1109.3709 [astro-ph.CO].

[245] G. Holder, I. G. McCarthy, and A. Babul, "The Sunyaev-Zeldovich Background," *Mon. Not. Roy. Astron. Soc.* **382** (2007) 1697, arXiv:astro-ph/0702727.

[246] H. Trac, P. Bode, and J. P. Ostriker, "Templates for the Sunyaev-Zel'dovich Angular Power Spectrum," **727** no. 2, (Feb., 2011) 94, arXiv:1006.2828 [astro-ph.CO].

[247] A. Terrana, M.-J. Harris, and M. C. Johnson, "Analyzing the cosmic variance limit of remote dipole measurements of the cosmic microwave background using the large-scale kinetic Sunyaev Zel'dovich effect," *JCAP* **1702** no. 02, (2017) 040, arXiv:1610.06919 [astro-ph.CO].

[248] A.-S. Deutsch, E. Dimastrogiovanni, M. C. Johnson, M. Münchmeyer, and A. Terrana, "Reconstruction of the remote dipole and quadrupole fields from the kinetic Sunyaev Zel'dovich and polarized Sunyaev Zel'dovich effects," arXiv:1707.08129 [astro-ph.CO].

[249] K. M. Smith, M. S. Madhavacheril, M. Münchmeyer, S. Ferraro, U. Giri, and M. C. Johnson, "KSZ tomography and the bispectrum," arXiv:1810.13423 [astro-ph.CO].

[250] N. Hand *et al.*, "Evidence of Galaxy Cluster Motions with the Kinematic Sunyaev-Zel'dovich Effect," **109** no. 4, (July, 2012) 041101, arXiv:1203.4219 [astro-ph.CO].

[251] F. De Bernardis *et al.*, "Detection of the pairwise kinematic Sunyaev-Zel'dovich effect with BOSS DR11 and the Atacama Cosmology Telescope," *JCAP* **03** (2017) 008, arXiv:1607.02139 [astro-ph.CO].

[252] **DES, SPT** Collaboration, B. Soergel *et al.*, "Detection of the kinematic Sunyaev–Zel'dovich effect with DES Year 1 and SPT," *Mon. Not. Roy. Astron. Soc.* **461** no. 3, (2016) 3172–3193, arXiv:1603.03904 [astro-ph.CO].

[253] J. C. Hill, S. Ferraro, N. Battaglia, J. Liu, and D. N. Spergel, "Kinematic Sunyaev-Zel'dovich Effect with Projected Fields: A Novel Probe of the Baryon Distribution with Planck, WMAP, and WISE Data," *Phys. Rev. Lett.* **117** no. 5, (2016) 051301, arXiv:1603.01608 [astro-ph.CO].

[254] **Planck** Collaboration, N. Aghanim *et al.*, "Planck intermediate results. LIII. Detection of velocity dispersion from the kinetic Sunyaev-Zeldovich effect," *Astron. Astrophys.* **617** (2018) A48, arXiv:1707.00132 [astro-ph.CO].

[255] **ACTPol** Collaboration, E. Schaan *et al.*, "Evidence for the kinematic Sunyaev-Zel'dovich effect with the Atacama Cosmology Telescope and velocity reconstruction from the Baryon Oscillation Spectroscopic Survey," *Phys. Rev. D* **93** no. 8, (2016) 082002, arXiv:1510.06442 [astro-ph.CO].

[256] Y.-Z. Ma, G.-D. Gong, N. Sui, and P. He, "Constraining the optical depth of galaxies and velocity bias with cross-correlation between the kinetic Sunyaev–Zeldovich effect and the peculiar velocity field," *Mon. Not. Roy. Astron. Soc.* **475** no. 1, (2018) 379–390, arXiv:1711.08756 [astro-ph.CO].

[257] S. Y. Sazonov and R. A. Sunyaev, "Microwave polarization in the direction of galaxy clusters induced by the CMB quadrupole anisotropy," **310** (Dec., 1999) 765–772, astro-ph/9903287.

[258] N. Itoh, Y. Kohyama, and S. Nozawa, "Relativistic corrections to the sunyaev-zeldovich effect for clusters of galaxies," *The Astrophysical Journal* **502** no. 1, (1998) 7.

[259] A. Challinor, M. Ford, and A. Lasenby, "Thermal and kinematic corrections to the microwave background polarization induced by galaxy clusters along the line of sight," *Mon. Not. Roy. Astron. Soc.* **312** (2000) 159–165, arXiv:astro-ph/9905227 [astro-ph].

[260] M. Kamionkowski and A. Loeb, "Getting around cosmic variance," *Phys. Rev.* **D56** (1997) 4511–4513, arXiv:astro-ph/9703118 [astro-ph].

[261] D. Baumann, A. Cooray, and M. Kamionkowski, "Small - scale cosmic microwave background polarization from reionization," *New Astron.* **8** (2003) 565–573, arXiv:astro-ph/0208511 [astro-ph].

[262] A. R. Cooray and D. Baumann, "CMB polarization towards clusters as a probe of the integrated Sachs-Wolfe effect," *Phys. Rev.* **D67** (2003) 063505, arXiv:astro-ph/0211095 [astro-ph].

[263] W. Hu, "Reionization revisited: secondary cmb anisotropies and polarization," *Astrophys. J.* **529** (2000) 12, arXiv:astro-ph/9907103 [astro-ph].

[264] G. Lavaux, J. Diego, H. Mathis, and J. Silk, "Sunyaev–zel'dovich polarization as a probe of the intracluster medium," *Monthly Notices of the Royal Astronomical Society* **347** no. 3, (2004) 729–739.

[265] A. Amblard and M. White, "Sunyaev–zel'dovich polarization simulation," *New Astronomy* **10** no. 5, (2005) 417–423.

[266] M. Shimon, Y. Rephaeli, B. W. O'Shea, and M. L. Norman, "Cmb polarization due to scattering in clusters," *Mon. Not. Roy. Astron. Soc.* **368** (2006) 511–517, arXiv:astro-ph/0602528 [astro-ph].

[267] E. F. Bunn, "Probing the universe on gigaparsec scales with remote cosmic microwave background quadrupole measurements," *Phys. Rev.* **D73** (2006) 123517, arXiv:astro-ph/0603271 [astro-ph].

[268] A. Hall and A. Challinor, "Detecting the polarization induced by scattering of the microwave background quadrupole in galaxy clusters," *Phys. Rev.* **D90** no. 6, (2014) 063518, arXiv:1407.5135 [astro-ph.CO].

[269] E. Alizadeh and C. M. Hirata, "How to detect gravitational waves through the cross-correlation of the galaxy distribution with the CMB polarization," *Phys. Rev.* **D85** (2012) 123540, arXiv:1201.5374 [astro-ph.CO].

[270] A.-S. Deutsch, M. C. Johnson, M. Münchmeyer, and A. Terrana, "Polarized Sunyaev Zel'dovich tomography," *JCAP* **1804** no. 04, (2018) 034, arXiv:1705.08907 [astro-ph.CO].

[271] J. Meyers, P. D. Meerburg, A. van Engelen, and N. Battaglia, "Beyond CMB cosmic variance limits on reionization with the polarized Sunyaev-Zel'dovich effect," *Phys. Rev.* **D97** no. 10, (2018) 103505, arXiv:1710.01708 [astro-ph.CO].

[272] R. Tuluie and P. Laguna, "The imprint of proper motion of nonlinear structures on the cosmic microwave background," *Astrophys. J.* **445** (1995) L73–L76, arXiv:astro-ph/9501059 [astro-ph].

[273] N. Aghanim, S. Prunet, O. Forni, and F. R. Bouchet, "Moving gravitational lenses: Imprints on the CMB," *Submitted to: Astron. Astrophys.* (1998) , arXiv:astro-ph/9803040 [astro-ph]. [Astron. Astrophys.334,409(1998)].

[274] A. Cooray, "Nonlinear integrated Sachs-Wolfe effect," *Phys. Rev.* **D65** (2002) 083518, arXiv:astro-ph/0109162 [astro-ph].

[275] S. Yasini, N. Mirzatuny, and E. Pierpaoli, "Pairwise Transverse Velocity Measurement with the Rees–Sciama Effect," *Astrophys. J.* **873** no. 2, (2019) L23, arXiv:1812.04241 [astro-ph.CO].

[276] A. Challinor and F. van Leeuwen, "Peculiar velocity effects in high resolution microwave background experiments," *Phys. Rev.* **D65** (2002) 103001, arXiv:astro-ph/0112457 [astro-ph].

[277] **Planck** Collaboration, N. Aghanim *et al.*, "Planck 2013 results. XXVII. Doppler boosting of the CMB: Eppur si muove," *Astron. Astrophys.* **571** (2014) A27, arXiv:1303.5087 [astro-ph.CO].

[278] **Planck** Collaboration, N. Aghanim *et al.*, "Planck 2018 results. III. High Frequency Instrument data processing and frequency maps," arXiv:1807.06207 [astro-ph.CO].

[279] A. Notari and M. Quartin, "Measuring our Peculiar Velocity by 'Pre-deboosting' the CMB," *JCAP* **1202** (2012) 026, arXiv:1112.1400 [astro-ph.CO].

[280] A. Lewis, A. Hall, and A. Challinor, "Emission-angle and polarization-rotation effects in the lensed CMB," *JCAP* **1708** no. 08, (2017) 023, arXiv:1706.02673 [astro-ph.CO].

[281] A. Cooray and N. Seto, "Did wmap see moving local structures?," *JCAP* **0512** (2005) 004, arXiv:astro-ph/0510137 [astro-ph].

[282] P. D. Meerburg, J. Meyers, and A. van Engelen, "Reconstructing the Primary CMB Dipole," *Phys. Rev.* **D96** no. 8, (2017) 083519, arXiv:1704.00718 [astro-ph.CO].

[283] S. Yasini and E. Pierpaoli, "Beyond the Boost: Measuring the Intrinsic Dipole of the Cosmic Microwave Background Using the Spectral Distortions of the Monopole and Quadrupole," *Phys. Rev. Lett.* **119** no. 22, (2017) 221102, arXiv:1610.00015 [astro-ph.CO].

[284] S. Yasini and E. Pierpaoli, "Generalized Doppler and aberration kernel for frequency-dependent cosmological observables," *Phys. Rev.* **D96** no. 10, (2017) 103502, arXiv:1709.08298 [astro-ph.CO].

[285] J. F. Navarro, C. S. Frenk, and S. D. White, "The Structure of cold dark matter halos," *Astrophys. J.* **462** (1996) 563–575, arXiv:astro-ph/9508025.

[286] G. Stein, M. A. Alvarez, J. R. Bond, A. van Engelen, and N. Battaglia, "The Websky Extragalactic CMB Simulations," arXiv:2001.08787 [astro-ph.CO].

[287] A. Cooray and R. K. Sheth, "Halo Models of Large Scale Structure," *Phys. Rept.* **372** (2002) 1–129, arXiv:astro-ph/0206508 [astro-ph].

[288] A. Leauthaud, J. Tinker, P. S. Behroozi, M. T. Busha, and R. H. Wechsler, "A Theoretical Framework for Combining Techniques that Probe the Link Between Galaxies and Dark Matter," **738** no. 1, (Sep, 2011) 45, arXiv:1103.2077 [astro-ph.CO].

[289] A. Leauthaud, J. Tinker, K. Bundy, P. S. Behroozi, R. Massey, J. Rhodes, M. R. George, J.-P. Kneib, A. Benson, and R. H. o. Wechsler, "New Constraints on the Evolution of the Stellar-to-dark Matter Connection: A Combined Analysis of Galaxy-Galaxy Lensing, Clustering, and Stellar Mass Functions from z = 0.2 to z =1," **744** no. 2, (Jan, 2012) 159, arXiv:1104.0928 [astro-ph.CO].

[290] A. A. Berlind and D. H. Weinberg, "The Halo occupation distribution: Towards an empirical determination of the relation between galaxies and mass," *Astrophys. J.* **575** (2002) 587–616, arXiv:astro-ph/0109001 [astro-ph].

[291] R. K. Sheth, H. J. Mo, and G. Tormen, "Ellipsoidal collapse and an improved model for the number and spatial distribution of dark matter haloes," *Mon. Not. Roy. Astron. Soc.* **323** (2001) 1, arXiv:astro-ph/9907024 [astro-ph].

[292] **DES** Collaboration, A. Palmese *et al.*, "Stellar Mass as a Galaxy Cluster Mass Proxy: Application to the Dark Energy Survey redMaPPer Clusters," *Mon. Not. Roy. Astron. Soc.* **493** no. 4, (2020) 4591–4606, arXiv:1903.08813 [astro-ph.CO].

[293] R. Murata, T. Nishimichi, M. Takada, H. Miyatake, M. Shirasaki, S. More, R. Takahashi, and K. Osato, "Constraints on the mass-richness relation from the abundance and weak lensing of SDSS clusters," *Astrophys. J.* **854** (2018) 120, arXiv:1707.01907 [astro-ph.CO].

[294] W. Hu and T. Okamoto, "Mass reconstruction with cmb polarization," *Astrophys. J.* **574** (2002) 566–574, arXiv:astro-ph/0111606 [astro-ph].

[295] T. Okamoto and W. Hu, "CMB lensing reconstruction on the full sky," *Phys. Rev.* **D67** (2003) 083002, arXiv:astro-ph/0301031 [astro-ph].

[296] D. N. Limber, "The Analysis of Counts of the Extragalactic Nebulae in Terms of a Fluctuating Density Field.," **117** (Jan., 1953) 134.

[297] N. Kaiser, "Weak gravitational lensing of distant galaxies," *Astrophys. J.* **388** (1992) 272.

[298] N. Kaiser, "Weak lensing and cosmology," *Astrophys. J.* **498** (1998) 26, arXiv:astro-ph/9610120 [astro-ph].

[299] M. LoVerde and N. Afshordi, "Extended Limber Approximation," *Phys. Rev.* **D78** (2008) 123506, arXiv:0809.5112 [astro-ph].

[300] A. Lewis, A. Challinor, and A. Lasenby, "Efficient Computation of CMB Anisotropies in Closed FRW Models," *Astrophys. J.* **538** (2000) 473, arXiv:astro-ph/9911177 [astro-ph].

[301] D. Blas, J. Lesgourgues, and T. Tram, "The Cosmic Linear Anisotropy Solving System (CLASS). Part II: Approximation schemes," **7** (July, 2011) 034, arXiv:1104.2933.

[302] R. Takahashi, M. Sato, T. Nishimichi, A. Taruya, and M. Oguri, "Revising the Halofit Model for the Nonlinear Matter Power Spectrum," **761** (2012) 152, arXiv:1208.2701 [astro-ph.CO].

[303] A. Mead, J. Peacock, C. Heymans, S. Joudaki, and A. Heavens, "An accurate halo model for fitting non-linear cosmological power spectra and baryonic feedback models," **454** no. 2, (2015) 1958–1975, arXiv:1505.07833 [astro-ph.CO].

[304] A. Mead, C. Heymans, L. Lombriser, J. Peacock, O. Steele, and H. Winther, "Accurate halo-model matter power spectra with dark energy, massive neutrinos and modified gravitational forces," **459** (2016) 1468–1488, arXiv:1602.02154 [astro-ph.CO].

[305] **VIRGO Consortium** Collaboration, R. E. Smith, J. A. Peacock, A. Jenkins, S. D. M. White, C. S. Frenk, F. R. Pearce, P. A. Thomas, G. Efstathiou, and H. M. P. Couchmann, "Stable clustering, the halo model and nonlinear cosmological power spectra," **341** (2003) 1311, arXiv:astro-ph/0207664 [astro-ph].

[306] K. M. Smith, M. S. Madhavacheril, M. Münchmeyer, S. Ferraro, U. Giri, and M. C. Johnson, "KSZ tomography and the bispectrum," *ArXiv e-prints* (Oct., 2018) , arXiv:1810.13423.

[307] D. Green, J. Meyers, and A. van Engelen, "CMB Delensing Beyond the B Modes," *JCAP* **1712** no. 12, (2017) 005, arXiv:1609.08143 [astro-ph.CO].

[308] S. Foreman, P. D. Meerburg, J. Meyers, and A. van Engelen, "Cosmic variance mitigation in measurements of the integrated Sachs-Wolfe effect," arXiv:1811.00529 [astro-ph.CO].

[309] C. M. Hirata and U. Seljak, "Analyzing weak lensing of the cosmic microwave background using the likelihood function," *Phys. Rev.* **D67** (2003) 043001, arXiv:astro-ph/0209489 [astro-ph].

[310] M. Millea, E. Anderes, B. D. Wandelt, and M. Millea, "Bayesian delensing of CMB temperature and polarization," arXiv:1708.06753 [astro-ph.CO].

[311] T. Namikawa, D. Hanson, and R. Takahashi, "Bias-hardened CMB lensing," **431** (May, 2013) 609–620, arXiv:1209.0091 [astro-ph.CO].

[312] P. Zhang, "The dark flow induced small-scale kinetic Sunyaev-Zel'dovich effect," *MNRAS* **407** (Sept., 2010) L36–L40, arXiv:1004.0990 [astro-ph.CO].

[313] U. Seljak, "Extracting primordial non-gaussianity without cosmic variance," *Phys. Rev. Lett.* **102** (2009) 021302, arXiv:0807.1770 [astro-ph].

[314] N. Dalal, O. Dore, D. Huterer, and A. Shirokov, "The imprints of primordial non-gaussianities on large-scale structure: scale dependent bias and abundance of virialized objects," *Phys. Rev.* **D77** (2008) 123514, arXiv:0710.4560 [astro-ph].

[315] E. V. Linder, "Cosmic growth history and expansion history," *Phys. Rev.* **D72** (2005) 043529, arXiv:astro-ph/0507263 [astro-ph].

[316] E. V. Linder and R. N. Cahn, "Parameterized Beyond-Einstein Growth," *Astropart. Phys.* **28** (2007) 481–488, arXiv:astro-ph/0701317 [astro-ph].

[317] J. R. Bond and A. S. Szalay, "The Collisionless Damping of Density Fluctuations in an Expanding Universe," *Astrophys. J.* **274** (1983) 443–468.

[318] A. Cooray and X.-l. Chen, "Kinetic Sunyaev-Zel'dovich effect from halo rotation," *Astrophys. J.* **573** (2002) 43, arXiv:astro-ph/0107544.

[319] J. Chluba and K. Mannheim, "Kinetic Sunyaev-Zeldovich effect from galaxy cluster rotation," *Astron. Astrophys.* **396** (2002) 419–428, arXiv:astro-ph/0208392.

[320] J. M. Z. Matilla and Z. Haiman, "Probing gaseous galactic halos through the rotational kinematic Sunyaev-Zeldovich effect," *Phys. Rev. D* **101** no. 8, (2020) 083016, arXiv:1909.04690 [astro-ph.GA].

[321] E. J. Baxter, B. D. Sherwin, and S. Raghunathan, "Constraining the Rotational Kinematic Sunyaev-Zel'dovich Effect in Massive Galaxy Clusters," *JCAP* **06** (2019) 001, arXiv:1904.04199 [astro-ph.CO].

[322] S. C. Hotinli, M. Mathew, and D. Neal, "Probing dark energy microphysics with the kinetic Sunyaev Zel'dovic effect," *Astrophys. J.* (2020) , arXiv:astro-ph/2020.XXX [astro-ph].

[323] M. S. Madhavacheril, N. Battaglia, K. M. Smith, and J. L. Sievers, "Cosmology with kSZ: breaking the optical depth degeneracy with Fast Radio Bursts," arXiv:1901.02418 [astro-ph.CO].

[324] CHIME/FRB Collaboration, "CHIME/FRB Discovery of Eight New Repeating Fast Radio Burst Sources," **885** no. 1, (Nov., 2019) L24, arXiv:1908.03507 [astro-ph.HE].

[325] P. Zhang and M. C. Johnson, "Testing eternal inflation with the kinetic Sunyaev Zel'dovich effect," *JCAP* **1506** no. 06, (2015) 046, arXiv:1501.00511 [astro-ph.CO].

[326] **DESI** Collaboration, A. Aghamousa *et al.*, "The DESI Experiment Part I: Science,Targeting, and Survey Design," arXiv:1611.00036 [astro-ph.IM].

[327] D. Contreras, M. C. Johnson, and J. B. Mertens, "Towards detection of relativistic effects in galaxy number counts using kSZ Tomography," arXiv:1904.10033 [astro-ph.CO].

[328] E.-M. Mueller, F. de Bernardis, R. Bean, and M. D. Niemack, "Constraints on gravity and dark energy from the pairwise kinematic Sunyaev-Zeldovich effect," *Astrophys. J.* **808** no. 1, (2015) 47, arXiv:1408.6248 [astro-ph.CO].

[329] N. Battaglia, "The tau of galaxy clusters," **8** (Aug., 2016) 058, arXiv:1607.02442.

[330] **Planck** Collaboration, Y. Akrami *et al.*, "Planck 2018 results. X. Constraints on inflation," arXiv:1807.06211 [astro-ph.CO].

[331] G. P. Holder, K. M. Nollett, and A. van Engelen, "On Possible Variation in the Cosmological Baryon Fraction," *Astrophys. J.* **716** (2010) 907–913, arXiv:0907.3919 [astro-ph.CO].

[332] C. Gordon and J. R. Pritchard, "Forecasted 21 cm constraints on compensated isocurvature perturbations," *Phys. Rev.* **D80** (2009) 063535, arXiv:0907.5400 [astro-ph.CO].

[333] D. Grin, O. Dore, and M. Kamionkowski, "Compensated Isocurvature Perturbations and the Cosmic Microwave Background," *Phys. Rev.* **D84** (2011) 123003, arXiv:1107.5047 [astro-ph.CO].

[334] D. Grin, O. Dore, and M. Kamionkowski, "Do baryons trace dark matter in the early universe?," *Phys. Rev. Lett.* **107** (2011) 261301, arXiv:1107.1716 [astro-ph.CO].

[335] T. L. Smith, J. B. Muñoz, R. Smith, K. Yee, and D. Grin, "Baryons still trace dark matter: probing CMB lensing maps for hidden isocurvature," *Phys. Rev.* **D96** no. 8, (2017) 083508, arXiv:1704.03461 [astro-ph.CO].

[336] J. B. Muñoz, D. Grin, L. Dai, M. Kamionkowski, and E. D. Kovetz, "Search for Compensated Isocurvature Perturbations with Planck Power Spectra," *Phys. Rev.* **D93** no. 4, (2016) 043008, arXiv:1511.04441 [astro-ph.CO].

[337] D. Grin, D. Hanson, G. P. Holder, O. Doré, and M. Kamionkowski, "Baryons do trace dark matter 380,000 years after the big bang: Search for compensated isocurvature perturbations with WMAP 9-year data," *Phys. Rev.* **D89** no. 2, (2014) 023006, arXiv:1306.4319 [astro-ph.CO].

[338] C. Heinrich and M. Schmittfull, "BAO Modulation as a Probe of Compensated Isocurvature Perturbations," arXiv:1904.00024 [astro-ph.CO].

[339] T. Moroi and T. Takahashi, "Cosmic density perturbations from late decaying scalar condensations," *Phys. Rev.* **D66** (2002) 063501, arXiv:hep-ph/0206026 [hep-ph].

[340] D. H. Lyth and D. Wands, "The CDM isocurvature perturbation in the curvaton scenario," *Phys. Rev.* **D68** (2003) 103516, arXiv:astro-ph/0306500 [astro-ph].

[341] R. Barkana and A. Loeb, "Scale-dependent bias of galaxies from baryonic acoustic oscillations," **415** no. 4, (Aug, 2011) 3113–3118, arXiv:1009.1393 [astro-ph.CO].

[342] F. Schmidt, "Effect of relative velocity and density perturbations between baryons and dark matter on the clustering of galaxies," *Phys. Rev.* **D94** no. 6, (2016) 063508, arXiv:1602.09059 [astro-ph.CO].

[343] A. Barreira, G. Cabass, D. Nelson, and F. Schmidt, "Baryon-CDM isocurvature galaxy bias with IllustrisTNG," arXiv:1907.04317 [astro-ph.CO].

[344] P. McDonald and U. Seljak, "How to measure redshift-space distortions without sample variance," *JCAP* **0910** (2009) 007, arXiv:0810.0323 [astro-ph].

[345] C. He, D. Grin, and W. Hu, "Compensated isocurvature perturbations in the curvaton model," *Phys. Rev.* **D92** no. 6, (2015) 063018, arXiv:1505.00639 [astro-ph.CO].

[346] T. Moroi and T. Takahashi, "Effects of cosmological moduli fields on cosmic microwave background," *Phys. Lett.* **B522** (2001) 215–221, arXiv:hep-ph/0110096 [hep-ph]. [Erratum: Phys. Lett.B539,303(2002)].

[347] C. Gordon and A. Lewis, "Observational constraints on the curvaton model of inflation," *Phys. Rev.* **D67** (2003) 123513, arXiv:astro-ph/0212248 [astro-ph].

[348] C. H. Heinrich, D. Grin, and W. Hu, "Lensing Bias to CMB Measurements of Compensated Isocurvature Perturbations," *Phys. Rev.* **D94** no. 4, (2016) 043534, arXiv:1605.08439 [astro-ph.CO].

[349] C. Bonvin and R. Durrer, "What galaxy surveys really measure," **84** no. 6, (Sep, 2011) 063505, arXiv:1105.5280 [astro-ph.CO].

[350] A. Challinor and A. Lewis, "Linear power spectrum of observed source number counts," **84** no. 4, (Aug, 2011) 043516, arXiv:1105.5292 [astro-ph.CO].

[351] C. M. Hirata, "Tidal alignments as a contaminant of redshift space distortions," *Mon. Not. Roy. Astron. Soc.* **399** (2009) 1074, arXiv:0903.4929 [astro-ph.CO].

[352] C. S. Lorenz, D. Alonso, and P. G. Ferreira, "Impact of relativistic effects on cosmological parameter estimation," *Phys. Rev.* **D97** no. 2, (2018) 023537, arXiv:1710.02477 [astro-ph.CO].

[353] D. Alonso, P. Bull, P. G. Ferreira, R. Maartens, and M. Santos, "Ultra large-scale cosmology in next-generation experiments with single tracers," *Astrophys. J.* **814** no. 2, (2015) 145, arXiv:1505.07596 [astro-ph.CO].

[354] N. Weaverdyck, J. Muir, and D. Huterer, "Integrated Sachs-Wolfe map reconstruction in the presence of systematic errors," *Phys. Rev.* **D97** no. 4, (2018) 043515, arXiv:1709.08661 [astro-ph.CO].

[355] O. Umeh, C. Clarkson, and R. Maartens, "Nonlinear relativistic corrections to cosmological distances, redshift and gravitational lensing magnification: I. Key results," *Class. Quant. Grav.* **31** (2014) 202001, arXiv:1207.2109 [astro-ph.CO].

[356] D. Jeong, F. Schmidt, and C. M. Hirata, "Large-scale clustering of galaxies in general relativity," **85** no. 2, (Jan., 2012) 023504, arXiv:1107.5427 [astro-ph.CO].

[357] A. Raccanelli, F. Montanari, D. Bertacca, O. Doré, and R. Durrer, "Cosmological Measurements with General Relativistic Galaxy Correlations," *JCAP* **05** (2016) 009, arXiv:1505.06179 [astro-ph.CO].

[358] R. A. Sunyaev and Y. B. Zeldovich, "The velocity of clusters of galaxies relative to the microwave background. The possibility of its measurement," *Monthly Notices of the Royal Astronomical Society* **190** no. 3, (03, 1980) 413–420. https://doi.org/10.1093/mnras/190.3.413.

[359] D. Baumann, S. Ferraro, D. Green, and K. M. Smith, "Stochastic Bias from Non-Gaussian Initial Conditions," *JCAP* **1305** (2013) 001, arXiv:1209.2173 [astro-ph.CO].

[360] B. Leistedt, H. V. Peiris, and N. Roth, "Constraints on Primordial Non-Gaussianity from 800 000 Photometric Quasars," *Phys. Rev. Lett.* **113** no. 22, (2014) 221301, arXiv:1405.4315 [astro-ph.CO].

[361] U. Seljak, N. Hamaus, and V. Desjacques, "How to Suppress the Shot Noise in Galaxy Surveys," **103** no. 9, (Aug., 2009) 091303, arXiv:0904.2963 [astro-ph.CO].

[362] P. McDonald and U. Seljak, "How to evade the sample variance limit on measurements of redshift-space distortions," **2009** no. 10, (Oct., 2009) 007, arXiv:0810.0323 [astro-ph].

[363] H. Gil-Marín, C. Wagner, L. Verde, R. Jimenez, and A. F. Heavens, "Reducing sample variance: halo biasing, non-linearity and stochasticity," **407** no. 2, (Sept., 2010) 772–790, arXiv:1003.3238 [astro-ph.CO].

[364] E. Bellini and I. Sawicki, "Maximal freedom at minimum cost: linear large-scale structure in general modifications of gravity," *JCAP* **07** (2014) 050, arXiv:1404.3713 [astro-ph.CO].

[365] L. Knox and Y.-S. Song, "A Limit on the detectability of the energy scale of inflation," *Phys. Rev. Lett.* **89** (2002) 011303, arXiv:astro-ph/0202286.

[366] M. Kesden, A. Cooray, and M. Kamionkowski, "Separation of gravitational wave and cosmic shear contributions to cosmic microwave background polarization," *Phys. Rev. Lett.* **89** (2002) 011304, arXiv:astro-ph/0202434.

[367] U. Seljak and C. M. Hirata, "Gravitational lensing as a contaminant of the gravity wave signal in CMB," *Phys. Rev. D* **69** (2004) 043005, arXiv:astro-ph/0310163.

[368] K. M. Smith, D. Hanson, M. LoVerde, C. M. Hirata, and O. Zahn, "Delensing CMB polarization with external datasets," **2012** no. 6, (June, 2012) 014, arXiv:1010.0048 [astro-ph.CO].

[369] B. D. Sherwin and M. Schmittfull, "Delensing the CMB with the Cosmic Infrared Background," *Phys. Rev. D* **92** no. 4, (2015) 043005, arXiv:1502.05356 [astro-ph.CO].

[370] P. Larsen, A. Challinor, B. D. Sherwin, and D. Mak, "Demonstration of cosmic microwave background delensing using the cosmic infrared background," *Phys. Rev. Lett.* **117** no. 15, (2016) 151102, arXiv:1607.05733 [astro-ph.CO].

[371] J. Carron, A. Lewis, and A. Challinor, "Internal delensing of Planck CMB temperature and polarization," *JCAP* **05** (2017) 035, arXiv:1701.01712 [astro-ph.CO].

[372] J. Carron and A. Lewis, "Maximum a posteriori CMB lensing reconstruction," *Phys. Rev. D* **96** no. 6, (2017) 063510, arXiv:1704.08230 [astro-ph.CO].

[373] J. Carron, "Optimal constraints on primordial gravitational waves from the lensed CMB," *Phys. Rev. D* **99** no. 4, (2019) 043518, arXiv:1808.10349 [astro-ph.CO].

[374] S. Bashinsky and U. Seljak, "Neutrino perturbations in CMB anisotropy and matter clustering," *Phys. Rev.* **D69** (2004) 083002, arXiv:astro-ph/0310198 [astro-ph].

[375] D. Baumann, D. Green, J. Meyers, and B. Wallisch, "Phases of New Physics in the CMB," *JCAP* **1601** (2016) 007, arXiv:1508.06342 [astro-ph.CO].

[376] G. Mangano, G. Miele, S. Pastor, T. Pinto, O. Pisanti, and P. D. Serpico, "Relic neutrino decoupling including flavor oscillations," **729** (2005) 221–234, arXiv:hep-ph/0506164 [hep-ph].

[377] A. D. Linde, "Chaotic Inflation," *Phys. Lett. B* **129** (1983) 177–181.

[378] A. A. Starobinsky, S. Tsujikawa, and J. Yokoyama, "Cosmological perturbations from multifield inflation in generalized Einstein theories," *Nucl. Phys. B* **610** (2001) 383–410, arXiv:astro-ph/0107555.

[379] M. Hindmarsh and T. Kibble, "Cosmic strings," *Rept. Prog. Phys.* **58** (1995) 477–562, arXiv:hep-ph/9411342.

[380] A. Vilenkin, "Cosmic Strings and Domain Walls," *Phys. Rept.* **121** (1985) 263–315.

[381] K. M. Smith, D. Hanson, M. LoVerde, C. M. Hirata, and O. Zahn, "Delensing cmb polarization with external datasets," *Journal of Cosmology and Astroparticle Physics* **2012** no. 06, (2012) 014.

[382] A. Challinor and A. Lewis, "Lensed CMB power spectra from all-sky correlation functions," *Phys. Rev.* **D71** (2005) 103010, arXiv:astro-ph/0502425 [astro-ph].

[383] C. M. Hirata and U. Seljak, "Reconstruction of lensing from the cosmic microwave background polarization," *Phys. Rev. D* **68** (2003) 083002, arXiv:astro-ph/0306354.

[384] W. R. Coulton, P. D. Meerburg, D. G. Baker, S. Hotinli, A. J. Duivenvoorden, and A. van Engelen, "Minimizing gravitational lensing contributions to the primordial bispectrum covariance," *Phys. Rev. D* **101** no. 12, (2020) 123504, arXiv:1912.07619 [astro-ph.CO].

[385] C. Antolini, Y. Fantaye, M. Martinelli, C. Carbone, and C. Baccigalupi, "N-body lensed CMB maps: lensing extraction and characterization," *JCAP* **02** (2014) 039, arXiv:1311.7112 [astro-ph.CO].

[386] J. Liu, J. C. Hill, B. D. Sherwin, A. Petri, V. Böhm, and Z. Haiman, "CMB lensing beyond the power spectrum: Cosmological constraints from the one-point probability distribution function and peak counts," *Phys. Rev. D* **94** no. 10, (2016) 103501, arXiv:1608.03169 [astro-ph.CO].

[387] V. Böhm, M. Schmittfull, and B. D. Sherwin, "Bias to CMB lensing measurements from the bispectrum of large-scale structure," *Phys. Rev. D* **94** no. 4, (2016) 043519, arXiv:1605.01392 [astro-ph.CO].

[388] T. Namikawa, "CMB Lensing Bispectrum from Nonlinear Growth of the Large Scale Structure," *Phys. Rev. D* **93** no. 12, (2016) 121301, arXiv:1604.08578 [astro-ph.CO].

[389] W.-H. Teng, C.-L. Kuo, and J.-H. Proty Wu, "Cosmic Microwave Background Delensing Revisited: Residual Biases and a Simple Fix," *arXiv e-prints* (Feb., 2011) arXiv:1102.5729, arXiv:1102.5729 [astro-ph.CO].

[390] B. D. Sherwin and S. Das, "CMB Lensing - Power Without Bias," *arXiv e-prints* (Nov., 2010) arXiv:1011.4510, arXiv:1011.4510 [astro-ph.CO].

[391] T. Namikawa and R. Nagata, "Lensing reconstruction from a patchwork of polarization maps," *JCAP* **09** (2014) 009, arXiv:1405.6568 [astro-ph.CO].

[392] T. Namikawa, "CMB internal delensing with general optimal estimator for higher-order correlations," *Phys. Rev. D* **95** no. 10, (2017) 103514, arXiv:1703.00169 [astro-ph.CO].

[393] A. B. Lizancos, A. Challinor, and J. Carron, "Impact of internal-delensing biases on searches for primordial B-modes of CMB polarisation," arXiv:2007.01622 [astro-ph.CO].

[394] A. Benoit-Lévy, K. M. Smith, and W. Hu, "Non-Gaussian structure of the lensed CMB power spectra covariance matrix," **86** no. 12, (Dec., 2012) 123008, arXiv:1205.0474 [astro-ph.CO].

[395] T. L. Smith and D. Grin, "Probing a panoply of curvaton-decay scenarios using CMB data," *Phys. Rev.* **D94** no. 10, (2016) 103517, arXiv:1511.07431 [astro-ph.CO].

[396] D. Tseliakhovich and C. Hirata, "Relative velocity of dark matter and baryonic fluids and the formation of the first structures," *Phys. Rev.* **D82** (2010) 083520, arXiv:1005.2416 [astro-ph.CO].

[397] N. Dalal, U.-L. Pen, and U. Seljak, "Large-scale BAO signatures of the smallest galaxies," *JCAP* **1011** (2010) 007, arXiv:1009.4704 [astro-ph.CO].

[398] S. Naoz, N. Yoshida, and N. Y. Gnedin, "Simulations of Early Baryonic Structure Formation with Stream Velocity: I. Halo Abundance," *Astrophys. J.* **747** (2012) 128, arXiv:1108.5176 [astro-ph.CO].

[399] D. Tseliakhovich, R. Barkana, and C. Hirata, "Suppression and Spatial Variation of Early Galaxies and Minihalos," *Mon. Not. Roy. Astron. Soc.* **418** (2011) 906, arXiv:1012.2574 [astro-ph.CO].

[400] T. Greif, S. White, R. Klessen, and V. Springel, "The Delay of Population III Star Formation by Supersonic Streaming Velocities," *Astrophys. J.* **736** (2011) 147, arXiv:1101.5493 [astro-ph.CO].

[401] M. McQuinn and R. M. O'Leary, "The impact of the supersonic baryon-dark matter velocity difference on the z 20 21cm background," *Astrophys. J.* **760** (2012) 3, arXiv:1204.1345 [astro-ph.CO].

[402] A. Stacy, V. Bromm, and A. Loeb, "Effect of Streaming Motion of Baryons Relative to Dark Matter on the Formation of the First Stars," *Astrophys. J.* **730** no. 1, (2011) L1, arXiv:1011.4512 [astro-ph.CO].

[403] A. Fialkov, R. Barkana, D. Tseliakhovich, and C. M. Hirata, "Impact of the Relative Motion between the Dark Matter and Baryons on the First Stars," *Mon. Not. Roy. Astron. Soc.* **424** (2012) 1335–1345, arXiv:1110.2111 [astro-ph.CO].

[404] J. Yoo, N. Dalal, and U. Seljak, "Supersonic Relative Velocity Effect on the Baryonic Acoustic Oscillation Measurements," *JCAP* **1107** (2011) 018, arXiv:1105.3732 [astro-ph.CO].

[405] J. R. Pritchard and A. Loeb, "21-cm cosmology," *Rept. Prog. Phys.* **75** (2012) 086901, arXiv:1109.6012 [astro-ph.CO].

[406] R. Barkana, "The Rise of the First Stars: Supersonic Streaming, Radiative Feedback, and 21-cm Cosmology," *Phys. Rept.* **645** (2016) 1–59, arXiv:1605.04357 [astro-ph.CO].

[407] J. B. Muñoz, "Robust Velocity-induced Acoustic Oscillations at Cosmic Dawn," *Phys. Rev.* **D100** no. 6, (2019) 063538, arXiv:1904.07881 [astro-ph.CO].

[408] D. R. DeBoer *et al.*, "Hydrogen Epoch of Reionization Array (HERA)," *Publ. Astron. Soc. Pac.* **129** no. 974, (2017) 045001, arXiv:1606.07473 [astro-ph.IM].

[409] R. Braun, A. Bonaldi, T. Bourke, E. Keane, and J. Wagg, "Anticipated Performance of the Square Kilometre Array – Phase 1 (SKA1)," *arXiv e-prints* (Dec., 2019) arXiv:1912.12699, arXiv:1912.12699 [astro-ph.IM].

[410] **SKA** Collaboration, D. J. Bacon *et al.*, "Cosmology with Phase 1 of the Square Kilometre Array: Red Book 2018: Technical specifications and performance forecasts," *Submitted to: Publ. Astron. Soc. Austral.* (2018) , arXiv:1811.02743 [astro-ph.CO].

[411] Y. B. Zel'Dovich, "Reprint of 1970A&A.....5...84Z. Gravitational instability: an approximate theory for large density perturbations.," **500** (Mar., 1970) 13–18.

[412] R. K. Sheth and G. Tormen, "Large-scale bias and the peak background split," **308** no. 1, (Sept., 1999) 119–126, arXiv:astro-ph/9901122 [astro-ph].

[413] S. Seager, D. D. Sasselov, and D. Scott, "RECFAST: Calculate the Recombination History of the Universe," June, 2011.

[414] A. Mesinger, S. Furlanetto, and R. Cen, "21CMFAST: a fast, seminumerical simulation of the high-redshift 21-cm signal," **411** no. 2, (Feb., 2011) 955–972, arXiv:1003.3878 [astro-ph.CO].

[415] J. C. Pober, A. R. Parsons, D. R. DeBoer, P. McDonald, M. McQuinn, J. E. Aguirre, Z. Ali, R. F. Bradley, T.-C. Chang, and M. F. Morales, "The Baryon Acoustic Oscillation Broadband and Broad-beam Array: Design Overview and Sensitivity Forecasts," *Astron. J.* **145** (2013) 65, arXiv:1210.2413 [astro-ph.CO].

[416] J. C. Pober *et al.*, "What Next-Generation 21 cm Power Spectrum Measurements Can Teach Us About the Epoch of Reionization," *Astrophys. J.* **782** (2014) 66, arXiv:1310.7031 [astro-ph.CO].

[417] J. Pober, "21cmSense: Calculating the sensitivity of 21cm experiments to the EoR power spectrum," Sept., 2016.

[418] A. Liu, A. R. Parsons, and C. M. Trott, "Epoch of reionization window. I. Mathematical formalism," **90** no. 2, (July, 2014) 023018, arXiv:1404.2596 [astro-ph.CO].

[419] A. Liu, A. R. Parsons, and C. M. Trott, "Epoch of reionization window. II. Statistical methods for foreground wedge reduction," **90** no. 2, (July, 2014) 023019, arXiv:1404.4372 [astro-ph.CO].

[420] A. R. Parsons, A. Liu, J. E. Aguirre, Z. S. Ali, R. F. Bradley, C. L. Carilli, D. R. DeBoer, M. R. Dexter, N. E. Gugliucci, D. C. Jacobs, P. Klima, D. H. E. MacMahon, J. R. Manley, D. F. Moore, J. C. Pober, I. I. Stefan, and W. P. Walbrugh, "New Limits on 21 cm Epoch of Reionization from PAPER-32 Consistent with an X-Ray Heated Intergalactic Medium at z = 7.7" **788** no. 2, (June, 2014) 106, arXiv:1304.4991 [astro-ph.CO].

[421] L. Koopmans *et al.*, "The Cosmic Dawn and Epoch of Reionization with the Square Kilometre Array," *PoS* **AASKA14** (2015) 001, arXiv:1505.07568 [astro-ph.CO].

[422] J. S. Dillon and A. R. Parsons, "Redundant Array Configurations for 21 cm Cosmology," **826** no. 2, (Aug., 2016) 181, arXiv:1602.06259 [astro-ph.IM].

[423] A. P. Beardsley, M. F. Morales, A. Lidz, M. Malloy, and P. M. Sutter, "Adding Context to James Webb Space Telescope Surveys with Current and Future 21 cm Radio Observations," **800** no. 2, (Feb., 2015) 128, arXiv:1410.5427 [astro-ph.CO].

[424] S. C. Hotinli, M. Kamionkowski, and A. H. Jaffe, "The search for anisotropy in the gravitational-wave background with pulsar-timing arrays," *Open J. Astrophys.* **2** no. 1, (2019) 8, arXiv:1904.05348 [astro-ph.CO].

[425] R. S. Foster and D. C. Backer, "Constructing a Pulsar Timing Array," **361** (Sept., 1990) 300.

[426] M. Maggiore, "Gravitational wave experiments and early universe cosmology," *Phys. Rept.* **331** (2000) 283–367, arXiv:gr-qc/9909001.

[427] S. Burke-Spolaor, "Gravitational-Wave Detection and Astrophysics with Pulsar Timing Arrays," arXiv:1511.07869 [astro-ph.IM].

[428] A. N. Lommen, "Pulsar timing arrays: the promise of gravitational wave detection," *Rept. Prog. Phys.* **78** no. 12, (2015) 124901.

[429] G. Hobbs and S. Dai, "Gravitational wave research using pulsar timing arrays," *Natl. Sci. Rev.* **4** no. 5, (2017) 707–717, arXiv:1707.01615 [astro-ph.IM].

[430] N. Yunes and X. Siemens, "Gravitational-Wave Tests of General Relativity with Ground-Based Detectors and Pulsar Timing-Arrays," *Living Rev. Rel.* **16** (2013) 9, arXiv:1304.3473 [gr-qc].

[431] G. Hobbs, "The Parkes Pulsar Timing Array," *Class. Quant. Grav.* **30** (2013) 224007, arXiv:1307.2629 [astro-ph.IM].

[432] R. N. Manchester, G. Hobbs, M. Bailes, W. A. Coles, W. van Straten, M. J. Keith, R. M. Shannon, *et al.*, "The Parkes Pulsar Timing Array Project," **30** (Jan., 2013) e017, arXiv:1210.6130 [astro-ph.IM].

[433] **NANOGRAV** Collaboration, Z. Arzoumanian *et al.*, "The NANOGrav 11-year Data Set: Pulsar-timing Constraints On The Stochastic Gravitational-wave Background," *Astrophys. J.* **859** no. 1, (2018) 47, arXiv:1801.02617 [astro-ph.HE].

[434] L. Lentati *et al.*, "European Pulsar Timing Array Limits On An Isotropic Stochastic Gravitational-Wave Background," *Mon. Not. Roy. Astron. Soc.* **453** no. 3, (2015) 2576–2598, arXiv:1504.03692 [astro-ph.CO].

[435] J. P. W. Verbiest, Lentati, *et al.*, "The International Pulsar Timing Array: First data release," **458** no. 2, (May, 2016) 1267–1288, arXiv:1602.03640 [astro-ph.IM].

[436] S. Detweiler, "Pulsar timing measurements and the search for gravitational waves," **234** (Dec., 1979) 1100–1104.

[437] M. V. Sazhin, "Opportunities for detecting ultralong gravitational waves," **22** (Feb., 1978) 36–38.

[438]

[439] M. Rajagopal and R. W. Romani, "Ultralow frequency gravitational radiation from massive black hole binaries," *Astrophys. J.* **446** (1995) 543–549, arXiv:astro-ph/9412038.

[440] A. H. Jaffe and D. C. Backer, "Gravitational waves probe the coalescence rate of massive black hole binaries," *Astrophys. J.* **583** (2003) 616–631, arXiv:astro-ph/0210148.

[441] L. G. Book and E. E. Flanagan, "Astrometric Effects of a Stochastic Gravitational Wave Background," *Phys. Rev. D* **83** (2011) 024024, arXiv:1009.4192 [astro-ph.CO].

[442] C. J. Moore, D. P. Mihaylov, A. Lasenby, and G. Gilmore, "Astrometric Search Method for Individually Resolvable Gravitational Wave Sources with Gaia," *Phys. Rev. Lett.* **119** no. 26, (2017) 261102, arXiv:1707.06239 [astro-ph.IM].

[443] D. P. Mihaylov, C. J. Moore, J. R. Gair, A. Lasenby, and G. Gilmore, "Astrometric Effects of Gravitational Wave Backgrounds with non-Einsteinian Polarizations," *Phys. Rev. D* **97** no. 12, (2018) 124058, arXiv:1804.00660 [gr-qc].

[444] L. O'Beirne and N. J. Cornish, "Constraining the Polarization Content of Gravitational Waves with Astrometry," *Phys. Rev. D* **98** no. 2, (2018) 024020, arXiv:1804.03146 [gr-qc].

[445] W. Qin, K. K. Boddy, M. Kamionkowski, and L. Dai, "Pulsar-timing arrays, astrometry, and gravitational waves," *Phys. Rev. D* **99** no. 6, (2019) 063002, arXiv:1810.02369 [astro-ph.CO].

[446] B. Allen and A. C. Ottewill, "Detection of anisotropies in the gravitational wave stochastic background," *Phys. Rev. D* **56** (1997) 545–563, arXiv:gr-qc/9607068.

[447] A. Sesana, A. Vecchio, and M. Volonteri, "Gravitational waves from resolvable massive black hole binary systems and observations with Pulsar Timing Arrays," *Mon. Not. Roy. Astron. Soc.* **394** (2009) 2255, arXiv:0809.3412 [astro-ph].

[448] V. Ravi, J. Wyithe, G. Hobbs, R. Shannon, R. Manchester, D. Yardley, and M. Keith, "Does a 'stochastic' background of gravitational waves exist in the pulsar timing band?," *Astrophys. J.* **761** (2012) 84, arXiv:1210.3854 [astro-ph.CO].

[449] N. J. Cornish and A. Sesana, "Pulsar Timing Array Analysis for Black Hole Backgrounds," *Class. Quant. Grav.* **30** (2013) 224005, arXiv:1305.0326 [gr-qc].

[450] L. Z. Kelley, L. Blecha, L. Hernquist, A. Sesana, and S. R. Taylor, "Single Sources in the Low-Frequency Gravitational Wave Sky: properties and time to detection by pulsar timing arrays," *Mon. Not. Roy. Astron. Soc.* **477** no. 1, (2018) 964–976, arXiv:1711.00075 [astro-ph.HE].

[451] S. Kuroyanagi, K. Takahashi, N. Yonemaru, and H. Kumamoto, "Anisotropies in the gravitational wave background as a probe of the cosmic string network," *Phys. Rev. D* **95** no. 4, (2017) 043531, arXiv:1604.00332 [astro-ph.CO].

[452] M. Anholm, S. Ballmer, J. D. Creighton, L. R. Price, and X. Siemens, "Optimal strategies for gravitational wave stochastic background searches in pulsar timing data," *Phys. Rev. D* **79** (2009) 084030, arXiv:0809.0701 [gr-qc].

[453] C. M. Mingarelli, T. Sidery, I. Mandel, and A. Vecchio, "Characterizing gravitational wave stochastic background anisotropy with pulsar timing arrays," *Phys. Rev. D* **88** no. 6, (2013) 062005, arXiv:1306.5394 [astro-ph.HE].

[454] J. Gair, J. D. Romano, S. Taylor, and C. M. F. Mingarelli, "Mapping gravitational-wave backgrounds using methods from CMB analysis: Application to pulsar timing arrays," *Phys. Rev. D* **90** no. 8, (2014) 082001, arXiv:1406.4664 [gr-qc].

[455] S. Taylor *et al.*, "Limits on anisotropy in the nanohertz stochastic gravitational-wave background," *Phys. Rev. Lett.* **115** no. 4, (2015) 041101, arXiv:1506.08817 [astro-ph.HE].

[456] A. Hajian and T. Souradeep, "Measuring statistical isotropy of the CMB anisotropy," *Astrophys. J. Lett.* **597** (2003) L5–L8, arXiv:astro-ph/0308001.

[457] A. Hajian and T. Souradeep, "The Cosmic microwave background bipolar power spectrum: Basic formalism and applications," arXiv:astro-ph/0501001.

[458] N. Joshi, S. Jhingan, T. Souradeep, and A. Hajian, "Bipolar Harmonic encoding of CMB correlation patterns," *Phys. Rev. D* **81** (2010) 083012, arXiv:0912.3217 [astro-ph.CO].

[459] W. J. Kaufmann, "Redshift Fluctuations arising from Gravitational Waves," **227** no. 5254, (July, 1970) 157–158.

[460] F. B. Estabrook and H. D. Wahlquist, "Response of Doppler spacecraft tracking to gravitational radiation.," *General Relativity and Gravitation* **6** no. 5, (Oct., 1975) 439–447.

[461] M. V. Sazhin, "Opportunities for detecting ultralong gravitational waves," **22** (Feb., 1978) 36–38.

[462] S. Detweiler, "Pulsar timing measurements and the search for gravitational waves," **234** (Dec., 1979) 1100–1104.

[463] E. Roebber and G. Holder, "Harmonic space analysis of pulsar timing array redshift maps," *Astrophys. J.* **835** no. 1, (2017) 21, arXiv:1609.06758 [astro-ph.CO].

[464] L. G. Book, M. Kamionkowski, and T. Souradeep, "Odd-parity bipolar spherical harmonics," **85** no. 2, (Jan., 2012) 023010, arXiv:1109.2910 [astro-ph.CO].

[465] A. R. Pullen and M. Kamionkowski, "Cosmic Microwave Background Statistics for a Direction-Dependent Primordial Power Spectrum," *Phys. Rev. D* **76** (2007) 103529, arXiv:0709.1144 [astro-ph].

[466] S. Das, B. D. Wandelt, and T. Souradeep, "Bayesian inference on the sphere beyond statistical isotropy," *JCAP* **10** (2015) 050, arXiv:1509.07137 [astro-ph.CO].

[467] S. Shaikh, S. Mukherjee, S. Das, B. D. Wandelt, and T. Souradeep, "Joint Bayesian Analysis of Large Angular Scale CMB Temperature Anomalies," *JCAP* **08** (2019) 007, arXiv:1902.10155 [astro-ph.CO].

[468] C. Conneely, A. H. Jaffe, and C. M. Mingarelli, "On the Amplitude and Stokes Parameters of a Stochastic Gravitational-Wave Background," *Mon. Not. Roy. Astron. Soc.* **487** no. 1, (2019) 562–579, arXiv:1808.05920 [astro-ph.CO].

[469] Y. Ali-Haïmoud, T. L. Smith, and C. M. Mingarelli, "Fisher formalism for anisotropic gravitational-wave background searches with pulsar timing arrays," arXiv:2006.14570 [gr-qc].

[470] T. Okamoto and W. Hu, "Cosmic microwave background lensing reconstruction on the full sky," *Physical Review D* **67** no. 8, (2003) 083002.